ELECTROHYDRODYNAMIC DEPOSITION AND PATTERNING OF NANO-HYDROXYAPATITE FOR BIOMEDICAL APPLICATIONS

Xiang Li

A thesis submitted for the degree of

Doctor of Philosophy

Department of Mechanical Engineering
University College London
2009

Declaration

I, Xiang Li, confirm that the work presented in this thesis is my own. Where information has been derived from other sources, I confirm that this has been indicated in the thesis.

Xiang Li

Abstract

Electrohydrodynamic atomisation (EHDA) spraying is a promising materials deposition technique as it allows uniform and regular deposition, and offers a range of other advantages, such as low cost compared with other current techniques, easy set-up, high deposition rate, ambient temperature processing and the capability to generate specific surface topographies. This research is aimed at using EHDA spraying to produce hydroxyapatite (HA) deposition with desirable chemical, topographical and biological characteristics for bone implant. In principle, the EHDA process involves the flow of liquid/suspension from a needle under the influence of an electric field which results jetting and droplet formation.

In this work, phase-pure nano-sized hydroxyapatite (nHA) was synthesised and taken up in ethanol to prepare a suitable suspension for electrohydrodynamic flow processing. A range of key EHDA process control parameters, such as needle size, needle to substrate distance, suspension flow rate, applied voltage and spraying time, were studied and optimised. A uniform nHA coating with nanometer scale topographical features was successfully prepared on a commercially pure titanium substrate. Furthermore, due to the significance of the surface structure to the cellular response, a novel technique, namely template-assisted electrohydrodynamic atomisation (TAEA) spraying, was innovated to prepare a well-defined surface topography for guiding cell attachment, spread and growth of osteoblasts. A range of precise micro-scale uniform nHA geometries with high resolution were prepared on implants materials. Finally, to systematically investigate the effect of needle geometry to the electrospraying process, which has not been documented in the research field of this technique, an in-depth study was carried out to uncover the relationship between the needle exit angle and the droplet relic size. The droplet relic size, which is crucial for the deposition properties, has been significantly reduced via engineering the needle geometry during the electrospraying process.

The results of this work have demonstrated that EHDA deposition routes show great potential for the commercial preparation of nHA coatings and patterns for bone implants with enhanced bioactivity.

Acknowledgements

This thesis would not have been possible without the support of many people.

First of all, I would like to express my most sincere appreciation to Professor Mohan Edirisinghe and Dr. Jie Huang for their trust, guidance, advice and great support throughout this research work. No matter how I didn't do well in the beginning of my research, they had been extremely patient, hortative, and always enthusiastic to teach, and listen to my views. It was my fortune to have this precious opportunity to study and work with these two greatest supervisors in the world.

I am very grateful to Furlong Research Charitable Foundation for providing me a research scholarship which enabled me to do this research. I also thank Professor William Bonfield for the precious suggestions, great support and help during my research in the past years.

I am also thankful to my colleagues in my lovely research group, especially Dr. Zeeshan, Dr. Rafiq, Dr. Sunthar, Dr. Dongyang Sun, Dr. Dazhi Wang, Dr. Suren, Miss Anushini and Mr. Farook. They have been very understanding and helpful during my research work and life. It was my pleasure to work with them.

Last but not least, I would like to give a special thank to my wife, Lulu Pan, for her love, belief, support and help in the past years, without which I would not be brave enough to face this challenge in my life. I am so happy to spend the rest of my life with you forever. My special thanks also go to my presents, Mr Jiankang Li and Mrs Xiuying Sun, the kindest and greatest parents in the world. They've been working so hard to support my life and study in the past 28 years, but never asking for anything back. I hope I could be a son that both of you can be proud of in my life.

Without these important people present in my life, I can't have these achievements.

Thank you all.

Publications and Conference Presentations

Journal articles:

1. **Li X.**, Huang J. and Edirisinghe M.J., Novel patterning of nano-bioceramics: template-assisted electrohydrodynamic atomisation spraying. *Journal of Royal Society Interface,* vol. 5, pp. 253-257, Feb 2008.

2. **Li X.**, Ahmad Z., Huang J. and Edirisinghe M.J. Electrohydrodynamic coating of metal with nano-sized hydroxyapatite. *Journal of Biomedical Materials and Engineering,* vol. 17, pp. 335-346, 2007.

3. **Li X.**, Huang J. and Edirisinghe M.J., Development of nano-hydroxyapatite coating by electrohydrodynamic atomization spraying. *Journal of Material Science: Materials in Medicine.* vol. 19, pp. 1545-1551, 2007.

4. **Li X.**, Huang J. and Edirisinghe M.J., Development of template-assisted electrohydrodynamic atomization spraying for nanoHA patterning. *Key Engineering Materials,* vols. 361-363, pp 585 -588, Feb 2008.

5. **Li X**., Koller G.P., Huang J., Di Silvio L., Renton T., Edirisinghe M.J., Esat M. and Bonfield W., Effect of heat treatment of nano-hydroxyapatite coatings prepared using electrohydrodynamic deposition. *International Journal of Nano and Biomaterials*, in press.

6. **Li X**., Koller G.P., Huang J., Di Silvio L., Renton T., Esat M., Bonfield W., Edirisinghe M., A Novel Jet-based nHA Patterning Technique for Osteoblast Guidance. *Journal of Royal Society Interface*, in press.

7. **Li X.**, Huang J., Esat M., Bonfield W., Edirisinghe M., Generation of Small Droplet Relics from a Large Nozzle. In preparation.

International Patent Application:

Li X., Huang J., Edirisinghe M.J., Bonfield W. and Esat M. 'A novel method of creating an interlocked (high bond strength) bioactive coating on metallic substrates for orthopaedic applications', UK 0821927.1, December 2008.

Conference presentations:

1. **Li X.,** Huang J. and Edirisinghe M.J., Novel patterning of nano-bioceramics: template-assisted electrohydrodynamic atomization spraying. Oral presentation accepted by the 20th International Symposium of Ceramics in Medicine, University of Nantes, France, 2007 October.

2. **Li X**., Huang J. and Edirisinghe M.J., Development and optimisation of nano-hydroxyapatite coating by electrohydrodynamic atomisation spraying. Poster presentation accepted by the 21st European Conference on Biomaterials, Brighton, U.K., 2007 September.

3. **Li X**., Huang J. and Edirisinghe M.J., Development of template-assisted electrohydrodynamic atomization spraying for nanoHA patterning. Poster presentation accepted by UK Society for Biomaterials 6th Annual Conference, King's College, U.K., 2007 July.

4. **Li X**., Koller G.P., Huang J., Edirisinghe M.J., Bonfield W., Di Silvio L. and Esat M., Electrospraying of hydroxyapatite with controlled surface morphology to enhance cellular response. Poster presentation accepted by 8th World Biomaterials Congress, Amsterdam, The Netherlands. 2008, May

Table of Contents

Figure List

Table List

Chapter 1

Introduction

1.1 Background

There is an increasing demand for biomedical implants due to the increase in ageing population worldwide. In U.K., there were 43,000 hip replacements carried out in 2003 bringing mobility and relief from pain for patients, and this figure is believed to keep on rising. Hip prosthesis is designed to simulate the human anatomy and comprises an acetabular cup implanted into the hip and a femoral stem placed into the femur as shown in **Figure 1.1**. A number of different materials, such as 316L stainless steel, titanium, titanium alloy etc., have been used to replace many different parts of the human body. One of the most commonly performed orthopaedic procedures worldwide using these materials are total hip replacement as well as dental implants. However, studies have indicated that while metals provide satisfactory mechanical compatibility, the bioinertness of the metal or stress concentration related to the high stiffness of the metallic implant compared with that of bone may cause loosening at the bone-metal interface. Such processes could affect the long-term stability of the implant after surgery. Thus, the biomedical implants were carried out more successfully for elderly people. It is however still a challenge for the young who require much longer implant serving period.

In view of the afore-mentioned situation, considerable research interest to develop a new generation of biomedical materials with enhanced bioactivity is ongoing. Hydroxyapatite (HA), $Ca_{10}(PO_4)_6(OH)_2$, is similar in composition to bone mineral and

has been found to be bioactive and encourage bone ingrowth (Hench, 1998; Coathup *et. al.,* 2000; Capello *et. al.,* 1997). This material could be used not only in hip replacement, but also in other parts of the body such as the knee, shoulder or in dental applications. However, its poor mechanical properties limit its use in direct implantation. To combine the biological performance of HA and the mechanical properties of traditional metallic implant, the most successful approach is to apply a HA coating on the metallic implant surface. In additional, attention has also been focused on creating a well-defined surface topography of biomaterials, a feature that is known to initially affect biological response (Curis and Wilkinson, 1997). This suggests that cell activity could be up-regulated through optimization of the surface properties of the substrates.

To fulfil the needs, various coating techniques, including plasma spraying (Berndt *et. al*., 1990; deGroot *et. al*., 1987; Sun *et. al*., 2001), dip coating (Mavis and Tas, 2000), sputtering (Ozeki *et. al*., 2002), biomimetic coating and pulsed laser deposition (Cotell *et. al*., 1992), have been utilized to deposit bioceramic coatings like HA onto implant surface. Of these methods, plasma spraying is the most commonly used method of coating application owing to its ability to process uniform and continuous coating. However, there still remain a number of concerns regarding the properties of coatings produced using this method. Plasma-sprayed HA coatings tend to resolve and detach over time (Radin and Ducheyne, 1992), which will influence the long-term stability of the implants. Decomposition of HA coating into other calcium phosphate phases, such as tricalcium phosphate (TCP), alpha tricalcium phosphate (α-TCP) etc., has been reported (Radin and Ducheyne, 1992), which will again influence the stability of the implant in the biological fluid. Furthermore, all these coating techniques are still not capable of controlling and therefore up-regulating the surface topography of HA coated implants.

Electrohydrodynamic atomisation (EHDA) spraying, also known as electrospraying or electrostatic atomisation, is a promising technique as it allows uniform and regular deposition. EHDA processing is a phenomenon that a liquid flow subjected to a high voltage, breaks up into droplets. The liquid under electric stress due to high potential difference between the needle and the ground electrode, emit plume of droplets which is called as spray. This phenomenon was first reported as far as in the 18th century by Zeleny (Zeleny, 1914). Taylor (1964) was the first to calculate analytically the process by balancing the surface tension force and the electric field force acting on the droplet at the end of the needle. Subsequently, many researchers contributed to the understanding of this phenomenon (Jone and Thong, 1971; Ganan-Calvo, 1997; Hartman *et al.*, 1999a&b). After the discovery of mass spectroscopy of large biomolecules by Fenn *et al*. (1989), this phenomenon had become a well-established procedure for processing materials for different applications.

The main reported factors affecting this process are flow rate, applied voltage and liquid properties (e.g. density, electrical conductivity, surface tension and viscosity). For a specific liquid at a specific regime of these factors different electrohydrodynamic modes can take place, such as spindle mode, cone-jet mode and multi-jet mode. The mode focused in this research is the cone-jet mode due to its stability and ability to produce monodisperse droplets. This mode usually takes place at relative low flow rates, with droplets formed at the tip of the needle. The liquid meniscus shape is transformed into conical shape as a result of the electric force on the surface induced by an applied voltage between the needle and the ground electrode. Electrohydrodynamic atomisation in the cone-jet mode can be described as three different processes. The first process is acceleration of the liquid in the liquid cone. This process is the result of the force

balance of surface tension, viscosity and electric force in the liquid surface inertia and viscous stresses. During this process conical shaped liquid is formed. The second process is the break up of the jet into droplets, which is also called droplets production process. In this process a highly charged jet is formed at the apex of the cone because of the acceleration of the surface charge. The accelerated liquid in the jet further breaks up into droplets. The third process is the development of the spraying after droplet production. Secondary and satellites may be accompanied with the production of the primary droplets (Hartman *et al.*, 2000; Cloupeau and Prunet-Foch, 1989; Jaworek and Krupa, 1998; Ganan-Calvo, 1999).

As a jet-based technique, the liquid droplet size that EHDA spraying can achieve is crucial for the deposition properties. The primary droplet size in the stable cone-jet mode is independent of the applied voltage and depends mainly on the liquid flow rate. The secondary droplets also depend on the liquid physical properties in addition to the liquid flow rate. There exist an optimum flow rate, the minimum flow rate and the maximum flow rate for the stable cone-jet mode, at which the droplet size distribution with minimum standard deviation can be achieved (Cloupeau and Prunet-Foch, 1989). The primary droplet size can range from submicron to hundreds of micrometers depending on the droplet production process parameters (Hartman *et al.*, 2000). After the jet break-up, a conical spraying is observed with secondary droplets on the outer regions and primary droplets in the inner regions. Electrical interactions between highly charged droplets and the difference in inertia due to size difference are the main reasons behind this ‘size segregation effect’ in the conical spray.

Compared to other current coating techniques, EHDA spraying offers a range of advantages, such as low cost, easy set-up, high deposition rate, room temperature

process, suitability for industrial production. Furthermore, spraying the selected substrate area via masking the substrate during the process makes it possible to pattern specific features using EHDA spraying. A novel technique, namely template-assisted electrohydrodynamic atomisation (TAEA) spraying, was innovated to prepare a well-defined HA surface topography for guiding cellular attachment, spread and growth of osteoblasts. It is therefore the intention of this project to process HA depositions and patterns on the metal surfaces using electrohydrodynamic atomisation spraying.

1.2 Aims and objectives of the research

The primary aim of this research is to understand the fundamentals of electrohydrodynamic processing to utilise this route to prepare hydroxyapatite (HA) depositions with desirable chemical, topographical and biological characteristics for bone implants. Two derived techniques, electrohydrodynamic (EHDA) deposition and template-assisted electrohydrodynamic atomisation (TAEA) spraying, are aimed to be investigated and developed so that the uniform HA coatings can be deposited and the precisely well-defined HA patterns can be prepared to guide the osteoblasts orientation. Furthermore, the research also aims at an in-depth study of the needle geometry effect to electrospraying process, which still haven't been well documented in the past electrospraying related studies, to understand the fundamentals in improving the quality of the depositions and patterns. To achieve these objectives, several studies in different stages are necessary, which will be arranged into three separate sections as follows.

Firstly, a nano-hydroxyapatite (nHA) suspension is prepared and the physical properties of such suspension are studied to verify its compatibility with the electrohydrodynamic processing before the actual nHA deposition preparation. The study and optimisation of

a range core processing parameters, which are needle to substrate distance, suspension flow rate, applied voltage and spraying time, need to be carried out since they are essential to the uniform nHA coating preparation. To improve the mechanical properties of nHA coated Ti plate, a study of heat treatment is needed in order to uncover the suitable post treatment condition for the nHA deposition preparation. The scanning electron microscope (SEM) and X-ray diffraction (XRD) are used to characterise the nHA deposition morphology and composition. The *in-vitro* study using a human osteoblast (HOB) will enable to characterise the biological properties, such as toxicity, biocompatibility and bioactivity, of the nHA coated Ti plates prepared.

Secondly, to investigate TAEA spraying technique for nHA patterning process needs to achieve the following objectives. Essentially, the suitable ground electrode configuration for TAEA patterning needs to be investigated. To improve the resolution of the nHA patterns (the minimum dimension of the patterns that can be achieved), the fundamental mechanism of the patterning process needs to be studied, and utilised to optimise the patterning procedure. The effect of the nHA pattern characteristics (topography and dimension) to the attachment and orientation of the osteoblasts is to be investigated using an *in-vitro* study.

As afore-mentioned, as a novel coating technique, reducing droplet size and its standard deviation is crucial for improving the quality of the nHA coating and the resolution of the nHA patterns. The geometry of needle is important to the electric field distribution and therefore the electrical force at the needle tip, which is actually the main driver of the electrohydrodynamic spraying. Therefore, the modification of needle geometry is a logically effective way to control the droplet size during EHDA process. To study and investigate its effect, a range of needles with different tip angles and diameters are

going to be used for EHDA spraying. The condition for achieving the stable cone-jet mode using each individual needle is needed for the subsequent analysis. The relationship between the droplet relic size distribution and needle tip angle and its mechanism are going to be investigated and studied. Based on the study above, a nHA pattern using TAEA spraying with the chosen modified needle is going to be prepared and characterised to prove the findings.

1.3 Structure of the thesis

Chapter 1 introduces the project background and the electrohydrodynamic processing route. The chapter briefly introduces some drawbacks of the current implant materials prepared using the traditional techniques and requirements of the bone implant materials, and briefly reviews the fundamental theory and basic process of EHDA spraying and TAEA spraying. It also introduces the aims, the objectives and the scope of this research.

Chapter 2 is dedicated to a critical literature review associated with this research. The natural human bone tissue and current bone implant related biomaterials, including Ti and hydroxyapatite (HA) used in this research, are introduced and discussed to specify the objectives of this research. The current coating and patterning techniques for bone implant materials processing are discussed subsequently to explain the motivation of the development and utilisation of EHDA processing and its derived patterning technique. To understand the mechanism of EHDA processing, various modes of this processing are discussed in details. The jet break-up mechanism and the droplet production processes and controlling parameters in stable cone-jet mode are also discussed in this chapter. Finally, the chapter also states the properties influencing the

electrohydrodynamic processing including liquid physical properties and processing parameters.

Chapter 3 gives a detailed description of the experimental procedures. This chapter discusses the materials and preparation of the nHA suspension and TiO_2 sol used for the research carried out in chapter 4, 5 and 6. The characterisation techniques and procedures are described. The equipment used for the electrohydrodynamic processing is discussed in details. Details of the designs for the template-assisted electrohydrodynamic processing development are also described.

Chapter 4 elucidates the work of characterisation and electrohydrodynamic deposition of nHA suspension. In this chapter, the first part is to investigate the physical properties of the nHA suspension and compare such properties with the pure ethanol which is a typical liquid for electrohydrodynamic processing. Subsequently, the chapter also includes a systematic investigation of the optimised condition for electrospraying the nHA suspension and post heat treatment condition for uniform nHA coatings. The characterisation work in this chapter is constructed by the coating properties (surface morphology and chemistry composition) characterisation using the electron scanning microscope and X-ray diffraction, and *in-vitro* study using human osteoblast (HOB) to characterise the biological properties, such as cytotoxicity, biocompatibility and bioactivity.

Chapter 5 discusses the work of development and improvement of template-assisted electrohydrodynamic (TAEA) spraying for nHA patterning process. The research in this part reveals the patterning process is highly dependant on the ground electrode configuration and the spraying droplet size that produced during spraying. Subsequently,

a comprehensive study is also included in the chapter to uncover the mechanism of this patterning process and improve the nHA pattern resolution (the minimum dimension of the pattern that can be achieved). The surface topography and chemistry composition of all nHA patterns that prepared are also characterised in this chapter using electron scanning microscope (SEM) and X-ray diffraction (XRD), and finally the effect of the prepared nHA patterns to the cell attachment, growth and orientation is characterised via an in-vitro study using human osteoblast. Based on the findings of the studies above, the relationship between the nHA pattern topography (height and width) and cellular responses is also discussed in last section of this chapter.

Chapter 6 focuses an in-depth study and analysis of the effect of needle geometry to the size of liquid droplet relic produced using electrohydrodynamic processing. Due to the significance of droplet size to the coating uniformity and the pattern resolution, the relationship between the droplet relic size distribution and the needle geometry, such as diameter and needle top angle is going to be quantitatively compared and investigated. The mechanism of this effect will be also concluded in this chapter. Finally, a range of nHA patterns with high resolution are prepared using TAEA processing based the knowledge gained from the study above to further prove the significance of this study.

Chapter 7 makes the comprehensive conclusions based on the investigations carried out in chapters 4, 5 and 6, and sets out the future plan of actions in order to further exploit the research and novel methods to produce thin coatings and high-resolution patterns for biomedical applications. It also addresses the need for further research in this particular field for commercial success.

1.4 Benefits of the research

This research helps the scientific community by strengthening their knowledge about the electrohydrodynamic processing of biomaterials and industrial community by innovative, safe and cheap processing techniques to produce biocompatible coatings and high resolution patterns with improved biological properties for biomedical applications.

In the first part of this research, a nano-hydroxyapatite coating has been successfully produced on the surface of metallic substrates by electrohydrodynamic atomization spraying. The processing parameters for coating have been optimized and the structure of the coating was improved by post-deposition heat treatment. Thus, a uniform bioactive coating of ~ 2 μm has been achieved on a typical substrate used in orthopaedics by a novel method. This is a crucial step forward in obtaining advanced HA coatings for biomedical applications. Also, the coating technique proved to be a simple, fast and economical process that can be implemented for the deposition of nano-biomaterials on a chosen metallic substrate.

In second section of the research, a new method for the creation of topography with bioactive materials has been uncovered and elucidated. Nano-sized HA topographies with different uniform micro-scale patterns have been successfully prepared on non-conducting glass and conducting titanium substrates by a template-assisted electrohydrodynamic (TAEA) spraying. Furthermore, an in-depth study of the novel TAEA process has resulted in improving the resolution of the patterns generated. Mainly by increasing the substrate temperature to 80°C, lines of ~15 μm width have been prepared. In addition, these lines are higher and sharper in comparison to lines deposited at a lower temperature. The *in-vitro* study demonstrated that the HOB cell

behaviour and orientation on these patterns have been controlled and modulated by this patterning technology. TAEA spraying is a promising technique in engineering bioactive surfaces and for generating future implant materials for guided bone tissue regeneration. This is an important forward step in regulating the topographies of bioactive substances on implant surfaces, particularly those of metallic origin.

From a tiny bioceramics coated tooth implant to a huge novel materials coated spaceship, from coating based industry to biological engineering, controlling and reducing a droplet relic size has become more and more important to our lives in the modern society. Electrohydrodynamic atomization has been one of the most common and novel techniques. To improve the material properties to a desired level to suit industrial applications, the reduction of substance droplet relic's size during the process is always a challenge. The final section of this study is to demonstrate the effect of the needle geometry to the liquid droplet relic size during EHDA spraying. In this section, the quantitative relationship between the needle tip angle and the liquid droplet relic size distribution is discussed. This in-depth investigation provides anther different thinking and a simply way of improving the surface properties of implamt.

Figure

Figure 1.1. Hip prosthesis implant inside the hip joint

Chapter 2

Literature Review

Bone is a complex, living tissue that is continuously being torn down and replaced by biologically remodelling in order to adapt to stress requirements. Biomaterial is defined as a material used for the repair and reconstruction of diseased or damaged parts of the muscle-skeletal. In this chapter, a brief history from natural bone properties to different biomaterials and developing trend of the bone implant materials is reviewed. This will help to specify the limitation of the traditional implant materials and coating techniques, and therefore provide the motivation of the study and research of the novel implant material.

Since the introduction of hydroxyapatite coated implants, there have been a number of techniques employed in the deposition of hydroxyapatite to the metallic surface. However, compared to different techniques, attention is paid to EHDA processing due to a range of advantages it offers, such as low cost, easy set-up, high deposition rate and room temperature process. An introduction of the mechanism, classification and characteristics of EHDA spraying technique in detail helps to provide a comprehensive understanding of such process procedure to further investigate the optimized electrospraying process conditions. In addition, the crucial effect of surface morphology to initial cell attachment and the current patterning techniques will be introduced. It provides the motivation for the research and development of well-defined HA pattern processing using template-assisted electrohydrodynamic atomisation (TAEA) processing evolved from EHDA processing. The mechanism of TAEA process for

bioceramic patterning will be also discussed in this chapter to pave the way to the subsequent improvement study for processing the nHA patterns with high resolution.

2.1 Bone

2.1.1 Bone structure

The structure of bone has been classified in to a number of hierarchical levels (**Figure 2.1**). At the macroscopic level, mature bone exists in two main forms: spongy or cancellous bone and compact or cortical bone. Cancellous bone is a cellular material consisting of a connected network of rods or plates. Cancellous bone is present at the ends of long bones while cortical bone forms the diaphysis of bone. In general, the major support bone consists of an outer load bearing shell of cortical bone with a medullary cavity containing cancellous bone towards the bone ends.

On the microscopic level, the mineral-containing fibres (collagen fibres) are arranged into lamellar sheets of thickness around 1 to 7 μm. About 4 to 20 lamellae, which are arranged in concentric rings around the Haversian canal, will form an osteon (Park, 1987). Each adjacent lamella has a different orientation of collagen.

The ultra microstructure of bone has been built up with the mineral component which are apatite mineral crystals and the organic component which are collagen fibres. Calcium phosphate crystals provide the stiffness to the bone. The crystals, which present in the form of plates or needles, are 40 nm to 60 nm long, 20 nm wide and 1.5 to 5 nm thick. Collagen in the form of microfibers can be considered as a matrix. The diameter of the collagen fibres present in bone varies from 100 to 2000 nm. It provides

the toughness and elasticity to bone. As shown in **Figure 2.1**, the apatite crystals lay up parallel to the collagen fibres (Currey, 1983).

2.1.2 Mechanical characteristics of bone

In general, bone combines high strength and modulus of elasticity with ductility which helps bone to absorb sudden impacts. It can be considered as a composite material, formed by mineralized collagen fibres and hydroxyapatite. Organic phase of bone, which is mainly mineralized collagen fibres, exhibits high toughness, low modulus, and other characteristics of polymer materials. And at the meantime, the inorganic components, which mainly exist as hydroxyapatite, provide stiffness to bone. As a result, bone has mechanical properties in-between those of collagen and hydroxyapatite. However, the structure of bone is more complex than a two-phase material and the mechanical properties of bone is influenced by a number of factors, for instance, water content, mineral content (Currey, 1981), bone density, microstructure (*i.e.* cancellous bone or cortical bone), *etc*.

The properties of bone also depend on the direction of applied load with respect to the bone. Studies showed that Young's modulus, tensile and compressive strength are higher in the longitudinal direction than those in the radial or tangential direction (Reilly and Burstein, 1975). Furthermore, It was found that the stiffness of cortical bone decreased as the angle increased in relation to the longitudinal axis of the shaft, while the energy dissipated was also found to increase as the angle increased from 0 to 90^{o} (Bonfield and Grynpas, 1977).

Understanding of the microstructure and properties of the nature bone will help to design suitable materials for replacement.

2.1.3 Bone cells

There are three types of cells in bone tissue that are of special interest: osteoblast, osteocyte and osteoclast, which are responsible for the production, maintenance and absorption of bone, respectively. Osteoblasts are specifically responsible for maintaining normal equilibrium between bone formation and bone absorption, and are also involved directly or indirectly in all forms of skeletal disease. These cells normally present as a plump form. However, they can turn to a much flattened appearance and spread on their flat surfaces parallel to and in close contact with the bone surface when they are not engaged in bone formation. Furthermore, the cells can also present in other morphologies when meeting different surface structures, i.e. it can become elongated to the surface with grooves. The impact of the surface structure to the cellular response will be discussed in later sections. During remodelling, osteoblasts are able to mineralize into calcified tissue layer by layer and subsequently differentiate into other type of cells, osteocytes. Osteocytes are of a spidery shape, and are responsible for sustaining the supply of oxygen, nutrients and minerals throughout the bone. Osteoclasts are cells that absorb the old mineralized matrix though their proteolytic enzymes so that new bone tissue can grow.

2.2 Biomaterials

In 70s, biomaterial was considered as a systematically and pharmacologically inert substances designed for implantation within or incorporation with living systems (Park,

1987). No material implanted in living tissue remains inert (Hench, 1991). Indeed, all materials elicit a response from living tissue. There are mainly four types of tissue-implant response summarized in **Table 2.1**.

Table 2.1. Types of Implant-Tissue Response (Hench, 1998)

If the material is toxic, the surrounding tissue dies;
If the material is non-toxic and biologically active (almost inert), a fibrous tissue of variable thickness forms;
If the material is non-toxic and biologically active (bioactive), an interfacial bond forms;
If the material is non-toxic and dissolves, the surrounding material replaces it

Accordingly, biomaterials have been classified into bioinert, bioactive and biodegradable. Bioinert materials do not show direct contact with the surrounding organic tissue. Bioactive materials form a direct chemical bond with tissue. And, biodegradable materials (resolvable biomaterials) degrade gradually over time and are replaced by the natural host tissue.

Generally, an implant material needs to be nontoxic, noncarcinogenic, strong corrosion resistance in the biological environment and have adequate mechanical strength including fatigue life. The first use of bone implant reportedly dates back to the prehistoric to Greece where it is believed Hippocrates used golden wires to treat bone fracture (Myer, 2003). And, the use of a metallic hip implants was reported 1940 when vitallium, a form of cobalt-chromium, was first implanted in a human being (Teoh,

2004). Until present, the metallic implant materials are still being most commonly utilized for the total hip replacement due to its mechanical strength.

2.2.1 Traditional metallic implant materials

The use of metallic implants has become a well-established approach for nearly a century. The main metals utilized for bone implant applications are 316L stainless steel, cobalt-chromium alloy, commercially pure titanium and its alloy (Ti6Al4V).

2.2.1.1. 316L stainless steels

The increase in chromium content can increase the corrosion resistance of various steel types. By adding more than 12% of chromium, the corrosion-resistant steels are made via the formation of a thin, chemically stable, and passive oxide film. The oxide film forms and heals itself in the presence of oxygen. Steels containing more than 12 percent of chromium are known as stainless steels.

Type 316L has its corrosion resistance improved by adding molybdenum and reducing the carbon content (<0.03%). The advantages of 316L stainless steel for medical implants include an oxide layer wearing on the substance which provides protection against corrosion and high tensile and compressive strengths. Moreover, the price of 316L stainless steels is one-tenth to one-fifth of other typical metallic biomaterials. However, the elastic modulus is substantially higher than that of cortical bone which causes stress shielding. The stress concentration at the implant-bone interface may cause the loosening in the period after the implantation due to the significant difference in the stiffness between the stainless steel and the natural bone. A further disadvantage is

nickel toxicity and corrosion in parts of the body where the oxygen is not sufficient enough to maintain the protective oxide (Teoh, 2004).

2.2.1.2 Cobalt-chromium alloy

Cobalt based alloy family is superior to stainless steel in terms of corrosion resistance and wear resistance. Vitallium (Co-30Cr-6Mo) was the first cobalt based alloy to be used in hard tissue replacement. By modifying vitallium, a number of alloys have since been introduced such as Co-Cr-Mo alloy, Co-Ni-Cr-Mo-W-Fe alloy and Co-Ni-Nr-Mo alloys (Teoh, 2004). Co-based alloys also have sound mechanical properties such as high tensile and compressive strengths. Unfortunately, a major concern regarding the utilization of Co-based alloys is the potential release of chromium which is known to cause cancer (Black and Hastings, 1998). The use of these materials also exposes implant-bone interface to the risk of loosening because of material's bioinertness as well as stress concentration related to the significant difference of the mechanical properties of implant material compared with that of bone. To overcome the major limitations of Cobalt-chromium alloy, a new metallic materials, of which the mechanical properties more mimics that of natural bone, is needed for implant applications.

2.2.1.3 Titanium and titanium alloy

Currently, commercially pure titanium and its alloy (Ti6Al4V) are the most widely used metallic implant materials worldwide. A new generation of implants with high strength, light weight has been developed with the utilization of them. Their relatively low elastic modulus reduces the occurrence of stress concentration at the bone-implant interface, which is a big step forward in the research of metallic implant materials (Teoh, 2004, Myer, 2003). Furthermore, titanium and its alloy also have superior machinability, formability and corrosion resistance under biological environment as compared to

stainless steels and Co-based alloys. Like 316L stainless steel, and Co-based alloy, they are biocompatible due to the formation of a bioinert oxide layer at the surface.

However, titanium and its alloy have non-preferable tribological properties in that they have a high coefficient of friction. Thus wear particles may easily form if they rub against bones. Another disadvantage of them is that they are not capable to form a direct bonding between the metallic implant and organic tissue due to their bioinertness. Therefore, the long-term instability at bone-implant becomes a major concern the use of titanium and its alloy for the bone implant applications. Due to the need of bioactive materials for long-term success, the attentions have been paid on the research and development of new biomaterials, e.g. calcium phosphate ceramic.

2.2.2 Calcium Phosphate Ceramics

Calcium phosphates (listed in **Table 2.2**), with varying calcium to phosphate ratios, are the major inorganic constituents of bone and they hold great promise as biomaterials for bone implantation since they have the ability to directly bond with bone. Calcium phosphate implants, due to their bioactivity, are expected to created good contact with bone and to reduce the rejection issues.

Table 2.2. Calcium Phosphate Phases

Phases	Formula	Structure	Ca/P Ratio
Hydroxyapatite (HA)	$Ca_{10}(PO_4)_6(OH)_2$	Hexagonal	1.67
Alpha tricalcium phosphate (α-TCP)	α-$Ca_3(PO_4)_2$	Monoclinic	1.50
Beta tricalcium phosphate (β-TCP)	β- $Ca_3(PO_4)_2$	Rhombohedral	1.50
Tetracalcium phosphate (TTCP)	$Ca_4P_2O_9$	Monoclinic	2.0
Oxyhydroxyapatite (OHA)	$Ca_{10}(PO_4)_6(OH)_{2-2x}(O)_x(\square)_x$	Hexagonal	1.67
Amorphous calcium phosphate (ACP)	n/a	n/a	n/a

The calcium phosphate family includes numerous compounds that might have applicability to the manufacture of orthopaedic implants. However, these compounds differ in their stability and biological properties, which enable them to fulfil the requests for different purposes. The most important parameters are the molar Ca/P ratio, basicity/acidity and solubility. The lower the Ca/P molar ratio is, the more acidic and water-soluble the calcium phosphate is (Legeros, 1993). The following sub-sections are to discuss the stability and biological properties of some well-known calcium phosphate compounds, which are significant to their utilisation for the biomedical applications.

2.2.2.1 Stability of calcium phosphate ceramics

The temperature and presence of water, either during processing or in the service environment, are two crucial factors to influence the stability of calcium phosphate ceramics (de Groot and Legeros, 1998). At the body temperature (37°C), only two calcium phosphates are stable when contacting with aqueous solutions such as body fluids. At pH < 4.2, the stable phase is dicalcium phosphate ($CaHPO_4.2H_2O$); meanwhile, at pH > 4.2, HA is formed.

From a chemical point view, HA ($Ca_{10}(PO_4)_6(OH)_2$) is the closest to bone mineral and a direct bonding at HA-bone interface was observed (Fujiu and Ogino, 1984; Toth *et. al*., 1995). However, HA is different from biological apatite, a high Ca/P ratio and carbonate content, some vacancies and numerous ionic substitutions. Generally, at physiological pH, HA is a very stable phase, and the dissolution rates of the other phases are much higher than HA, which is in the order of ACP >> TTCP > α-TCP > OHA > β-TCP >> HA (Legeros, 1993; Gross and berndt, 1997). Calcium oxide (CaO) has no biocompatibility and dissolves significantly more than TCP, thus it is a detrimental phase that should be avoided (Lide, 1990). β-TCP cannot be precipitated from aqueous solutions. It is a high temperature phase of calcium phosphates, which only can be prepared by thermal decomposition. At temperature above 1125°C, it transforms into the high-temperature phase α-TCP. In biomedicine, β-TCP is used in calcium phosphate bone cements. α-TCP is normally prepared from β-TCP at heating above 1125°C and it might be considered as a high temperature phase of β-TCP.

Therefore, from the comparison above, HA is the most promising compound for bone replacement served in the physiological environment in the calcium phosphate family. More details regarding the high temperature resistance of HA are given in Section 2.2.3,

and the following sub-section will introduce the biological characteristics of calcium phosphate ceramics.

2.2.2.2 Biological properties of calcium phosphate ceramics

Biodegradation of calcium phosphate ceramics is mainly caused by three factors, which are (1) physiochemical dissolution that depends on the solubility product of the material and local pH of its environment, (2) physical disintegration into small particles due to preferential chemical attack on grain boundaries, and (3) biological factors which result in a decrease in pH concentrations, thereby influencing the characteristics of calcium phosphate ceramics (Toth *et al.*, 1995; de Aza *et al.*, 1996; Ito *et al.*, 1997). Calcium phosphate ceramics with a Ca/P ratio ranging from 1.33 to 1.65, which are defined as calcium-deficient apatites, are known to be of biological importance as the Ca/P ratio of bone is lower than the stoichiometric value of synthetic HA. In addition, these ceramics are found to act as catalysts in several organochemical reactions, such as dehydration and dehydrogenation of primary alcohols, leading to the formation of aldehydes and ketones (Bett *et al.*, 1967). On the other hand, Driessens (1983) has shown that calcium phosphate ceramics with a Ca/P ratio of less than 1.0 are not suitable for biological implantation, and as such, monocalcium phosphate monohydrate (MCPM) and hydrated calcium phosphate (DCP) are not biocompatible with bone. TCP has been reported to show a favourable bone response (Klein *et al.*, 1983; van Blitterswijk *et al.*, 1986) and several studies did report that HA demonstrated good biocompatibility when implanted is soft and hard tissue (van Blitterswijk *et al.*, 1985 and 1990; Jansen *et al.*, 1990).

2.2.3 Hydroxyapatite

2.2.3.1 Structure

Hydroxyapatite (HA, $Ca_{10}(PO_4)_6(OH)_2$) has a hexagonal lattice with a space group $P6_3/m$. This space group is characterised by a six-fold c-axis perpendicular to three equivalent a-axes (a_1, a_2, a_3) at angles 120° to each other with a = b = 0.9418 nm and c = 0.6884 nm. **Figure 2.2** illustrates the unit cell and it contains a complete representation of the apatite crystal. The capital 'P' signifies that the unit cell is typical of the hexagonal system, in which the a- and b- axes are equal, but different to c- axis; the interaxial angles of 'α' and 'β' are 90° and the 'γ' angle is 60°. The '6_3/m' symbol shows that there is a six-fold axis parallel to the c-axis so that equivalent points are brought into correspondence when the whole structure is rotated 60° around the c-axis. In addition to the 60° rotation, the '6_3' symbol defines that the structure is translated along the c-axis for a distance of one half (3/6) of the c-axis length. Lastly, the '/m' symbol defines that the lattice points are symmetrically allocated about a mirror plane being perpendicular to the c-axis (Posner *et al.*, 1958).

As shown in **Figure 2.3**, the ten calcium atoms belong to either Ca(I) or Ca(II) subsets depending on their environment. Four 'columnar' calcium (Ca) atoms occupy the Ca(I) positions: two at level z = 0 and two at z = 0.5. The remaining six 'hexagonal' Ca atoms Ca(II) are arranged in triangular coordinate groups: one group of three Ca atoms is located at z = 0.25 and the other group of three at z = 0.75. The successive triangles are rotated 60° with respect to one another and form 'tunnels' parallel to the c-axis. These tunnels contain the hydroxide (OH) ions, which are located at the corners of the unit cell at z = 0.25 and z = 0.75 respectively. The network of phosphate (PO4) groups provides the skeletal framework which gives the apatite structure its stability (Young, 1967).

2.2.3.2 Stability

HA decomposes to other calcium phosphate phases at high temperature. Furthermore, it was found that the decomposition of HA occurred in three stages: An increase in the temperature was accompanied by a gradual loss of OH ions (dehydroxylation) followed by transformation of HA in to oxyhydroxyapatite (OHA) around 1000 - 1360°C. OHA was further dehydrated resulting in the formation of oxyapatite (OAP). Above 1360°C, the OAP decomposed into tricalcium phosphate (α-TCP) and tetracalcium phosphate (TTCP) such that in the range 1450-1500°C only these phases could be perceived by X-ray diffraction. The entire process could be presented as the following equations.

$$Ca_{10}(PO_4)_6(OH)_2 \rightarrow Ca(PO_4)_6(OH)_{2-2X}O_X\Delta_X + xH_2O$$

$$Ca_{10}(PO_4)_6(OH)_{2-2X}O_X\Delta_X \rightarrow Ca_{10}(PO_4)_6O + (1-x)H_2O$$

$$Ca_{10}(PO_4)_6O \rightarrow 2Ca_3(PO_4)_2 + Ca_4(PO_4)_2O$$

Where Δ is a vacancy

Since those calcium phosphate phases are not stable in the body fluid, the decomposition should be avoided during the process for the long-term biostability of the implant materials.

Moreover, a principal limitation of HA is its low fracture toughness (0.9 - 1.3 MPa $m^{1/2}$) when compared with cortical bone (2 – 12 MPa $m^{1/2}$) (Behiri and Bonfield, 1984), which leads to the applications for this material being limited to non-load bearing parts of the skeleton, such as middle ear implants or as coating on metal (or alloy) implants. Indeed, HA coated metallic implant materials become the most successful approach for the total hip replacement and dental implant. It very well combines the excellent mechanical properties of the metallic materials and the preferable bioactivity of HA.

There are a numerous methods to deposit HA on metal as discussed in the following section.

2.3 Current coating techniques

The modification and enhancement of the surface properties of biomedical materials is becoming of increasing interest. One of the major areas of development is in the study of biomaterials with sophisticated coatings to meet the requirements of biocompatibility with human tissues and blood. Therefore, a number of the coating techniques have been developed to process the bioactive ceramics coating on the metallic implant surface, to enhance the biological properties of the traditional implant materials and reduce the healing period for orthopaedic implant applications. The coating techniques can be mainly classified into three major categories: the wet technique, the physical vapour technique and the spraying technique. HA coatings produced via different methods exhibit different thickness, surface chemistry, morphology and therefore different performance during implantation. Each of these methods will be discussed in further details.

2.3.1 Wet technique

Wet technique can be categorized into sol-gel deposition, electrophoretic deposition and biomimetic deposition.

2.3.1.1 Sol-gel deposition

The sol-gel deposition is firstly uncovered and documented by Ebelmen in 1846. He pointed that under the influence of humidity, a silicon alkoxide solution can transform

from a clear liquid into a transparent solid that heated to form silicon dioxide (Reuter, 1991). Since then, sol-gel method has become a common approach for preparing glasses and ceramics thin films. Normally, the sol-gel route consists of three main steps: 1> Preparing a homogeneous precursor solution of the desired metal component; 2> Depositing the sol on the targeted substrate and undergoes hydrolysis under controlled conditions to produce a gel containing the hydrated metal oxide; 3> Drying, compacting and sintering the gel to produce a ceramic or glassy material at a temperature much lower than that required by the conventional melting process.

The sol-gel deposition had been also used as a method which can result in coatings with an exactly similar chemical and microstructural composition as HA, provided a sol is correctly mixed in solution with the desired components (Gross *et al.*, 1998; Weng and Baptista, 1999). The coatings are then fired to remove the undesirable organic constituents, leaving behind as pure an HA coating as possible. The prepared coatings are dense and adhere strongly to the underlying substrate. Generally, the technique is simple, and with the use of moderate temperatures, there is little effect on the structural stability of the HA coating. However, the chemical and phase purity of the coatings are very much dependent on the purity of the precursor materials used to prepare the sol, and its processing parameters which requires stringent control.

A homogeneous HA thin coating on titanium substrate was successfully prepared using alkoxide precursors (calcium diethoxide in ethanol, and triethyl phosphate in ethanol and ethanediol) prepared in a moisture-free atmosphere and allowed to age for 24 h by Gross and co-workers in 1998 (Gross *et al.*, 1998). A prefire process at 500°C was required to remove most of the organic constituents followed by a final firing at 800°C in air to densify the coatings. However, the titanium substrates were observed to oxidize

at that temperature. Dense and smooth HA coatings on titanium substrates were obtained by Weng and Baptista (1999), using mixed ethanol solution of calcium nitrate ($Ca(NO_3)_2$) and phosphate oxide (P_2O_5), fired at 500°C in air. XRD analysis revealed that small amounts of carbonated HA was present in the HA coating, but was eliminated when heat-treated at a high firing temperature of 750°C. However, cracks were observed in the coatings. The coatings obtained in this study have an adhesive strength of more than 14 MPa.

The advantages of the sol-gel deposition reside in the high purity of the HA precursors, the homogeneity of the components at the molecular level, the low processing temperature when compared with the powder processing method. Moreover, the sol-gel deposition enable to prepare thin coatings on the complex shapes to suit different implant applications. The disadvantages of sol-gel deposition are mainly two points, which are (1) the process requires precise control over process conditions, e.g. heat treatment control, and (2) the raw materials to prepare the precursor are normally expensive, thus this process doesn't well suit the industry application.

A coating technique, namely 'Dipping deposition', which also belongs to sol-gel technique catalogue, has been used as a simple and low cost coating technique for orthopedic implants. Furthermore, this process route also offers other advantages, such as high deposition rate and more importantly enabling coating of complex shapes, such as screws, pins. However, several drawbacks of this technique have also been reported. For instance, it's difficult to prepare the thin coating via this technique, and due to the thermal expansion mismatch between the thick coating (0.05 mm – 0.5 mm) and metal substrate, the internal stress at the interface between the coating and metallic substrate

may present and lead to the cracks in the coating or the delamination during the implantation.

2.3.1.2 Biomimetic deposition (BMD)

A biomimetic process for calcium phosphate coating preparation on a substrate has been investigated by several authors (Tanashi *et al.*, 1994; Oliveira *et al.*, 2002). In this methodology, the substrates are immersed in a simulated body fluid (SBF) with a composition similar to the human blood plasma at 37°C for several days, in order to promote the formation and growth of a biologically active bone-like layer. Generally, this is a simple and low cost temperature process, which is also capable for coating substrates of complex shape.

Tanashi *et al.* (1994) managed to obtain dense and uniform layers of bonelike apatite coating on different polymer substrates with a fairly strong adhesive strength (poly-ether sulfone was the highest at 4.40 MPa). They stated that subjecting the substrates to the first treatment (soaking in SBF at 36.5 °C with the presence of $CaO\text{-}SiO_2$-based glass) was essential for the formation of bonelike apatite coatings, and the coating thickness increased with the induction period, before the substrates were immersed in the second treatment (immersing in 1.5SBF at 36.5 °C for 6 days). Oliveira and co-workers (2002) had successfully produced bonelike apatite layer on polymeric substrates using sodium silicate gel as an inducting agent, which greatly reduced the growing period for the formation of bonelike layer to 6 h. Furthermore, they found that by increasing the SBF concentration, it was possible to obtain an apatite layer close to that of the bone apatite structure. It has been reported that a Ca/P ratio between 1.5 and 1.67 was achieved in this study.

However, the success of achieving the CaP layer on the substrate using this technique requires quite complicated operation procedures, such as replenishment of SBF, maintaining the pH of SBF. Moreover, the processing is of a very low deposition rate, which means it requires extremely long induction and growing periods to form the coating layers on the substrate surface.

2.3.1.3 Electrophoretic deposition (EPD)

Electrophoretic deposition is a process involves the migration of charged particles/ions towards a counter charged electrode, whereby deposition of the coating take place. As shown in **Figure 2.4**, the basic processing setup consists of two metal electrodes, one of which is the targeted substrate, coating substance suspension and a low voltage supply. In this process, the powder particles must be fine enough to remain in suspension during deposition. Thus, nanoparticles are used. This technique needs a subsequent densification treatment in order to sinter the coating. Therefore, coating shrinkage and cracking may occur. EPD is basically a simple, low cost and non-line-of-sight process which can be used to coat substrate of complex shapes.

Wei *et al.* (1999a) have shown that crack-free HA coatings on titanium substrates could be prepared using equiaxed nanosized HA particles synthesized by the metathesis method, and ambient-aged for 10 days. In addition, they found that dense HA coatings could be achieved on titanium and stainless steel substrates at a firing temperature range of 875 to 1000°C, with a heating rate of 100 °C/h, holding time of 1 h and cooling rate of 50 °C/h. The problem of cracking could be overcome via using dual coating procedures (coat, sinter, coat and sinter). The values of the interfacial shear strength on titanium and stainless steel substrates were approximately 12 and 22 MPa respectively, compared to the shear strength of bovine cortical bone of 34 MPa (Wei *et al.*, 1999b),

which the coating prepared in this way may face the delamination risk during the clinical practices. However, analytical analyses such as FTIR, Ca/P ratio and EDS were reported.

2.3.2 Physical vapour technique

Although vapour technique, as one of the oldest techniques used for depositing metal and metal alloy thin films, has been widely used in the laboratory and in industry for many years, the research of its application for process HA coating for biomedical applications only started since 1990s. Normally, there are three sequential basic steps take place during the process:

1. A vapour is generated by subliming or boiling a source material;
2. The vapour is transported from the source to the substrate, and
3. The vapour is condensed to a solid film on the targeted substrate surface.

In the following sub-sections, three specific physical vapour techniques, which are pulse laser deposition (PLD), Magnetron sputtering and Ion beam sputtering (IBS), are going to be discussed.

2.3.2.1 Pulsed laser deposition (PLD)

Pulsed laser deposition is one of the physical vapour deposition techniques, which can be utilized to prepare single and multi layer films of a wide range of target materials on various substrates (Jayadevan and Tseng, 2002). To prepare HA coated implant materials using this technique, the ablation HA target used for deposition is first prepared. The substrate is then placed on a stage normal to the target in the deposition chamber which is evacuated prior to deposition. The substrate is heated and an argon-

water vapour mixture is introduced into the chamber. Next, an ArF or KrF excimer laser is guided into the chamber to strike the target at an incidence angle of 45°. A representation of the pulsed laser deposition technique is shown in **Figure 2.5**.

Wang and co-worker (1997) have shown that pure, uniform crystallized HA films with thickness of around 10 μm were obtained on titanium substrates when an argon-water vapour mixture with a pressure of 4.3×10^{-1} Torr and a substrate temperature of 500 to 600 °C were used, together with the ArF excimer laser of wavelength 193 nm during deposition. XRD data indicated that the coatings consisted mostly of HA phases, with very little amounts of other calcium phosphate phases such as TCP, TTCP and CaO. Furthermore, FTIR pattern showed that the coatings were similar, except for the less sharp peaks observed. The Ca/P ratio of the film was nearly 1.99 (compared to 1.79 for the target). Interestingly, the value of the Ca/P ratio was higher in the region near to the substrate surface, and decreased nearer to the coating surface.

In 1997, Garcia-Sanz *et al.* were able to obtain an almost uniform and smooth film across the titanium substrates, using water vapour as the working gas with a pressure of 0.45 mbar and substrate temperature kept at 455 °C, and an ArF laser beam of wavelength 193 nm. At a high magnification, it revealed that the coating was formed by a net work of fine polygonal HA crystallites of sizes raging from 100 to 500 nm. In addition, the tensile strength values obtained from the pull test were higher than 58 MPa.

The process parameters controlled the coating's properties have also been reported by Zeng and Lacefield (2000a, 2000b and 2000c). With the induction of water vapour into the argon working gas, it was possible to obtain HA as the major phase in the coating with a Ca/P ratio relatively close to 1.67, here 1.77 and 1.82 for 355 nm and 266 nm

wavelength laser respectively. Coatings obtained by the 355 nm wavelength laser were rough and porous, thus faster dissolution and reprecipitation in physiological medium as compared to coatings obtained by the 266 nm wavelength laser which were more smooth and dense. They also found that a high substrate temperature (more than 450 °C) tended to increase the Ca/P ratio, but was able to achieve a crystalline structure rather than amorphous.

2.3.2.2 Magnetron sputtering

The basic sputtering deposition involves removal of atoms from the surface of a material by energetic ion bombardment and collection of the sputtered species on a solid surface (substrate). Magnetron sputtering, which is one of the sputtering techniques, is a well established technology in areas such as microelectronics, magnetic film s and solar controls. Only recently, this method has be incorporated into the biomedical field (Ruddell *et al.*, 2000; Ozeki *et al.*, 2001; Ong *et al.*, 2002; Wolke *et al.*, 1994; Hulshoff *et al.*, 1995). It is an efficient method for the production of coatings with controlled microstructure in a reproducible way. The advantages of magnetron sputtering are listed as follows (Kukla, 1997):

1. High thickness uniformity;

2. High stability of deposition rate and layer properties for long un-interrupted production time;

3. Good adhesion and high density of deposited film; and

4. ability to coat all types of materials, such as high melting points metals, metal alloys and compounds, metal oxides, nitrides or even carbides.

A simple magnetron sputtering system (**Figure 2.6**) comprises of (1) a sputtering chamber containing the working gas which forms plasma, (2) a substrate holder for

putting a substrate in the chamber, and (3) a sputtering target for depositing a film of atoms of the material onto the surface of the substrate. **Figure 2.7** shows a schematic diagram of the momentum exchange processes that occur during magnetron sputtering. Positive ions of an inert gas from plasma are accelerated towards the target of the material to be deposited. Free atoms of the target material are 'knocked out' when the ions collide with the target. A portion of the free atoms are collected on the surface of the substrates and thus form a thin film. In magnetron sputtering, magnets are positioned behind the target, with magnetic field lines penetrating the target and forming arcs over its surface. The magnetic field helps to confine the electrons in an area near the target surface, which results in an increased concentration of electrons, producing a high density of ions and thus enhancing the sputtering yield.

In magnetron sputtering, the film deposition rate is principally controlled by the power input to the sputtering target. With a high power input, more electrons will arrive at the sputtering target. 'Knocking out' the target atoms and hence, a high deposition yield is obtained. In addition, the deposition rate is also influenced by the pressure and electrode spacing. With increasing pressure, the deposition rate will drop due the scattering of the depositing flux. As atoms from the target are scattered by the intervening gas atoms before reaching the substrate, some material loss is inevitable during the deposition. This can be minimized by having small electrode spacing. However, problems such as lack of film uniformity and substrate heating can arise.

Van Dijk *et al.* (1995a) were able to deposit calcium phosphate thin coatings on titanium alloy (Ti-6Al-4V) substrates using magnetron sputtering at an argon (Ar) pressure ranging from 2.6×10^{-3} to 2.6×10^{-2} mbar. The distance between the target and substrate was kept at 75 mm and the total sputtering time was 2 h. They found that the

deposition rate and Ca/P ratio increased with increasing Ar pressure. However, no relationship was found between the Ar pressure and density of the films. FTIR spectra revealed that more distinct phosphate (PO_4) peaks were seen after sputtering at higher Ar pressure, but no distinctive differences were observed in the XRD patterns. They found that the hydroxyl (OH) peaks, characteristic of HA, appeared in the FTIR spectrum if sputtering was carried out at a water vapour pressure that was 5 % of the Ar pressure.

Again, van Dijk and co-worker (1995a and 1995b) showed that the deposition rate increases from 0.29 to 1.75 μm/h as the discharge power level increases from 200 to 800 W. A more crystalline film was obtained at a higher discharge power level, but with the formation of TTCP. No significant relationship between the power level and Ca/P ratio or film's density was obtained.

The authors also showed that a more oriented crystalline HA-like film was obtained after annealing for 2 to 4 h at temperatures ranging from 400 to 1200 °C under dry Ar or Ar-water vapour flow. However, CaO, TCP and TTCP were obtained at annealing temperature more than 600 °C, with crack formation. The Ca/P ratio decreased with increasing annealing temperature (van Dijk *et al.*, 1995a, 1995b and 1996).

However, there are also some disadvantages of this technique, which restrict its application in biomedical industry. The core drawback is that it normally takes hours to prepare a film of a few hundred nanometer thickness. Furthermore, this technique requires a complex operation and high cost.

2.3.2.3. Ion beam sputtering (IBS)

Basically, ion beam sputtering consists of two steps: cleaning and deposition. In the cleaning stage (**Figure 2.8a**), the substrate is fixed to a rotating stage of the sputtering system where it is cleaned using an ion beam, inside a chamber filled with high purity inert gas. In the deposition stage (**Figure 2.8b**), the cleaned substrate is moved into position to be coated. Another ion beam is used to sputter atoms from the target, causing an accumulation of the sputtered atoms on the substrates. The final stage of the ion beam sputtering involves post deposition treatments to convert the amorphous coating into a crystalline type.

Ong and co-worker (1992) have demonstrated that amorphous calcium phosphate thin coatings of approximately 1 μm could be deposited on titanium substrates by the IBS process at an argon pressure of about 4×10^{-4} Torr, with an ion-beam energy of 100 eV and 40.7 mA. With post heat treatment at 600 °C in air for 1 h, the amorphous coatings transformed into crystalline HA-type structure, as determined by XRD, but microcracks started to appear on the coating surface. They also found that solubility of the coatings in saline solution was greatly reduced for heat-treated samples.

2.3.3 Spraying techniques

Spraying technique for biomedical applications can be classified into different methods such as plasma spraying, vacuum plasma spraying and high-velocity oxy-fuel spraying. Each of these methods will be discussed in further detail.

2.3.3.1 Plasma spraying (PS)

Plasma spraying is the most popular and commercialized method to fabricate calcium phosphate coatings (Deram *et al.*, 2003; McPherson *et al.*, 1995; Radin and Ducheyne, 1992). It is the technique (**Figure 2.9**) in which a direct current electric arc is struck between two electrodes, turning a stream of gas passing though this arc into a plasma of high temperature of up to 20,000 °C and with a high speed of up to 400 m/s. A powder (metallic or ceramic) is then fed into the plasma, and impinged in a molten state towards the substrate surface with a layer of the same composition as the powder. This coating prepared using this technique is normally of uniform and dense morphology, and with good adhesion to the targeted substrate.

Deram and co-workers (2003) managed to prepare 150 μm thick hydroxyapatite (HA) coating on titanium substrates using plasma spraying with a mixture of argon and nitrogen gases as the plasma working gas at a stand-off distance of 80 mm. Differential thermal analysis (DTA) analysis indicated a small endothermic peak at around 1390°C, corresponding to the transformation of HA into other decomposition products. This was further confirmed from the X-ray diffraction (XRD) analysis which indicated small visible TTCP peaks are around 2θ = 30 to 31 °. They also found that the Ca/P ratio varied in the range of 1.5 to 2.6, as determined by wavelength dispersive spectral X-ray analysis.

McPherson *et al.* (1995) have successfully obtained plasma-sprayed calcium phosphate coatings on stainless steel substrates. They found that at low input torch power, amorphous coatings were obtained, but with increasing input torch power, a mixture of HA, amorphous and increasing proportions of CaO and TTCP were determined. In addition, they found that the Ca/P ratio increased with input torch power. Heat treatment

of the coatings at 600 °C for 1 h in air resulted in the recrystallization of the amorphous phase with a corresponding increase in the HA XRD peak intensity.

Furthermore, Fadin and Ducheyne (1992) investigated plasma-sprayed calcium phosphate ceramic coatings onto flat or porous titanium alloy substrates, of thickness about 70 to 80 μm. Using HA as the starting powder, they found that the plasma-sprayed coatings consisted of apatite, α-TCP and TTCP, as determined by the XRD analysis. On the other hand, using β-TCP as the starting powder, the coatings consisted mainly of α-TCP due to the phase transformation at the high processing temperature. All calcium phosphate ceramic coatings, regardless of the starting powder, showed significant increase in the bulk dissolution rate when immersed in a simulated physiological medium, which may lead to the loosening during the implantation.

2.3.3.2 Vacuum plasma spraying (VPS)

The principle of vacuum plasma spraying is similar to plasma spraying, except that this process takes place in a controlled vacuum atmosphere as shown in **Figure 2.10**. The essential of VPS is to avoid oxidation or nitrogen uptake, especially for coating metallic substrates. The spraying particles in this process have greater kinetic energy because they experience lower friction and collision losses during the travel in the vacuum environment, thus resulting in coatings with good adhesion and fewer pores.

Gledhill *et al.* (1999) managed to prepare thick dense HA coating of 40 μm in thickness onto titanium substrates using VPS. They found that there was a good adhesion between the coating and substrate, and no evidence of cracking between coating layers or through its thickness, although several microcracks were observed on the coating surface. Moreover, the crystallinity level of the coating was lower when compared to

the starting powder, which may weaken its stability in the physiological environment during the clinical practices.

Tsui and co-workers (1998) have shown that calcium phosphate coating of thickness up to 500 μm could be deposited on to titanium, tungsten or mild steel substrates. They found that the porosity and crystallinity levels decreased while the amount of non-HA phases increased, with increasing input power. In addition, the extent of microcracking in the coatings decreased, thus increasing the Young's modulus and interfacial adhesion as the power level was increased.

2.3.3.3 High-velocity oxy-fuel spraying (HVOF)

This spraying process uses high velocity combustion of mixtures of oxygen and a fuel gas (hydrogen or propylene) to heat and propel the semi-molten to molten powdered coating material at hypersonic velocities, onto the substrate surfaces (**Figure 2.11**). Generally, coatings produced by this process have better density, bonding strength and hardness than most other spraying techniques.

HA-type coatings of thickness about 76 μm on titanium substrates were achieved by Haman *et al.* (1995), with minute cracks appearing on the coating surfaces. Both the XRD and Fourier Transform Infrared Spectroscope (FTIR) results revealed that the coating exhibited an almost HA-type structure and chemistry, with small amounts of TCP and TTCP present. In addition, immersion results after 12 weeks indicated that no significant change was observed on the HA-type coatings, except the formation of more cracks and CaO on the surfaces.

Overall, all spraying techniques have the same drawbacks. Due to the sophisticated equipment involved, they are expensive to use. Moreover, there is a large number of process parameters involved. As these are high temperature processes, they tend to affect the structural stability of the HA coating, by decomposing into other calcium phosphate phases like amorphous calcium phosphate (ACP), TCP, TTCP and CaO. Post-deposition heat treatment is thus needed to crystallize and ACP, or to cause ACP and TCP to hydrolyze into HA.

To summarize the as-discussed deposition techniques above for processing HA coating, a comparison is given below to list the advantages and disadvantages of such techniques in **Table 2.3**.

Table 2.3 The comparison of coating techniques for HA coated implant materials (Wang *et al*., 2006; Li *et al*., 2002; Besra and Liu, 2007; de Groot *et al*., 1998; Cleries *et al*., 1998; Yan *et al.*, 2006; Garciasanz *et al*., 1997; de Groot *et al*., 1998; Radin and Ducheyne, 1992; Sun *et al*., 2001; Choy 2002)

Techniques		Typical coating thickness	Advantages	Disadvantages
Wet Technique	Sol-gel deposition	< 1 μm	Produces thin coating; Enables coatings of complex shapes; Involves low process	Requires precise control over process conditions; Expensive raw materials.
	Dip coating	50- 500 μm	Easy Set-up; Low cost; High deposition rate; Enable coating of complex shapes.	Thermal expansion mismatch between thick coating and substrate may cause internal stress at interface and therefore cracks.

Wet Technique	Biomimetic deposition (BMD)	< 30 μm	Low temperature required; Capable for complex shapes; Forms bone-like apatite.	Very low deposition rate; Replenishment of SBF; Requires constant pH of SBF; Complicated operation;
	Electrophoretic deposition (EPD)	25-35 μm	Capable for complex shapes; room temperature process; Low-cost	Low deposition rate; Low bonding strength at the interface;
Physical Vapour Technique	Pulsed laser deposition (PLD)	0.05-0.5 μm	Produces dense coatings; Uniform morphology; High stability of deposition rate; Good adhesion of coating;	Line of sight process; Complex operation required; Low deposition rate; High cost;
	Magnetron sputtering	0.05-0.5 μm		
	Ion beam sputtering (IBS)	0.05-0.5 μm		
Spraying technique	Plasma spraying (PS)	30-200 μm	High deposition rate; Produces uniform and dense coatings; Good adhesion of coating;	Involves high temperature which can cause other unstable amorphous calcium phosphate phases (ACP); High-cost process; Involves complex operation.
	Vacuum plasma spraying (VPS)	< 500 μm		
	High-velocity oxy-fuel spraying (HVOF)	30-200 μm		

To overcome the weakness of the deposition techniques above to achieve the HA coated implant materials with high quality and suit the industrial production, the research and innovation for novel process technique is still ongoing. Electrohydrodynamic

atomisation (EHDA) spraying for HA coated implant was investigated under this background. To help to understand the basic principle and mechanism of this technique, a comprehensive discussion is given as follows.

2.4 Electrohydrodynamic atomization (EHDA) spraying

This section is dedicated to a critical literature review associated with this research. The following sub-sections will discuss the basic principles, various modes of electrohydrodynamic processing, the mechanism of the stable cone-jet mode which is essential for EHDA deposition, the effect of the physical properties of the liquid to EHDA deposition, controlling parameters for the process, and other techniques developed based on EHDA process.

2.4.1 Introduction

Electrohydrodynamic processing is a process where a liquid breaks up into spray droplets under the drive of an electrical field. Various modes of electrohydrodynamic processing were reported, of which the stable cone-jet is of specific interest. Under such mode, liquid flowing through a capillary maintained at high potential is subjected to an electric field, which leads to elongation of the meniscus to a form of jet and subsequently the jet deforms and breaks up into fine droplets. This basic phenomenon seems to be simple technique to appearance, it could be more complex in understanding the exact phenomenon due to inter-link between the liquid properties and the dependence on the liquid flow rate, applied voltage and needle geometry to certain extent.

Since the beginning of last century electrohydrodynamic phenomenon has been documented and attracted considerable interest from a fundamental point of view. The pioneering work by Zeleny in 1914 with a needle carrying liquid and a ground electrode set up subjected to a high voltage that marked the important break through into this exciting field of research. However, the existence of the steady state mode has not been satisfactorily explained and reported until 1964. Mr Taylor firstly derived the conditions for a meniscus to exist in equilibrium in conical form under the competing actions of electric field and surface tension (Taylor, 1964). He studied the break-up of a droplet using glycerine and glycerine-water mixture when an electric field is applied to the capillary tube carrying the liquid. He found that the liquid does not vibrate before spraying but rather it would adopt a conical shape when a liquid is conducting. He also measured the conical shape to be have a sharp apex at a semi-vertical angle that was nearly equal to 49.3 °, which has been called 'Taylor Cone' since then. This is the angle at which a conical meniscus of a conducting liquid can exist in equilibrium under an applied electric field. The captured pictures of his investigation are shown in **Figure 2.12.**

Since then, a number of studies were carried out to investigate the influence factors to this steady state mode aiming at utilizing this phenomenon as a processing technique. Jones and Thong (1971) found that electrical dispersion of a jet of kerosene into spray of monodisperse droplets could only be achieved within a certain range of applied voltage and the droplet size is almost independent of voltage however a function of liquid flow rate. Mutoh *et al.* (1979) stated that the steady state mode only exist if the conductivity of the liquid between certain limits. Later in 1980, it was found that the decrease in droplet diameter can be achieved via increasing the applied potential by Nagorynyi and Bezrukov (1980). This finding suggested the necessary conditions for

producing smaller droplets. Furthermore, Smith (1986) carried out a study on the effect of the liquid physical properties, such as conductivity, surface tension and viscosity, on the process, which will be discussed in the following sections in details.

Based on the previous pioneered studies, more systematic and quantitative studies were carried in 90s. The classification of functional modes of electrohydrodynamic processing was described by Cloupeau and Prunet-Foch (1990). For constant liquid properties and flow rate electrohydrodynamic processing presents through several visual and measurable differences with increasing applied voltage. These differences were defined as spray modes; the particular spray mode achieved depends on the operation conditions. They also described the specific characteristics of each mode. Thereafter, Jaworek and Krupa (1999a) characterised and defined the modes of electrohydrodynamic processing, which provide the fundamental science for utilizing such phenomenon as a deposition technique for the current biomedical engineering.

The follow section will introduce the characteristics and discuss the mechanism of each electrohydrodynamic processing modes in details.

2.4.2 Modes of electrohydrodynamic processing

The modes of electrohydrodynamic processing are characterised and defined by two criteria (Jaworek and Krupa, 1999a):

(1) The geometrical form of the liquid at the outlet of the capillary (drop, spindle, jet), and

(2) The type of the jet behaviour in its disintegration into droplets.

Based on such criteria, the spraying modes can be divided into two groups. The first group comprises of the modes in which only fragments of liquid are ejected from the capillary without a continuous jet, including the dropping, micro-dripping, spindle, multi-spindle, and ramified-meniscus modes. The second group belongs to the modes, in which the liquids characteristically issues a capillary in the form of a long continuous jet which disintegrates into droplets after travelling to a distance, usually a few millimetres. The stable cone-jet, precession, oscillating-jet, multi-jet and ramified-jet modes are included in this group. The meniscus and the jet can be stable, vibrate, and rotate spirally around the capillary axis in the second group. There can also be corona discharge, which will be discussed later in this section.

2.4.2.1 Dripping mode

The dropping mode of electrohydrodynamic processing is commonly obtained at low applied voltage, which is very similar to the dropping observed at electrically neutral conditions. The drops take the shape of regular spheres at the capillary exit and detach from the capillary as the gravity force, the electric force overcome the surface tension force. After the drop detachment, the meniscus contracts back to form a hemispherical-like meniscus.

Figure 2.13 shows the schematic diagram of the dropping mode and its real image captured by high speed camera. In the dropping mode, the time of the drop formation is much longer than the fall of the former drop, so the droplet charge does not affect the drop formation. However, when the voltage increases the meniscus elongates and the drop becomes smaller with an increased emission frequency. This is due to two factors, which are the reduction in the surface tension of the liquid due to the electric charges on the surface creating an electrostatic pressure opposite to the capillary pressure, and the

attraction of liquid towards plate due to the action of the electric field on the charges located at the end of the hanging droplet (Cloupeau and Prunetfoch, 1990). To increase the applied voltage further, the drop can connect with the capillary by a thread, which subsequently breaks off as the drop falls down and a sibling can be generated from the thread. Furthermore, in the dripping mode, the emission of droplets may occur at regular time intervals, without the creation of satellites, so that all the droplets have the same size. Generally, the droplets diameter remains greater than that of the capillary, thus leading to the emission of large droplets at low frequencies. At a specific flow rate, the maximum emission frequency may increase and the minimum droplet diameter may decrease significantly if the diameter of the capillary is reduced (Cloupeau and Prunetfoch, 1990).

2.4.2.2 Micro-dripping mode

To increase further the applied voltage than the value for the dropping mode, the electric force close to the capillary exit becomes sufficiently high to keep a stable hemispherical or ellipsoidal meniscus. The micro-dripping mode differs from the dropping mode as the meniscus does not contract back after the droplet detachment. A small droplet, which is much smaller than the capillary diameter, is formed at the tip of the meniscus, where the electric field is much stronger. The droplet gets detached from the meniscus and does not undergo further disruption. The micro-dropping mode is usually observed at low applied voltages, at which the electric stress due to the field is not sufficient to form connective thread, and volume flow rates.

Figure 2.14 shows the real image and schematic diagram of the micro-dropping mode. The size of the droplets can range from a few micrometers up to about a hundred of micrometers in diameter (Jaworek and Krupa, 1999a). The frequency of the emission of

the droplets ranges from a few tens up to a few thousands of droplets per second. In addition, it is of interest that the emission in microdripping mode sometimes takes place at very regular time intervals, giving droplets of uniform size (Cloupeau and prunetfoch, 1990). It was also noticed that the space charge formed by formerly generated droplets is too weak to influence the droplets generation process, and when the flow rate and applied voltage increase, the space charge builds up by the charged droplets and gas ions, which may disturb the emission of regular drops. This means the microdripping mode and the previously discussed dropping mode can only be generated in a limited range of applied voltage and flow rate.

2.4.2.3 Spindle mode

As the applied voltage is increased even higher, the space charge begins to build-up by the detaching droplets, which affects the meniscus at the capillary exit. Therefore, it is no longer possible to accomplish the regular drop emission.

The spindle mode is generated at high flow rate with sufficiently high electric field where the liquid is elongated in the direction of the electric field, taking the shape of a thick jet which detaches as a vast spindle-like fragment. The characteristic time when the liquid is supplied to the capillary is nearly equal to or shorter than the characteristic time of the jet formation therefore, high electric field detaches a fragment of liquid before a continuous jet is formed. Spindle mode operates at higher voltage than the previously discussed two modes, and it differs from these two modes in the following aspects: (1) it operates at higher voltage and thus the high potential detaches a fragment of liquid before a continuous jet is formed; (2)no regular droplet can be ejected from the meniscus but elongated fragments; (3) in the spindle mode, the smaller droplets can be disrupted into different sizes due to the electric force; (4) the meniscus contacts to its

initial shape after detachment and a new spindle-like fragment starts to be formed; and (5) the characteristic time that liquid is provided to the capillary is nearly equal to or shorter than the jet formation time.

Figure 2.15 shows the real image and the schematic diagram of the spindle mode. Under the spindle mode, electric field is still too low to form a long continuous jet for a given flow rate, and only a spindle-like jet is detached from the capillary. Increase in the applied voltage can cause the single jet to become multiple jets. The main droplets are usually different in size, with diameters varying from 300 μm to 1000 μm (Jaworek and Krupa, 1999a).

2.4.2.4 Multi-spindle mode

When the voltage in the spindle mode is increased, the spindle-like jet detaches from the capillary will become multiple, and this mode with multiple spindle-like jets is named as multi-spindle mode. Under such mode, the droplet generation process is caused by the increased electric field between the electrodes and also is influenced by the space charge of the detaching droplets. The liquid velocity at the outlet of the capillary is higher than the characteristic velocity of the jet formation and a sufficiently high excitation field causes the liquid to elongate faster from the capillary compared to previously discussed modes, and detaches a fragment of liquid. The formerly generated droplets are still close to the capillary outlet, and the field generated by them deflects are still close to the capillary axis. The droplet generation in the multi-spindle mode is similar to the spindle mode, but spindles are emitted periodically from distinct points at the circumference of the capillary, usually in the form of short spindle-like jets, one piece of liquid at an instant (Jaworek and Krupa, 1999b).

Figure 2.16 shows the real image and schematic diagram of the multi-spindle mode. The piece of liquid can disintegrate into a few smaller droplets after detaching. The jet emission sites seem to be distributed uniformly on the capillary rim. The space charge deforms the axisymmetrical structure of the meniscus of the issuing liquid repulsing it off the capillary axis (Jaworek and Krupa 1999b). Moreover, the number of the points of jet emission may increases as the applied voltage is increased.

2.4.2.5 Oscillating-jet mode

The increase in the liquid flow rate while at the same applied as multi-spindle mode, can lead the jet to become continuous and steadily connected with the capillary. The intermittent drop generation is substituted b a continuous jet which oscillates or rotates because of the space charge of formerly emitted droplets and gas ions. **Figure 2.17**(a) shows the schematic diagram of the oscillating-jet mode. In such mode, the jet issues smoothly from the meniscus at the needle tip, changing its position to an oscillating one. The jet disintegrates into small but unequal droplets due to kink instabilities. The jet deflects off the capillary axis because of space charge; however when the droplets are removed to the collecting plate the jet starts to move back. Aerosol is sprayed into a cone of an elongated ellipsoidal base and an apex angle grater than 90°. The droplets are smaller than 200 μm in diameter. Furthermore, it has also been observed that some of the dispersed droplets don't attain the collecting plate surface, instead of which they flow back to the upper electrode. The returning droplets have to be oppositely charge, and are probably created by disruption of very weakly charged droplets on which the electric dipole is induced (Jaworek and Krupa, 1999b).

2.4.2.6 Precession mode

The precession mode is characterized by that the liquid detaches from the capillary in a skewed cone form which then smoothly changes in to a thin jet as the schematic diagram shown in **Figure2.17** (b) (Jaworek and Krupa, 1996). In such mode, both the cone and the jet rotate regularly around the capillary axis taking the shape of a fragment of a spiral. The jet, with diameter of less than 100 μm becomes thinner at its end, also rotates spirally. The jet disintegrates into small droplets under the influence of repulsive electrostatic forces and probably also due to the centrifugal forces, at the distance of about 5 – 10 mm from the tip of the capillary. Moreover, the jet becomes longer with the increasing voltage. This mode of spraying allows generation of fine aerosols forming uniform spatial dispersion. The droplets are finer compared to oscillating-jet mode. The droplets are of a lower mobility and take a longer time to reach the collecting electrode (Jaworek and Krupa, 1999a). Compared to the oscillating-jet mode, the droplets achieved under this mode are finer, and are of lower mobility and take a longer time to reach the collecting electrode.

The oscillating-jet mode and precession mode belong to transitional mode which lies between the spindle/multi-spindle mode and the stable cone-jet mode, which will be discussed later. Such intermittent mode can also be named as unstable (intermittent) cone-jet mode (Jayasinghe and Edirisinghe, 2004). Under the unstable cone-jet mode, the liquid jet formed at the tip of capillary is similar to the configuration of stable cone-jet mode. However, the rotation of the cone and the jet, and the fragment formation in a spiral shape differ from the stable cone-jet mode. The following section is going to introduce and discuss the stable cone-jet mode, which is essential for utilizing electrohydrodynamic processing for different applications.

2.4.2.7 Cone-jet mode

With the increasing applied voltage, a stable cone-jet mode can be achieved from the unstable cone-jet mode. In such mode, the liquid issues from the capillary in the form of a regular, axisymmetric cone with a thin jet (10 – 100 μm in diameter) at its apex, stretching along the capillary axis (Jaworek and Krupa, 1999a). The end part of the jet undergoes instabilities of two types, varicose and kink. In the case of varicose instabilities, the waves are generated on the surface of the jet, but the jet does not change its linear position. The wave contracts in the nodes, and the jet disintegrates into droplets, which further flow close to the capillary axis. In the case of kink instabilities the jet moves irregularly off the axis of the capillary, and breaks up into fine droplets due to electrical and inertial forces. The aerosol is spread out off the axis, but nearly uniformly in the spray cone of the apex angle of about 50 - 60°.

The schematic diagram and the real image of stable cone-jet mode are shown **Figure 2.18**a&b. The jet remains stable on the length of a few millimetres from the capillary exit due to the weak lateral electric field. The field generated by sprayed droplets is nearly symmetrical and the lateral forces on the jet remain the equilibrium. The space charge in the cone-jet mode is much more stable than in other spraying modes since the droplets are smaller and of lower mobility, which is one of the most attractive advantages of such spraying mode. A steadily uniform spatial dispersion of the aerosol can be generated, which is desired for the deposition and coating process. Another fundamental advantage is that the droplets breaks up at the jet end are homogeneous and the size from a few micrometers in diameter to several tens of micrometers can be obtained. The mechanism of the cone-jet mode will be discussed in detail in the later section.

2.4.2.8 Multi-jet mode

The multi-jet mode can usually be achieved from the cone-jet mode by increasing the applied voltage. **Figure 2.19** shows the schematic diagram and the real image of multi-jet mode captured by high speed camera. When the applied voltage increases in the cone-jet mode, the cone depth and the jet diameter decrease until a critical level at which the Taylor cone becomes skewed, leading to a single jet at the rim. This situation is unstable and two or more jets at opposite sides relative to the axis or three symmetrically distributed on the rim of the capillary are formed. At the meantime, the meniscus becomes flat with only short cones at the emission points. The jets disintegrate into small droplets due to kink instabilities, forming a fine mist around the capillary axis. The aerosol does not fill the whole volume but is only dispersed in a few narrow streams which seem to be located uniformly around the axis. Moreover, the number of the emission points increases with the increase in voltage and flow rate, and each jet is formed faster and becomes thinner due to the increasing shear stresses.

The reason for the transforsation from the stable cone-jet mode to the multi-jet mode is the limited velocity of the jet formation as compared to the liquid velocity at the outlet of the capillary, resulting from the higher flow rate (Jaworek and Krupa, 1999a). At higher applied voltage, the extra charge build-up on the surface of the Taylor cone result in multiple jets. It has also been reported that the droplets obtained in the multi-jet mode are smaller than a few micrometers in diameter, but with significant standard deviation (Jaworek and Krupa, 1999b).

2.4.2.9 Corona discharge

The corona discharge occurs when the electric field between the needle and the ground electrode becomes larger than the electrical breakdown threshold of the surface energy

of liquid surrounding air interface. If the corona discharge occurs before the electrical field initiating the stable cone-jet mode is reached, it can prevent the establishment of this mode. The phenomenon is likely to occur especially when the liquids are of high surface tension and thus require a high electric field to offset the capillary pressure (Cloupeau and Prunet-Foch, 1989).

2.4.3 Mechanism of stable cone-jet mode

As introduced earlier, the stable cone-jet mode is crucial for the EHDA deposition processing. The understanding of the fundamental mechanism of such mode is therefore important for utilizing EHDA coating process with precise controlling. Hartman and co-workers established a physical model to assist the understanding of the stable cone-jet mode of the electrohydrodynamic process (Hartman *et al.*, 1999a). In this model, the stable cone-jet mode has been divided into three stages: (1) Acceleration of the liquid in the liquid cone; (2) jet break – up (Droplet production); (3) evolution of spraying after droplet production. Such three processes will be discussed in detail in the following sub-sections. Furthermore, apparently, since the droplets size is also crucial for the deposition morphology and quality, and is significantly influenced by droplet evaporation during the electrohydrodynamic process. Thus, the droplet evaporation after the previously introduced three processes will be also discussed as an important part of the stable cone-jet mode electrohydrodynamic process.

2.4.3.1 Acceleration of the liquid in the liquid cone

The stable liquid cone is formed as result of the balance of liquid pressure, liquid surface tension, liquid viscosity, gravity and electric stresses in the liquid surface. This conical shape (also called Taylor cone), which balanced the surface tension and the

electric stress, was firstly analytically calculated by Taylor (1964). A Taylor cone forms when the outward stress due to applied electric field balances the inward stress due to liquid surface tension. The various forces influencing such phenomenon are shown in **Figure 2.20**. The main drive of the cone-jet mode formation is the electric force, and therefore electric field. Thus the creation of a permanent stable jet requires a penetration of the electric field lines in the liquid, therefore the liquid must not be a perfect conductor. Only this penetration allows the appearance of a component of the electric field tangential to the liquid surface, which is acting on the surface charges, creates a force which drives the liquid and accelerates the jet downstream (Clopeau and Prunet-Foch, 1990).

2.4.3.2 Jet break-up

The jet break-up process is also called droplet production process (Hartman, 1999a). There are two mechanisms can lead to the emission of liquid from the tip of a Taylor cone. In one mechanism, ions, neutral atoms and droplets are emitted from the liquid surface due to instabilities brought on by the intense electric filed at the tip or in the other mechanism; liquid is ejected via the formation of jet of liquid which breaks into droplets after some length due to surface instabilities (Rulison and Flagan, 1994). The second mechanism is most commonly observed.

At the bottom of the cone, the charges are mainly conducted through charge convection. Every liquid has a minimum flow rate, below which a stable cone-jet mode can not be achieved. At this minimum flow rate the jet breaks up due to axisymmetric instabilities. The instabilities are also called varicose instabilities. At high flow rate, the current through the liquid cone increases. With increasing current, the surface charge on the jet also increases. Above a certain surface charge the jet break-up will also be influenced

by lateral instabilities of the jet. These instabilities are also called kink instabilities. When the influence of these instabilities increases, the size distribution of main droplets become wider (Cloupeau and Prunet-Foch, 1989), which is preferable for processing uniform coatings. One may also need to be mentioned is that there exists a minimum and a maximum flow rate for each given applied voltage that seems to be related to the meniscus stability. The stable cone-jet mode changes to multi-jet mode when the flow rate is below the minimum flow rate, and also may change to microdripping mode when the flow rate is above the maximum value at the certain applied voltage (Ganan-Calvo, 1996). Such characteristic determines that the stable cone-jet mode can be only achieved at the certain flow rate range for a specific liquid, beyond which other electrohydrodynamic modes will present.

2.4.3.3 Evolution of spray after droplet production

The liquid jet at the bottom of the Taylor cone will eventually disintegrate into droplets, which was catalogued as the third process of the stable cone-jet mode (Hartman *et al.*, 1999b). Electrical interaction between the highly charged droplets with different sized, and thus inertia, causes a size segregation effect due to high mobility. Smaller droplets, also called satellite droplets, are found at the edge of the spray and the larger sized droplets, which were also called main droplets, are found in the centre of spraying (Ganan-Calvo *et al.*, 1994; Hartman *et al.*, 1999a, 1999b); At the moment of production, the distance between main droplets and secondary droplets is small, approximately half of the distance between main droplets.

The studies of droplets behaviour during spraying were also carried out by Hartman and his co-workers (Hartman *et al.*, 2000). He stated that the droplets radial travelling velocities are much lower than the axial velocities. It also shows that the initial radial

positions and the axial velocities for the main droplets and secondary droplets are almost equal. Due to the difference in droplet charge, droplet diameter and droplet mass, the electric force and the inertia of a large droplet will differ from those of a small droplet. The small droplet has a lower inertia than the large droplet, which results a larger acceleration for the smaller droplet. As a result of that, the distance between the main droplet and the secondary increases, and the small droplet will attain a higher radial velocity. This characteristic determines that the spraying pattern achieved using EHDA process is of circular shape, and the coating growth rate in the centre of the circular coating is higher than that at the edge.

As afore-introduced, the understanding of the classic physical model of the stable cone-jet mode electrohydrodynamic process is important for utilizing this phenomenon. However, another process, called droplet evaporation which takes place paralleled to the spraying, is also important to be discussed due to its significant impact on the droplet size evolution and distribution, which are the well-known factors to influence the final deposition properties.

2.4.3.4 Droplet evaporation

While evaporation does not alters droplet transport significantly after the jet break – up in the stable cone-jet mode, but it can drastically reduce the droplet size depending on the solvent properties, environment humidity, surrounding air movement and environmental temperature (Wilhelm *et al.*, 2003). If the highly charged droplets evaporate, then the size of the droplet will decrease, and therefore the Rayleigh limit for the droplet charge can be reached. In that case, droplet fission can take place which further changes the produced size distribution as illustrated in **Figure 2.21**. Rayleigh

(1978) showed the relationship between the droplets radius and Rayleigh limit as follows:

$$Q_R = 8\pi\left(\gamma\varepsilon_0 r_d^3\right)^{1/2},$$

where Q_R is the Rayleigh charge limit (C), γ is the surface tension (Nm^{-1}), r_d is the droplet radius (m) and ε_0 is a constant, 8.85 x 10^{-12} F/m.

For a specific liquid, the physical properties, such surface tension, and the dielectric constant of the vacuum are constant. During the spraying, the liquid droplet radius r_d decreases due to evaporation, the Rayleigh charge limit for the charged droplet decreases accordingly. When the Rayleigh charge limit decreases below the original charge of the droplet, droplet fission occurs to reduce the charge of the individual droplets. Therefore, the charged droplet becomes small in size. The droplet size distribution can be shifted to a small size region due to this effect.

2.4.4 The effect of physical properties of the liquid to electrohydrodynamic spraying

As afore-introduced, apart of the processing parameters, such as flow rate and applied voltage, the physical properties also have a big impact on achieving the stable cone-jet mode. The following sections are going to discuss the effect of the core physical properties of the liquid on the stable cone-jet mode electrohydrodynamic processing to pave the way towards the systematic investigation of utilizing such technique for biomedical applications.

2.4.4.1 Electrical conductivity

Electrical conductivity is the most important liquid physical property in controlling both the stability of the cone-jet mode electrospraying and the produced droplet size. For the liquid droplet at the capillary exit to be transformed into a conical shape, sufficient electrical conductivity in the liquid is necessary. If the electrical conductivity is too low it can not be processed in the stable cone-jet mode as there is not enough charge build up in the liquid. If it's too high the processing is not possible as the electrical discharge (corona discharge due to the surrounding air) would occur before attaining the required applied voltage for the stable cone-jet mode (Hartman *et al.*, 2000).

A number of studies have been carried out on the effect of such liquid property. The maximum liquid electric conductivity for a stable electrospray was 10^{-3} Sm^{-1} reported in 1971 (Jones and Thong, 1971). Later, it was also investigated that the stable cone-jet mode could also be achieved when the liquid conductivity was above 10^{-5} Sm^{-1} (Mutoh *et al.*, 1979).

This phenomenon was explained by Cloupeau and Prunet-Foch in 1989. They stated that the electrical conductivity is the most important for the stable cone-jet mode electrohydrodynamic processing since a liquid with too low conductivity cannot be atomized due to lack of tangential stress caused by the charges. This was established as the driving force responsible for forming the jet. Their investigation proved that electric conductivity as the most important physical property in maintaining the stability of the electrospraying and controlling the droplet size.

2.4.4.2 Surface tension

In order to form and maintain a stable cone-jet mode, the surface tension has to be overcome by the electric stresses. The major role of this parameter in the droplet formation process is to influence the size and shape of the droplets. The higher the surface tension, the larger electric field (higher applied voltage) is required, and this may also lead to the greater probability of electrical discharge occurring due to the surrounding air. The onset applied voltage for the stable cone-jet spray increases with the liquid surface tension increases (Smith, 1986). The stable cone-jet mode may not be achieved when the liquid surface tension is too high, as the electric field required exceeds that for the electric break down in the gas surrounding the cone (Tang and Gomez, 1995).

2.4.4.3 Viscosity

Another vital liquid property which plays a significant role in the jet break-up (droplet formation) process and influence the droplet size is viscosity. An increase in viscosity can lead to a lower dominant wave number, and the lower dominant wave numbers will lead to the increase of the droplet size in electrohydrodynamic processing (Weber, 1931). It was found that liquid viscosity significantly influences the number of satellite droplets. During droplet formation process, the high viscosity had been demonstrated to be important in two aspects. First, high viscosity enhances the damping of the initial oscillations of the interface remaining meniscus at the capillary immediately following the detachment of the previous drop. Second, viscosity plays a key role in keeping the primary droplet nearly spherical in shape as it's detaching from the capillary.

Furthermore, investigations were carried to study the effect of viscosity on the relic size produced by electrohydrodynamic processing by Jayasinghe and Edirisinghe (2002).

They stated that the greatest effect of the viscosity is upon the relic size. Bigger relics were produced when using liquid of higher viscosity.

2.4.5 Controlling parameters of EHDA spraying process

Based on the above discussion of the mechanisms of the electrohydrodynamic processing, it can be concluded that a range of key process parameters, such as liquid flow rate, applied voltage and the capillary-substrate distance, need to be studied and investigated for the further deposition process. Liquid flow rate directly affects the velocity of the liquid, and therefore significantly influence the stability of the cone-jet mode (Hartman *et al.*, 1999a), the droplet size (Jayasinghe and Edirisinghe, 2004) and therefore the eventual deposition morphology. The applied voltage determines the magnitude of the electric field, the main drive of the EHDA processing. It's crucial to the stability of the cone-jet mode and the droplet size distribution. The change of the capillary-substrate distance changes the droplets travel distance and period, which also influence the droplet size due to the degree of the evaporation of the liquid. Furthermore, the core physical properties of the liquid, including conductivity, surface tension and viscosity, are also important for maintaining the stable cone-jet mode EHDA processing. Therefore, the control of these parameters is essential for preparing nHA coated implant materials using this technique.

2.4.6 Electrohydrodynamic patterning

The technologies of processing bone implant materials have been developing rapidly for nearly three decades so far. The core challenge is to process biomaterials to better mimic the human natural organs in term of the mechanical and biological properties.

Recently, attention has focused on creating a well-defined surface topography of biomaterials, a feature that is known to affect initial biological response (Curtis and Wilkinson 1997). A number of studies have been conducted to evaluate the relationship between surface structure, dimensions and tissue growth on HA (Tan and Saltzman 2004; Rosa *et. al.* 2003). These findings suggest that cell activity could be up-regulated through optimization of the surface properties of the substrates to further enhance the implant materials bioactivity and thus reduce the healing period and pain. To fulfil these needs, the development of a new generation coating procedure, which allows easy, selective and well-defined patterning, is required.

Electrohydrodynamic processes basically offer the capability of producing patterning by printing (Ahmad *et. al.* 2007, Wang *et al*., 2005). In terms of biological response, printing patterns with topography can be much more effective than simply depositing a continuous coating on the substrate (Huang *et. al.* 2004a, b). The electrohydrodynamic print-patterning device comprises an electrohydrodynamic apparatus (**Figure. 2.21**) coupled together with an X-Y-Z patterning system (Wang *et al*., 2005). The needle allows flow of a suspension at precise low flow rate using a syringe pump. An electric field was applied between the needle and the point ground electrode. Servo-motors drive x and y directions and mini-stepping technology controls the z direction. The bottom of the x-axis is mounted on a base plate and the cradle of it is placed directly on the y-axis keeping a very low profile. The bottom of the z-axis is mounted separately and has a special yoke attached to its stepper-motor driven cradle, which holds the electrohydrodynamic apparatus. The device is operated using a programmable motion-controller-PC unit. The glass substrate is positioned closed to the cone-jet break-up point for the pattern deposition. In this way, several different grid patterns incorporating both lines and spots were printed on the glass slide (Fig. 2.22). The line thickness, the

spacing between the lines and the spots could be changed as desired. And, the lines and spots printed contain dense packing of nHA particles.

However, using the electrohydrodynamic printing technique, the lines patterned show discontinuity at some locations and there is variation in thickness of the lines observed. The edge of the lines is irregular and a few droplet-relics are scattered outside the line. Another concern of this patterning technique is that it is not capable for preparing the nHA patterns on conducting materials surface due to its setup and process mechanism.

Therefore, considerable research is still ongoing for developing new patterning techniques for improving the pattern quality as well as overcoming the limitation of the current electrohydrodynamic printing technique for biomedical applications. Therefore, a novel patterning technique, namely template-assisted electrohydrodynamic atomisation (TAEA) spraying, has been innovated to process the well-defined microscale bioceramic patterned titanium implant materials. The TAEA process evolves from electrohydrodynamic atomization spraying (EHDA) and uses novel ground electrode configurations and templates. Similar to EHDA process, TAEA processing setup consists of a nozzle (needle) connected to a high voltage supply and a specifically designed ground electrode. A suspension or liquid containing the functional material to be deposited is fed to the nozzle, kept at a high voltage, at a controlled flow rate. Out of several different spraying modes, the stable patterning cone-jet mode, which is the steadiest mode of spraying, could regularize the break-up of jet to generate fine and uniform droplets of a few micrometers in size. In TAEA, droplets are driven by the electrical force to attach to the substrate as well as the template on top of it.

After evaporation of the solute or liquid carrier, the deposited material particles distribute uniformly on the substrate and template. By removing the template, a deposition of well-defined patterns can be achieved on the substrate surface. As a jet-based patterning technique, the dimension of the patterns largely depends on the spacing size in the template. A template with a small spacing size can lead to patterns with small dimensions. However, another striking factor is the droplet size produced after jetting. To create a precise high-resolution HA pattern, it has to be ensured that the nHA suspension droplets can be small enough to pass through the tiny spacing of the template and attach to the targeted substrate. Furthermore, after the suspension droplets attach to the substrate, their spreading can also lead to coarse edges of the patterns. Therefore, the reduction of the droplets size and the control of the droplets spreading on the substrate become the major challenges in controlling this process. Due to the nature of electrohydrodynamic spraying that was discussed in previous sections, the liquid droplets form after the jet break-up and travel to the actual target substrate. Changing the solvent or the substrate surface temperature could significantly influence suspension evaporation and the deposited relic size without causing any other complexities during the patterning. The investigation, processing mechanism and its optimisation are introduced and discussed in detail in Chapter 5.

Figures

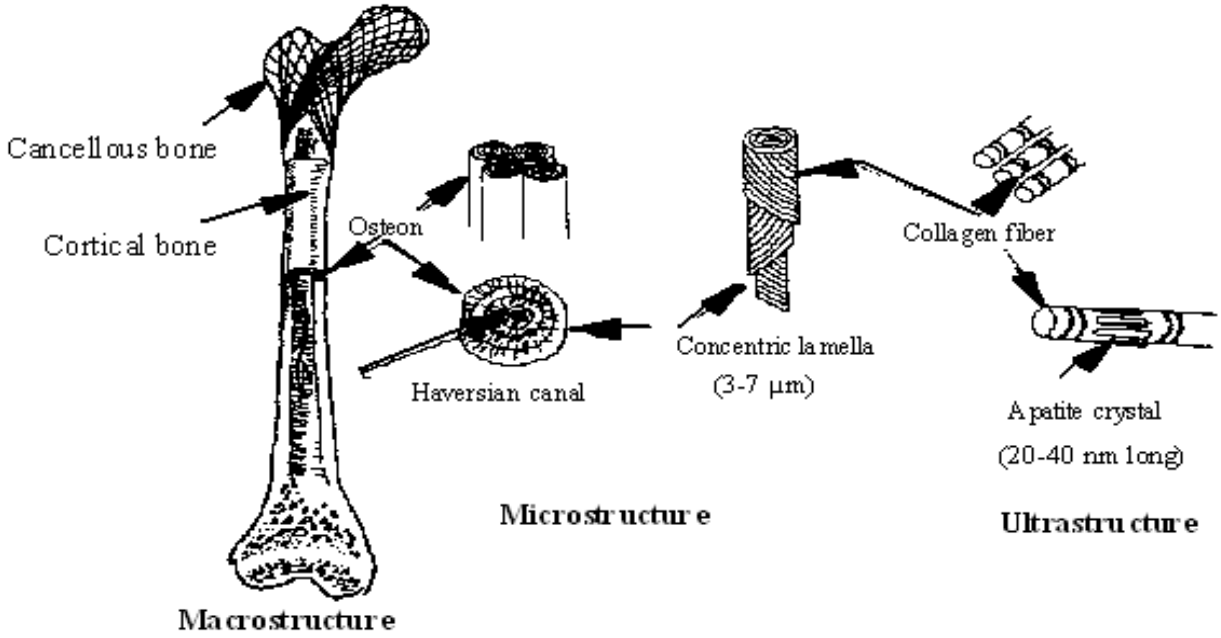

Figure 2.1 Macro-, micro- to ultramicro- structure of bone (Park, 1987)

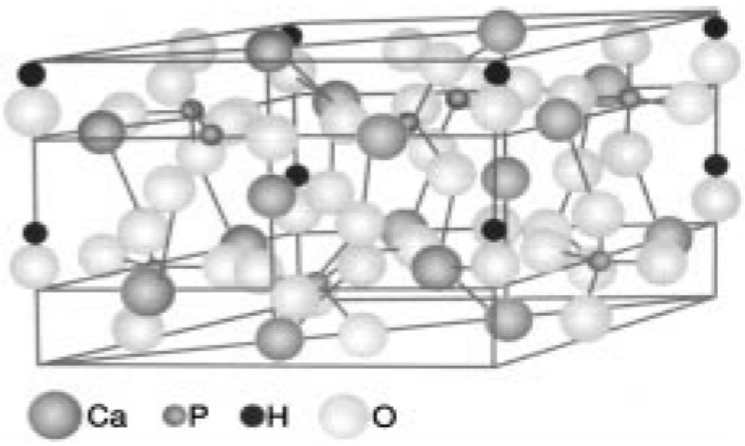

Figure 2.2 Unit cell of apatite crystal projected along a-axis (Aoki, 1991)

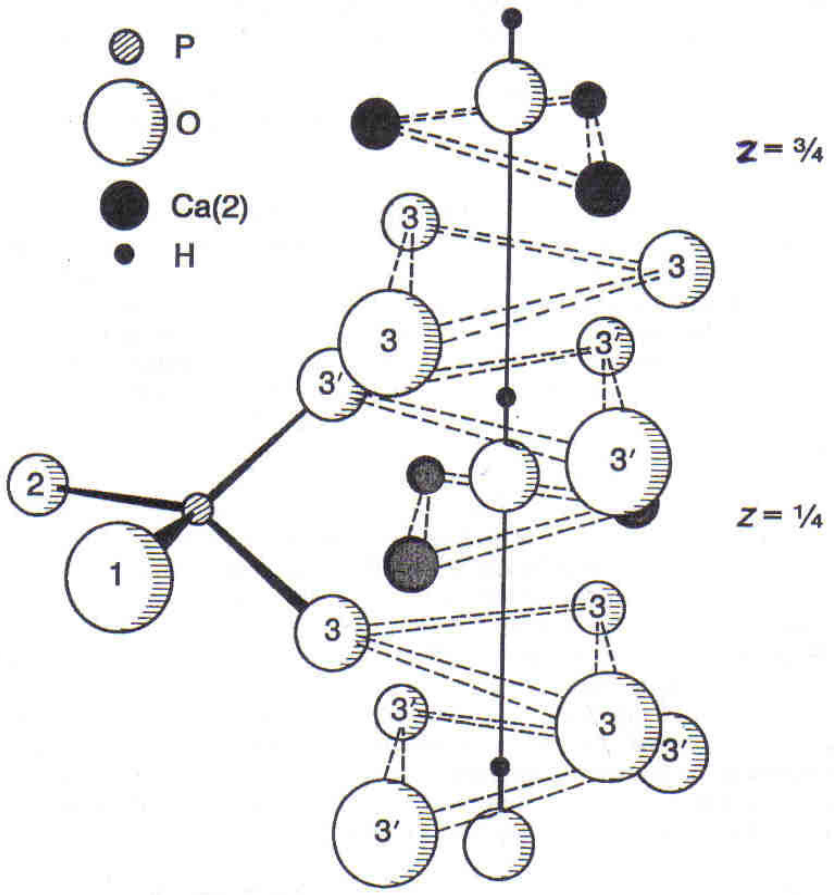

Figure 2.3 Arrangement of ions around the vertical axis at the corners of the apatite unit cell (Young, 1967)

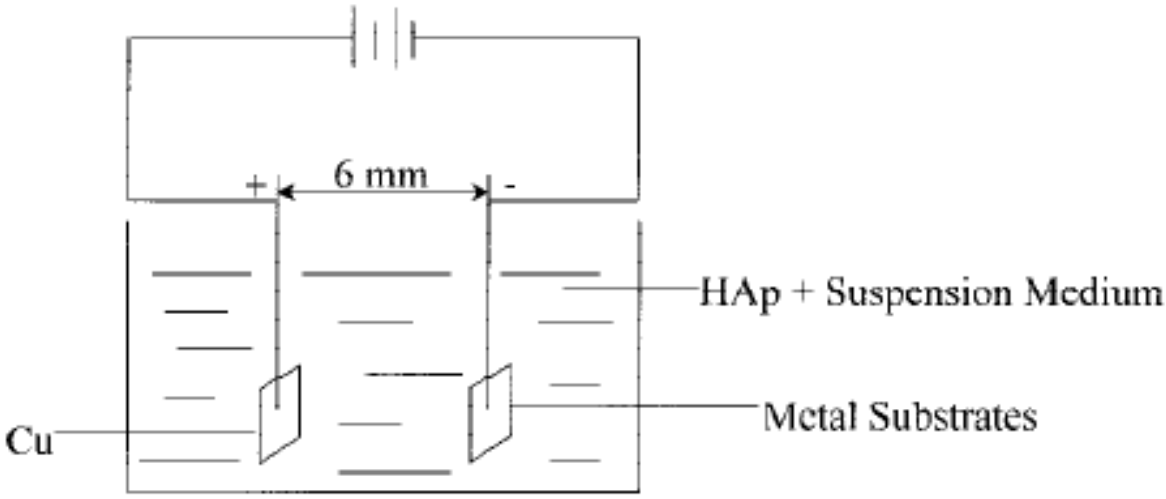

Figure 2.4 Schematic representation of electrophoretic deposition technique (Wei *et al.*, 1999a)

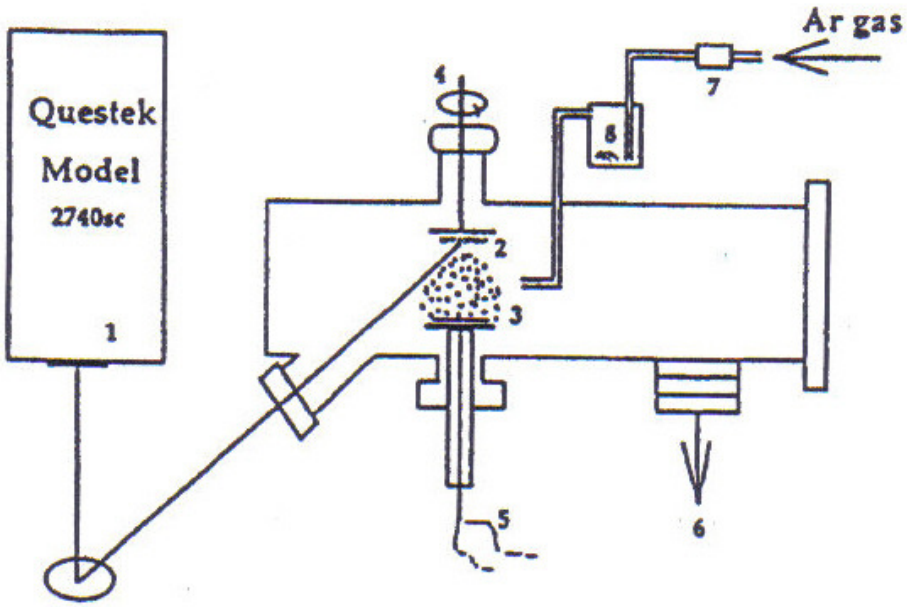

Figure 2.5 Schematic representation of pulsed laser deposition technique (1. ArF excimer laser; 2. Target; 3. Heated Ti substrate; 4. Rotation motor; 5. Substrate heater; 6. Turbomolecular pump; 7. Mass flow control meter for argon gas; 8. Water bath) (Wang *et al.*, 1997)

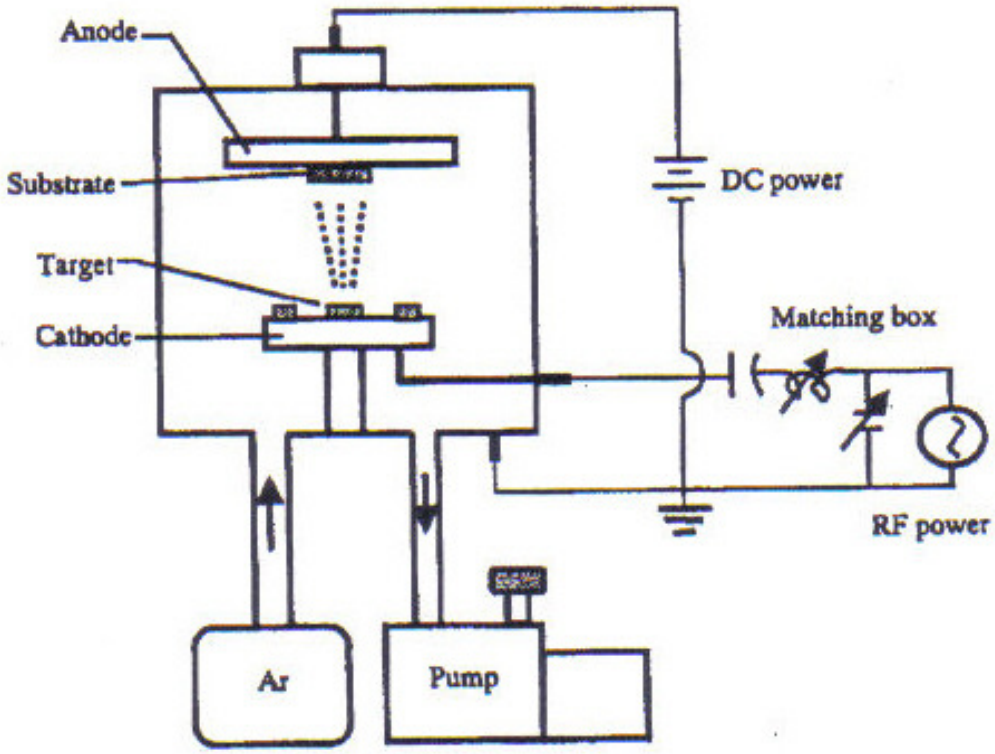

Figure 2.6 Schematic representation of a magnetron sputtering system (Ding *et al.*, 1999)

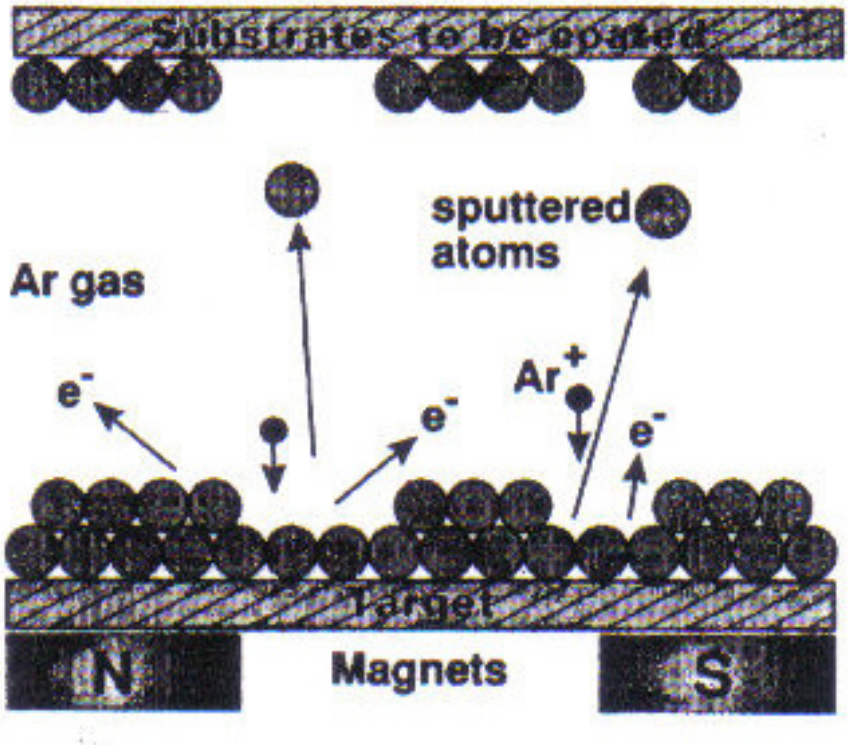

Figure 2.7 Schematic representation showing momentum exchange processes that occur during magnetron sputtering (de Groot *et al.*, 1998)

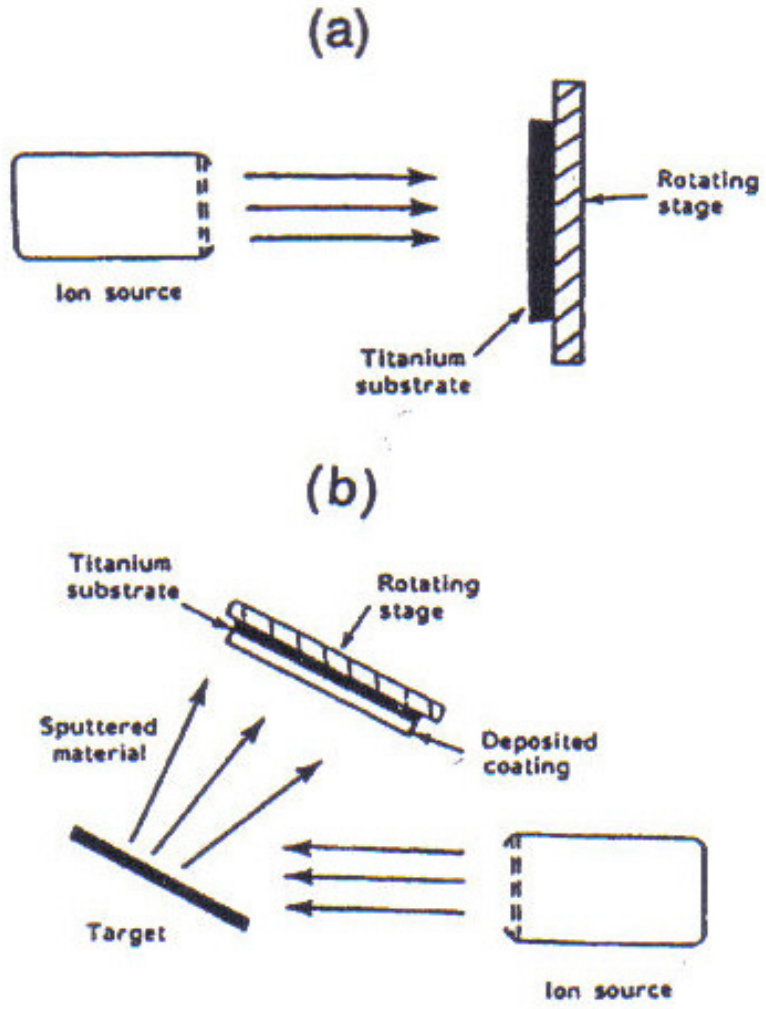

Figure2.8 Schematic representation of the ion beam sputtering technique (Ong *et al.*, 1992)

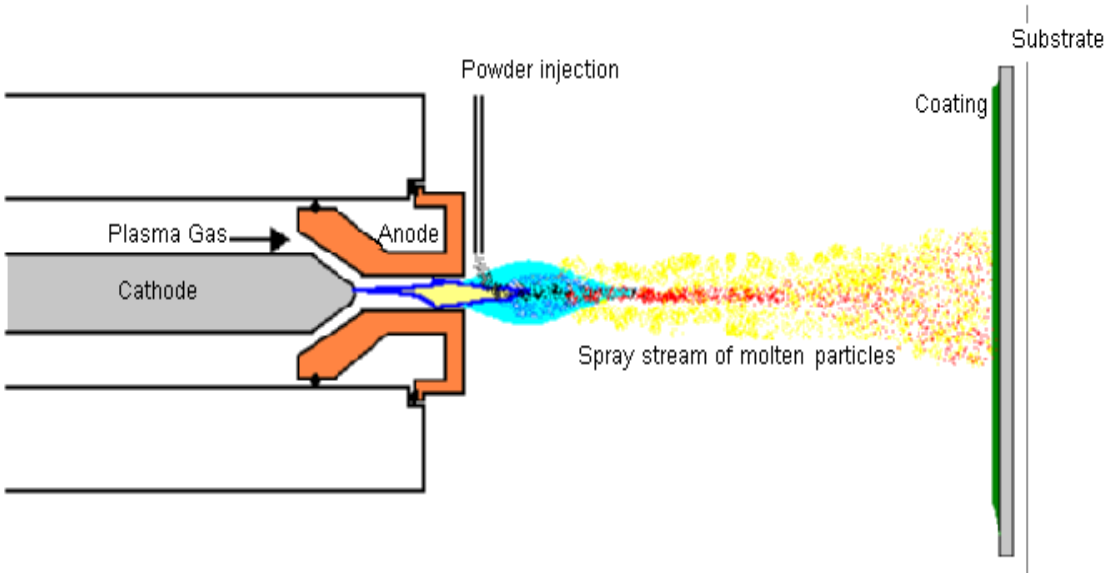

Figure2.9 Schematic representation of the plasma spraying technique

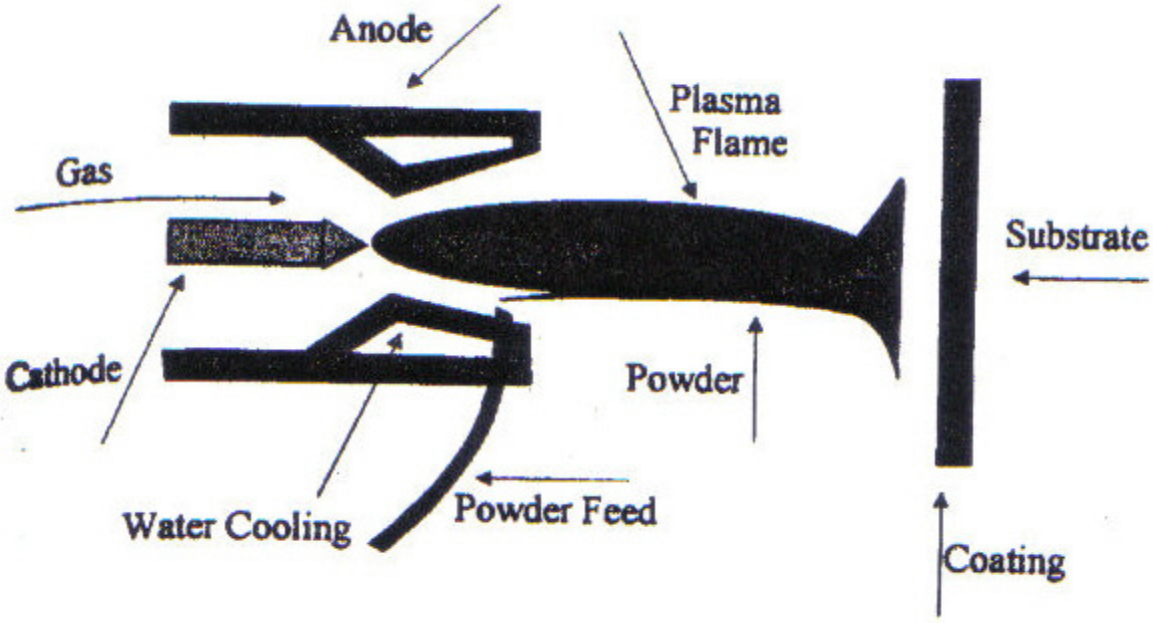

Figure2.10 Schematic representation of the vacuum plasma spraying technique (Gledhill *et al.*, 1999)

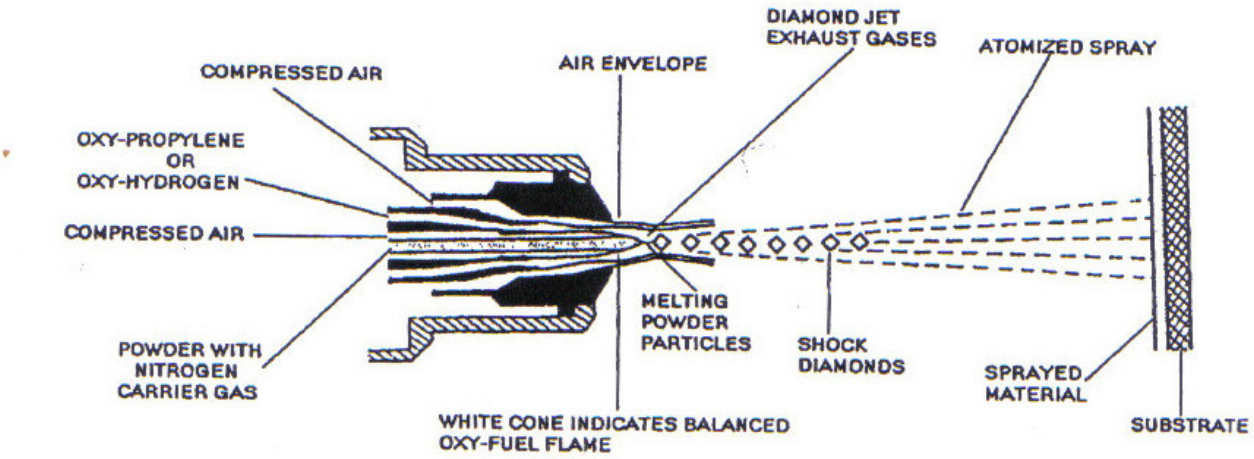

Figure2.11 Schematic representation of the high-velocity oxy-fuel spraying technique (Lewis, 2000)

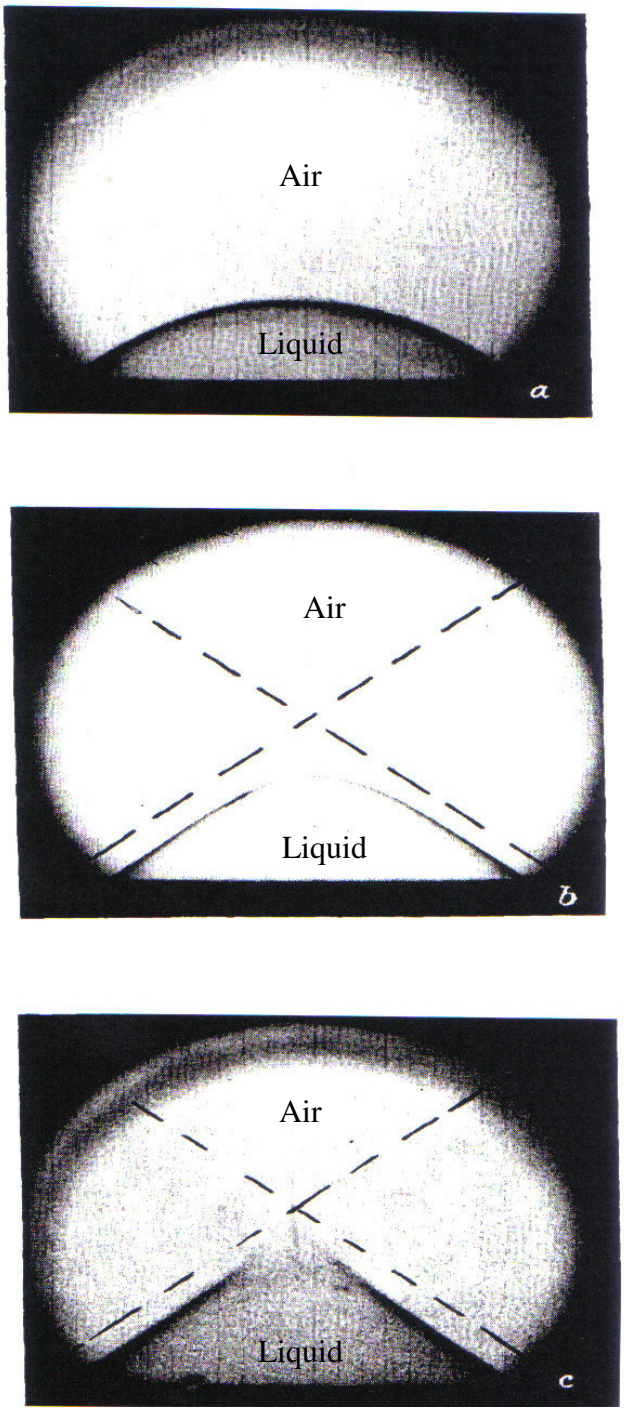

Figure2.12 a, b and c stages involved in achieving the steady state cone (Taylor, 1964)

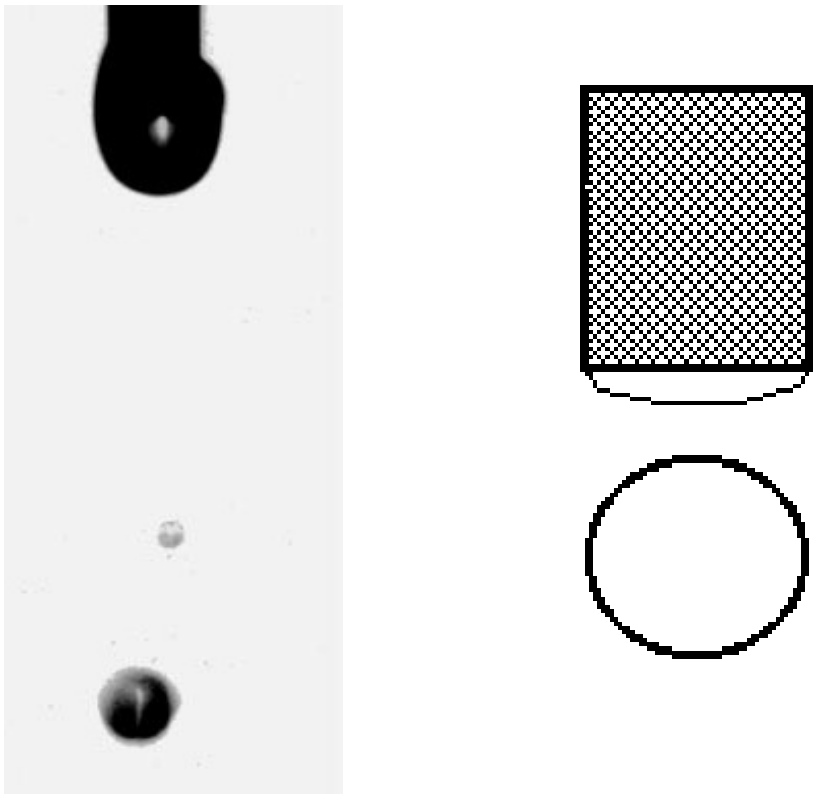

(a) (b)

Figure2.13 (a) the real image (Jaworek and Krupa, 1999b) and (b) schematic diagram illustrating dripping mode in electrohydrodynamic atomisation

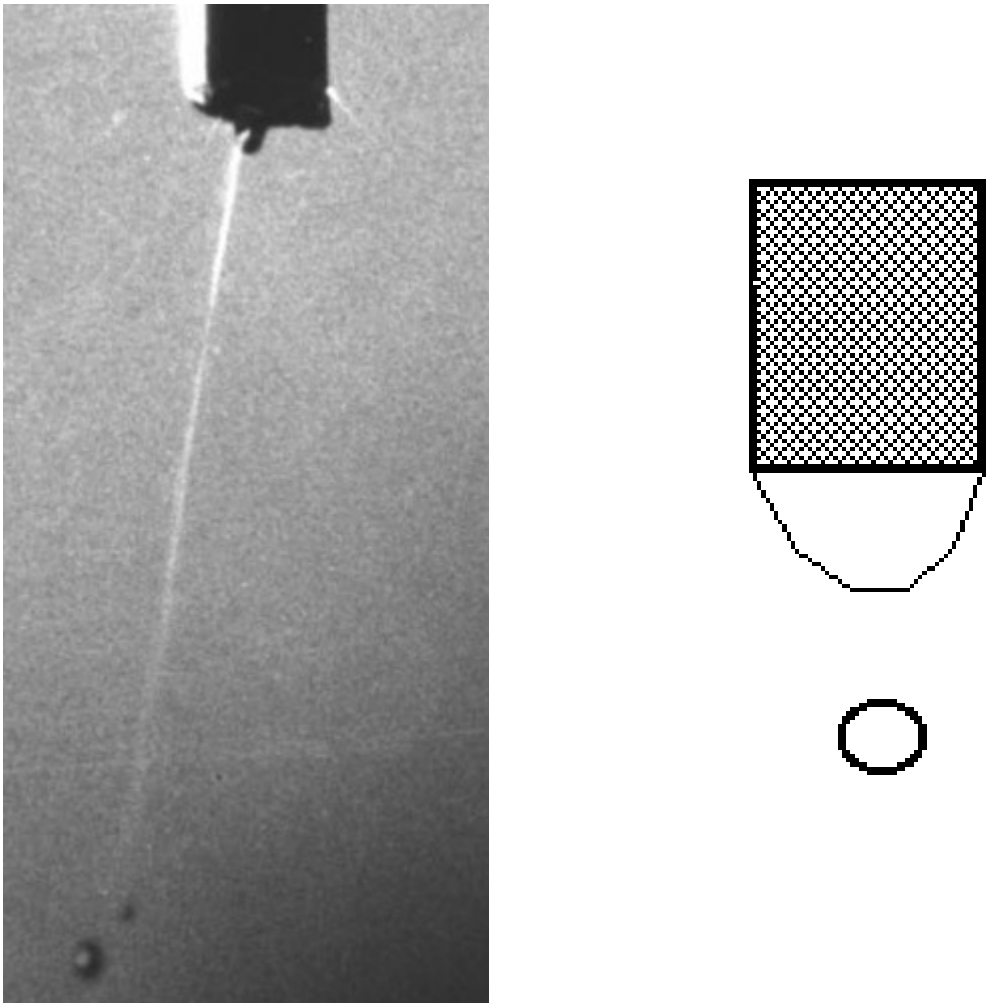

(a) (b)

Figure2.14 (a) The real image (Jaworek and Krupa, 1999b) and (b) schematic diagram illustrating micro-dripping mode in electrohydrodynamic atomisation

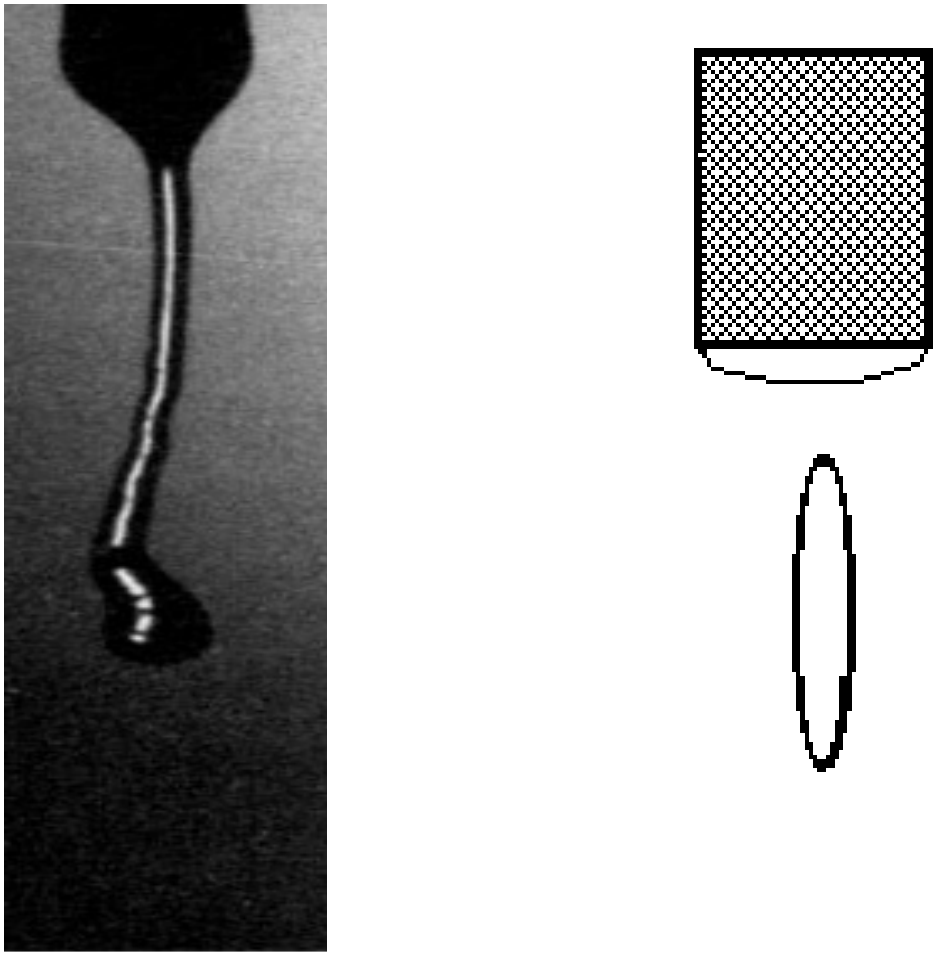

(a) (b)

Figure 2.15 (a) The real image (Jaworek and Krupa, 1999b) and (b) schematic diagram illustrating spindle mode in electrohydrodynamic atomisation

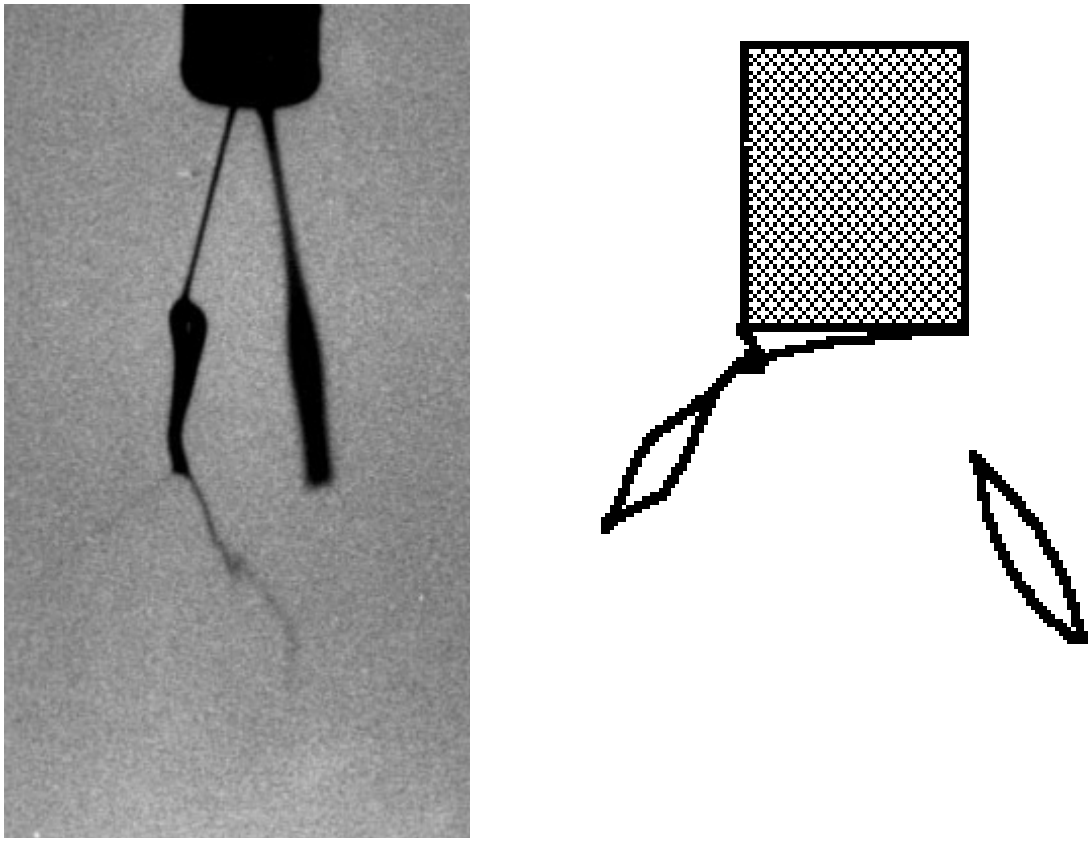

(a) (b)

Figure 2.16 (a) The real image (Jaworek and Krupa, 1999b) and (b) schematic diagram illustrating multi-spindle mode in electrohydrodynamic atomisation

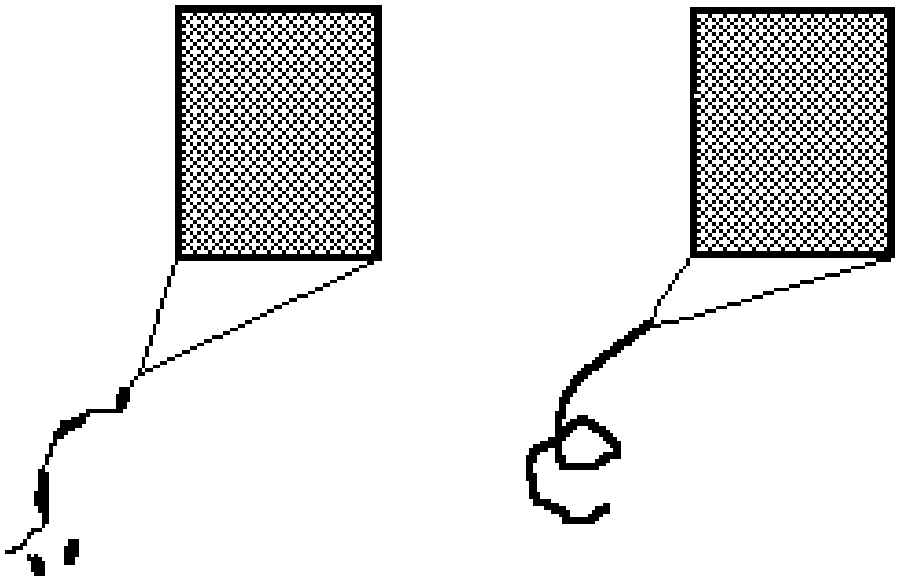

(a) (b)

Figure 2.17 Schematic diagrams illustrating (a) oscillatory jet mode and (b) precession mode

.

(a)

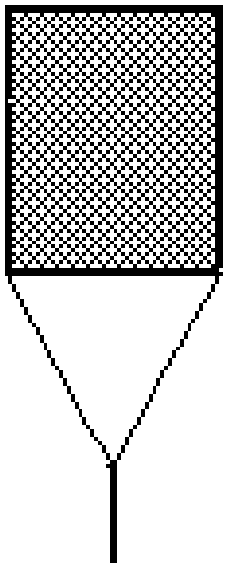

(b)

Figure 2.18 (a) The real image (Jaworek & Krupa, 1999b) and (b) schematic diagram illustrating the stable cone-jet mode in electrohydrodynamic atomisation

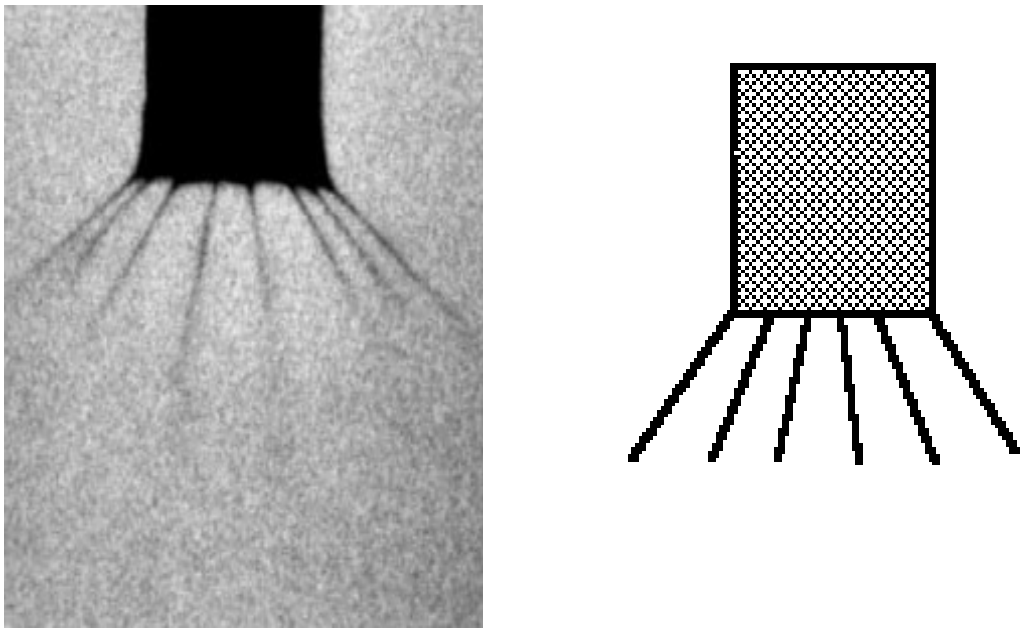

(a) (b)

Figure 2.19 (a) The real image (Jaworek & Krupa, 1999b) and (b) schematic diagram illustrating the multi-jet mode in electrohydrodynamic atomisation

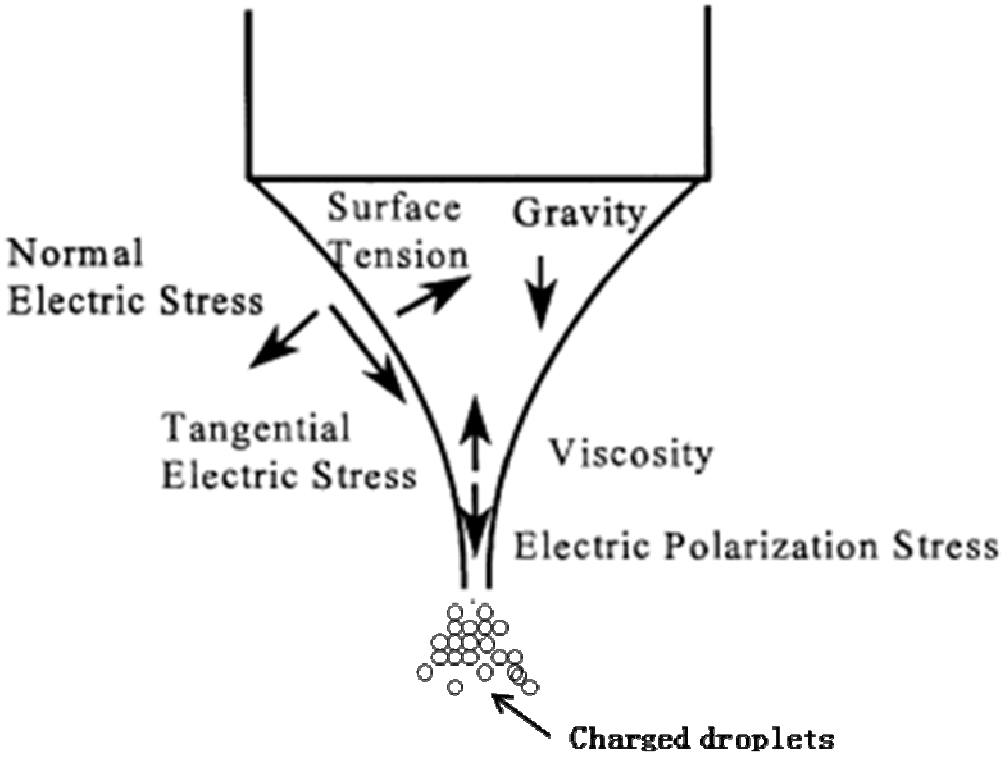

Figure 2.20 Schematic diagram of the forces influencing on a Taylor cone (Hartman, 1999a)

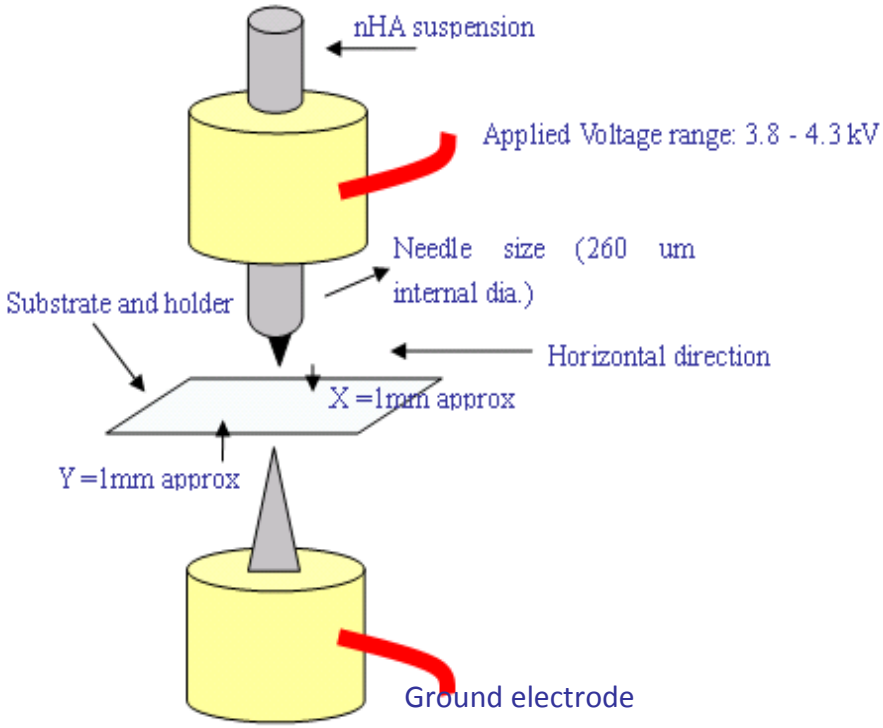

Figure 2.21 Needle, substrate and point ground electrode arrangement in the electrohydrodynamic printing apparatus. (Ahmad *et al*., 2006)

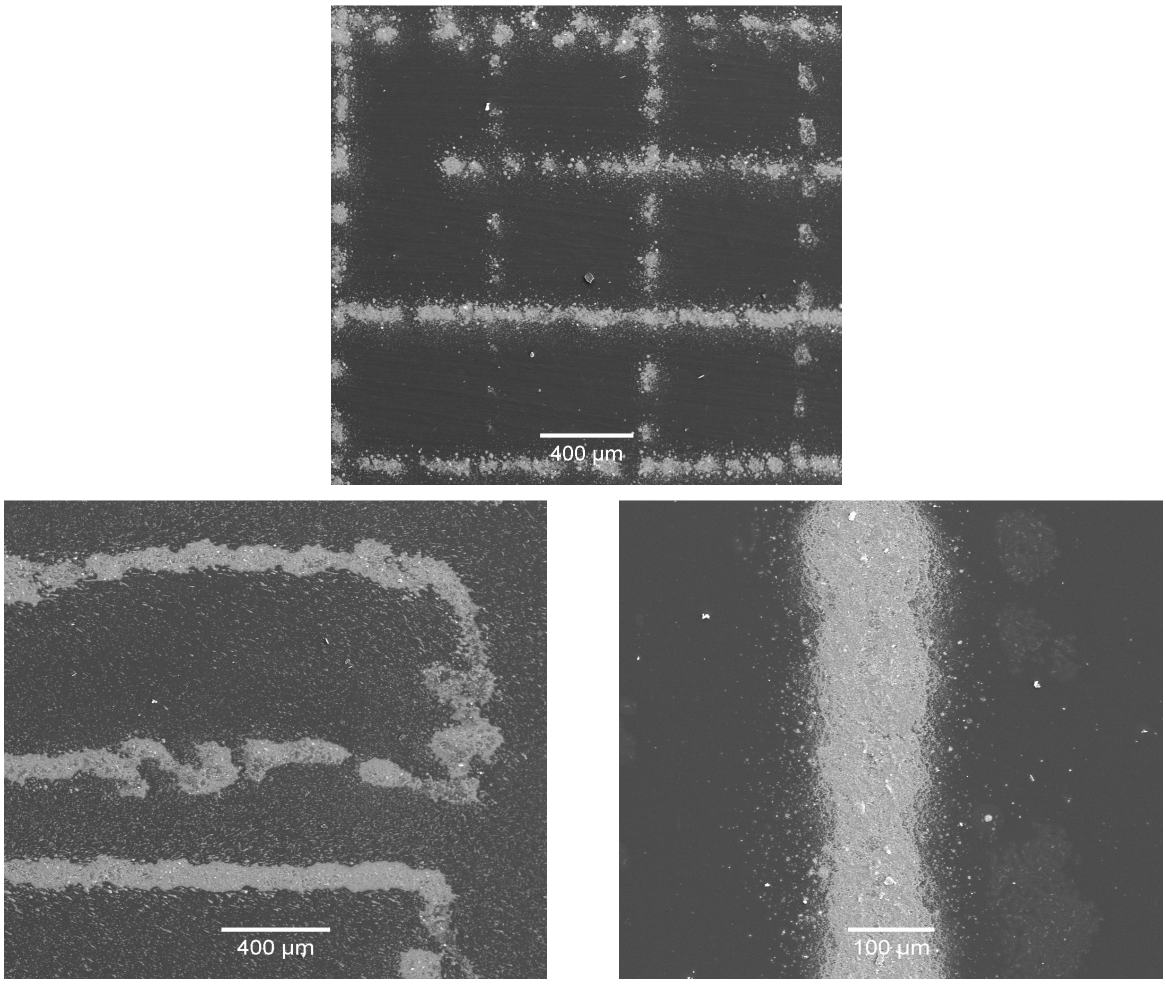

Figure 2.22 Optical micrographs of the patterns printed by electrodydrodynamic printing technique

Chapter 3

Experimental Details

This chapter introduces the experimental procedures that were followed during the investigations. The materials used, corresponding supplier and product details are given. The preparation and characterisation of nano-hydroxyapatite suspension (nHA) are discussed. A description of the electrohydrodynamic processing and the equipments used are given. The methods and equipments for the nHA deposition characterisation are also introduced in this chapter. Subsequently, the experimental details of the investigation of template-assisted electrohydrodynamic atomisation (TAEA) spraying are also included in this chapter. Finally, a description of the experimental procedures for investigating the effect of the needle geometry to the droplet relic size using EHDA processing is also given.

3.1. Materials

The main materials involved in this project are nano-hydroxyapatite (nHA) and titania (TiO_2), of which the suspension and the sol were prepared specifically, and the preparation is described in **Section 3.2**. The solvents used for the nHA suspension preparation are introduced. Substrate materials, such as Titanium and silicon wafer, are also introduced in details as follows.

3.1.1 Substrate materials.

3.1.1.1 Titanium

The titanium substrate used in **Chapters 4 and 5** for deposition of nHA was Grade 1 (ASTM F67) commercially-pure Ti (cpTi) plate (Advent Research Materials, Oxford,

UK) of 0.5 mm thickness. The Ti plate was cut into square shape substrates with the width and the length of 5 mm and 10 mm, respectively. The cpTi plates were then polished using a selection of silicon carbide grinding papers (No.800, No.1200, No.2400 and No.4000). Before used for the deposition, the plates were subjected to a sequential cleaning regime of acetone degreasing, rinsing in ethanol, sonication in deionised water for 5 minutes each, and subsequent air drying.

3.1.1.2 Silicon wafer

The substrates used in Chapter 5 also include silicon wafer supplied by Si-Mat Silicon materials, Germany. The specification of such material is shown in **Table 3.1**.

Table 3.1 Specification of Silicon wafer

Type/Dopant	P / B	Thickness	525 ± 25 μm
Orientation	<1 0 0>	Front surface	Polished
Resistance	10 -20 Ω cm	Back surface	Etched

The silicon wafer was also cut into square shape substrate plates with 5 mm and 10 mm in width and length, respectively. Before use, the silicon substrate was rinsed using ethanol, washed using deionised water and subsequent air dry.

3.1.2 Solvents for nHA suspensions

In this research, pure ethanol (99.7 %wt, BDH laboratory Supplies, Poole, UK) and Dimethylacetamide (DMAc, $CH_3C(O)N(CH_3)_2$, Sigma-Aldrich, U.K.) were used as the solvent of nHA suspensions, and the pure ethanol was taken as a standard material to

calibrate the characterization devices. The main difference in the physical properties of these two solvent is the evaporability. At ambient temperature, DMAc evaporates much more slowly than the pure ethanol. The other properties of ethanol and DMAc at the ambient temperature (22 °C) are given in **Table 3.2**.

Table 3.2 Properties of ethanol and DMAc

	Density ($kg\ m^{-3}$)	Electrical conductivity ($S\ m^{-1}$)	Viscosity (MPa s)	Surface tension $mN\ m^{-1}$
Ethanol	790	3.4×10^{-5}	1.3	23
DMAc	940	2×10^{-5}	1.9	32

3.2 Preparation of nHA, nHA suspensions and TiO_2 sol.

3.2.1 Preparation and Characterisation of nano-sized HA

nHA was synthesized by a precipitation reaction between calcium hydroxide (Sigma-Aldrich, Pooles, UK) and orthophosphoric acid (Sigma-Aldrich, Pooles, UK). Both reagents were AnalaR grade. 0.3M orthophosphoric acid was added drop wise to a 0.5M calcium hydroxide solution under continuous stirring at room temperature, while the pH was kept above 10.5 by the addition of ammonia solution (Sigma-Aldrich, Pooles, UK). Stirring was maintained for a further 16 hours after complete addition of the reactants. The precipitate obtained was allowed to settle for a further week and then washed with boiling water. The morphology of the nHA particles was examined using a JEOL

200CX transmission electron microscopy (TEM) with an accelerating voltage of 200keV.

3.2.2 nHA suspension preparation

To make the HA suspension suitable for EHDA processing, ethanol was added as a liquid carrier of the suspension. The originally prepared nHA suspension with water solvent was heated at 60 °C with constant stirring to evaporate most of the water content in the suspension and then added pure ethanol at specific amount. The nHA and ethanol mixture was then further stirred using a magnetic stirrer with ultrasound for 15 minutes. A range of HA concentrations (6-12.5wt %) was prepared and investigated to achieve electrohydrodynamic spray deposition in the stable cone-jet mode, and the suspension containing 6wt% of nHA was found to be most suitable (Ahmad *et al.*., 2006).

In the investigation of the effect of solvent evaporability to the TAEA patterning resolution, which is introduced in Section 5.4.1., DMAc was used as a nHA suspension solvent with low evaporability to compare the nHA/ethanol suspension during the process. Similarly to the nHA/ethanol suspension preparation, the originally prepared nHA suspension with water solvent was heated at 60 °C with constant stirring to evaporate most of the water content in the suspension and then added the DMAc at specific amount. The nHA and ethanol mixture was then further stirred using a magnetic stirrer with ultrasound for 15 minutes. The concentration of the nHA/DMAc suspension was controlled at the same level of the nHA/ethanol suspension (6 wt %) for the comparison study.

3.2.3 TiO_2 sol preparation

Titanium (IV) isopropoxide (Ti[OCH(CH3)2]4) supplied by Sigma-Aldrich, was used as a precursor in this research. The precursor sol was prepared by transferring specific volume of precursor to an air tight bottle containing pure ethanol, and the resulting solution was stirred using magnetic stirrer for 3 h at ambient conditions.

The success of the electrohydrodynamic processing depends on stable solution for sufficient time. The titania sol obtained using 2 wt% of precursor was very stable and no sedimentation occurred on standing indefinitely, thus such titania sol was used to for this study.

3.3 Characterization of TiO_2 sol, nHA particles and its suspensions

The properties of liquid are crucial for EHDA process. Therefore, the density, pH, surface tension, viscosity, electrical conductivity and relative permittivity of the 6 wt% nHA suspension and 2 wt% TiO_2 sol were measured. All the measuring equipments were initially calibrated using pure ethanol to validate reference data. The densities of the samples were calculated using the standard density bottle and the pH was measured using a standard pH probe and meter. Surface tension was measured using a Kruss Tensiometer K9 (Wilhlmy's plate method). Viscosity was evaluated using a Visco-Easy rotational viscometer. Electrical conductivity was assessed using a HACH SensION ^{Tm} 156 probe. Relative permittivity was estimated using the standard capacitance method.

The characterisation method and equipment for each core property are introduced and discussed in the following subsections.

3.3.1. Density

The density of the suspension/sol was measured using the well-established standard density bottle method with the volume of 10 ml (VWR, Lutterworth, UK). The mass of both the empty bottle and bottle filled with samples were measured on a chemical balance (AND HF-1200G A&D Instruments Ltd, Japan) which was capable of giving precise value up to the four decimals. Five consecutive measurements were taken ad average value of five density readings has been reported in this thesis, and all the measurements were carried out in ambient temperature and the density bottle was calibrated with ethanol.

3.3.2. Electrical conductivity

The electrical conductivity of suspension/sol was measured using a HI-8733 conductivity probe (HANNA instruments Ltd., Bedfordshire, UK) for the research carried out. It comprises of a meter panel and a conductivity probe. The meter panel is for setting the measurement range and read the result from the monitor while the probe is used to immerse in the examined liquid. The measuring range of this meter is 0.0 to 199.9 / 0 to 1999 μS/cm and 0.00 to 19.99 / 0.0 to 199.9 mS/cm, respectively. The resolution of the measurement using this instrument is 0.1 / 1 μS/cm and 0.01 / 0.1 mS/cm, respectively. The measurement is performed at the ambient temperature.

The electrode probe was always cleaned with distilled water and dried up before each measurement. The electrical conductivity measurements were taken by using ~30ml of

suspension in a beaker. The electrode was immersed in the liquid up to the specified mark for a specified time and reading shown on the meter was recorded. The air bubbles residing in the suspension were removed by shaking the suspension gently before reading. Five consecutive readings were taken and averaged for all investigations.

3.3.3 Surface tension

Surface tension was measured using a Kruss Tensiometer K9 (Wilhlmy's plate method) during the investigations. The plate was hanged from a hook and a breaker containing the suspension was placed on the stage below that. The plate was completely immersed in to the suspension and gradually lifted up. The reading recorded at point for which the surface of the liquid just detaches from the plate without breaking the surface gives the surface tension value. Generally, 100 ml liquid was used for this measurement using a 100 ml beaker, which is sufficient to fully immerse the plate. The instrument was calibrated using ethanol before measuring the suspension/sol at every instance. The plate was also washed using deionised water and air dried before each measurement. Five consecutive surface tension readings were taken to obtain the mean value to ensure the accuracy of the characterisation.

3.3.4. Viscosity

The viscosity of the suspension/sol was measured using a U-tube viscometer (A type, Schott Instruments GmbH, Germany). The kinematic viscosity (ν) was measured in water bath at 20 °C for the research undertaken. This was determined by measuring the time (t) taken by samples to travel between the two marked regions in the U-tube viscometer. The time was recorded using a stop watch with millisecond accuracy. Then,

the kinematic viscosity was obtained by multiplying the viscometer constant (C, 0.003 for Type A U-tube) with the time (t).

$$\nu = Ct \quad \textbf{(Equation 3.1)}$$

Subsequently, the dynamic viscosity (η) was calculated by multiplying the kinematic viscosity with the relative density (ρ) of the suspension which can be obtained using a density bottle (described in section 3.3.1).

$$\eta = \nu\rho \quad \textbf{(Equation 3.2)}$$

The viscometer was calibrated using deionised water before the measurement. The average value of five measurements was taken as the final reading.

3.4 Experimental set-up and equipments

The instruments set-up of the electrohydrodynamic atomisation processing is introduced in this section. The experimental designs and the specification of each component used are introduced.

3.4.1 Equipment configuration

The equipment set-up of electrohydrodynamic atomisation processing is illustrated in **Figure 3.1**. The needle, which is held in epoxy resin, was connected to the power supply. The needle was also connected to a syringe, which is fixed on a syringe pump, using a silicone tube, to control the flow rate. The distance between the needle and the

substrate was set at a range of value to achieve the nHA deposition with difference morphologies in the studies. The metallic substrate was earthed so that it acted as the grounded electrode. A high speed camera in conjunction with an optical fibre light source was used to observe the jet and record the scene of the spraying region with a connected computer. The voltage applied on the needle was adjusted and the flow rate was controlled in order to achieve the cone-jet mode of electrohydrodynamic spraying. At a specific flow rate, the cone-jet mode was achieved within a range of applied voltage. Thus, the relationship between the applied voltage and flow rate for the suspension jetting in the cone-jet mode was studied to investigate the optimised spraying condition, under which the stable cone-jet mode can be achieved.

3.4.2 Ground electrode configurations

As afore-discussed, the electric stress is the main drive for the electrohydrodynamic processing. The electric stress is determined by the electric field between the needle connected with high voltage supply and ground electrode configuration. For different purposes, the different ground electrode configurations were used for coating and patterning preparation, which is introduced in the following sub-sections.

3.4.2.1 Electrohydrodynamic atomisation processing

For the uniform nHA coating preparation using EHDA processing, the ground electrode is directly connected to the metallic substrate. Electric field is directly generated between the needle and grounded substrate. Therefore, the position, shape of the substrate can also influence the actual electric field during the EHDA processing.

3.4.2.2 Template-assisted electrohydrodynamic processing

To investigate nHA patterns on titanium substrate using TAEA processing, two different grounded electrode configurations were used as shown in **Figure 5.1**. One was directly grounded substrate (**Figure 5.1**b). The setup of such configuration is similar to the previous coating preparation setup, but with a gold template covered on the grounded substrate. The other was the substrate kept on a silicon wafer fully covering a metallic ground electrode (**Figure 5.1**a). In this case the electric field is generated between the needle and the actual ground electrode underneath the silicon wafer. The target substrate has zero influence to the electric field, which is different to the previous setup. The template, which determined the architecture of the pattern deposited, was placed on the substrate. Gold templates of different mesh sizes and geometries were used in the experiments.

3.4.3 Infusion pump

The pump used to eject the suspension through the needle was a precision PHD syringe pump (Infuse/Withdraw PHD 4400 Hpsi Programmable syringe Pump, Harvard Apparatus Ltd., UK). It includes a microcontroller that can control a small distance stepper motor. The motor drives a lead screw and a pusher blocker. Several operations, which include the infuse/defuse mode transform, the syringe mode selection and the flow rate value; can be selected via the operation keypad. In this study, 1 ml plastic syringes (BD Plastipak^{tm}, VWR, Lutterworth, UK) were fixed on the pump and the infuse mode that the ejects the liquid out was selected. The pump was calibrated using silicone oil – 500 (VWR, Lutterworth, UK, density 971 kg/cm^3) before the deposition process.

3.4.4 High voltage supply

The high voltage supply used, which is the key component of the electrohydrodynamic processing, is a FC30 P4 120 W regulated high voltage DC power supply (Glassman Europe Ltd., Hampshire, UK). The output voltage range and the output current range of this device are 0-30 kV and 0-4 mA, respectively. The operating temperature can vary from -20°C to 50°C. However, in this study, the work was carried at ambient temperature.

3.4.5 Data recording

The observation of the spraying region was achieved via a high definition digital camera (MOCAM-4000 high-speed camera, Weinberger AG, Dietikon, Switzerland) in conjunction with an optical fibre light source. The camera contains a high-end CMOS sensor which can record ultra-high-speed phenomena. The lens on the camera allows focusing on objects down to a few microns from a distance of approximately 5 cm. A computer was connected to the camera to display the image on the screen using a Mikrotron MotionBLITZ v 3.0.7 software.

3.4.6 Furnace

There are two furnaces used in **Chapter 4**, which allows changing the heat treatment environment. A laboratory chamber furnace (Lenton Thermal Design Ltd., UK) was utilized to sinter nHA coated titanium plate in air. The temperature and output power of

this furnace is 1600°C and 5 kW, respectively. The furnace is equipped with a temperature/programme controller (Eurotherm 2216) by which the target temperature, dwell time and the heating ramp can be programmed.

Another one is a laboratory tube furnace (Lenton Thermal Design Ltd., UK) which was used to heat treat the nHA coated titanium plate in the argon atmosphere (Zero grade, BOC Ltd., UK) to prevent substrate oxidation. This maximum temperature of this furnace is 1200°C, and it's also with a temperature/programme controller which provides the same function as previous one. The argon atmosphere flow can be controlled using a pressure controller at the cylinder. The ceramic tube in the furnace was modified at the two ends, at which the stainless steel seals were fixed to prevent the air flowing in the heating environment.

3.5 The needle designs for the study of needle geometrical effect

The needle for the electrohydrodynamic processing is made from a stainless steel capillary mounted in the resin as illustrated in **Figure 3.2**. An electrical conductive metal capillary, which can be of different diameters, was connected with a wire, and it was mounted in epoxy resin for 24 hours to insulate and impart rigidity. The epoxy resin is mixed using Epo-set resin and Epo-set hardener (MetPrep Ltd., Coventry, UK) at volume ratio 4:1.

For the study of the effect of the needle geometry carried out in **Chapter 6**, a range of needles of difference geometries were designed and manufactured. As illustrated in **Figure 3.3**, the tips of the needles were polished to the specific angles, which are 15°, 30°, 45° and 60°. In the study, such different needles were used for

electrohydrodynamic processing to investigate the different spraying scenarios, and the impact of the needle orifice angle to the deposited relics size distribution.

3.6 Characterisation of nHA deposits

For the studies that carried out in **Chapter 4**, **Chapter 5** and **Chapter 6**, the composition of the nHA deposits, including coatings, patterns, was characterised using a X-Ray diffraction (XRD), and the morphology and microstructure were observed and characterised using a optical microscope and a field emission scanning electron microscope (SEM). Furthermore, an *in-vitro* study using human osteoblast cells was also carried out to characterise the biological properties of the nHA coatings and patterns. The experimental procedures and the equipments used are introduced in detail in the following subsections.

3.6.1 X-Ray diffraction (XRD)

X-ray diffraction (XRD) is a versatile technique that can be used to determine the spacing between the layers in a crystal structure and thus identify the present phase or phases. Basically, it's scattering of x-rays by crystals with accompanying variation in intensity due to interference effect. When the x-ray beam falls on crystals scattered radiation is produced by the all atoms. The scattered waves spread out spherically from all the atoms in the sample and the interference effects of the scattered radiation from the different atoms cause the intensity of the scattered radiation to exhibit maxima and minima in various directions. This is used for identification of crystal phase and orientation of the given material. This intensity of scattered radiation could be related to the angle of the incident x-ray hitting the crystal by Bragg's law (Cullity, 1978).

$$n\lambda = 2d\sin\theta$$ (**Equation 3.1**)

where, θ is angle which the incident ray makes with the crystal plane, d is distance between the same set of planes, λ is wavelength of the x-ray and n is an integer.

When using this technique, x-rays are incident on the parallel planes within the crystal and reflect. A detector scans the intensity of the reflections over the preset 2θ range. If the path difference of the reflected beams is an integer multiple of the wavelength, constructive interference will occur between them. Therefore, a trace of peaks with varying intensity at certain angles can be obtained over the entire 2θ range, thus the d spacing can be calculated by Bragg equation so that the phase information can be identified.

In this research, a Bruker D8 Discover X-Ray diffractometer (BRUKER AXS Ltd., Germany) was used to determine the phase evolution of the nHA coated titanium plates after heat treatment. The XRD scanning range was 25˚ ~ 40˚, the size and period of each angular increment was set at 0.02˚ and 5s, respectively.

3.6.2 Optical microscopy

To investigate the optimised processing parameters for coating, the analysis and observation of the liquid droplet relics are fundamentally important. In the study, a Nikon ME600 optical microscope (Nikon, Japan) was used to examine the shape and size of the relics collected on the microscope glass slides. The microscope was equipped with an incident illuminating unit in which the light can come from either sides of the

specimen. To observe the relics on the transparent substrate, e.g. microscope glass slides, the bottom light was used (**Chapter 5 & 6**), and the top light can be used to observe the nHA relics/deposition on the titanium plate (**Chapter 4 & 5**). There are five objectives equipped in this microscope including 5×, 10×, 20×, 50× and 100×. The measurement for the relic size and the pattern dimensions was carried out using software, called image tool.

3.6.3 Scanning electron microscopy (SEM)

To characterise the morphology and microstructure of the nHA depositions/patterns, a Jeol JSM 6300F field emission scanning electron microscope (FE-SEM, JEOL Ltd., Herts, UK) was used. It's a high resolution SEM equipped with a field emission emitter, which can achieve a resolution of ~1.5 nm. The accelerating voltage can be set between 0.5 kV and 30 kV, and the working distance (the emitter-objective distance) is varied between 15 mm and 35 mm.

In the SEM, the electrons are generated in a source and accelerated by a strong electrical voltage gradient. With electromagnetic coils an electron gun is formed scans the sample and secondary electrons are produced by interaction with the atoms at the surface of the sample. Theses electrons contain the information that is employed to reconstruct a very detailed image of the surface topography of the objectives. An aluminium stub stuck with carbon sticker was used to hold the samples. Before placed in the SEM chamber, if the samples are insulating materials, such as nHA ceramic, they need to be gold coated with a sputtering machine (Edwards Sputter coater S150B) for 2 minutes to released the electrons so that sample surface will not be charged during the examination. For the

work carried out in **Chapter 4**, **Chapter 5** and **Chapter 6**, the nHA depositions were examined with the accelerating voltage of 15 kV and working distance set at 15 mm.

3.6.4 *In-vitro* study for biological properties of nHA coated Ti

To characterise the biological properties of the nHA coating and patterns, an *in-vitro* study was carried out. The specific biological properties of nHA deposits, such as cytotoxicity, the impact to the osteoblast attachment, were qualitatively and quantitatively characterised and investigated. The following subsections are to introduce the cell culture procedure, AlamarBlueTM cytotoxicity assay, cell morphology observation and immunocytochemistry of cytoskeleton in detail.

3.6.4.1 Cell culture

For cell-based assays, nHA coated and patterned titanium plates were sterilized using 70% (v/v) ethanol prior to use and were air dried in a Class II cabinet to maintain sterility. Primary human osteoblasts (HOB) were obtained from patients undergoing routine third molar extraction using an isolation method reliant on the differential migration of cells from the explanted bone fragments (Di Silvio, 1995; Di Silvio and Gurav, 2001). Briefly, the bone chips were cultured under sterile conditions until osteoid seams were seen and then digested using collagenase (100U/mL) and trypsin (300 U/mL) solution.

The cells obtained in this way were cultured in 25 cm^2 tissue culture flasks at 37 ºC, 95 % relative humidity and 5 % CO_2 until ~80 % confluency was achieved. The culture medium used was Dulbecco's Minimal Essential Medium (DMEM), supplemented with 10 % foetal calf serum (FCS), 5 mL of non-essential amino acids, 75 μg/mL ascorbic

acid, 20 mM L-glutamine, 20 mM 4-(2-hydroxyethyl)-1-piperazineethanesulfonic acid (HEPES) buffer, and penicillin G-sodium and streptomycin at 100 U mL^{-1} each. All reagents for tissue culture were obtained from Sigma-Aldrich (Poole, UK) unless stated otherwise. Media changes were carried out every three days. 4 x 10^4 cells were seeded on experimental substrates and were incubated at 37ºC, 5% (v/v) CO_2 and 95% relative humidity. The cell culture periods for the nHA coated Ti plates were set at 1 day, 3 days, 7 days, 14 days and 21 days (chapter 4), and the cell culture periods were controlled at 3 days to observe the initial cell attachment and alignment for the nHA patterned surfaces (Chapter 5).

3.6.4.2 AlamarBlue™ cytotoxicity assay

The AlamarBlue™ (Serotec, UK) assay allows a continuous assessment of cell proliferation over prolonged periods of time as it is non-toxic to cells and does not require the killing of the cells in order to obtain the measurements (Ahmed *et. al.,* 1994). AlamarBlue™ is an indicator that can be used to quantitatively measure the proliferation of cells in culture. As cells grow in culture, the mitochondrial electron-carrier complex activity, and therefore the cellular metabolic state, maintains a reductive environment in the surrounding medium. The non-fluorescent blue AlamarBlue™ dye responds to the reductive environment by forming a fluorescent red dye. While this assay has found widespread application in the field of cytocompatibility testing of biomaterials (Ahmed *et al*., 1994), it is however not suitable for all cell-material interactions thereby limiting the use of this assay.

To assess the impact of surface structure and chemistry, 4 x 10^4 HOB cells were seeded per well onto differentially treated titanium substrates, toxic PVC strips and Thermanox™ tissue culture plastic controls surfaces (Nunc SA, Roskilde, Denmark).

The substrates were incubated for 24 hr at 37 ºC, 5 % (v/v) CO_2 and 98 % relative humidity. After the initial incubation, the medium was aspirated and frozen at -80 °C for further analysis and replaced by 1 mL of phenol red-free HOB medium containing 10% (v/v) AlamarBlue™. After 4 hr incubation, the medium was again aspirated and 100 µL aliquots placed in a 96-well plate, after replacing the medium in the wells with fresh HOB basal medium. The 96-well plates were subsequently analysed using an Opsys plate reader (Dynex Technologies, San Diego, USA) with a 570 nm filter (630 nm reference). The measurements of AlamarBlue™ reduction, which were carried out in the work of chapter 4, were repeated at 3, 7, 14, and 21 days post-seeding.

3.6.4.3 HOB cells' morphology on nHA coated Ti

The observation of the morphology of the human osteoblast cultured was studied using JSM 6300F field emission scanning electron microscope (more detail seen in **Section 3.6.3**). HOB cells cultured nHA coatings (**Chapter 4**) and nHA patterns (**Chapter 5**) were incubated in HOB medium for 24 hours. At the end of the culture period, the cells were fixed by the addition of glutaraldehyde, and the cells membrane and cytoskeleton stabilised by osmium tetroxide, tannic acid and uranyl acetate, prior to desiccation by graded ethanol and hexamethyldisalazane, with the procedure outlined in **Table 3.3**Error! Reference source not found.. The samples were subsequently mounted on SEM aluminium stubs using carbon dag, gold sputter coated to an approximate thickness of 50 nm, and observed in SEM at an accelerating voltage of 15 kV and a viewing distance of 15 mm.

Table 3.3 Specimen preparation procedure for SEM imaging of cultured HOB cells on disk surfaces

Procedure	Time
1.5 % (v/v) glutaraldehyde in 0.1 M sodium cacododylate (NaCA), pH 7.4	60 min
0.1 M NaCA buffer washes	3 x 5 min
1 % (w/v) Osmium tetroxide in 0.1 M NaCa	60 min
0.1 M NaCA buffer washes	5 x 3 min
1 % (w/v) tannic acid in 50 mM NaCa	60 min
0.1 M NaCA buffer washes	3 x 5 min
20 % ethyl alcohol	2 x 5 min
30 % ethyl alcohol	2 x 5 min
40 % ethyl alcohol	2 x 5 min
50 % ethyl alcohol	2 x 5 min
60 % ethyl alcohol	2 x 5 min
70 % ethyl alcohol	2 x 5 min
0.5 % (w/v) uranyl acetate in 70% ethyl alcohol	30 min
90 % ethyl alcohol	2 x 10 min
96 % ethyl alcohol	2 x 5 min
Absolute ethyl alcohol	2 x 5 min
Hexamethyldisalazane (HMDS)	3 x 2 min

3.6.4.4 Immunocytochemistry of cytoskeleton

After culture of the nHA coated or patterned Ti plates, the cell medium was removed by aspiration and the cells were washed with phosphate-buffered saline (PBS) and then fixed in 3.7 % (w/v) phosphate-buffered formaldehyde solution for 1800s at 4°C. The

cells were then washed with PBS, permeabilised using PBS supplemented with 0.4 % (v/v) Triton X-100 and 1 % sucrose kept at 4°C for 10 min, and subsequently the PBS washed again. To minimise unspecific binding of the antibodies, the disks were then blocked with a 1 % (w/v) solution of bovine serum albumin in PBS for 600s. The cells were then stained using 50 ng/mL Hoechst 33258, and phalloidin-FITC conjugate (1:50; Sigma-Aldrich, Poole, UK) for 3600s at 37 °C, then washed, and the secondary goat-α-mouse IgG Texas red conjugate was applied for a further 1800s at 37°C, prior to a final washing step with PBS for 1800s.

The visualisation was carried out using a Leica SPII confocal microscope equipped with a LED Diode laser to excite the Hoechst 33258 fluorophore at 405 nm. The emission wavelength range chosen was 415-470 nm. The FITC and Texas red conjugates were excited using a HeNe laser at 488 nm (and an emission range of 505-535 nm) and 543 nm (and emission range of 600-640 nm), respectively. Visualisation was carried out on the inverted samples, using a Leica HCX PL APO 63x oil immersion lens with a numerical aperture of 1.4 and pinhole size equivalent to 1 Airy band resolution was used. An overlay was created using the LCSLite software package (Leica, Wetzlar, Germany).

Figures

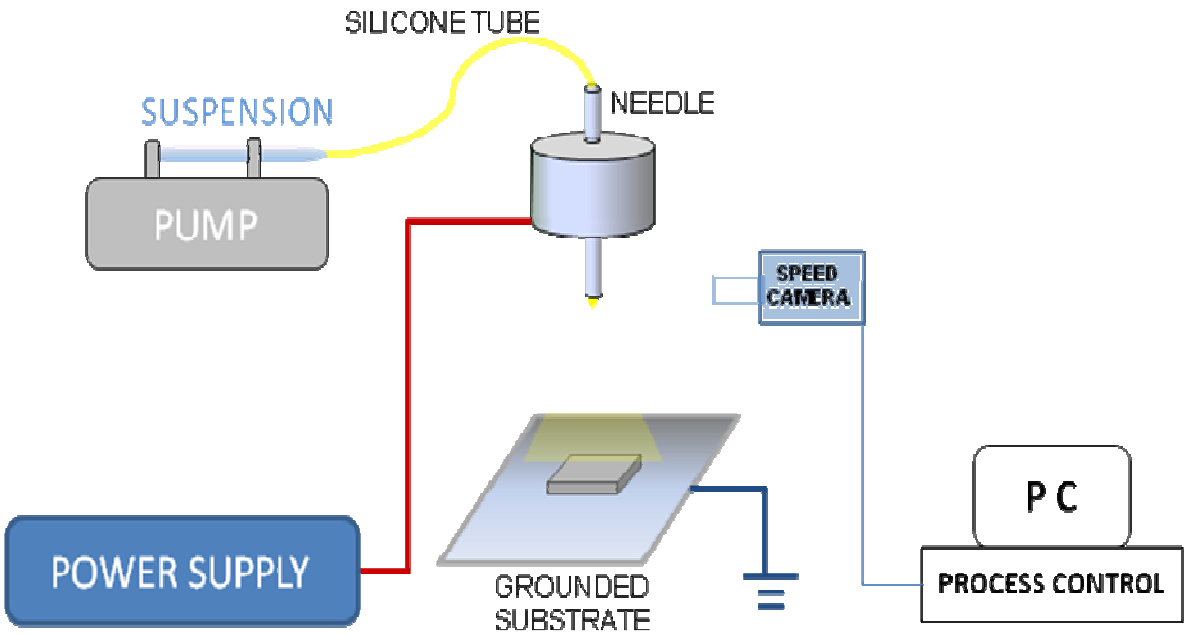

Figure 3.1 Schematic diagram illustrating the experimental setup of electrohydrodynamic processing route

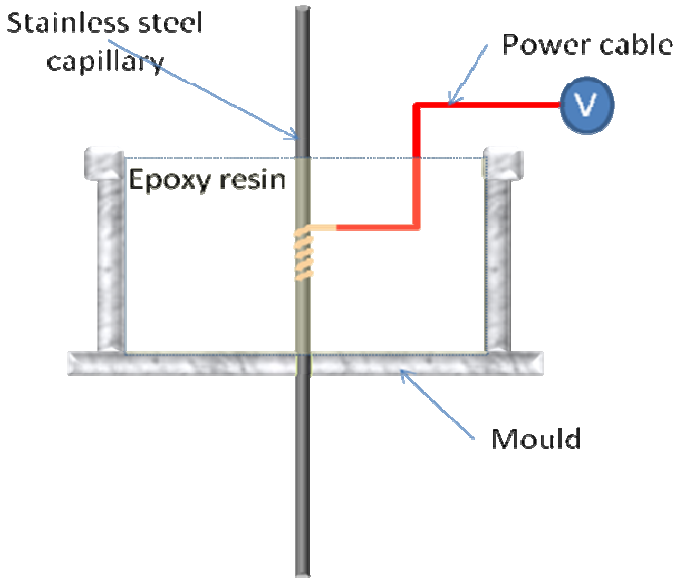

Figure 3.2 Schematic diagram illustrating the needle design for electrohydrodynamic processing

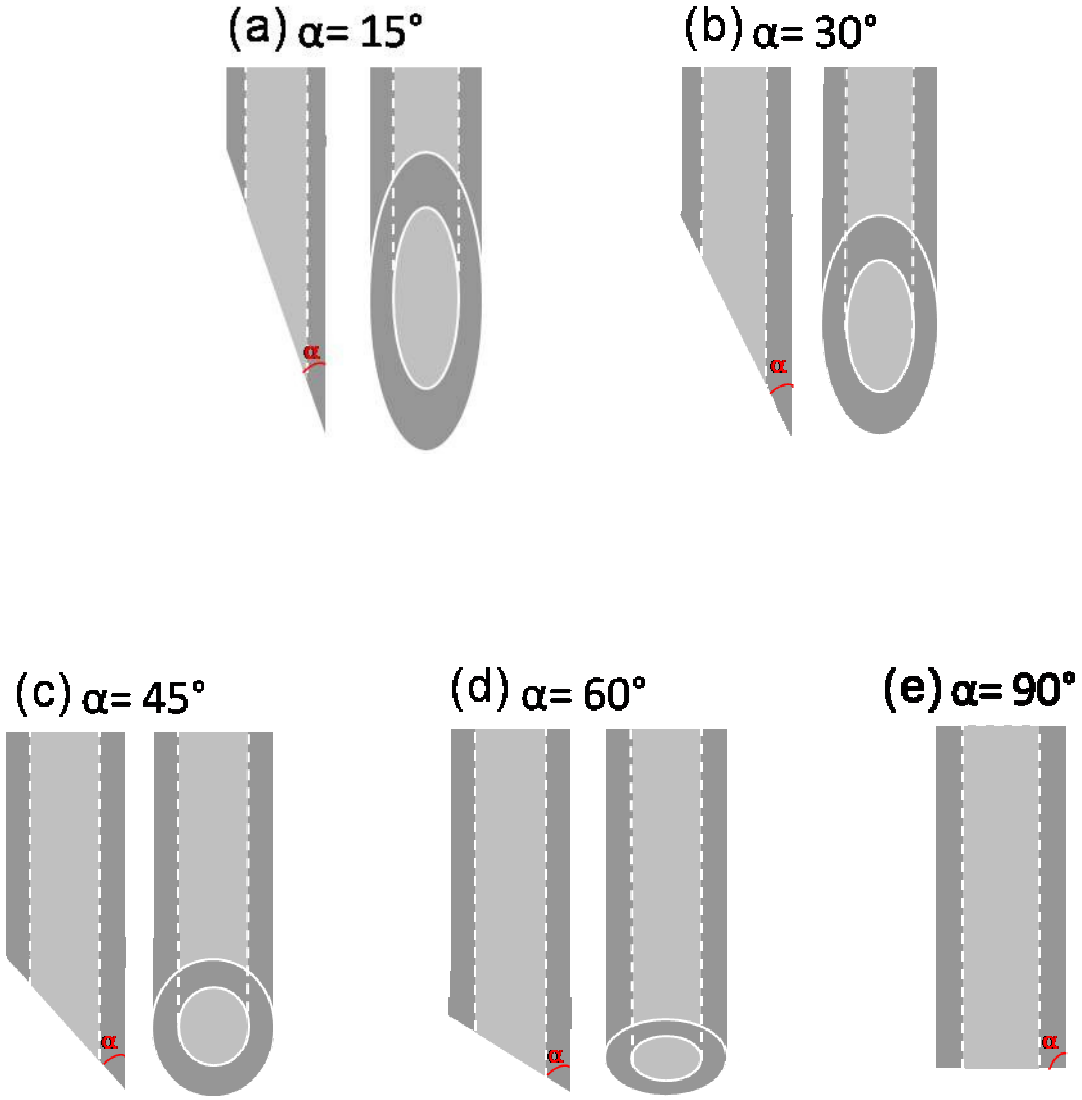

Figure 3.3 Schematic diagrams illustrating the needles with different tip angles**.**

Chapter 4

Electrohydrodynamic coating of metal with nano-sized hydroxyapatite

This chapter describes the investigation of processing nHA uniform coating using electrohydrodynamic atomisation (EHDA) spraying. As fore-introduced, the suspension is jetted from a needle under an electric field during EHDA spraying. Obtaining the stable cone-jet mode of EHDA spraying is critical for improving the quality and the morphology of HA coatings, therefore the effects of several key processing parameters, such as distance between the needle and substrate, suspension flow rate, applied voltage and spraying time, were studied in this work. The nHA coatings processed under different spraying parameters were compared according to uniformity and microstructural integrity. It was found that all of these parameters had a very significant influence on the morphology and thickness of nHA coating prepared. An as-deposited nHA coating with uniform morphology was successfully achieved using EHDA spraying. Furthermore, a study of the effect of subsequent heat treatment, which is normally needed to enhance the mechanical properties of nHA coatings, is also included in this chapter. It was found that the nHA coating surface roughness reduces marginally with the increase of heat treatment temperature. However, the surface roughness evolution due to the heating does not show significant influence on the proliferation and early attachment of primary human osteoblast (HOB) cells. This study forms the foundation for the further development of nHA patterning technique carried out in Chapter 5.

4.1. Characteristics of nHA and its suspension

Transmission electron micrograph (TEM) examination (**Figure4.1**b) revealed that the nHA particles were 75 ± 23 nm long, 39 ± 7 nm wide (mean of 50 particles). X-ray diffraction results (**Figure4.1**a) revealed the presence of all the major HA peaks, and no secondary phase was detected, which confirmed the purity of nHA prepared.

Ethanol is well known to give stable cone-jet mode electrohydrodynamic jetting and droplet generation (Grace and Marijnissen, 1994), and its surface tension, electrical conduction and viscosity are key parameters in achieving this. Ethanol was added as a liquid carrier for HA suspension preparation. Within a range of HA concentration, 6%wt was found to be most suitable for achieve the stable cone-jet mode (Ahmad *et. al.,* 2007). Thus, the physical properties, which are density, viscosity, surface tension and electrical conductivity, of HA suspension (6wt. %) and the comparison with ethanol is shown in **Table 4.1**. The nHA in the suspension resulted in the viscosity being increased by five times compared to the pure ethanol. The increase in viscosity will result in the generation of coarser droplets during jetting (Jayasinghe and Edirisinghe, 2002). The electrical conductivity of nHA suspension has been dramatically decreased. This is due to the large amount of the dielectric nHA ceramic particles existing in the suspension.

Table 4.1. Properties of ethanol and nHA suspension

Sample	Density/kgm^{-3}	Viscosity/ MPa s	Surface tension/ mNm^{-1}	DC electrical conductivity/ Sm^{-1}
Ethanol	790	1.3	23	$3.4x10^{-4}$
Suspension	930	6.8	28	$1.2x10^{-4}$

4.2 EHDA spraying parameters investigation for nHA coating

The equipment used for electrohydrodynamic atomisation (EHDA) spraying was described in chapter 3. The study nHA deposition preparation using EHDA process includes four subsections, which are the influence of needle-substrate distance, the influence of flow rate, the influence of applied voltage and the influence of spraying time, as described in the following. The processing was performed using a needle of ~310 μm in inner diameter unless stated otherwise.

4.2.1. The influence of needle-substrate distance

As the needle-substrate distance plays an important role in influencing the liquid droplet dimension during EHDA spraying, it is necessary to study the influence of the needle-substrate distance on the nHA coating morphology. During this investigation, nHA suspension (6%wt) was syringed to the needle at a flow rate of 10 μl/min. The applied voltage between the needle and the grounded substrate was set at 4.3-5.2 kV. The needle-substrate distance was varied from 10 to 40 mm. A range of nHA coatings were prepared and compared in terms of surface morphology.

The morphology of nHA coatings, when the distance between the needle and grounded substrate set at 10 mm, 20 mm, 30 mm and 40 mm, is shown in **Figure 4.2**. Smooth and uniform nHA coating was obtained when the needle-substrate distance was set at 20 mm. At short distance (10 mm), the nHA coating showed a rough texture (**Figure 4.2**a). This is due to larger suspension droplets impinging on the substrate. With the increase of the distance, the nHA deposit became smoother due to the decrease of the suspension droplet sizes as evaporation of ethanol increased during transit. However, when the

distance was set at 30 mm (**Figure 4.2**c) and 40 mm (**Figure 4.2**d), the substrate exhibited less nHA coverage compared with the coating produced with the distance set at 20 mm (**Figure 4.2**b). Thus, the integrity of the nHA coating was greatly affected. The reason for that is there was insufficient liquid phase for the nHA particles to spread on the substrate after deposition. Therefore, among the chosen distances, 20 mm is considered as an optimised distance between the needle and the grounded Ti substrate. Compared with the coating set at 20 mm (**Figure 4.2**b), the one at 30 mm (**Figure 4.2**c) is much more non-uniform.

4.2.2. The influence of flow rate

As discussed above, flow rate is a crucial parameter of influencing EHDA characteristic. Furthermore, flow rate was also found to have a significant impact on the droplet size under cone-jet mode EHDA spraying. Investigating the influence of the flow rate is therefore a crucial step of the research of nHA coating processing using EHDA technique.

To study the influence of the flow rate, the needle-substrate distance was set at 20 mm, which was investigated in Section 4.2. The morphology of the nHA coating produced varied with the increase of flow rate from 5 to 35 μl/min. The applied voltage was set to suit the flow rate to achieve stable cone-jet mode. At the lowest flow rate of 5 μl/min and 10 μl/min, the nHA coating was rougher in texture and covered only a part of the substrate (Shown in **Figure 4.3** a&b). A low flow rate decreased the velocity of the suspension arriving at the needle outlet, and therefore affected the cone and jet formation and the subsequent droplets generation process during the jet break-up. The droplet size tends to be smaller at a lower flow rate and this tends to make the coating

more discontinuous. As flow rate was increased, the coating was continuous; however, at 30 μl/min (**Figure 4.3**d), the coating produced was rougher, and more non-uniform. At 35 μl/min, the cone-jet became unstable, and a coating could not be prepared. Thus, a suspension flow rate of 20 μl/min resulted in the most uniform and integrated coating morphology. (**Figure 4.3** c)

To rank the effects of the flow rate and the distance between the needle and the substrate on EHDA processing of nHA suspension, the nHA coatings prepared under different conditions was scored according to the morphology achieved. A 3-D profile of the scores was established as shown in **Figure 4.4**. This shows that the nHA coating produced with a flow rate of 20 μl/min and the distance of 20 mm achieved the top score. Therefore, to obtain a uniform and integrated nHA coating, these parameters should be used for this suspension.

4.2.3. The influence of applied voltage

As the applied voltage is also a crucial parameter for achieving the stable cone-jet mode, which is essential for obtaining a continuous stream of suitable size droplets for uniform coating during spraying, the investigation of the appropriate applied voltage range is important for simplifying the EHDA spraying control through out the depositing process. The relationship between voltage applied and flow rate is shown in **Figure 4.5** and in this map the stable cone-jet mode (**Figure 4.6**a) can only be achieved when the flow rate and the applied voltage are in a distinctive envelope. Otherwise, the unstable cone-jet mode (**Figure 4.6**b) or the multi-jet mode (**Figure 4.6**c) will be in operation. Therefore, for the 6 wt% nHA suspension and the needle of 300 μm in internal diameter,

the applied voltage need to be adjusted in the range of 4.3-5.2 kV when the optimised flow rate (20 μl/min) is in use.

4.2.4. The influence of spraying time

As a jet-based coating technique, the EHDA spraying period is well-known to be an important factor in influence the HA coating thickness and therefore its properties. Therefore, the study of the spraying period becomes a fundamental and important in the systematic investigation of HA coating preparation using EHDA spraying. In this part of work, the EHDA process parameters were chosen according to the duration of the period investigated. HA coatings on the substrate with spray time varied from 30 to 1200 s are shown in figure 4.6. For a spray time of 30s (**Figure 4.7**a), the HA coating surface exhibits uniform topography and no cracks were observed. When the spray time increased to 60s (**Figure 4.7**b), overall, the uniformity still prevailed and the coating was crack-free, although aggregation of HA nanoparticles was found occasionally. Small cracks were observed in the coating when the spray time was 300s (**Figure 4.7**c). If the spraying time was much longer (20 min), cracking increased appreciably (**Figure 4.7**d). Therefore, uniform, crack-free coatings were obtained when the spray time was <60s, and 30s can be used for further investigation.

Furthermore, when the spraying time was 15s, the thickness of the nHA deposit is approximately 1.4 μm, along with the increase of the spraying time, the thickness of the deposit was found to increase to 4.9 ± 0.3 μm at 120s. Therefore, as expected, the deposit thickness is directly proportional to the spraying time as shown in **Figure.4.8**. At the meantime, to produce the HA coating of 2 micrometers, it could take 15 hours using RF-sputtering deposition technique (Tao et. al. 2007). Further, if using

biomimetic deposition technique, the processing period could take even much longer to produce a HA coated implant materials. Therefore, compared to other coating techniques such as above, EHDA technique is apparently much more efficient, and therefore more suitable for a healthcare industrial production.

4.3. Electrohydrodynamic (EHDA) process for nHA coated Ti plates.

Using the 6wt% nHA suspension, a nHA coated Ti plate was produced using the optimised EHDA spraying parameters, which are a needle orifice size of 300 μm, a flow rate of 20 μl/min, the needle exit to substrate distance of 20 mm, the applied voltage of 4.3-5.2 kV and 30s spraying time, as investigated in the previous section. There are no cracks and particles aggregation observed in the coating surface (**Figure 4.9**a). The entire coating on titanium plate exhibits a uniform, integrated morphology with nano-scale rod-like nHA particles (30-40 nm × 50-100 nm) as expected (**Figure 4.9**b). The phase purity of HA was confirmed from the X-ray diffraction pattern of nHA coating on Ti (**Figure 4.10**). Only HA and Ti peaks were observed. **Figure 4.11** shows the cross section of the coating and the thickness of the nHA coating is 2.1 ± 0.4 μm (mean of three separately coated substrates).

4.4. Effect of heat treatment to nHA coating

To enhance the bonding between the HA coating and the Ti substrate, different heat treatment strategies were used on the nHA coatings. The impacts of these heat treatments to the nHA coating morphology and composition are discussed in this section.

4.4.1. Heat treatment in air

The nHA coated Ti plates were heat-treated in air at 600 ºC, increasing from the ambient temperature to 600ºC at 2 ºC/min, and holding at this temperature for 120 minutes. Then the furnace was switched off to cool the samples to ambient temperature.

The HA coatings on the Ti before and after heat treatment are compared using high magnification electron micrographs in **Figure 4.12**. Before heat treatment, the nano-hydroxyapatite particles are distinguishable in the coating. After heat treatment, as expected, the coating has become much denser, but in addition, the coating was more firmly attached to the Ti substrate and could not be scraped off with a metal chip. The densification of the HA on Ti can be increased further by using a higher temperature (Oktar F.N. *et al*., 2006) but this will also affect the conversion of Ti to TiO_2. **Figure 4.13** shows the XRD patterns of the coatings before and after heat treatment. All the HA peaks have remained after heat treatment and therefore it is clear that HA has not decomposed. Rutile TiO_2 peaks have appeared after heat treatment and this is expected due to reaction of the Ti with oxygen present in the heat treatment atmosphere.

The role of the TiO_2 layer can be considered as a discontinuity between the Ti and the nHA and therefore one can expect the bonding of the coating to the substrate to be weak. However, a number of studies (Kim *et al*., 2004; Lin *et al*., 2005; Roop Kumar and Wang, 2002), have proved that the TiO_2 layer acts as a buffer layer between HA coating and metallic implant and enhances the adhesion strength of HA coating. Furthermore, due to the brittleness nature of TiO_2 ceramic, the large amount of TiO_2 phase in the coating could cause a significant drawback of nHA coating toughness, which is

unacceptable for the clinical practices. Therefore, the control of TiO_2 amount during the process is still crucial for nHA preparation.

4.4.2 Heat treatment in argon

Using argon (or nitrogen) atmosphere during the heat treatment is the conventional and effective way to prevent the metal oxidation. The coatings on Ti plates were heat-treated in a static argon atmosphere (Zero grade) at 500 ºC, 700 ºC and 900 ºC. The heating rate and cooling rate were set at 2 ºC/min, and the dwell time at all temperatures was 120 minutes.

According to the low magnification SEM images, no significant difference exists in the HA coatings. However, a marginally increasing smoothness was observed with the elevation of heat treatment temperature. Thus, the deposited nHA coating (**Figure4.14**a) showed a relatively rougher surface than the surface heat-treated at 900ºC (**Figure4.14**d). This finding was confirmed by the confocal microscopy results. As shown in **Figure 4.15**, the roughness of deposited nHA coating was 4.2 µm. Meanwhile, the roughness of the heat-treated nHA coating was slightly lower, 2.1-2.9 µm. The marginal decrease in coating surface roughness is caused by the change in the nHA coating morphology due to heat treatment. An explanation could be the evolution of HA nano-particles at the high temperature as found in the following.

The small change in surface roughness is due to nHA ceramic particle 'growth' at high temperature. As shown in **Figure 4.16**a, before heat treatment, the nHA particles are distinguishable in the coatings. The particle size is <100 nm. However, after heat treatment, the HA particles become bigger. As shown in **Figure 4.16**b&c, the HA

particles in the coating heat-treated at 500ºC and 700ºC are less distinguishable than the ones in the deposited HA coating. The particles size increase appeared to be due to particle aggregation and conglutination. When the nHA coating was heat-treated at 900ºC (Figure4.16d), the HA particles became several hundred nanometers in diameter due to the enhancement of the same mechanism. This change and behaviour of the HA particles during heat treatment leads to the coating surface roughness reduction at a higher temperature.

Figure 4.17 shows the XRD patterns of the coatings after heat treatments. Compared with the XRD pattern of the as-deposited HA coating (**Figure 4.13**), all the HA peaks have remained after heat treatment and therefore it is clear that HA has not decomposed. Titanium peaks also show in all the patterns, this is due to the Ti substrates used for coating process. When heat-treated at 500ºC, the TiO_2 peaks have not appeared due to the argon atmosphere used. However, with the heat treatment temperature increasing, the TiO_2 peaks start to appear at 700ºC and further increase at 900ºC. This is due to the high activity of Ti metal at a higher temperature and small amount of oxygen impurity present in the argon atmosphere. However, compared with the nHA coated Ti heat-treated in air (**Section 4.4.1**), it has been a large improvement in controlling the TiO_2 content in nHA coatings (Lin and Yen, 2005; Oktar et. al., 2006). Furthermore, it has been reported that cpTi does not suffer a fall in tensile strength after heat-treating to 900ºC (da Rocha *et al.*, 2005). However, one could argue that fatigue properties are more important in an orthopaedic implant, but there is no systematic investigation of the influence of heat treatment on the fatigue properties of cpTi in the literature.

4.5. *In-vitro* study for the nHA coated Ti plates

As afore-investigated, the HA particles size increases significantly, and the morphology of nHA coating changes marginally with the increase of the heat treatment temperature. Some pre-clinical and clinical studies have shown that the degree of implant roughness correlates strongly to the degree of bioactivity of both dental and orthopaedic implants materials (Wennerberg *et al*., 1996a; Wennerberg *et al*., 1996b, Wennerberg, 2003; Wong *et al*. 1995; Albrektsson and Wennerberg, 2004). Therefore, an *in-vitro* study to characterise the bio-properties of nHA coated Ti prepared using EHDA spraying with subsequent heat treatment is of significant importance for the research in nHA coated metallic implant materials processing.

4.5.1 The proliferation of HOB cells on nHA coated Ti plates

As introduced in **Section 3.5.3**, the AlamarBlue^{TM} assay was used to assess the cytotoxicity and proliferative potential of the test surfaces when HOB cells were cultured directly on the surfaces for different culture periods. In this assessment, the cell culture periods were set at 1-day, 3-day, 7-day, 14-day and 21-day. The spectrophotometric absorbance readings are shown in **Figure 4.18**. The assessment indicated that all surfaces, apart from that of the PVC positive toxic control (not shown), supported cell growth over the 21-day study period. A decreased total metabolic activity was also observed to occur between 1 and 3 days for these surfaces. Further, the proliferation rates and terminal plateau level attained was similar for these surfaces, indicating favourable proliferation and the absence of cytotoxicity to the same degree of the 'gold-standard' tissue culture plastic (T C Plastic). This also indicated that the heat treatment temperature, and thus the particle size and surface roughness, did not affect

the proliferation rate of HOB cells. The PVC positive toxic control did not show growth any greater than that in the cell-free medium controls.

4.5.2 The morphology of HOB cells on nHA coated Ti plates

As well as cytotoxicity assays as described above, the cellular morphology can be used as an indication of cell health and differentiation. The scanning electron micrographs in **Figure 4.19** demonstrate the cell attachment and numerous cell filopodal processes anchoring to HA particles. HOB cells cultured on the uncoated cpTi plate surface appeared flattened and a spread-out morphology (**Figure 4.20**). However, cells cultured on HA substrates had adopted a three dimensional, lamellipodal morphology at the same time point, 3-day.

Following 21-day in culture it was difficult to make observations on the individual cellular morphology (**Figure. 19**). Instead, it was observed that the degree of surface coverage with cells was consistent among all tested samples. This was a positive indication that cell proliferation had occurred on all nHA coated Ti plates, and hence indicating that none of the test surfaces were cytotoxic.

Overall, the *in-vitro* study indicates that the heat treatment temperature does not cause any change on the bioactivity of nHA coated Ti plates. However, some studies have shown that the surface roughness could have a big impact on the cell behaviour. A rough surface allows greater mechanical interlocking and exposes a higher surface area for integration. Our cell assessment showed that the coating surface marginal roughness evolution due to the subsequent heat treatment did not show any big impact on the cell behaviour on the HA coating surfaces. This is due to the low magnitude of the

roughness change. In other words, with the increase of the heat treatment temperature, the reduction of the nHA coating roughness and morphology is too inadequate to change the HOB cell attachment and proliferation behaviour.

4.6 Summary

This study described in this section has led to three contributions with respect to the nHA coated implant materials processing using electrohydrodynamic (EHDA) spraying. Firstly, The 6 %wt nHA suspension was prepared and characterised. Using this suspension, a systematic investigation was carried out for the optimised EHDA spraying process parameters for nHA coating preparation. When the spraying process parameters were set at the needle-substrate distance of 20mm, the flow rate of 20µl/min, the applied voltage range of 4.3~5.2 kV, a uniform nHA coating could be achieved on titanium substrate, a typical substrate used in orthopaedics. Secondly, it was found that the nHA coating thickness is proportional to spraying period using the optimised EHDA process parameters above. When the spraying time was set at 15 seconds, the nHA coating could achieve ~1.4µm. As the spraying time increases to 120 minutes, the nHA coating thickness could achieve ~5µm, respectively. Compared to other coating techniques, such as biomimetic and sputtering, the coating 'growth' rate achieved using EHDA spraying is much more efficient. Thirdly, nHA coated Ti plates were subsequently heat-treated at different conditions. The HA coating surface roughness was found to marginally decrease with the increase of the heating temperature. This is due to the HA nano-particles 'growth' behaviour at higher temperature. The mechanism was further confirmed using high magnification SEM. The in-vitro study showed the HOB cell behaviour was not influenced by this marginal surface roughness change. All the nHA

coated Ti plates prepared using EHDA spraying were shown to provide appropriate surfaces for cell attachment and proliferation.

Based on this investigation, the electrohydrodynamic spraying technique has been further proved to be a promising technique for processing novel implant materials. This study also paves the way for the following work.

Figures

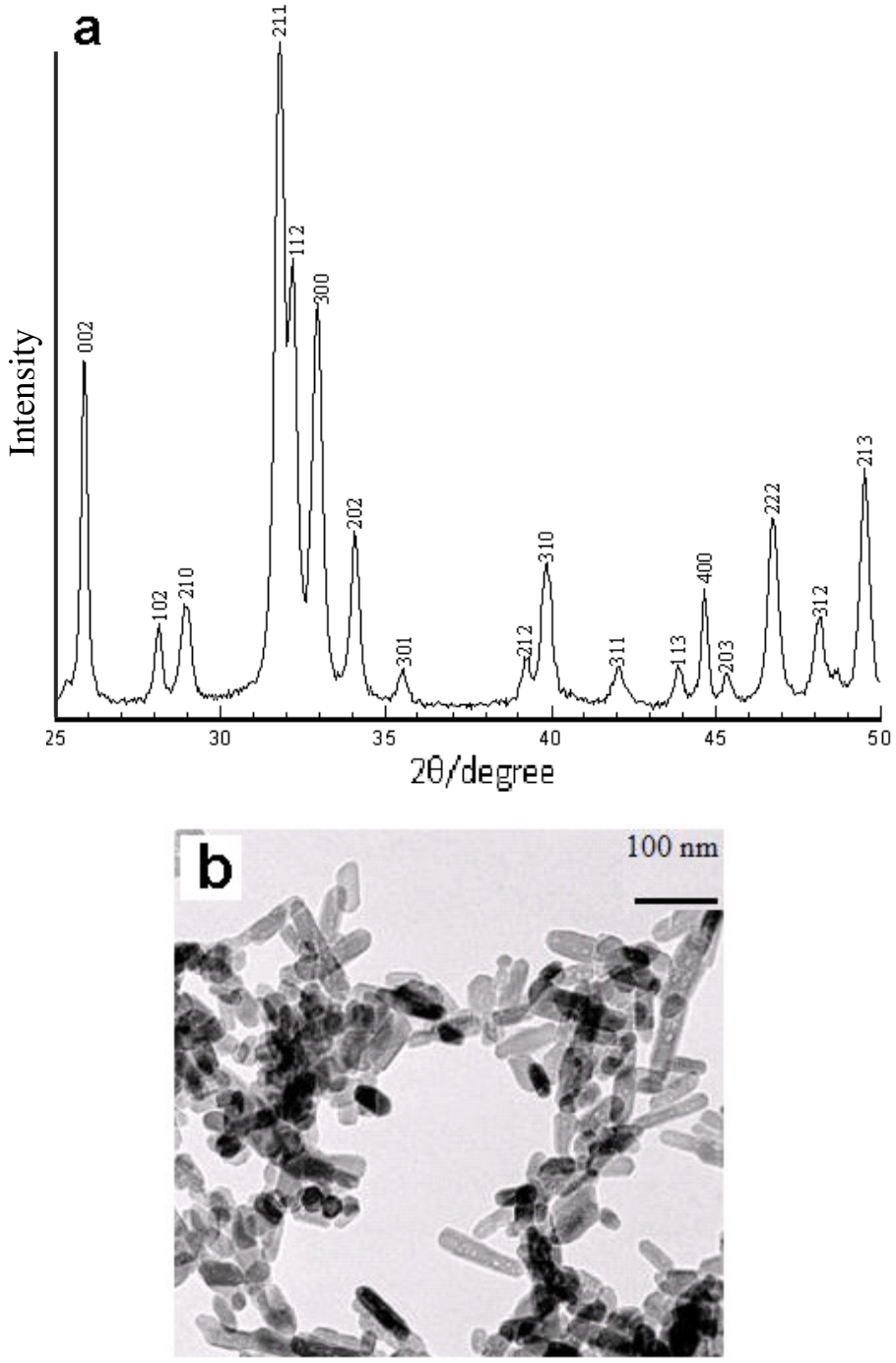

Figure 4.1. (a) X-Ray diffraction pattern, with indices of phases indicated and (b) transmission electron micrograph of the nHA synthesized

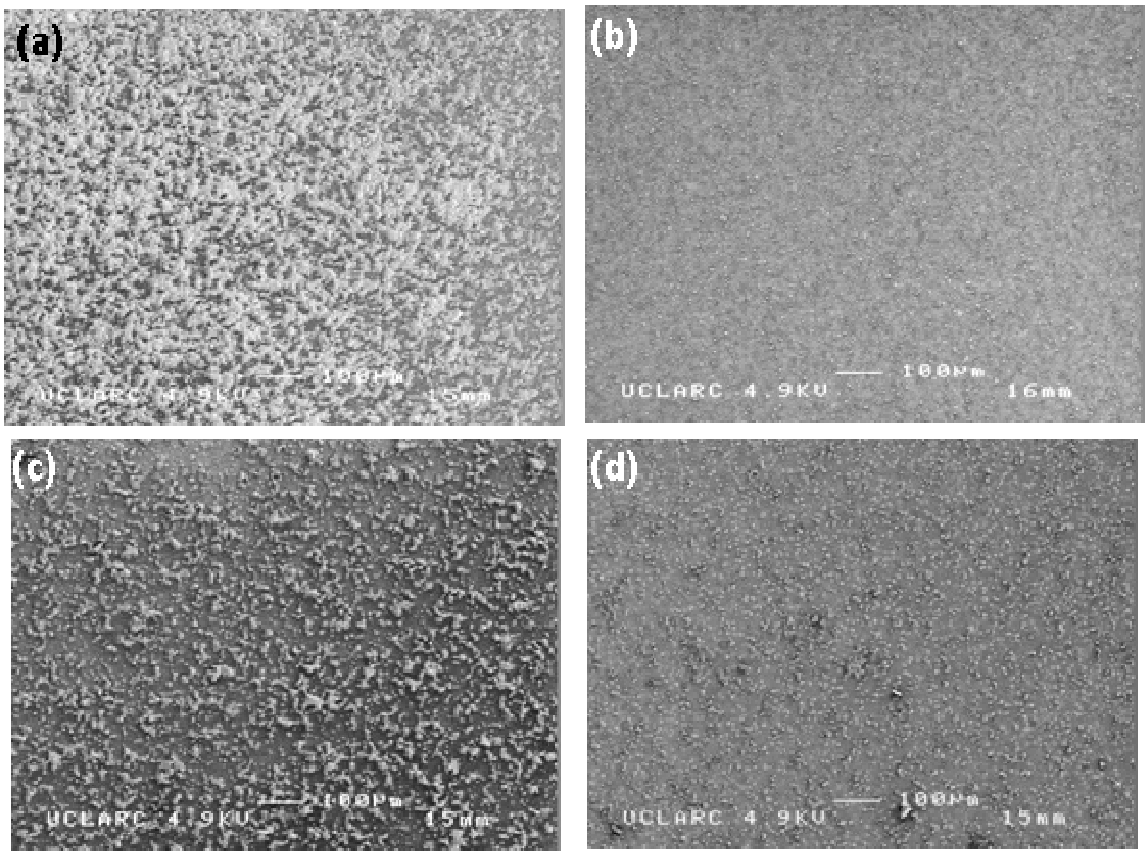

Figure 4.2. Scanning electron micrographs of nHA coatings produced with the distance between the needle and substrate set at (a) 10mm, (b) 20mm, (c) 30mm and (d) 40mm.

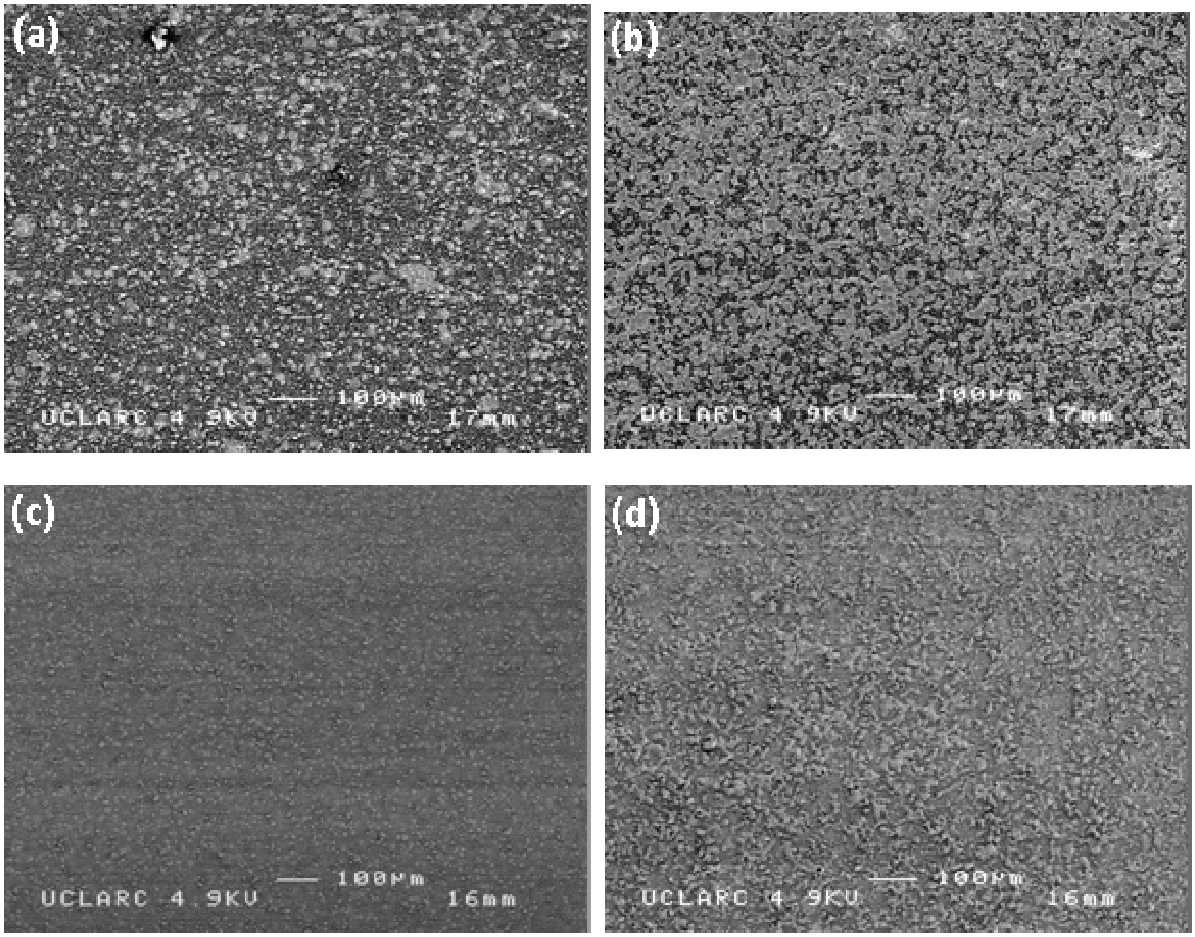

Figure 4.3. Scanning electron micrographs of nHA coatings produced with the suspension flow rate set at (a) 5µlmin^{-1}, (b) 10µlmin^{-1}, (c) 20µlmin^{-1} and (d) 30µlmin^{-1}.

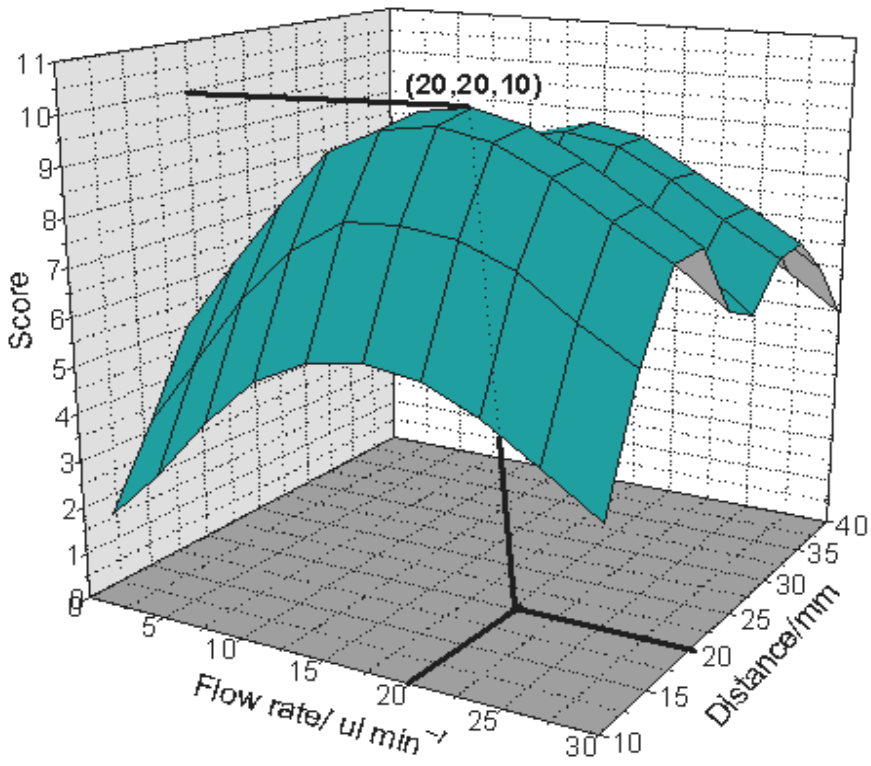

Figure 4.4. The interrelationship of flow rate of suspension and distance between needle and substrate and quality score for nHA coating obtained by EHDA processing.

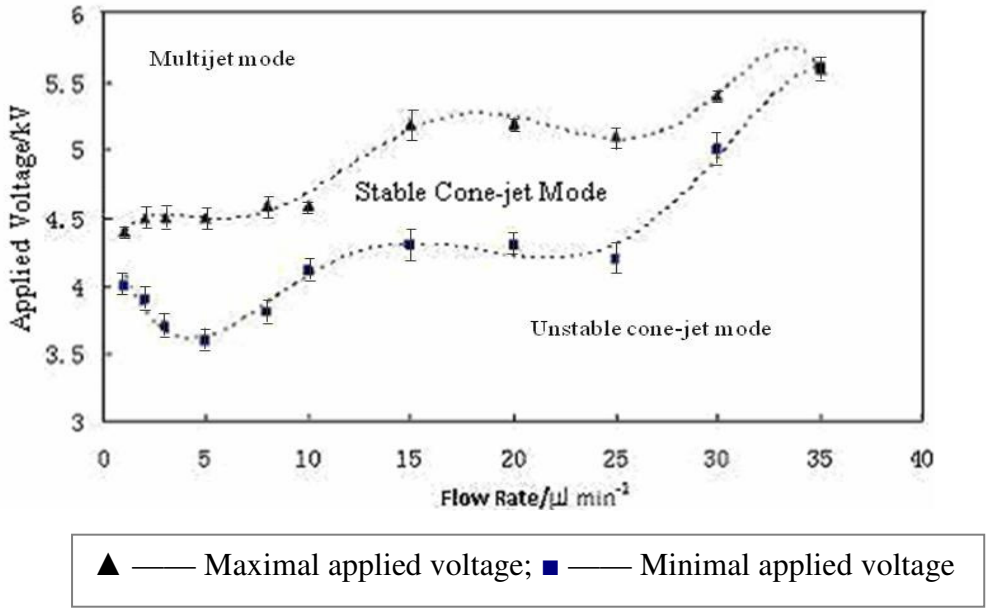

Figure 4.5. Relationship between applied voltage and flow rate for the 6wt% nHA suspension using a needle of 300 μm in internal diameter. Needle exit to substrate distance is 20mm. The lowest flow rate which can be set with the present equipment is 1μlmin^{-1} (Li *et. al.* 2007b).

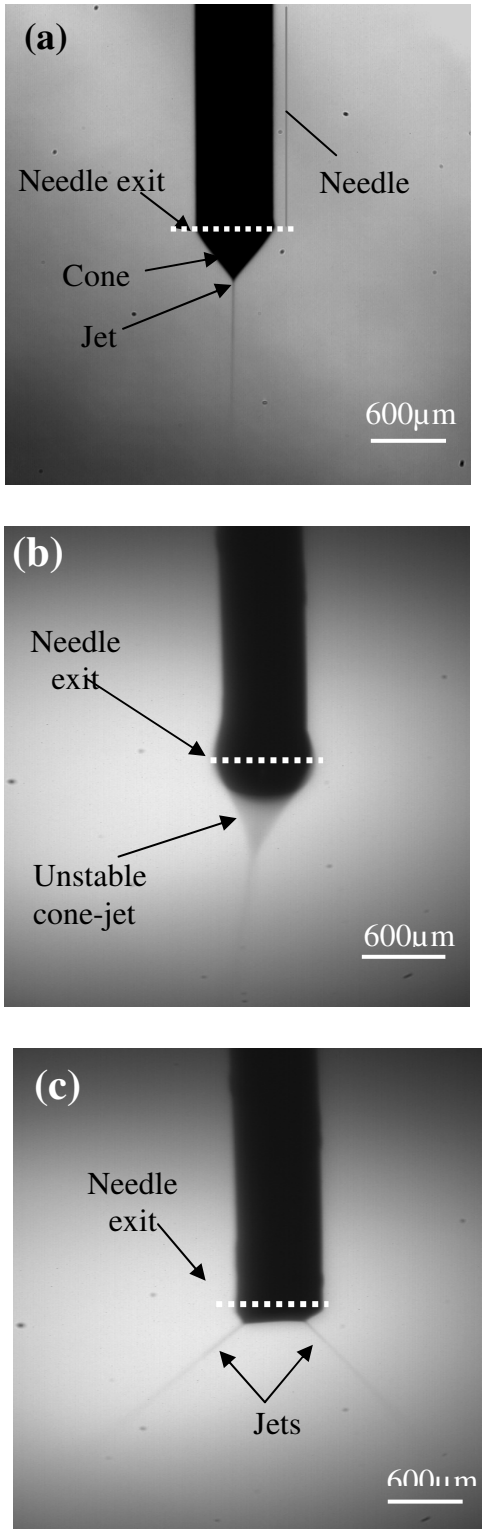

Figure 4.6. (a) Typical stable cone-jet mode obtained at 4.3-5.2kV and 20µl/min, (b) Unstable cone-jet mode and (c) Multi-jet mode.

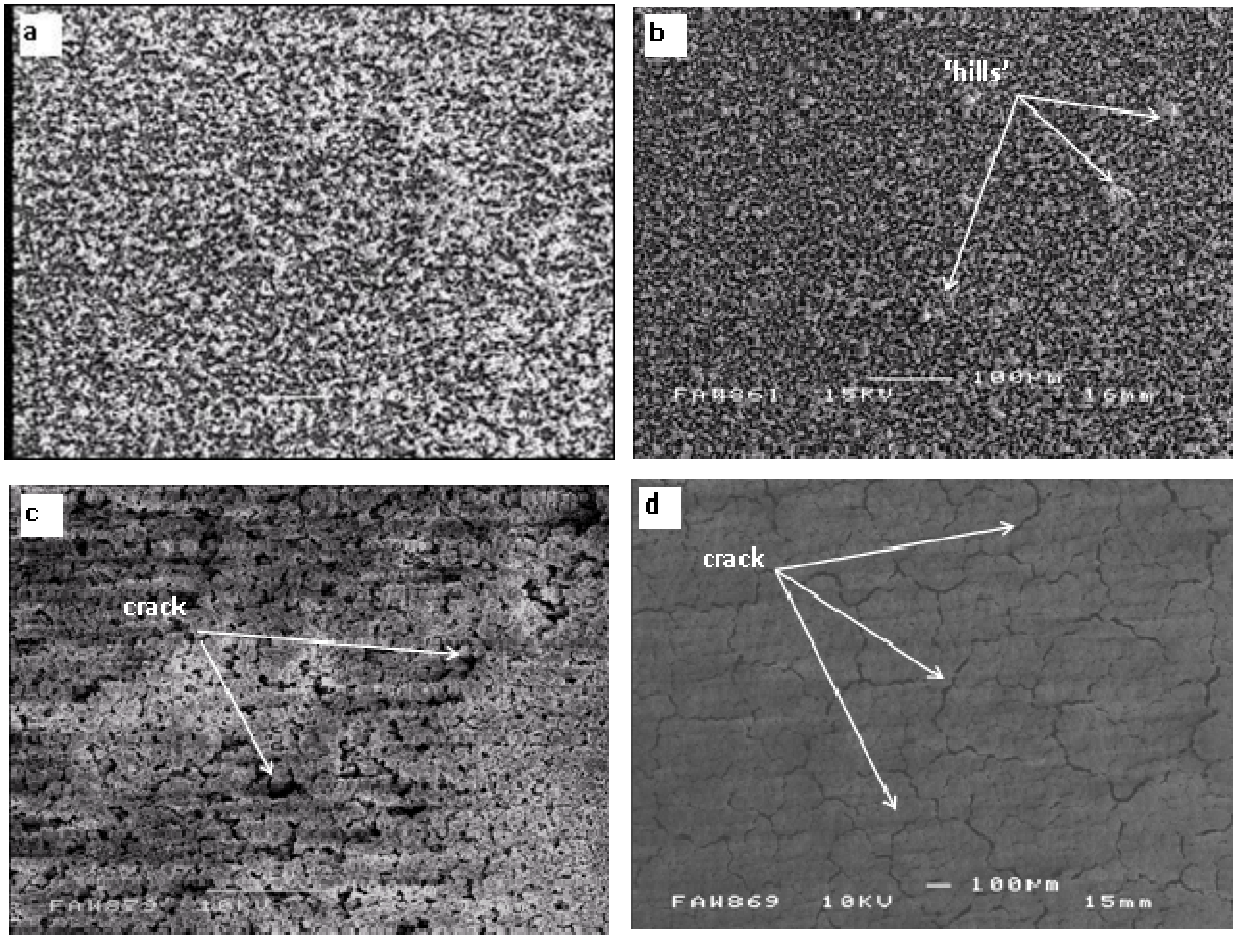

Figure 4.7. Scanning electron micrographs of nHA coatings on Al plate substrates with coating times of: (a) 30s, (b) 60s, (c) 300s and (d) 20 minutes.

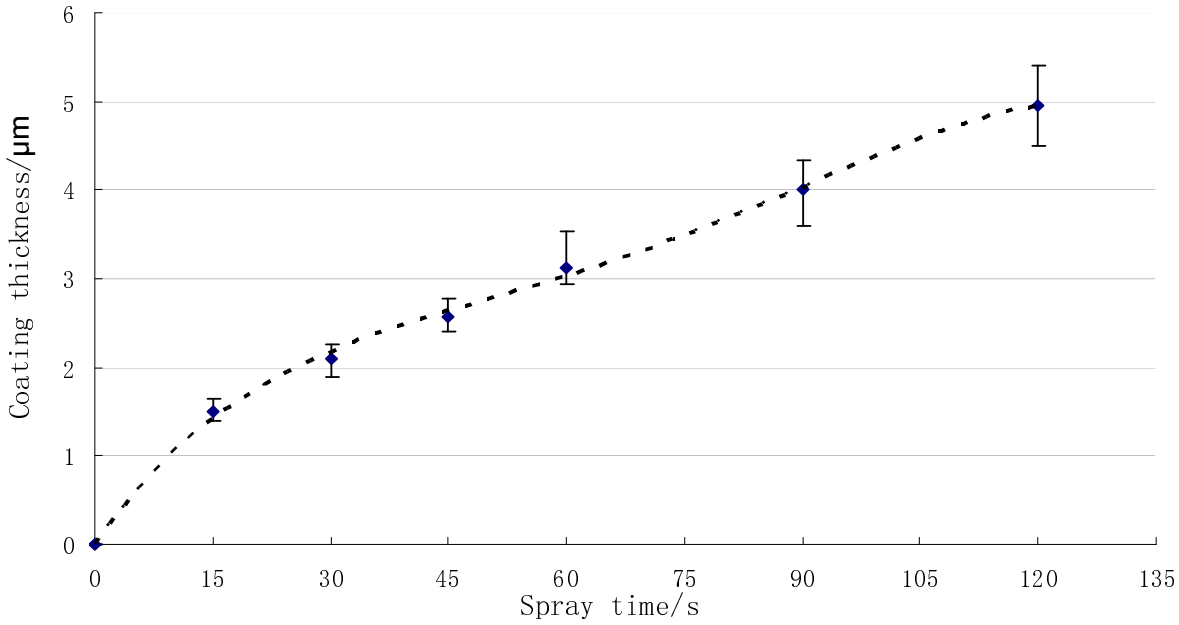

Figure 4.8. The relationship between nHA thickness and spray time for the 6wt% nHA suspension at 4.3-5.2 kV and 20 μl/min
0

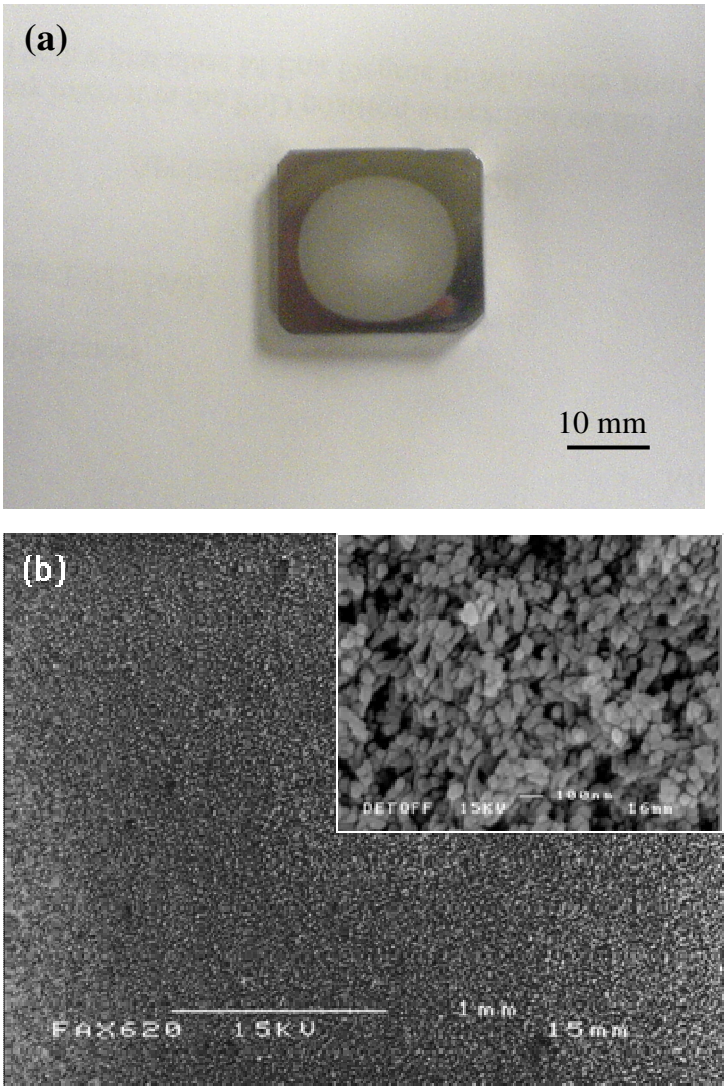

Figure 4.9. nHA coating on Ti plate, coating time in 30s. (a) Macro photograph showing coating uniformity and integrity and (b) Scanning electron micrograph showing the microstructure of the nHA coating

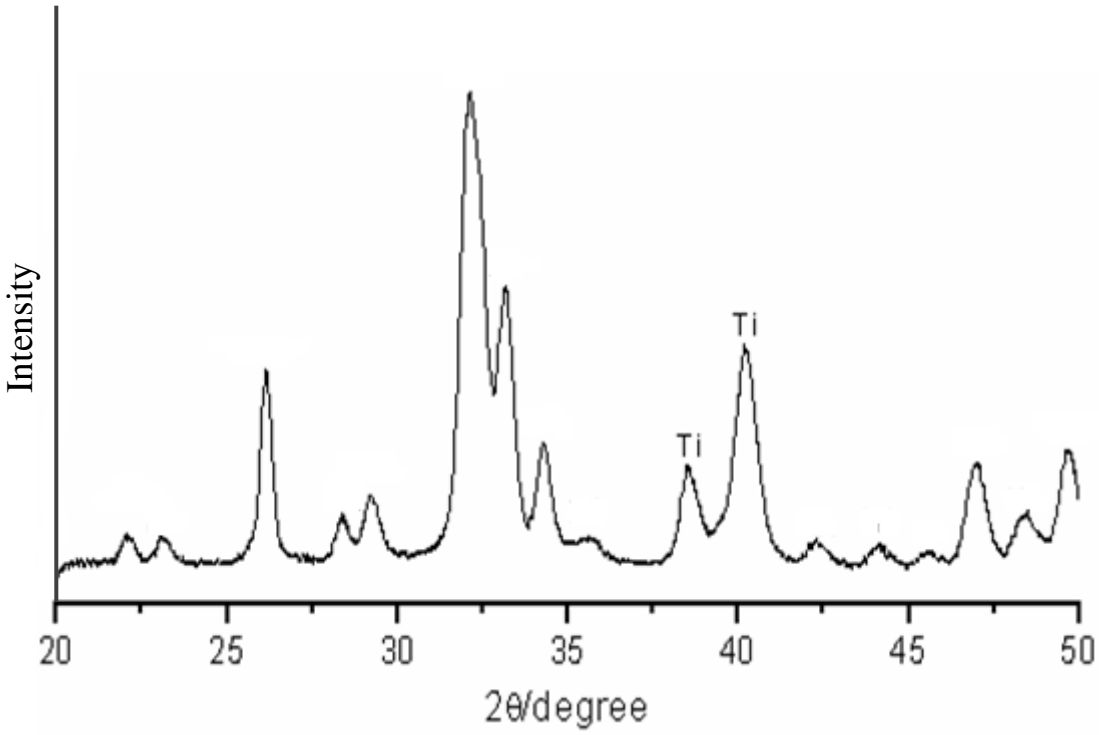

Figure 4.10. X-Ray diffraction pattern of the nHA coating prepared, all peaks not indicated belong to HA

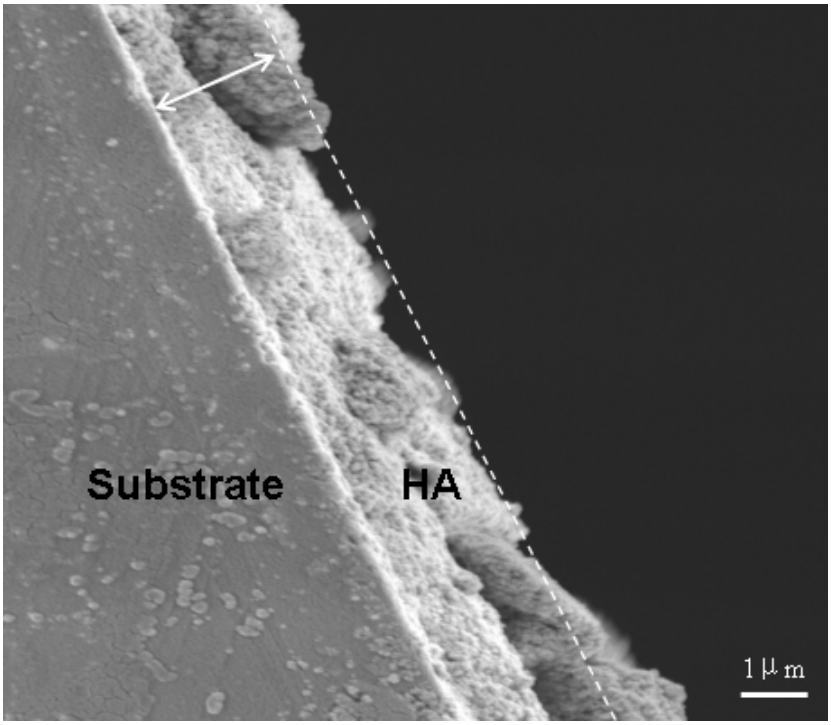

Figure. 4.11. Scanning electron micrograph of cross-sectional view of the coating on the Ti substrate prepared using the optimized spraying parameters

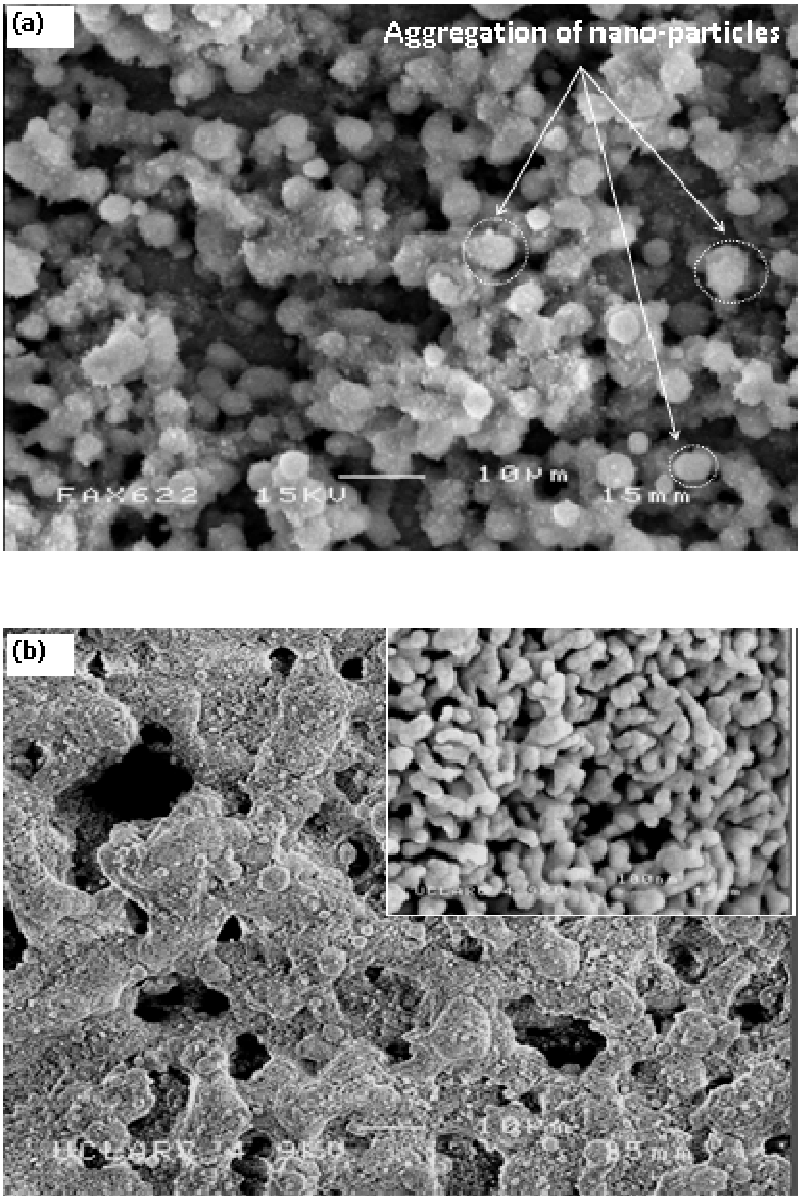

Figure 4.12. Scanning electron micrograph of as-deposited nHA coating and nHA after heat treatment in air.

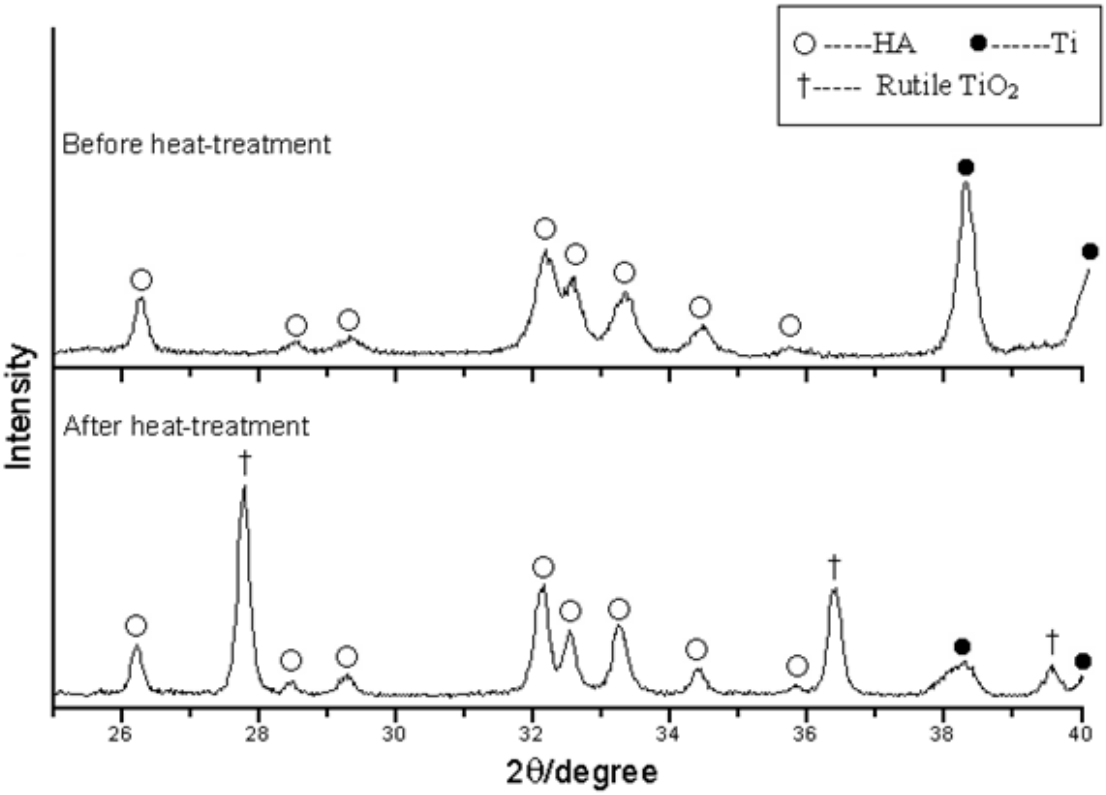

Figure 4.13. X-Ray diffraction pattern of the nHA coated Ti before and after heat treatment in air.

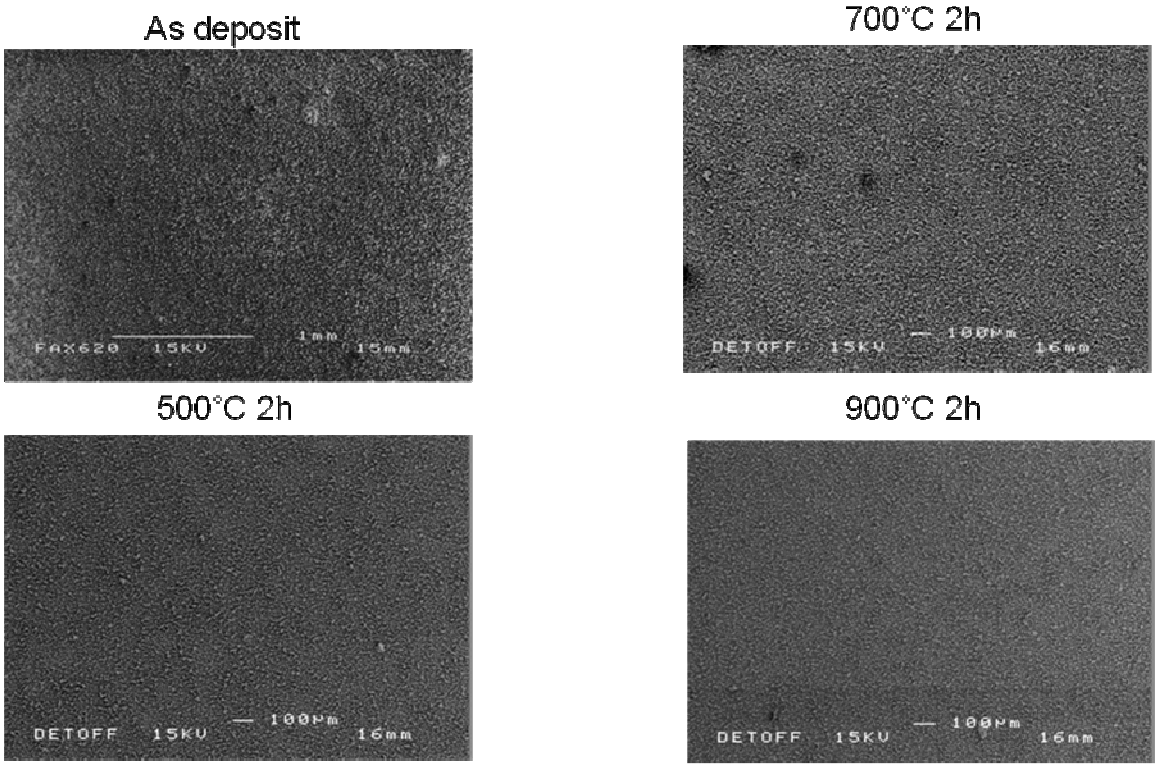

Figure 4.14. Scanning electron micrograph of as-deposited nHA coating and nHA after heat treatment at 500°C, 700°C and 900°C.

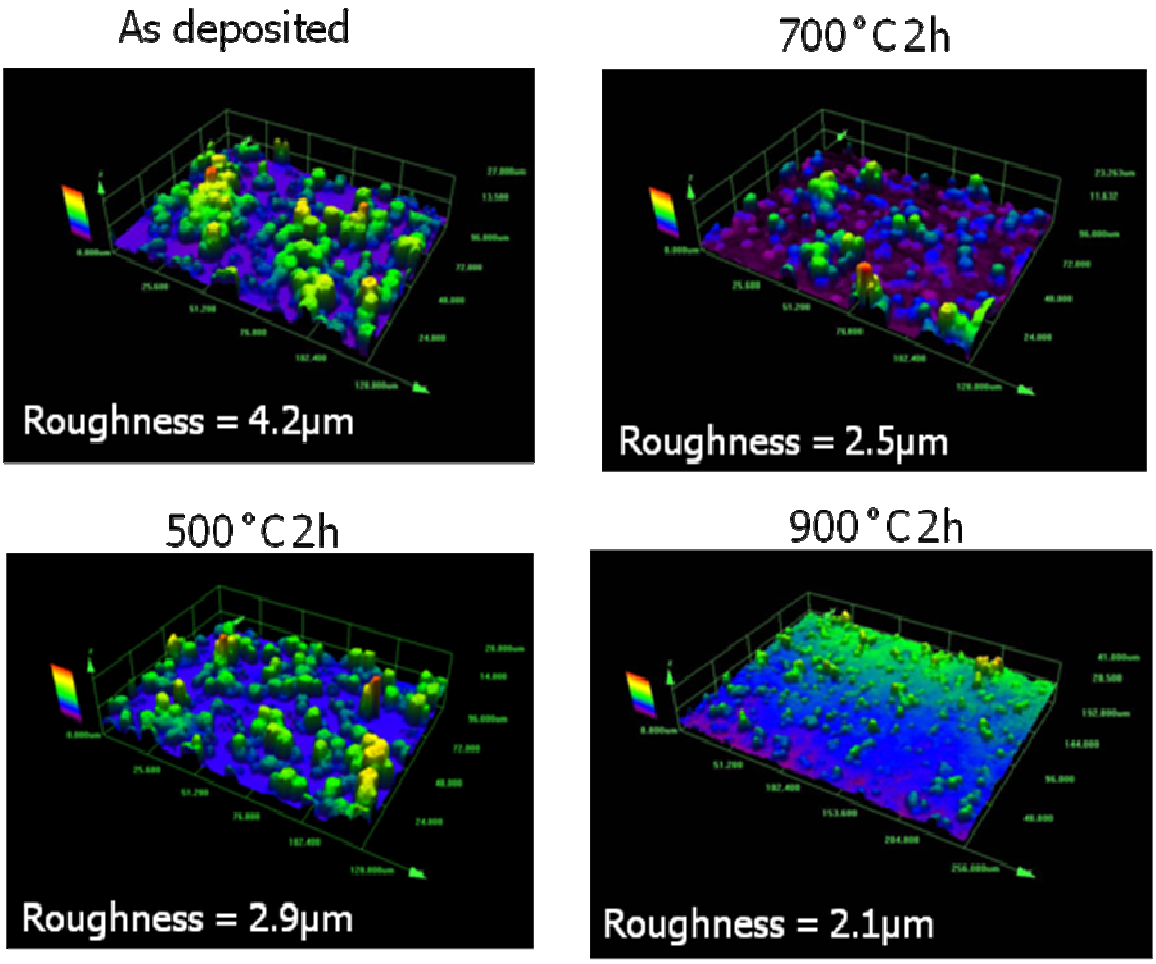

Figure 4.15. Confocal microscope images of nHA coatings before heat treatment and after heat treatment at 500°C, 700°C and 900°C.

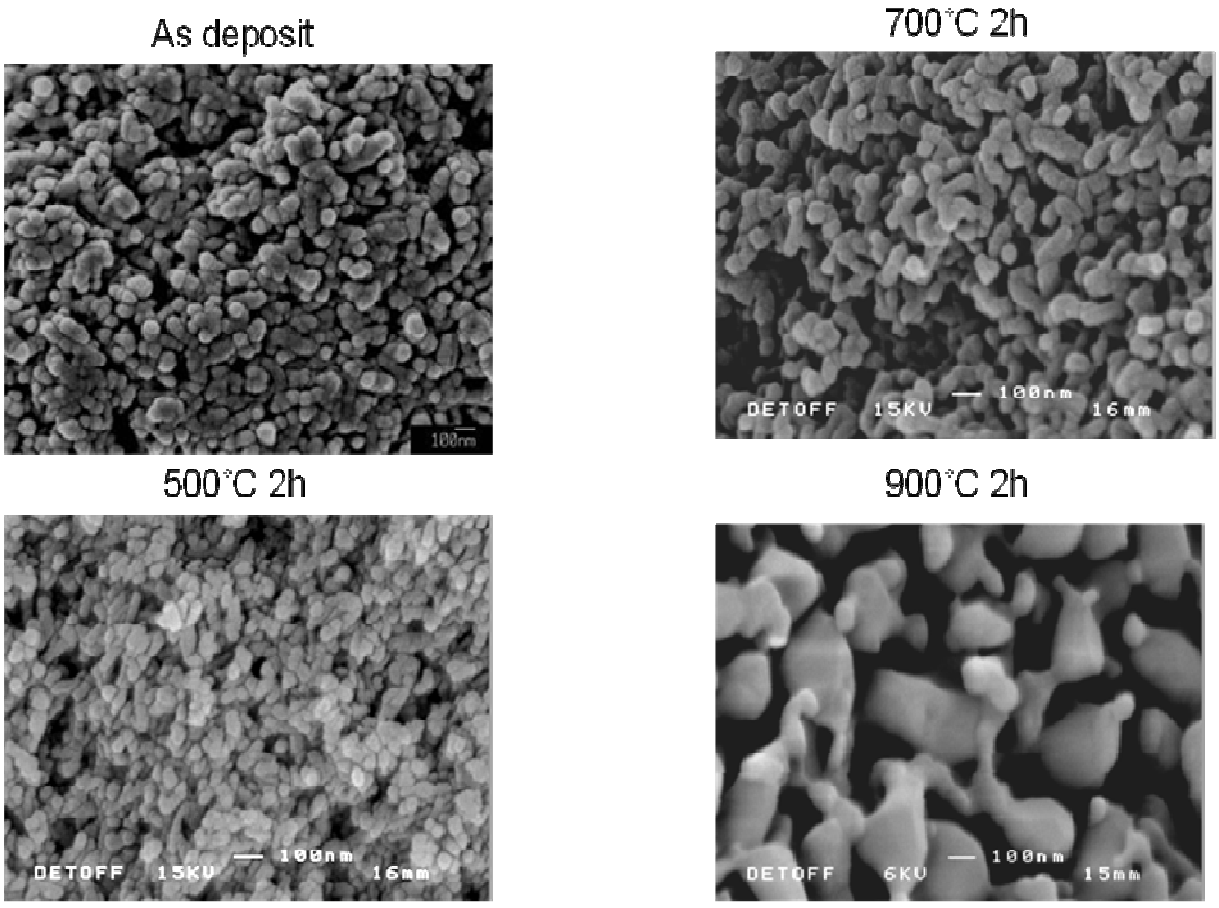

Figure 4.16. High magnification scanning electron micrographs of nHA deposits before heat treatment and after heat treatment at 500°C, 700°C and 900°C.

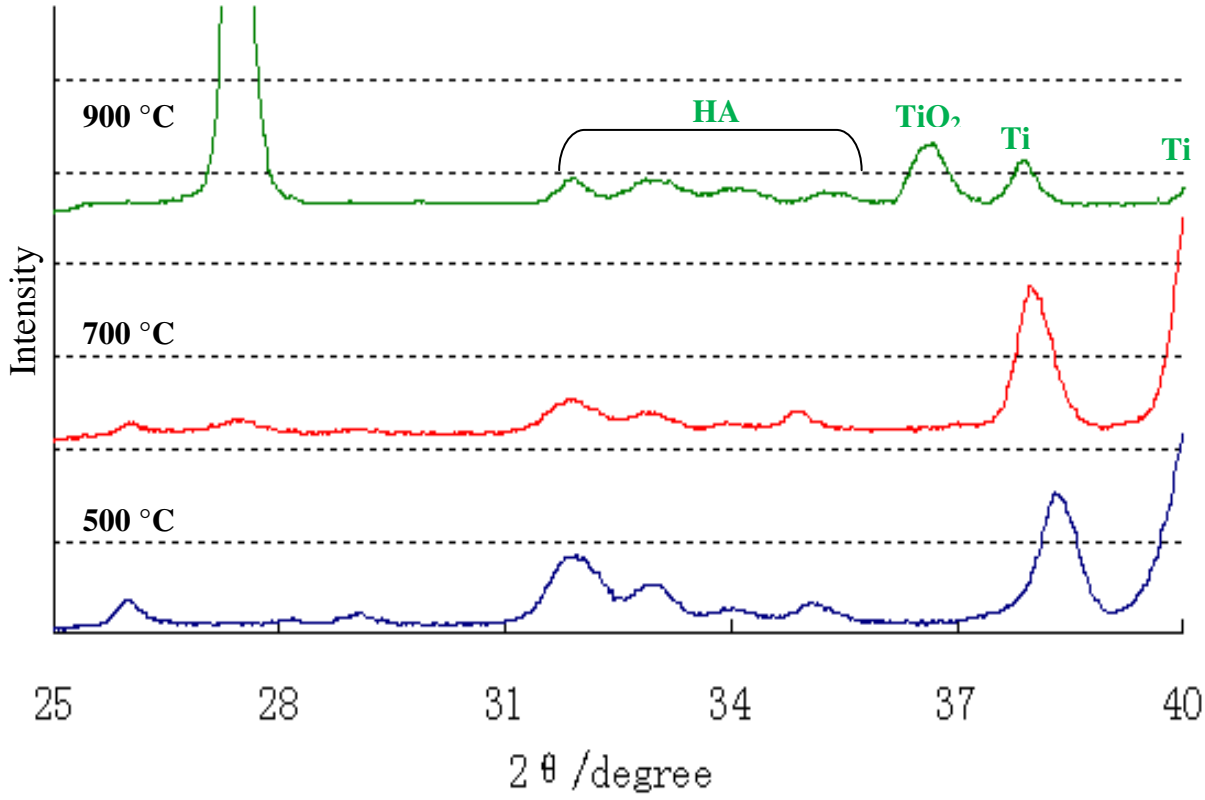

Figure 4.17. X-Ray diffraction patterns of the nHA coated Ti heat treated at 500°C, 700°C and 900°C.

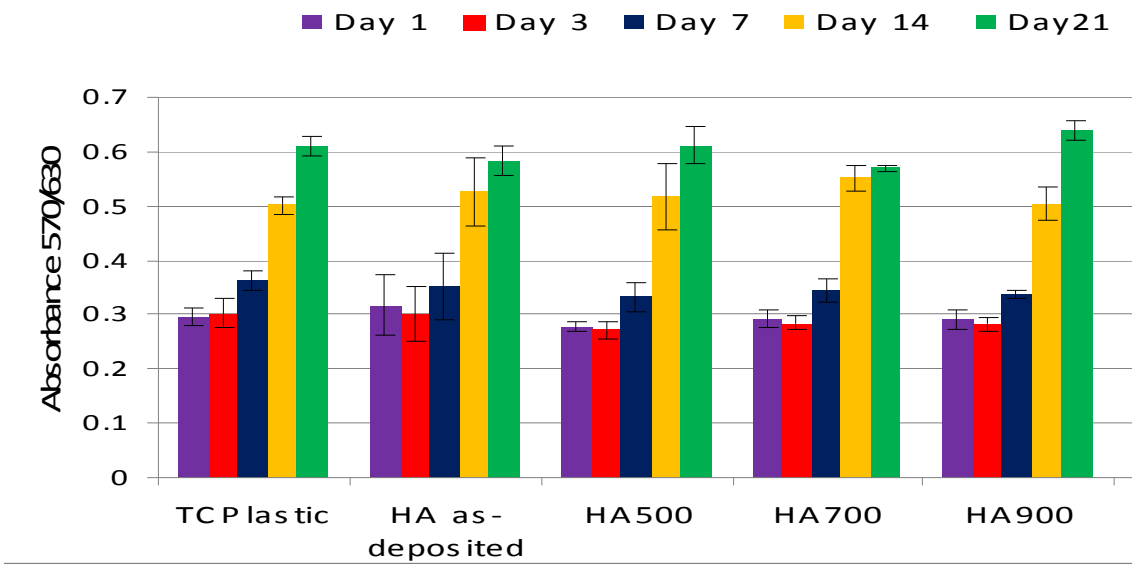

Figure 4.18. Proliferation of HOB cells on cpTi and HA coated Ti before heat treatment and heat treated at 500 °C, 700 °C and 900°C.

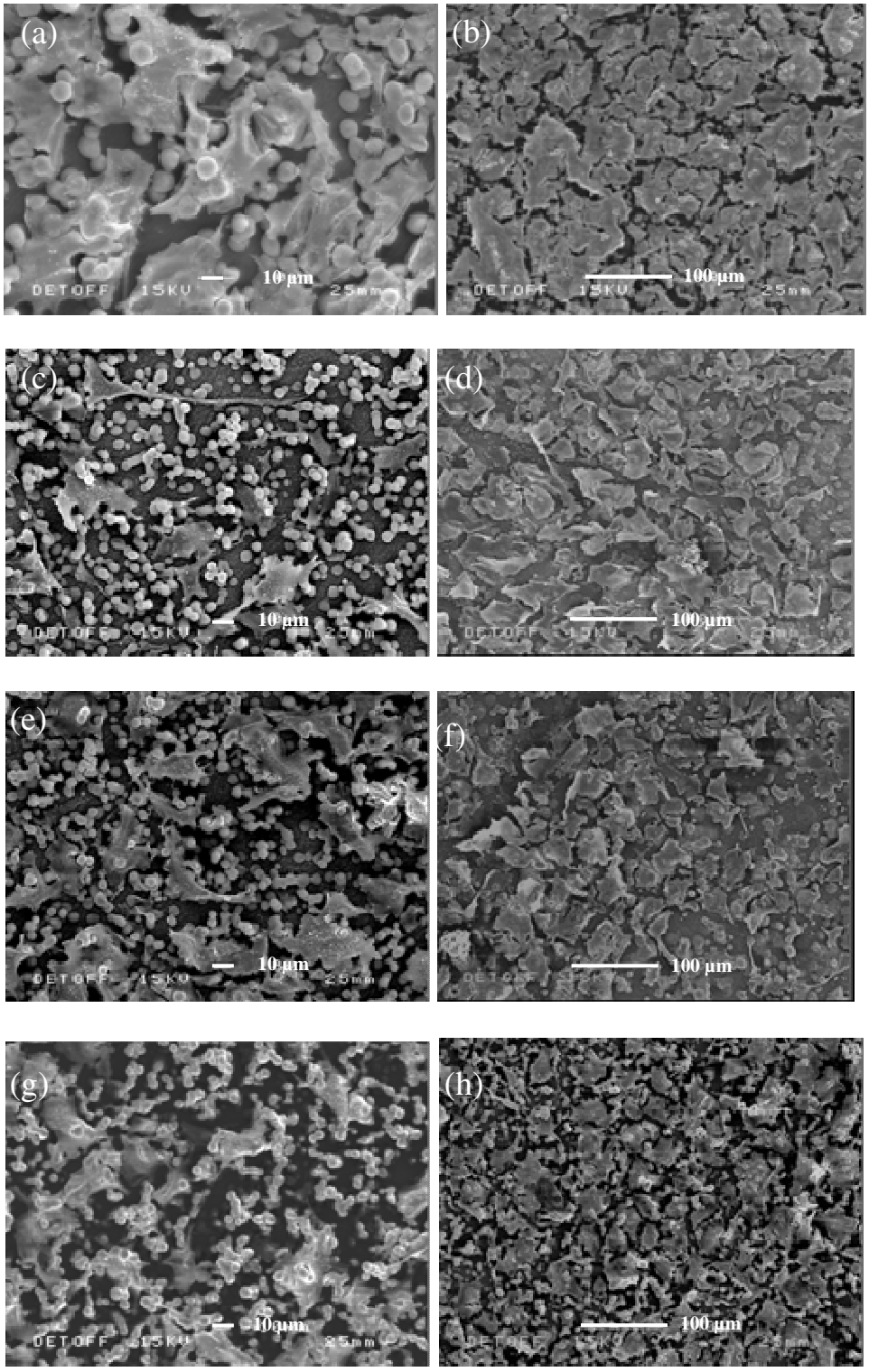

Figure 4.19. Scanning electron micrographs of HOB cells attached on an unheated nHA coated cpTi (a) (at day3) and (b) (at day21), and nHA coatings heat treated at 500°C (c) at day3 and (d) at day21, heat treated at 700°C (e) at day3 and (f) at day21, heat treated at 900°C (g) at day3 and (h) at day21.

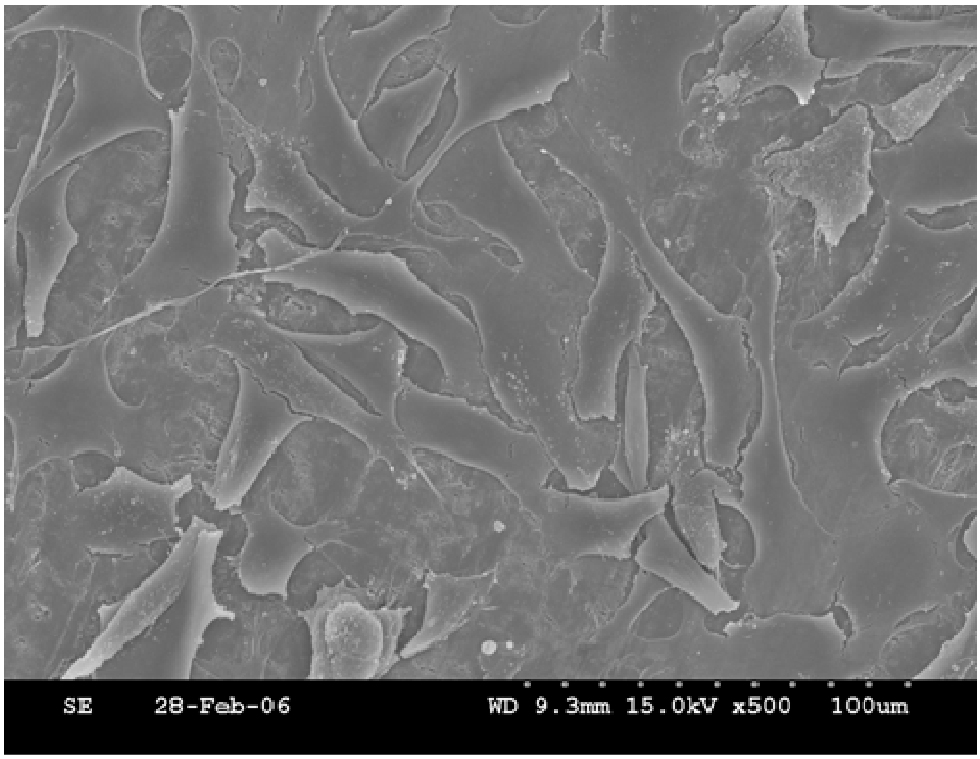

Figure 4.20. Scanning electron micrographs of HOB cells attached on cpTi surface

Chapter 5

Template-assisted electrohydrodynamic atomisation (TAEA) spraying for nHA patterning

As discussed in **Section 2.4.6**., a novel patterning technique, template-assisted electrohydrodynamic atomisation (TAEA) spraying, has been innovated in this study. This chapter is to describe the systematic investigation of processing uniform micro-scale nHA patterning using TAEA spraying. The core component of the processing setup is the specific designed ground electrode configuration. The investigation of the suitable configuration in discussed in the first section in this chapter to pave the way to the further patterning process study. Subsequently, this chapter discusses the preparation of nHA patterns with different geometries and dimensions using the TAEA processing. Based on this, a study of TAEA patterning resolution improvement, which was carried via studying the effect of the suspension solvent evaporability and the substrate temperature during process, is also included in this chapter. It was found that the suspension solvent with higher evaporability (fast evaporation rate) and the higher substrate temperature can lead to the small relics on the substrate during the patterning the process, and therefore the line shaped nHA patterns of ~15 μm in width was achieved. The characterisation of the biological properties of line-shaped nHA patterned Ti samples is discussed in the following section. An *in-vitro* study use human osteoblast (HOB) cells showed that the osteoblast attachment and orientation can be significantly regulated by the line-shaped nHA patterns, but differed by the variation of the dimension of the line patterning width and height. Based the previous investigations, a bonding enhanced TiO_2 interlocked nHA coating was investigated by combining the use of the TAEA patterning and EHDA deposition processes. The mechanism and

investigation of this novel bonding enhanced composite coating preparation are discussed and introduced in the final section. This study combined with the work carried out in chapter 4 forms the foundation and provide the motivation for the further investigation of the needle geometry effect of electrohydrodynamic processing carried out in **Chapter 6**.

5.1 Comparison of nHA suspensions with different solvents

As discussed in Section 4.1, the ethanol is known as a typical liquid to give stable con-jet mode electrohydrodynamic jetting and droplet generation, and in this section two solvents with different evaporability, which are ethanol and DMAc (Introduced in **Section 3.1.2**), were used as the liquid carriers of the 6 %wt nHA suspensions. Therefore, the values of the pure ethanol core physical properties, such as surface tension, electrical conduction and viscosity, were used as reference for the comparison of the nHA/ethanol suspension and nHA/DMAc suspension. Thus, the properties, which are density, viscosity, surface tension and electrical conductivity, of pure ethanol, nHA/ethanol suspension (6% wt) and nHA/DMAc suspension (6% wt) are shown in **Table 5.1**. The electrical conductivity of both nHA suspensions has been significantly decreased by almost three times. This is due to the dielectric nHA ceramic particles present in the suspensions. The viscosity and surface tension of the nHA/DMAc suspension are higher than those of nHA/ethanol suspension. This will lead to the higher applied voltage request to achieve the stable cone-jet electrohydrodynamic mode of spraying nHA/DMAc suspension than that when spraying nHA/ethanol suspension. The mechanism can be explained using the physical mode of the stable cone-jet mode (Hartman *et al*., 2000). The stable cone-jet mode is due to the balance of the electric stresses, including electric stress in the liquid surface, viscosity stress and surface

tension. When spraying a liquid with high viscosity and surface tension, a higher electric stress will be accordingly required to maintain the balance for the stable cone-jet mode. Therefore, the high applied voltage is needed using nHA/DMAc suspension during the spraying process.

Table 5.1. Properties of ethanol, 6%wt nHA/ethanol suspension and 6%wt nHA/DMAc suspension

Samples	Density (kgm^{-3})	Viscosity (mPa s)	Surface tension (mNm^{-1})	DC electrical conductivity (Sm^{-1})
Ethanol	790	1.3	23	3.4×10^{-4}
6%wt nHA/ethanol suspension	930	6.8	28	1.2×10^{-4}
6%wt nHA/DMAc suspension	1020	8.2	40	1.0×10^{-4}

The nHA/ethanol will be used for the investigation of the TAEA patterning process. However, during the subsequent patterning resolution improvement study, the nHA/DMAc suspension will be also used for comparison.

5.2 Electrode configuration investigation of TAEA patterning process

During the investigation of the TAEA patterning process, two ground electrode configurations, which are direct-grounded substrate configuration (**Figure. 5.1**a) and indirect-grounded substrate configuration (**Figure. 5.1**b), were designed. The following subsections will introduce and discuss the studies of using each ground electrode configuration for the nHA patterning process.

5.2.1 Direct-grounded substrate configuration

In the direct-grounded substrate configuration, the masked Ti substrate is directly connected to the grounded electrode. The electric conductive gold template, which was placed on the Ti substrate during the patterning process, was also grounded as shown in **Figure.5.1**a. However, no nHA patterns can be generated on the substrate even under the stable cone-jet patterning mode. It was found that most of the nHA droplets attached to the template rather than the targeted substrate as shown in **Figure 5.2**a. Along with the spraying process carried on, the nHA relics almost fully covered the template. Therefore, only few suspension droplets can pass through the grids in the template. Instead of the regular nHA patterns, only random relics exhibited on the Ti substrate (**Figure. 5.2**b).

Under such experimental setup, the template and substrate are connected to earth to act as a ground electrode, the charge distributes on the surface of both the gold template and the substrate. Therefore, the gold template and substrate all act as the ground electrode. Since the template is place on top of the substrate, thus the distance between the spraying needle and template (d_1) is shorter than the needle-substrate distance (D). Therefore, according to the Coulomb's Law:

$$\vec{E} = \frac{1}{4\pi\varepsilon_0}\frac{Q}{d^2}\hat{d} \qquad \textbf{(Equation 5.1)}$$

Where Q is the charge on the needle, d is the distance between the electrodes, $\hat{d}$ is the vector from the droplet to electric field evaluation point and ε_0 is a constant, defined as 1.

Therefore, the magnitude of electric field strength between the template and the needle ($\left|\vec{E}\right|_1$) is higher than that between the needle and substrate ($\left|\vec{E}\right|$).

$$\vec{F} = \vec{E} \cdot q \qquad \textbf{(Equation 5.2)}$$

Where F is the electric force generated on a charged particle in the electric field and q is the charge on a depositing droplet. Now, F_1>F, which means, for the charged droplets, the electric force e to a single suspension droplet between the needle and gold template is higher than that between the substrate and needle. Hence, it reflects the experimental findings. During the spraying under the direct electrode configuration, most of the suspension droplets attach onto the gold template rather than the substrate and nHA topographies cannot be generated on the substrate in this way.

5.2.2 Indirect-grounded substrate configuration

In comparison, the ground electrode set-up shown in **Figure 5.1**b could be much more capable and efficient in generating a pre-determined topography since the substrate and template are not grounded. Between the ground electrode and substrate, there is Si wafer (~1mm) which is dielectric. During spraying, droplets are driven by the electric field generated between the needle and the grounded conducting metal plate. Therefore, there is no difference in the driving electrical force to the template or to the substrate, the droplets could move and attach onto the template (**Figure 5.3**a) and substrate uniformly, which is significant to creating topographies on the substrate as the template is just simply removed after spraying (**Figure 5.3**b).

A more in-detail investigation of the nHA patterning using TAEA process was carried out after the determination of the ground electrode configuration, as discussed in the following section.

5.3 nHA patterning using TAEA process

5.3.1 TAEA process parameters

Freshly prepared 6 wt% nHA suspension was syringed to the needle at flow rates of 1-35 μl/min with the applied voltage between the needle and the ground electrode varied up to 6kV to investigate electrohydrodynamic spraying scenarios. The distance between the stainless steel needle and substrate (D) was fixed at 20 mm. Commercial pure titanium plates, which were polished using P4000 silicon carbide grinding paper, were used as substrates to be deposited with nHA. The thickness of titanium plates is 2 mm.

Similar to the nHA deposition work carried out in **Chapter 4**, an applied voltage range of 4.3-5.2 kV and a flow rate of 20 μl/min were used and stable cone-jetting was maintained throughout topography generation. When the spray time was 15s, the thickness of the nHA deposit is approximately 1.4 μm. Along with the increase of the spraying time, the thickness of the deposit was found to increase to 4.9 ± 0.5 μm at 120s. The deposit thickness is directly proportional to the spraying time.

5.3.2 nHA patterns prepared using TAEA patterning technique

As shown in **Figure 5.4**a, by using a hexagonal template HA nano-particles distributed into hexagonal islands on the substrate surface can be prepared in this way. The diameters of the islands could be controlled at 50μm and the spaces between the islands are 10μm. By using parallel and square templates on a polished titanium substrate, this method enabled the creation of line and square topography (**Figure 5.4** b&c) with each line of ~75 μm width and the distance between the lines was ~80 μm, and each square of side 50 μm and the space between the square islands was ~20 μm. **Figure 4**b exhibits the nanostructured particle assembly in the deposits. Nano-scale HA more closely mimics HA crystals in bone and thereby enhances bioactivity (Wang *et. al.* 2004; Lewandrowski *et. al.* 2003).

All nHA patterns prepared in this way exhibited uniform and ordered topography. The spaces between the islands were kept constant and varied only by a few micrometers, and by using the same template, the shape and size of islands in the entire coating was kept the same. Since the spray time was controlled at 30s during the process, the height of the 'islands' in the coatings was ~2 μm. The line patterns in Figure 4c can be compared directly with those generated using the electrohydrodynamic printing work (Ahmad *et. al.* 2006) and indeed the resolution, scatter control and uniformity of the patterns deposited in this work are superior.

The template can also be used as a substrate with more complex shape as it is coated according to the 'negative' of the pattern generated on the solid substrate. **Figure 5.5** shows gold mesh templates with different grid geometries coated with nHA and this is

the inverse (‘negative’) of the patterns. The HA nano-particles distributed uniformly on the entire template and was of the same thickness as in the case of the substrate.

5.4 Study of TAEA patterning resolution improvement

As a jet-based patterning technique, the dimension of the patterns largely depends on the grid size in the template. The template with small grid size can lead to patterns with small dimension on the substrate during the patterning process. However, another factor, which is crucial for the patterning, is the droplet size produced after jetting. To create a precise high-resolution nHA pattern, it has to be ensured that the nHA suspension droplets can be small enough to pass through the tiny spacing in the template and attach the targeted substrate. Furthermore, after the suspension droplets attach the substrate and form relics on the substrate, the spreading effect of the relics can also lead to coarse edges of the patterns. Therefore, the reduction of the droplets size and the control of the relics spreading on the substrate become the major challenges in the investigation. Due to the nature of the electrohydrodynamic processing, the liquid droplets form after the jet break-up and travel to the actual target substrate. Changing the suspension solvent and the substrate surface temperature during the patterning could be two effect ways to influence the solvent evaporation and control the deposited relics’ size without causing any complexity during the patterning process. The following subsections are going to introduce the studies carried out to investigate the effect of the suspension solvent evaporability and the substrate temperature to the nHA relic size, which is crucial for the nHA patterns. The objective of this section is to reduce the size of the droplets/relics via choosing the appropriate suspension solvent and controlling the substrate temperature, to therefore improve the nHA pattern resolution.

5.4.1 Effect of the suspension solvent evaporation

In this work, the deposition preparation was carried out at room temperature. Two different nHA suspensions, which are 6 wt% nHA/ethanol suspension and 6 wt% nHA/DMAc suspension, were used during the spraying. To simplify the comparison of nHA coating prepared using different suspensions, a fixed needle-substrate distance (20 mm) and liquid flow rate (20 μl/min) were set for the electrohydrodynamic processing. When nHA/ethanol suspension was used, the stable cone-jet mode was achieved under the applied voltage range at 4.3-5.2kV. When nHA/DMAc suspension was used, the applied was set at 4.8-6.0kV to achieve stable cone-jet mode. The nHA relics were collected on the silicon wafer without templates.

As expected, the nHA depositions prepared exhibited significant different surface morphologies. As shown in **Figure 5.6** the nHA coating prepared using ethanol-based nHA suspension presents rough morphology and relatively porous surface structure. The one prepared using DMAc-based nHA suspension exhibits entirely different scenario, which is with fully-covered and dense characteristics. The drive for this variation in surface morphology is the different suspension droplet spreading process involved during the coating process. As shown in the cartoon (**Figure 5.7**a), a single suspension droplet was assumed to be driving during the spraying process. When ethanol-based nHA suspension was used, during the travelling before eventually attaching the target substrate, large quantity of liquid phase (ethanol), which is of high evaporability, will evaporate-off. Therefore, the HA ceramic particle concentration with the droplet was significantly increased. Subsequently, the droplet cannot spread on the substrate surface due to the high viscosity led by high ceramic concentration, and therefore form an ‘island’ shape relic on the surface. These relics lead to a rough,

porous and less-covered coating surface. Meanwhile, as shown in **Figure 5.7**b, due to the weak evaporability of DMAc, the liquid phase remains during the spraying process. The concentration and viscosity of the nHA suspension won't be significantly influenced. The droplets form a high-covered, smooth deposit on substrate. The morphology of the relics of the two suspensions collected on Si wafer substrate further proves this mechanism. As shown in **Figure 5.8**a, the relics sprayed using ethanol-based nHA suspension exhibit 'island' shape. Meanwhile, the relics achieved using DMAc-based suspension show apparent spreading process (**Figure 5.8**b). This phenomenon has further reflected and proven the mechanism afore-mentioned.

For the TAEA patterning process, relics spreading effect can lead to coarse edges of nHA patterns, and thus significantly reduces the pattern resolution. Therefore, 6 %wt nHA/ethanol suspension was chosen for the subsequent studies, which are the effect of the substrate temperature and the further preparation of nHA patterns with high resolution using TAEA patterning process.

5.4.2 Effect of the substrate temperature

In this study, the freshly prepared 6 %wt nHA/ethanol suspension was used, and the suspension flow rate and needle-substrate distance were set at 10 µl/min and 40 mm. Compared with the processing parameters used in Section 5.3, the flow rate has been reduced by 50%, and the needle-substrate distance had been doubled. This is because a lower flow rate gives smaller droplets (Jayasinghe & Edirisinghe, 2004). Furthermore, the larger needle exit to substrate distance makes the droplet trajectory longer allowing more evaporation of the droplets before they land on the substrate. This helps to curtail the movement of suspension on the substrate. Commercially pure titanium substrate

plates were polished using P4000 silicon carbide grinding paper, and subsequently cleaned using acetone and ethanol. During the patterning process, the substrates were heated to 40°C and 80°C (the boiling point of ethanol solvent is ~78°C), and the spraying time was controlled at 30s. A range of gold templates with similar grid-spacing were used to mask the Ti substrate during patterning. The stable cone-jet mode (**Figure 5.9**a) was achieved when the applied voltage was controlled between 5.5kV and 6.1kV. Otherwise, the unstable cone-jet mode (**Figure 5.9**b) or the multi-jet mode (**Figure 5.9**c) was obtained, and these are rather turbulent jetting modes, which should be avoided during the patterning process.

When the Ti substrate was heated to 40°C which is nearly ~0.5 of the boiling point of the ethanol, nHA line patterns were generated using the stable cone-jet patterning mode. As shown in **Figure 5.10**a, the nHA line width was 32 μm with the standard deviation at 3 μm and the distance between the lines was 85 μm with a standard deviation of 6 μm. When the Ti substrate was further heated to the boiling point of ethanol the pattern dimensions were more than halved. As shown in **Figure 5.10**b, the nHA line width and the distance between the lines are 15 μm (standard deviation 2 μm) and 105 μm (standard deviation 3 μm), respectively. The resolution of the patterns has been significantly improved.

The major reason for the reduction in line width is the decrease in the droplet relic size achieved by increasing the substrate temperature, as uncovered by templateless spraying (coating). At the ambient temperature (**Figure 5.11**a), the nHA relics spread to form a coating. However, when the Ti substrate was heated to 40°C during spraying, the nHA relics become isolated and form 'island'-shaped deposits (**Figure 5.11**b). As shown in **Figure 5.11**c, very fine well-separated relics are seen on the substrate at a substrate

temperature of 80°C. At higher substrate temperatures, more ethanol in the deposited droplets evaporates and therefore the viscosity of the droplets on the substrate increases and restricts their spreading.

In additional to the reduction of the droplet relic diameter, the restriction of the droplets spreading due to the higher temperatures also changed the topography of the relics deposited. **Figure 5.12** shows the individual nHA relics deposited when the substrates were heated to 40°C and 80°C. The nHA relic mean size was 4.2 μm (standard deviation 0.8 μm) when deposited on the substrate held at 40°C (**Figure 5.12** a). However, the mean size of the nHA relics deposited at 80°C was reduced to 2.5 μm (standard deviation 0.5 μm) (**Figure 5.12** b). As the same spraying parameters and nHA suspension was used for deposition, the size range of the suspension droplets produced under the stable cone-jet mode are approximately the same, and therefore the mean volumes of nHA relics deposited at the different substrate temperatures are equal. Therefore, the volume ratio of nHA relics deposited on the same substrates at 40°C and 80°C would be related by the following equation:

$$\frac{V_{40^oC}}{V_{80^oC}} = \frac{D_{40^oC}{}^2 \times H_{40^oC}}{D_{80^oC}{}^2 \times H_{40^oC}} \approx 1 \quad \textbf{(Equation 5.3)}$$

Where, V is the mean volume of the nHA relics, D is the mean diameter of relics and H is the mean height of nHA relics. Therefore, the ratio of the mean heights of nHA relics deposited at 40°C and 80°C is ~1:3 and the mean height of a single nHA relic formed at 80°C is nearly three times the height of the nHA relic deposited at a lower temperature.

Due to this evolution of the nHA relics during spraying with heated substrate, the topography of the nHA lines has also been significantly influenced by the substrate

temperature. As shown in **Figure 5.13** a&b, the tandem scanning microscope images show that the base layer and the peak layer of the nHA lines prepared at 40°C substrate temperature. The base layer, which is shown as a dark region, is ~32 μm in width which matches the measurement on SEM images, and the peak layer of nHA line which is shown as a bright region is ~18 μm in width. The distance between the top and bottom, which shows the height of the nHA lines, is 6 μm with standard deviation of 1 μm. **Figure 5.14** a&b show the base layer and the peak layer of the nHA lines prepared at 80°C substrate temperature. The bottom layer is ~15 μm in width, and meanwhile the top layer of the lines is ~4 μm in width only. The height of the nHA lines is 16 μm with standard deviation of 2 μm. Therefore, the nHA lines prepared at 80°C substrate temperature present as sharp ridges on Ti surface compared to the nHA patterns prepared at 40°C substrate temperature.

The biological properties of these two prepared line shape nHA patterns were further characterised and compared via an *in-vitro* study. The cell attachment and orientation on the nHA patterned Ti plates were compared with the nHA coated Ti plate, which was discussed in **Chapter 4**, in the following section.

5.5 *In-vitro* study of nHA patterns

The line shape nHA patterned Ti plates investigated in the previous section were characterised using human osteoblast. The culture period for all the samples was controlled at 3 days. The cellular morphology and alignment on samples are discussed in follow.

The cellular morphology can be used as an indication of cell health and orientation. The scanning electron micrographs in **Figures 5.15 & 5.16** demonstrate the cell attachment and numerous cell filopodia anchoring to the nHA particles. However, different scenarios of cell morphology were observed on the HA patterns of different dimensions as discussed below.

In the case of broader nHA lines of a higher width, the HOB cells attach and align along the nHA lines as bioactive HA particles provide the preferable site for cellular attachment (**Figure 5.15**). However, the cells on the nHA lines with narrower width and larger height present an entirely different morphology. Instead of growing along the HA lines, the cells seem to attach and grow in the spacing between the lines (**Figure 5.16**). The separated appearance in the cell layer presented in **Figure 5.16** is due to the drying process during the SEM sample preparation.

The behaviour of the cells with respect to the TAEA patterns can be explained using the theory of Curtis and Wilkinson (1997). Cells were able to switch alignment from ridges to grooves depending on the dimensions. The HOB cell is ~40 μm. When the HA line matches the HOB cell dimension, the cells sit, attach and grow along their 'favourite' HA sites. However, if the HA lines are fine and have sharp ridges, instead of growing along the lines, they attach and grow between the ridges with filopodia anchoring to the nHA sites on the sides.

This was further proven by the fluorescent confocal microscopy visualization. The images showing differentially stained nuclei and cytoskeletal structures of HOB cells cultured on two nHA patterned surfaces using TAEA spraying are shown in **Figure 5.17**. Thus, the comparative study investigating two patterned HA structure

demonstrated a preferential cell adhesion to the HA substrate, with cells clearly aligning along the HA ridges created when the substrate heated at 40°C (**Figure 5.17**a). In the contrast, in **Figure 5.17**b, although the HOB cells distribute to the main direction of HA ridges. The cytoskeletons of the cells align to bridge the two sides which are the HA sharp ridges prepared when the substrate temperature was set at 80°C. This phenomenon clearly reflects the SEM observation results and its explanation.

5.6 TiO_2 interlocked nHA deposition preparation using EHDA and TAEA processing

5.6.1 Design concept

The interfacial stability is crucial to the implant material's performance for clinical applications. To enhance a composite material's properties, mechanical interlocking was induced as a common solution to improve the bonding and therefore the stability at the interface between the two different substances (Gao *et al*., 2008). Creating the surface texture is an effective way to achieve a mechanical interlocking at the interface (Dickson and Lepoutre, 1997). This interlocking approach was also used in processing the bioactive coatings with enhanced bonding strength. A number of investigations have demonstrated that the significantly improved bonding of coatings could be achieved via roughening the substrate surface before coating process (Mimura *et al*., 2004; Li *et al*., 2007; Zhang *et al*., 2001). Meanwhile, recently, some studies showed that the bonding of the HA coatings can also be enhanced by inducing a chemistry bonding. A continuous TiO_2 buffer layer pre coated at Ti substrate was found to significantly enhance the HA/Ti interfacial adhesion and therefore improve HA mechanical stability

during the clinical practices (Kim et. al., 2004; Lin and Yen, 2005; Roop Kumar and Wang, 2002).

Therefore, here we combine these two bonding enhancement concepts. The Ti substrates will be patterned with TiO_2 using TAEA to change the surface texture, and subsequently coated with HA using EHDA. This new TiO_2 interlocked HA coating on Ti substrate is to induce both the mechanical interlocking and chemistry bonding to improve implant material's functional performance for clinical practices.

5.6.2 TiO_2 interlocked nHA coating.

Using the previously investigated TAEA technique, freshly prepared 2 %wt TiO_2 sol was syringed to the needle at flow rates of 10 μl/min with the applied voltage varied up to 6 kV to ensure stable cone-jet patterning mode. The stainless steel needle used had an inner diameter of ~300 μm, and the needle-substrate distance was kept at 20 mm. The patterning time was controlled at 60 seconds. A range of templates with different geometries were used to mask the Ti substrate during patterning process. Subsequently, the TiO_2 patterned Ti substrates were directly earthed. The freshly prepared 6%wt HA suspension was feed into the needle at the flow rate of 20 μl/min. The substrate-needle distance was set at 40mm. The applied voltage was controlled between 4.3 to 5.2 kV to achieve the stable cone-jet spraying mode. The HA deposition time was controlled at 30 seconds.

As shown in **Figure 5.18**, by using a square template TiO_2 particles distributed into square-shaped islands on the Ti surface was prepared. The width of the islands was controlled at 42 μm with the standard deviation of 4 μm, and the spaces between the

islands are 48 μm with the standard deviation of 4 μm. By using parallel templates on a polished titanium substrate, the line shape TiO_2 patterns were also prepared on the Ti substrate as shown in **Figure 5.19**. The line width is 13 μm with the standard deviation of 3 μm, and the spacing between the lines is 65 μm with the standard deviation of 3 μm. All TiO_2 patterns prepared exhibit uniform and ordered topography. The spaces between the islands were kept constant and varied only by a few micrometers, and by using the same template and the same process parameters, the shape and size of islands in the entire coating was kept the same. After TAEA patterning process, the subsequent EHDA spraying process was carried out to prepare the bioactive HA layer on the interlocking pillars. As shown in **Figure 5.20**, the entire HA coating presents uniform and continuous topography, and from the optical microscopy image, it is clearly shown that the square and line shaped 'hills' distribute orderly in the HA coating. This new TiO_2 interlocked HA coating on Ti substrate induces both mechanical interlocking and chemical bonding and showed significantly improve the interfacial shear strength.

5.7 Summary

A novel patterning technique, template-assisted electrohydrodynamic atomisation (TAEA) spraying, was developed for the creation of topography with bioactive materials. Nano-sized HA topographies with different uniform micro-scale patterns have been successfully prepared on titanium substrates. Furthermore, an in-sight study of the mechanism of TAEA spraying has been carried out. Via increasing the process environment temperature and further optimizing the process parameters, nHA line-shaped pattern of ~15μm in width has been successfully achieved on Ti substrates. The resolution of this patterning technique has been significantly enhanced by fivefold. The *in-vitro* study demonstrated that the HOB cell behaviour and orientation have been

further controlled and up-regulated by the new nHA patterns prepared using TAEA patterning technique. Furthermore, combining the TAEA patterning and EHDA deposition, a novel bonding enhanced TiO_2 interlocked nHA coating was also innovated. This novel bioactive coating is expected to be used to overcome the interfacial instability of the current commercial nHA coated implant materials, and increase the implant serving life. TAEA spraying has therefore been further proven to be a promising technique in engineering the bioactive surfaces with superior shear strength for implant applications, and may be of promise to guided bone tissue regeneration.

Figures

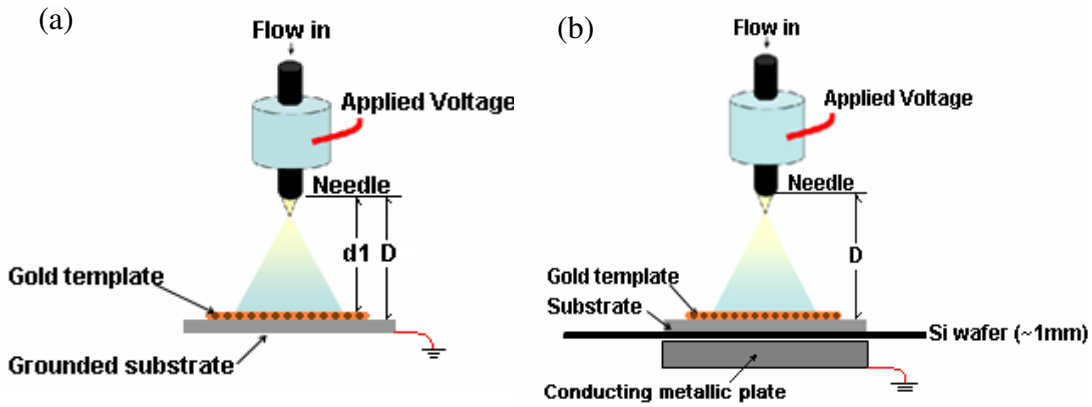

Figure 5.1. Schematic diagram illustrating (a) direct ground electrode configuration and (b) indirect ground electrode configuration employed for TAEA patterning investigation

(a)

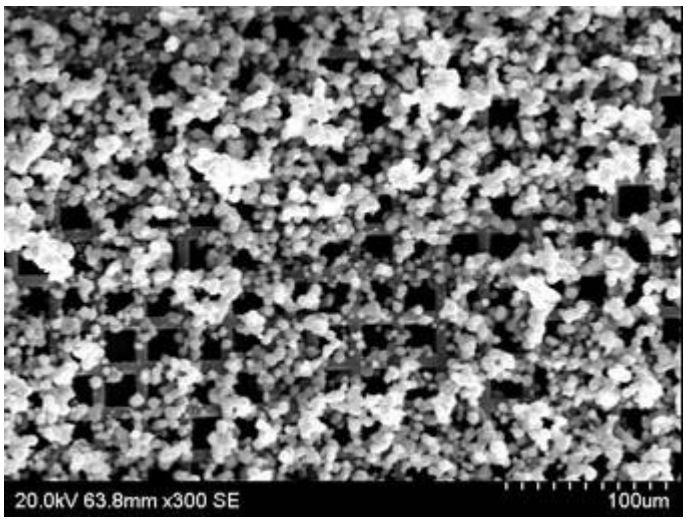

(b)

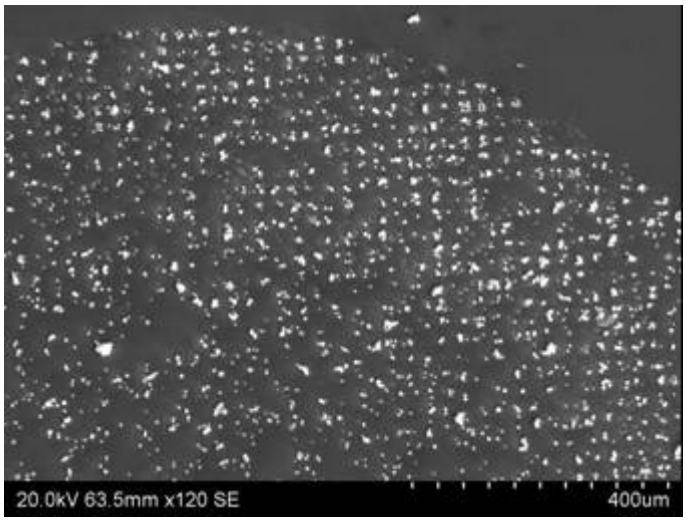

Figure 5.2. Scanning electron micrograph of (a) nHA deposited on the gold template and (b) nHA relics on the Ti substrate when the direct ground electrode configure was employed for TAEA patterning

(a)

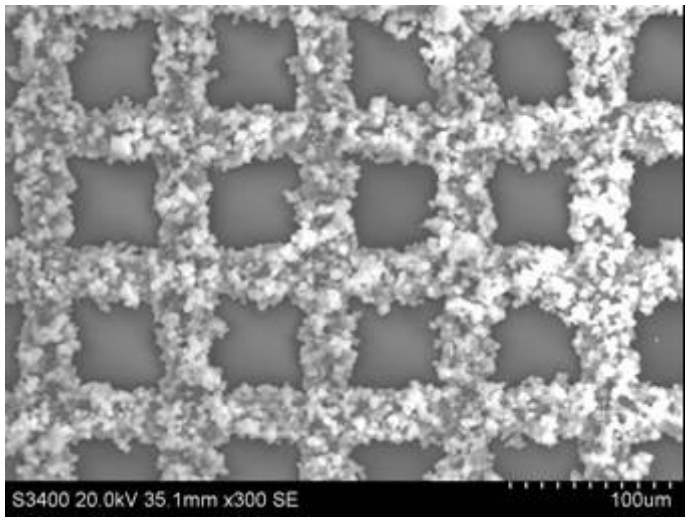

(b)

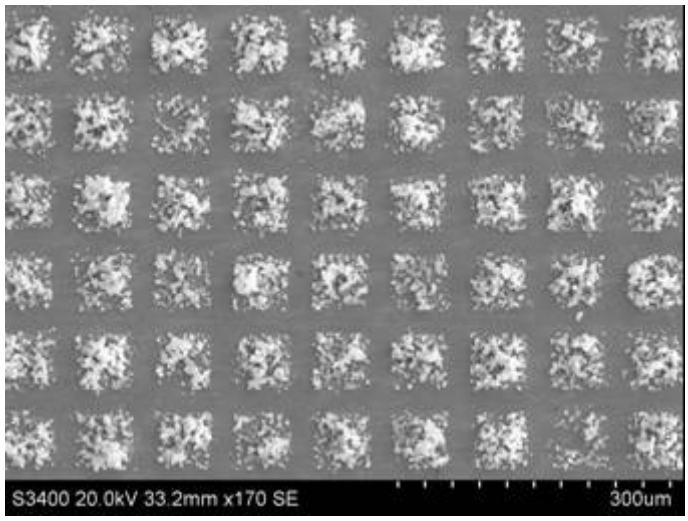

Figure 5.3. Scanning electron micrograph of (a) nHA deposited on the gold template and (b) nHA patterns on the Ti substrate when the indirect ground electrode configure was employed for TAEA patterning

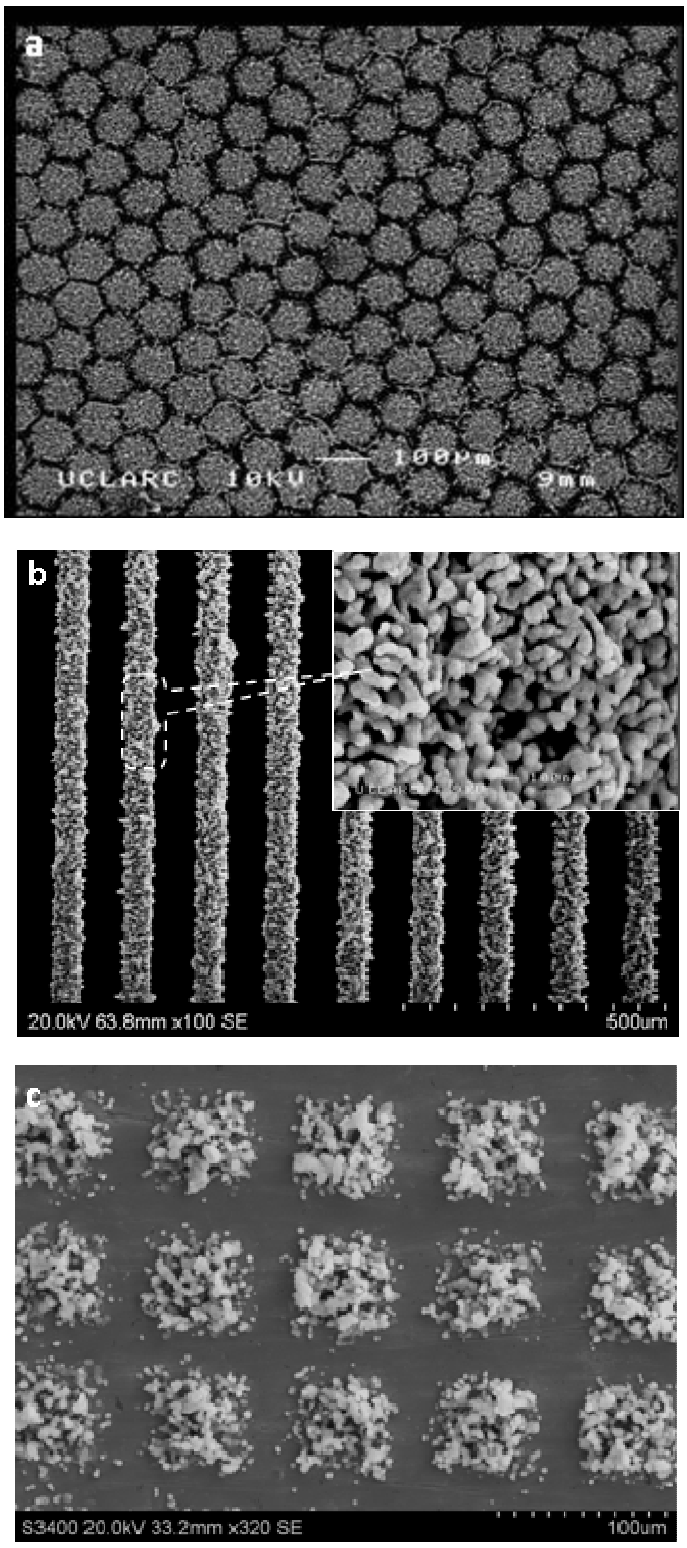

Figure 5.4. Scanning electron micrograph of (a) hexagonal nHA islands deposited on a glass substrate with the island diameter set at 50µm, (b) nHA lines deposited on a titanium substrate with the width set at 75µm and (c) square nHA islands deposited on a titanium substrate with the island diameter set at 50µm

(a)

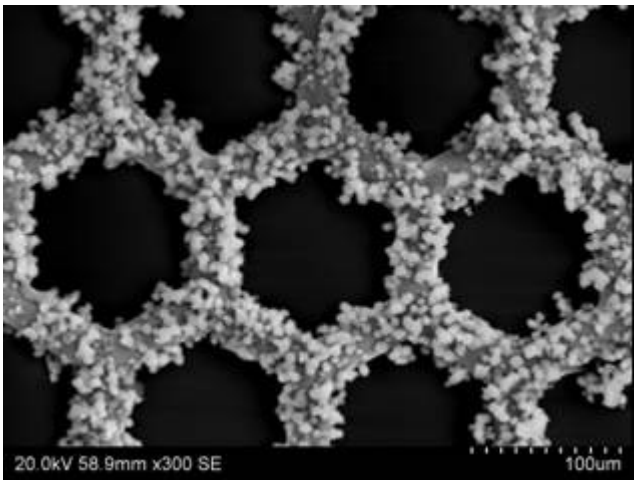

(b)

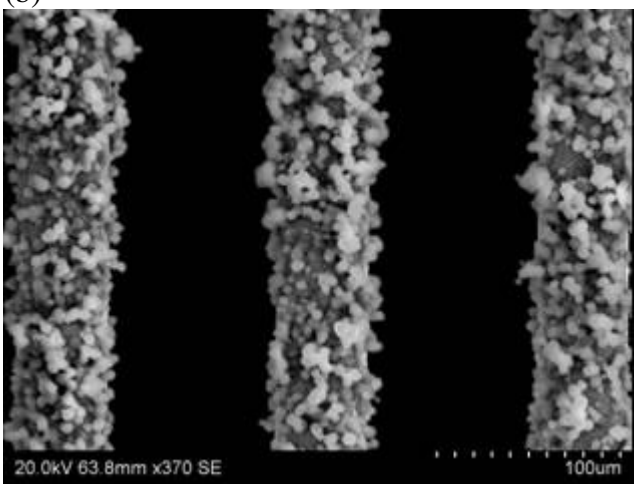

(c)

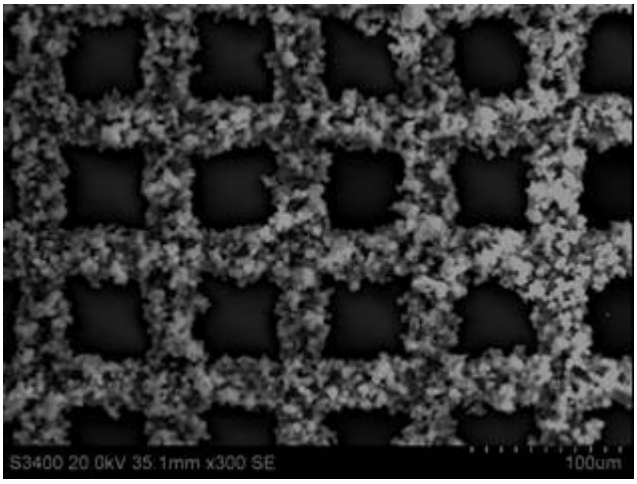

Figure 5.5. Scanning electron micrograph of nHA deposits on (a) hexagonal template, (b) line shape template and (c) square shape template

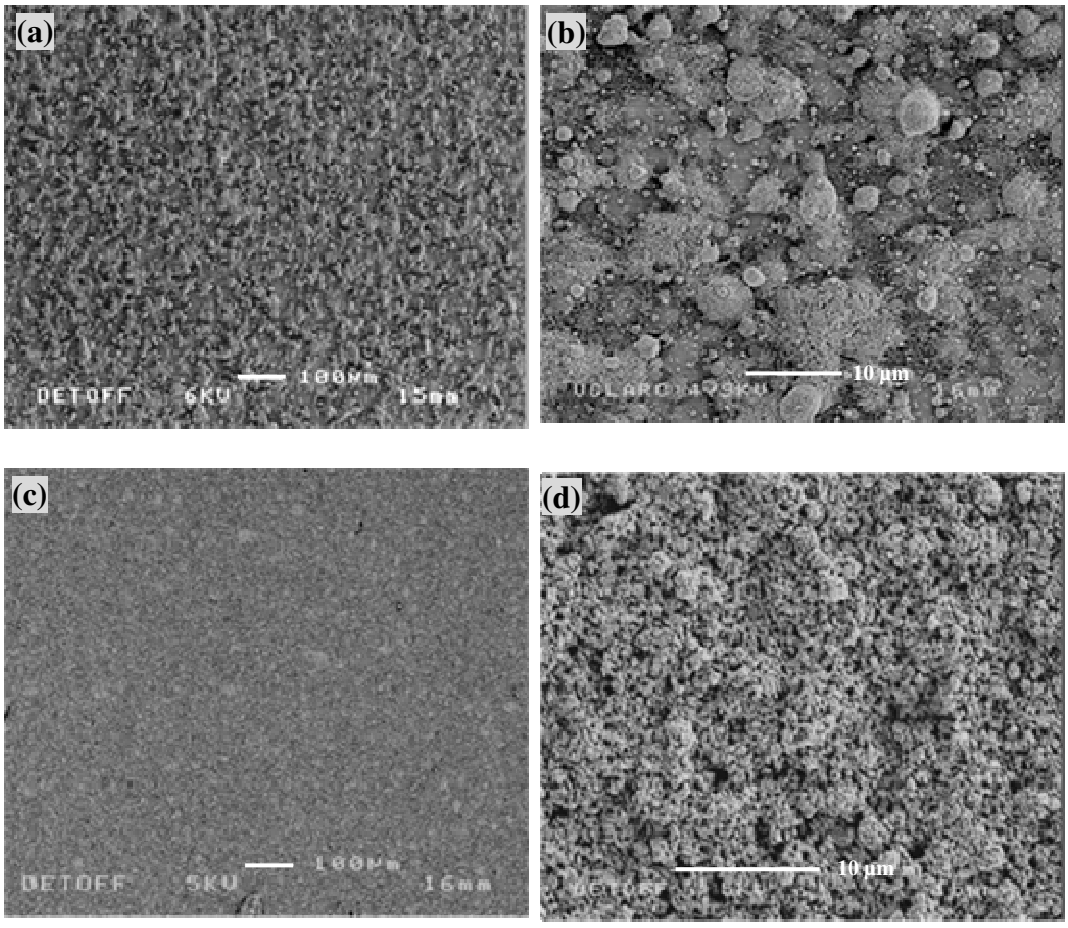

Figure 5.6. Scanning electron micrograph of (a), (b) nHA deposits using a 6 %wt nHA/ethanol suspension, and (c), (d) nHA deposits using a 6%wt nHA/DMAc suspension on Ti substrates using electrohydrodynamic spraying

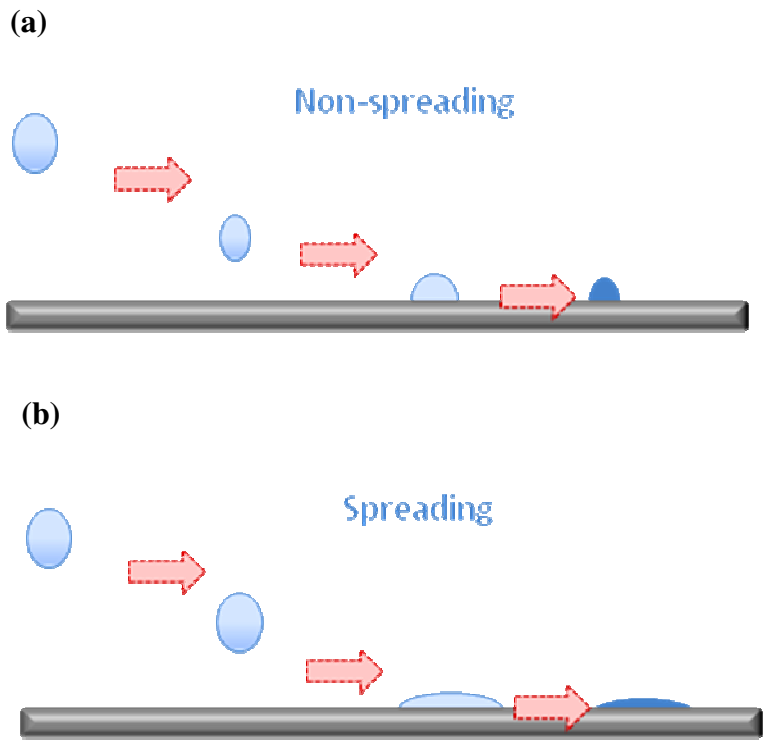

Figure 5.7. The cartoons of relic's (a) non-spreading behaviour and (b) spreading behaviour on the substrate.

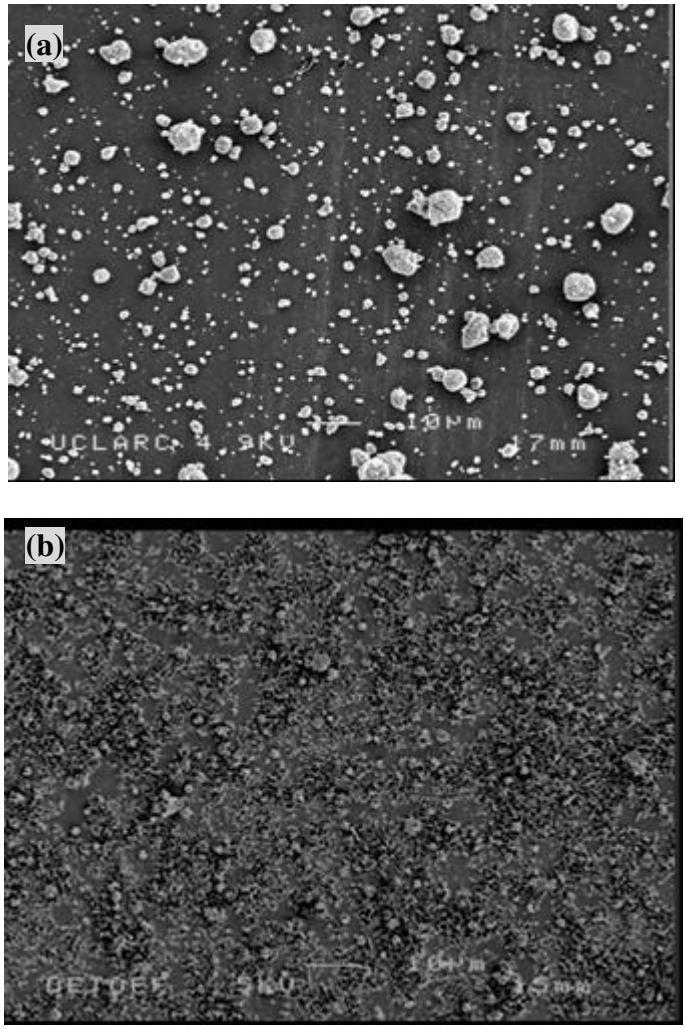

Figure 5.8. Scanning electron micrograph of (a) non-spreading nHA relics and (b) spreading nHA relics on Ti substrate

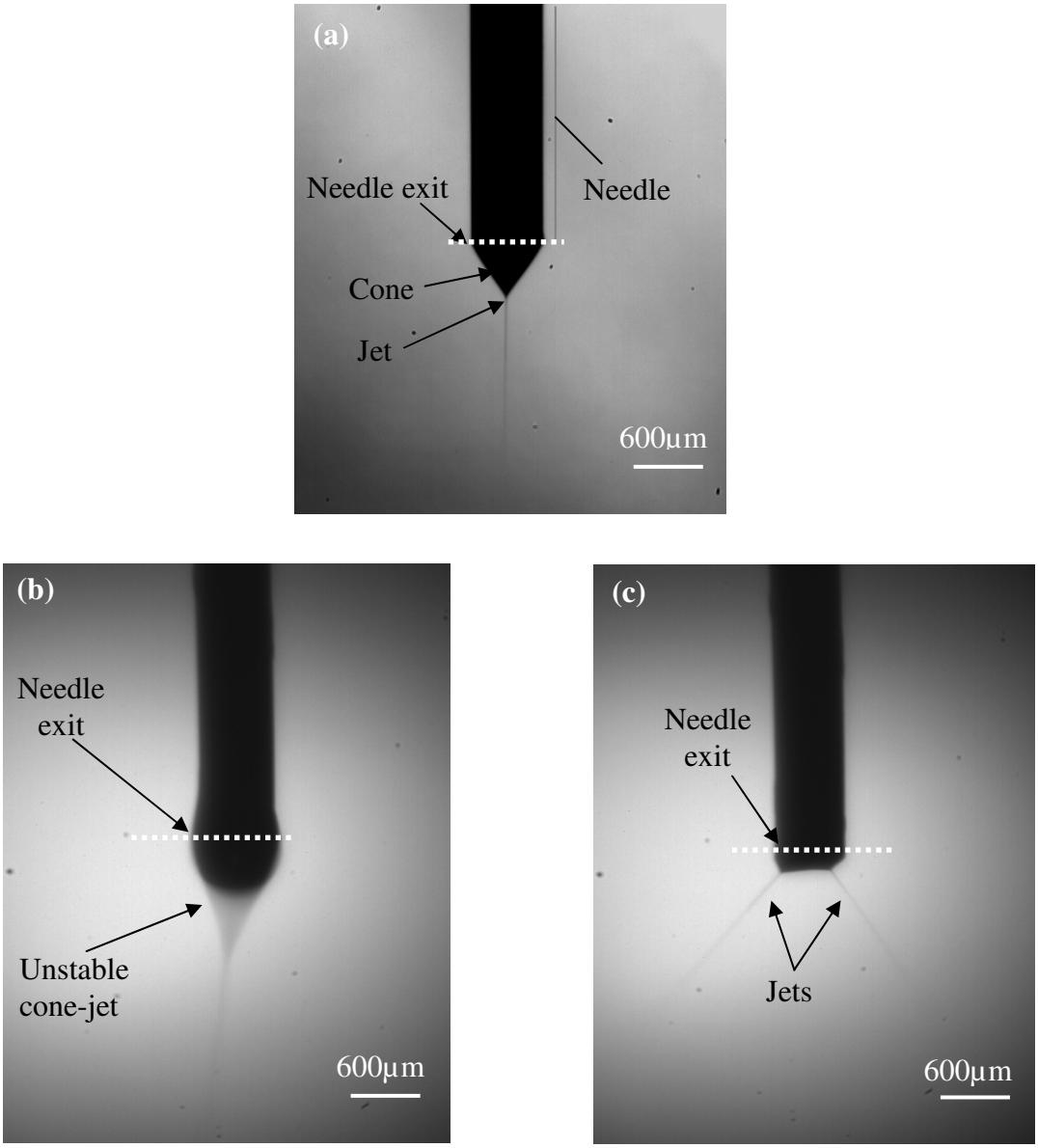

Figure 5.9. (a) Typical stable cone-jet mode obtained during the patterning process, (b) Unstable cone-jet mode and (c) Multijet mode

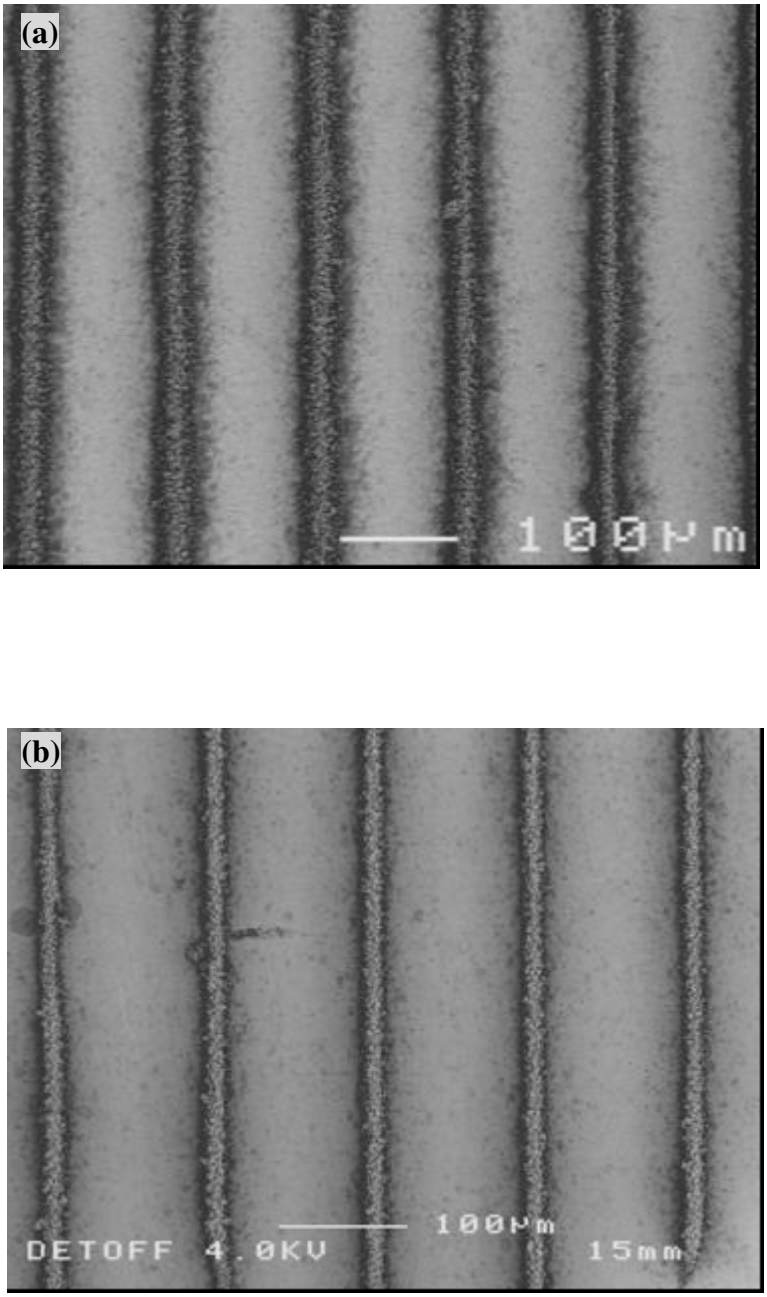

Figure 5.10. Scanning electron micrographs of (a) nHA patterns prepared at a substrate temperature of 40°C and (b) the pattern prepared at a substrate temperature of 80°C

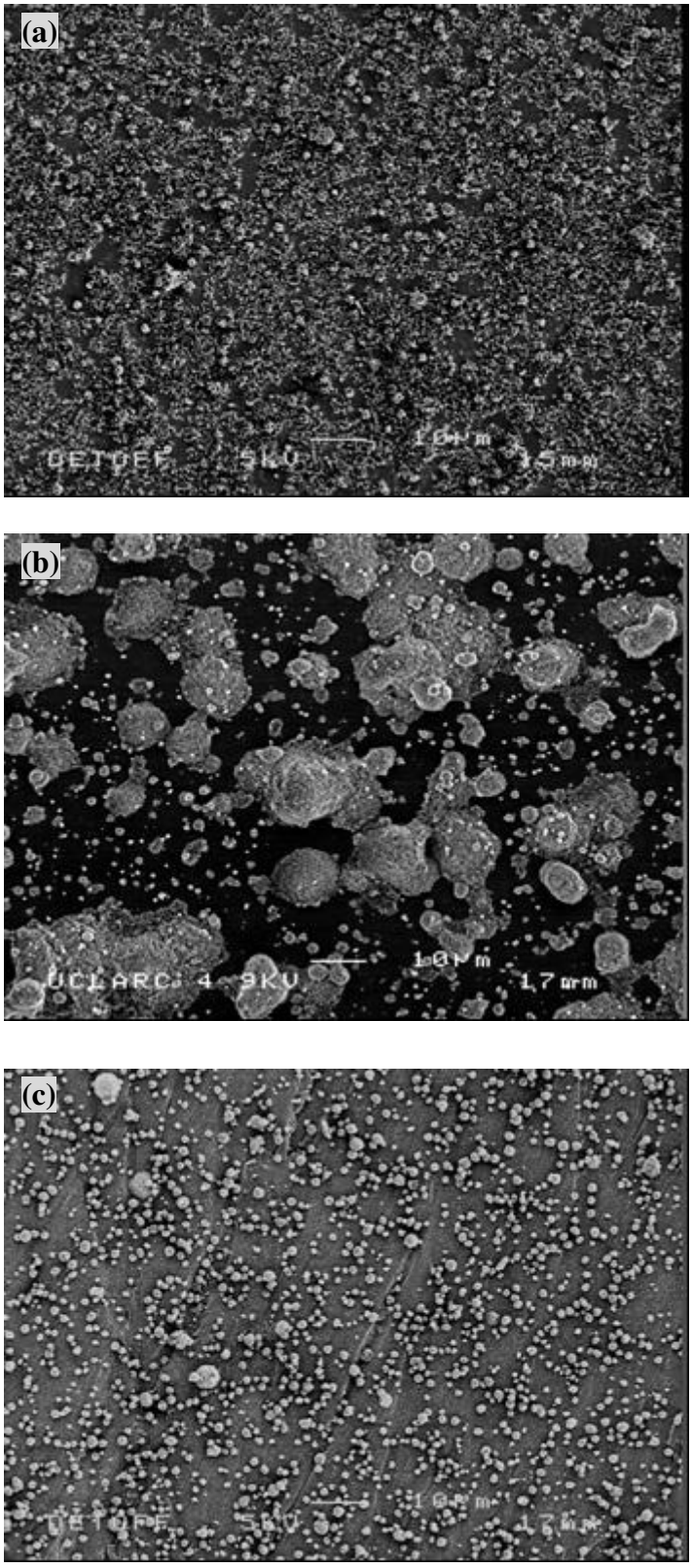

Figure 5.11. Scanning electron micrographs of (a) nHA relics deposited at the ambient temperature (25ºC), (b) nHA relics deposited at a substrate temperature of 40°C and (c) nHA relics deposited at a substrate temperature of 80°C

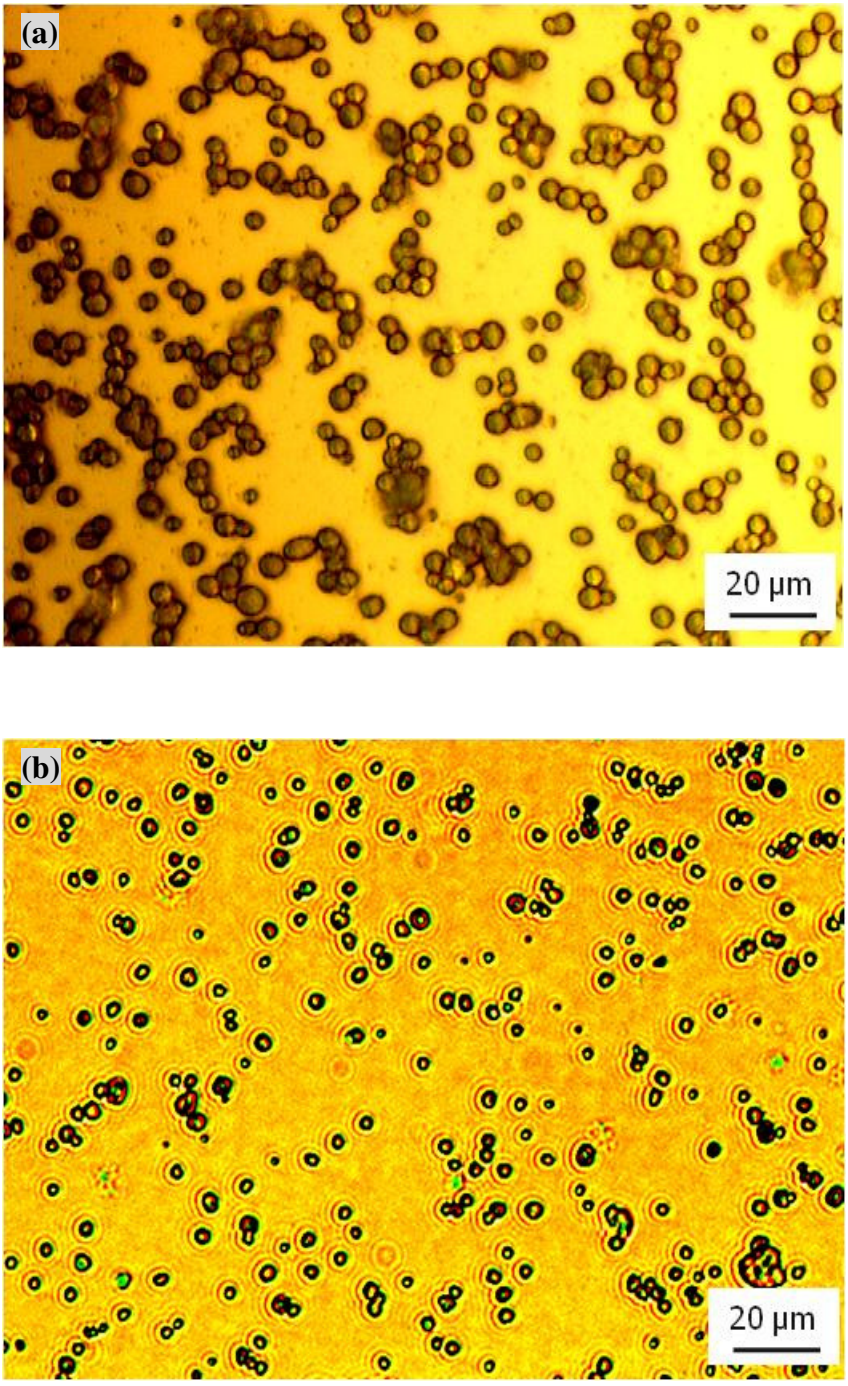

Figure 5.12. Optical images of (a) the nHA relics deposited at 40°C substrate temperature and (b) the relics deposited at 80°C substrate temperature

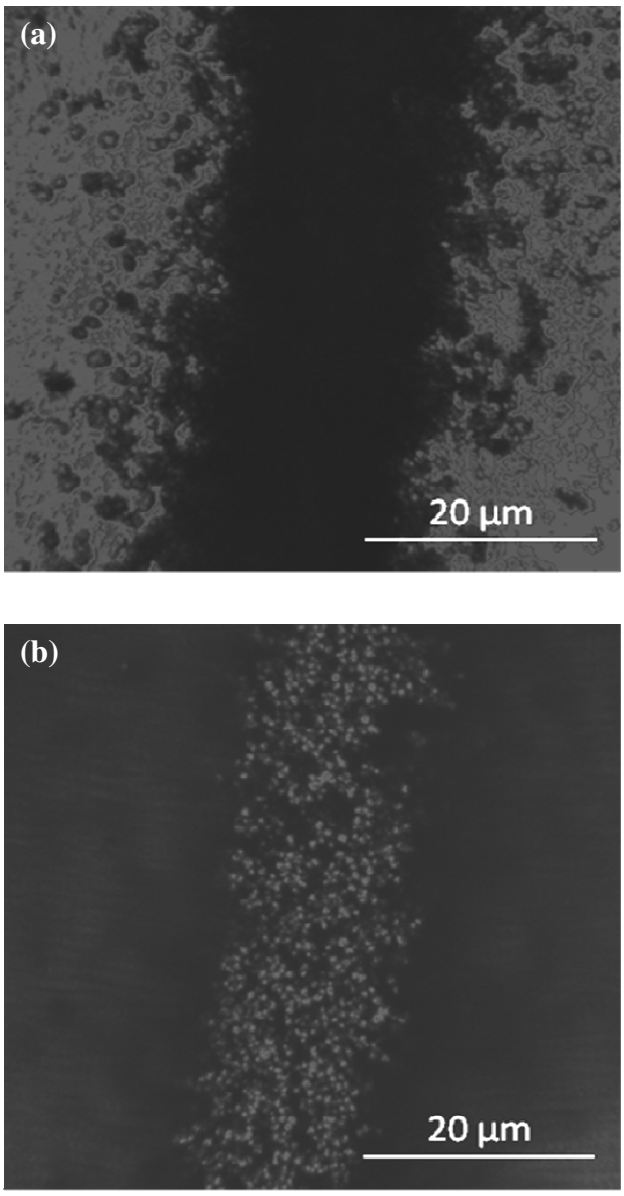

Figure 5.13. Tandem scanning micrographs of (a) base layer and (b) peak layer of the nHA patterns deposited at 40°C substrate temperature

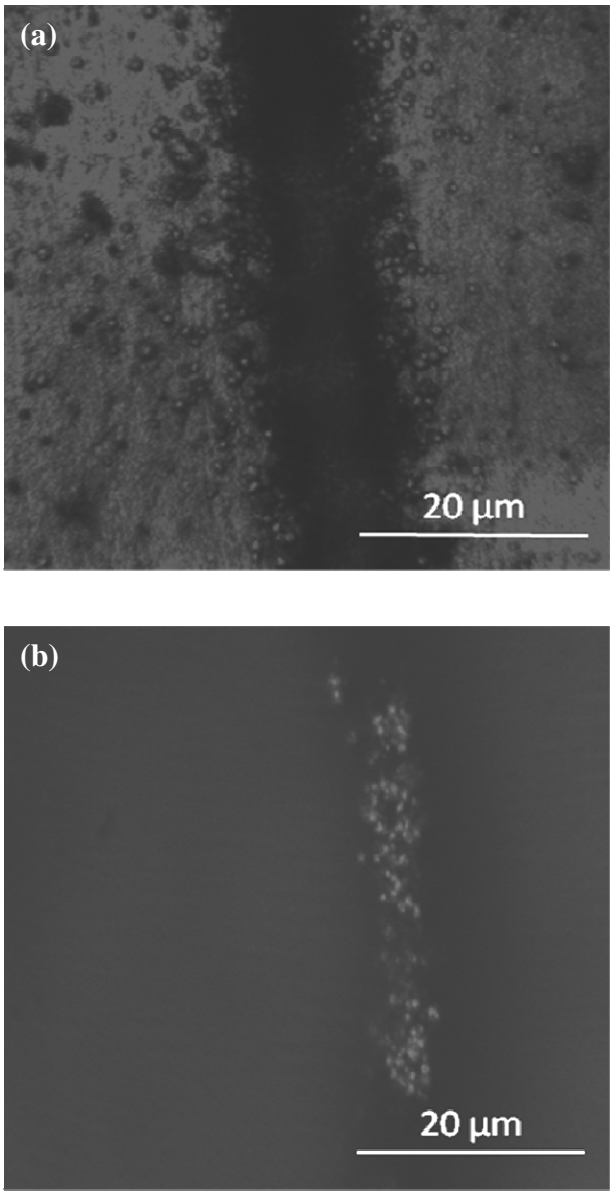

Figure 5.14. Tandem scanning micrographs of (a) base layer and (b) peak layer of the nHA patterns deposited at 80°C substrate temperature

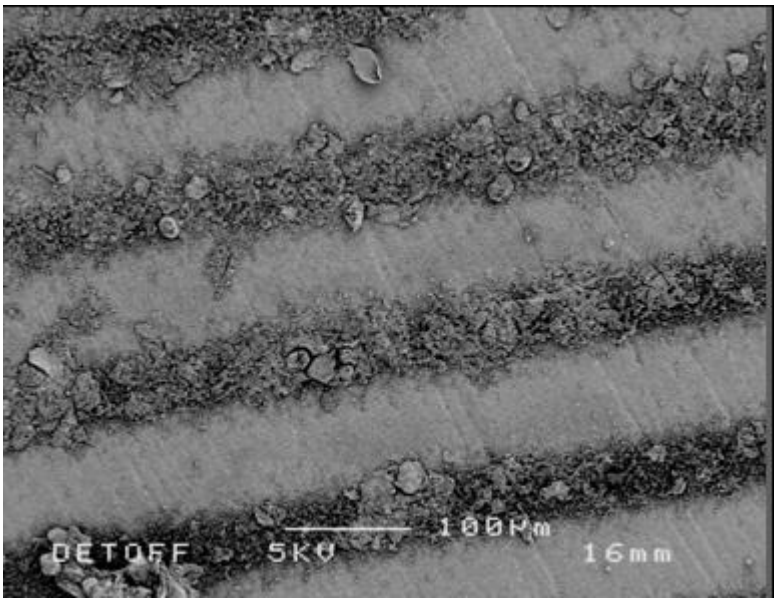

Figure 5.15. Scanning electron micrographs of HOB cells attached on the nHA patterns prepared when the substrate temperature is 40°C

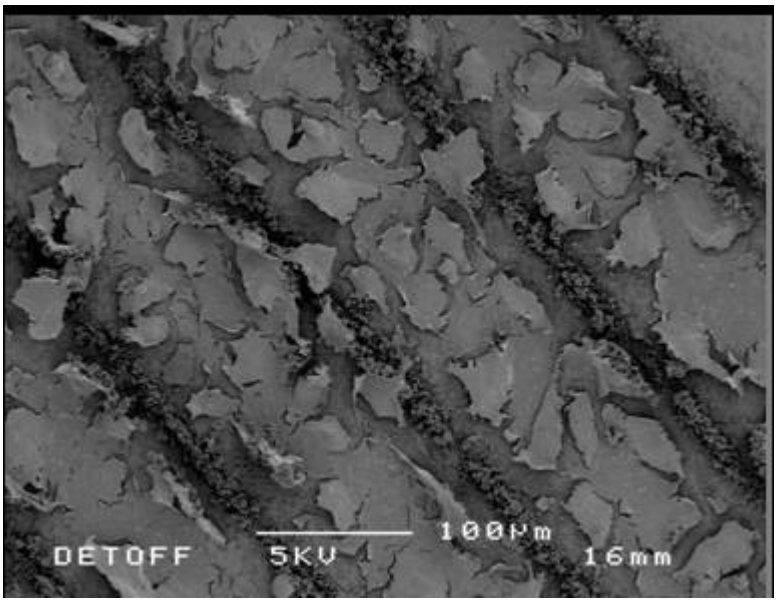

Figure 5.16. Scanning electron micrographs of HOB cells attached on the nHA patterns prepared when the substrate temperature is 80°C

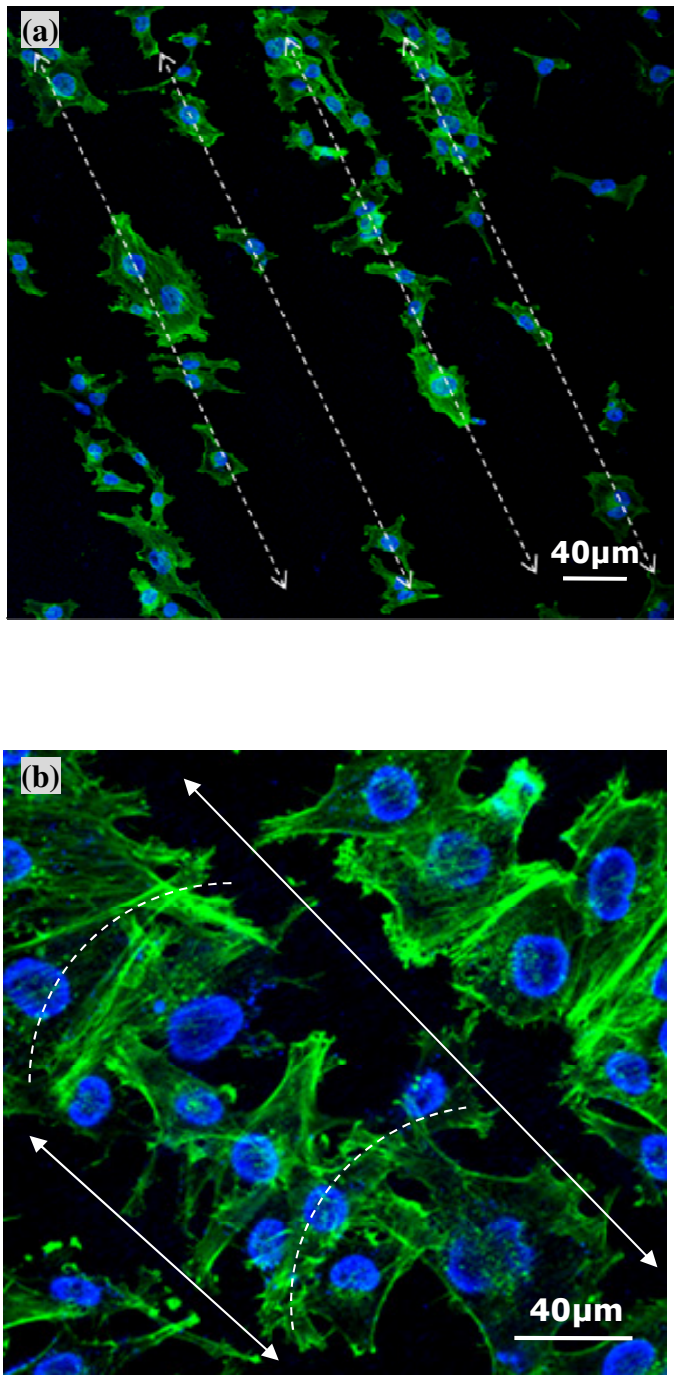

Figure 5.17. Confocal micrographs of actin cytoskeleton for HOB cells on nHA patterns sprayed at (a) 40°C substrate temperature and (b) 80°C substrate temperature

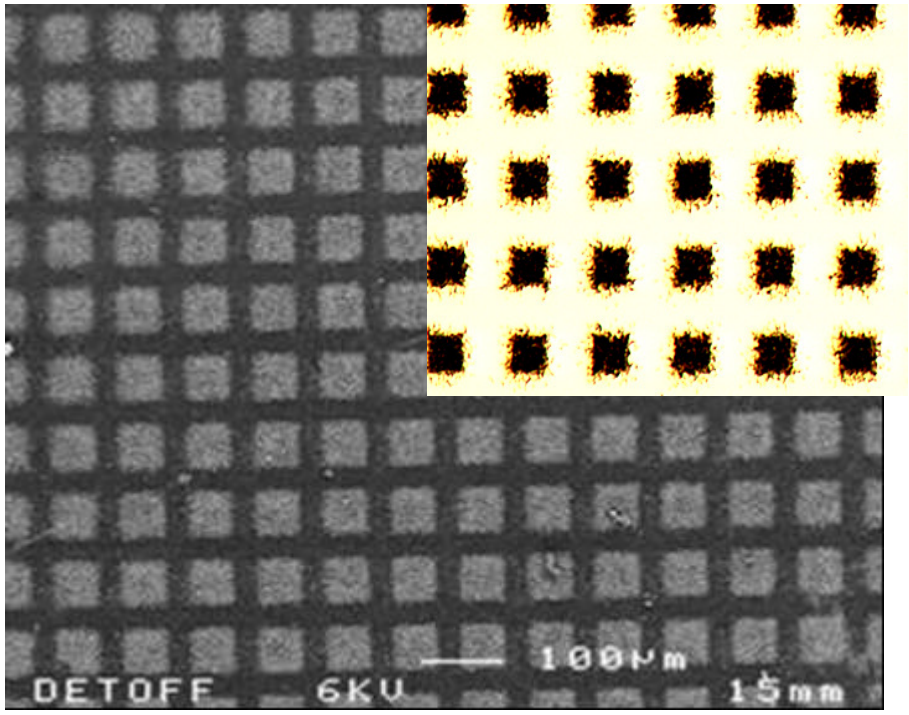

Figure 5.18. Scanning electron micrograph and optical microscopy image of square shape TiO_2 pattern

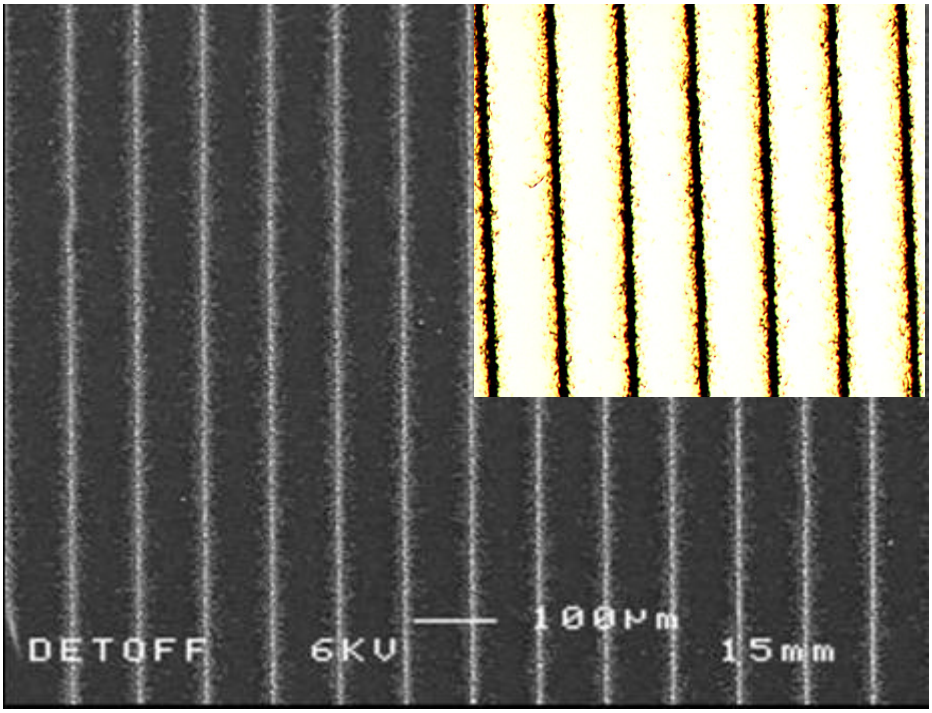

Figure 5.19. Scanning electron micrograph and optical microscopy image of line shape TiO_2 pattern

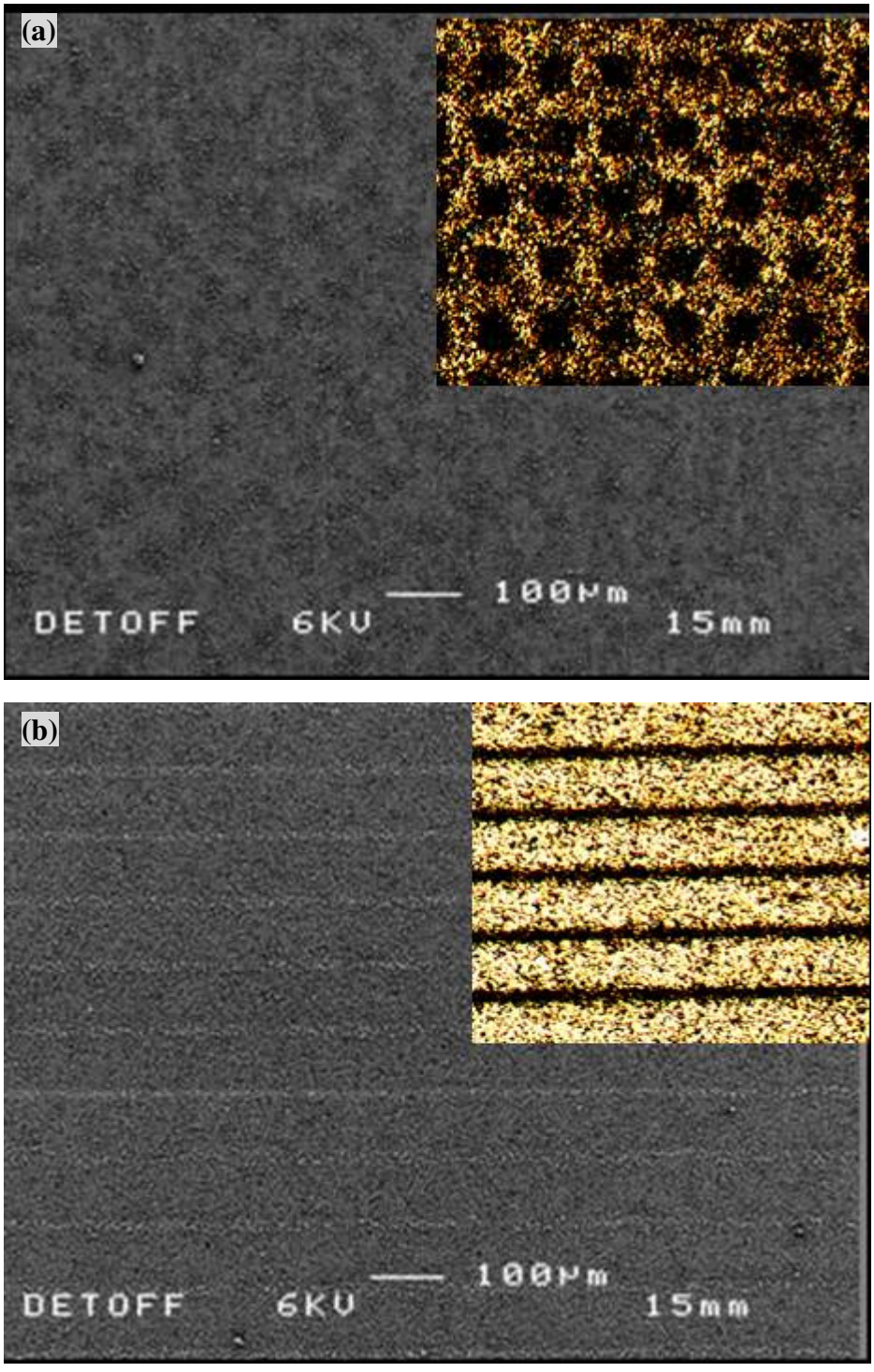

Figure 5.20. Scanning electron micrograph and optical microscopy image of (a) square-shaped TiO_2 interlocked HA coating and (b) line-shaped TiO_2 interlocked HA coating

Chapter 6

The influence of needle geometry on electrohydrodynamic spraying

Chapter 4 and **Chapter 5** have demonstrated the processing of nHA coating and patterns using electrohydrodynamic atomisation (EHDA) deposition and template-assisted electrohydrodynamic atomisation (TAEA) patterning. Dissimilarly to the previous investigations, the study discussed in this chapter is to uncover the influence of the needle geometry (one key factor in this technique) to the electrohydrodynamic processing and droplet relic size. The background of this study is introduced in first section of this chapter. The designs of the needle with different geometries and experimental method are described in the following section. Subsequently, the cone-jet spraying phenomena and droplet relic size distributions achieved using electrohydrodynamic processing setup with different needles are shown, explained and discussed. Furthermore, a line shape nHA pattern with high resolution prepared using the modified TAEA setup based on the previous findings is shown in the last section.

6.1 Background

For most coating procedures, the substances are deposited on the substrate as the relics in the form of droplets. Reducing the size of liquid droplets and relics is important for a wide variety of coating and deposition processes to create a desirable surface morphology and microstructure (Park *et al.*, 2007). This challenge provides the motivation for the research of the electrohydrodynamic jet-based techniques, which are based on a natural phenomenon that is the flowing liquid can form a conical shape

meniscus and jet at the tip of a nozzle, and break-up into fine droplets under a certain electric field. As introduced in the **Chapter 2**, this phenomenon was firstly reported by Zeleny in 1914. Following on his finding, Taylor gave a quantitative analysis on this phenomenon in 1964. He demonstrated that the form of the liquid cone under the electric field is due to the balance of electrostatic pressure and capillary pressure on the liquid surface. This characteristic of this phenomenon attracted the researchers' attention worldwide.

The term electrohydrodynamic atomization (EHDA) of liquids has therefore been coined to describe the form of atomization that occurs from a steady conical meniscus as opposed to other forms atomization. Later, a physical model was built to demonstrate the process of the cone-jet mode. Three phenomena were described within this mode (Hartman *et al*. 1999). The relationship of the main droplet size and the liquid flow rate in the cone-jet mode was also studied by Canan-Calvo in 1997. Not only the mechanism of cone-jet mode EHDA spraying, but also the effect of physical properties of the liquids on the EHDA processing in this mode was studied and well-documented in the past years. The research carried out by Gomez *et al*. (Gomez *et al.*, 1994), Canan-Calvo *et al*. Ganan-Calvo, 1997) and Hartman *et al.* (Hartman *et al.*, 1999) showed that liquid physical properties such as dc electrical conductivity, surface tension, viscosity and density play an important role in achieving a stable cone-jet mode.

Nowadays, based on the mechanism research of EHDA spraying, this process had been widely used for various applications in the past two decades. In 1989, it was first pioneered for mass spectroscopy of large biomolecules by Fenn (Fenn, 1989). Since then, It had been also used as a coating technique for a number of functional materials thin films preparation, e.g. $LiMn_2O4$ films (Zomeren *et al.*, 1994), $Pb(Zr, Ti)O_3$ (PZT)

films (Lu *et al.*, 2002), Zirconia films (Chen *et al.*, 1999). In the early years of this century, EHDA spraying was pioneered as a novel process technique for biomedical applications. For instance, it had been used to prepare a uniform bioceramic coating on metallic implant materials to enhance the bonding between the conventional implant and natural bone tissue (Leeuwenburgh *et al.*, 2003 and 2005). It was also developed into other techniques, such as 3-D printing and previously introduced template-assisted electrohydrodynamic atomization (TAEA) technique for preparing bioactive nHA patterns to up-regulate the cell behaviour. The research and development of EHDA spraying for other orthopaedic applications is still steadily on-going.

However, to the best of our knowledge, within the research work of EHDA spraying in the past years, there is no document to systematically demonstrate the influence of needle geometry, a vital factor for electric field which actually is the drive for the liquid to form cone-jet mode in EHDA spraying. Almost all the previously discussed studies and investigations are based on the capillary with regular geometry. It was only briefly mentioned recently that 'the geometry of the nozzle influences the cone-jet domain drastically' without giving any explanation on the influence phenomena and mechanism (Chen *et al.*, 1999). Therefore, to further understand electrohydrodynamic processing, this study will systematically investigate the influence of the nozzle orifice angle to the stability of cone-jet electrohydrodynamic mode and the relic size distribution produced under such mode, which is significant for the coating and patterning process for orthopedic applications.

6.2 Design and experimental method

6.2.1 Needle designs

The basic experimental setup is same to the previous sections as shown in **Figure 3.1**. It consists of a ground electrode and a needle (nozzle), which is connected to a high voltage supply. The liquid is fed to the needle by an infusion pump at a controlled flow rate. The flowing medium is subjected to an electrical field, which is generated by the applied voltage between the nozzle and ground electrode. However, five different stainless steel needles were designed for the study. The needle orifice angle varies from 15° to 90° as shown in **Figure 6.1**. The diameter of the needles is 1100 μm (inter Φ 800μm).

6.2.2 Method description

To investigate the influence of needle orifice angle to the stable cone-jet domain, pure ethanol was used as a spraying liquid, which has been previously proven to be an ideal solvent for EHDA spraying process. To further study the influence of the needle orifice angle to the relic size distribution, a TiO_2 sol of 2%wt was used during spraying for observing liquid relics on the optical microscope glass slide.

To investigate the influence of needle orifice angle on the stability of the cone-jet mode EHDA spraying of ethanol, the five different needles (15° - 90°) were used. In these experiments, the needle to substrate distance was kept at 40mm. Pure ethanol was

syringed to the needle; the flow rate was varied from 5 $\mu lmin^{-1}$ to the maximal value for stable cone-jet mode spraying. The applied voltage between the needle and the ground electrode was varied up to 7 kV to establish the modes of EHDA processing. At a chosen flow rate, the cone-jet mode was achieved within a range of applied voltage. Thus, the relationship between the applied voltage and flow rate for the suspension jetting in the cone-jet mode was established.

To investigate the influence of needle size on the deposited relic's size distribution, 2%wt TiO_2 sol was syringed into five different needles. The distance between needle tip and ground electrode and liquid flow rate were set at 40mm and $10\mu lmin^{-1}$, respectively. Microscope glass slides were used as substrates to collect the deposited relics. The collecting time was controlled at 10S. Three deposited glass slides were prepared for each needle. The collected relics on the glass slides were then observed and photographed using an optical microscope. 50 relics on each glass slide were stochastically chosen and measured.

6.3 Effect of the needle tip angle to cone-jet spraying mode

The achievement of the stable cone-jet mode is crucial for the electrohydrodynamic processing. In this section, the effect of needle tip angle to the cone-jet mode and stable cone-jet domain, in which the cone-jet mode can only be achieved and maintained, will be investigated.

6.3.1 The cone-jet mode phenomena achieved using different needles

As shown in **Figure 6.2**, using a conventional needle of which the orifice angle is 90°, the liquid cone forms symmetrically near the centre of the needle orifice (**Figure 6.2**e). However, it was observed an entirely different scenario while a needle with tilted outlet was used. As shown in **Figure 6.2**a-d, the liquid cone and jet asymmetrically form at needle exit. It is also observed that the diameter of the liquid cone dramatically reduced compared with the liquid cone formed at 90° needle orifice. As mentioned above, the stable cone-jet mode is due to the balance of the electric force, liquid surface tension, viscosity and liquid flow force. The drive for these different phenomena can only be the electric force difference at the needle tips. Logically, the electric field distribution at the needle tips has been changed due to the needle geometry modification. This phenomenon also demonstrates that the electric field, which drives the liquid to form the cone shape meniscus, is not symmetrical. It shows that electrical stress concentration occurs at the sharp tip of the tilted needle. The analysis and discussion regarding such mechanism will be discussed in **Section 6.3.3**.

6.3.2 The stable cone-jet domains achieved using different needles

When pure ethanol was used as the liquid for EHDA spraying, the relationship between applied voltage and flow rate is shown in **Figure 6.3**. The cone-jet mode can only be achieved when the flow rate and the applied voltage are in a distinctive domain. Therefore, the domain area can be seen as an important parameter for the stability of the cone-jet mode. For instance, higher flow rate up-limit shows the stable cone-jet mode can be achieved within a wider flow rate range, which facilitates the experimental control during the processing operation. As shown in **Figure 6.3**, the maximal liquid flow rates for achieving a stable cone-jet mode using the needle of 15°, 30°, 45°, 60°orifice angles are much higher than using needle of 90°. The needle of 45°angle shows the highest flow rate up-limit which is 68 μl/min. It's almost double the maximal

flow rate while using a conventional needle of 90° orifice angle. It was observed that the voltage range (ΔV between maximal applied voltage and minimal applied voltage) at a specific flow rate decreases with the decrease of the needle orifice angle.

6.3.3. Electric field concentration at the needle tip

The relationship between the needle orifice radius, which is equal to the liquid cone radius, and the magnitude of electric field was investigated by Jones and Thong in 1979 (Jones and Thong, 1979). It was assumed that irrespective of geometrical parameters, the same field conditions are required for the onset of the cone-jet mode. The potential V will then be related to the field required on the liquid surface situated at the capillary edge E, by

$$E = \frac{V}{f(R,h)} \quad \textbf{(Equation 6.1)}$$

Where f(R, h) is a geometrical function of the needle orifice radius R and the needle tip-to grounded plane distance h.

The best approximation (Smith, 1986) for this function was also given in this study as the following function (**Equation 6.2**).

$$f(R,h) = A \cdot R \cdot \ln(4h/R) \quad \textbf{(Equation 6.2)}$$

Where A is treated as an empirical constant ranging from 0.5 to 0.707.

Variation of the f(R, h) value with respect to the variation of R can be obtained from

$$\frac{df\ (R,h)}{dR} = A \cdot (\ln \frac{4h}{R} - 1) \quad \textbf{(Equation 6.3)}$$

When h >> R, which appears true during EHDA spraying, df(R, h)/dR > 0. This means that while the needle orifice radius reduces, the f(R, h) value will reduce and the electric field at the needle tip will increase accordingly when the same potential was applied.

This relationship was investigated based on an assumption that the needles used are of regular shape, of which the orifice angle is 90°. It seems to be not applicable in our case. However, if taking an in-sight analysis of the cone-jet mode formed using the tilted needles, a link bridging the needle orifice angle and an equivalent needle orifice radius could be observed.

As shown in **Figure 6.2**a-d, the images taken using the speed camera clearly showed that the cone-jet formed vertically towards the grounded plate. The diameter of liquid cones formed under different needles was found to increase significantly with the increase of the orifice angle. The minimal cone diameter and the maximal cone diameter appear while using 15°and 90°needle. To study and compare the electric field distribution at the needle tip, an equivalent needle of 90°orifice angle, highlighted in yellow in **Figure 6.4**, to form such liquid cones can be given to all the needles. By measuring the liquid conical meniscus diameter (equivalent nozzle diameter) when using ethanol as EHDA spraying liquid, the relationship between equivalent nozzle diameter and needle orifice angle was therefore investigated. As shown in **Figure 6.5**, the relationship is,

$L = AeBSin\alpha$ **(Equation 6.4)**

	Value
A	**83**
B	**3**

Where L is the equivalent nozzle diameter and α is the needle orifice angle.

Clearly, according to Equation 6.4, the equivalent nozzle diameter of the titled needle decreases with the needle exit angle, which means $L_{15°} < L_{30°} < L_{45°} < L_{60°} < L_{90°}$. Due to the relationship of the 90° needle radius and electric field as mentioned above, the electric field at the needle tips could easily be compared as shown in **Figure 6.6**. The relationship between the electric field and needle exit angle is given by the following equation.

$E = A\ Sin^2\alpha - B\ Sin\alpha + C$ **(Equation 6.5)**

	Value
A	**7**
B	**14**
C	**8**

Where E is the magnitude of electric field at the nozzle tip and α is the needle orifice angle.

Therefore, the electric field concentration occurs at the sharp needle tip. The relationship of the electric field near the needle tip is $E_{15°} > E_{30°} > E_{45°} > E_{60°} > E_{90°}$. There was indeed an electric field concentration occurred at the needle tip when the needle was titled to a small angle.

6.4 The influence of needle tip angle to relic size distribution

The previous section has demonstrated the impact of the needle tip angle on the stable cone-jet mode phenomena as well as its conditions. Based on this investigation, the

influence of the tip angle to the relic size distribution, which is well-known to be significant to the electrosprayed coating and pattern morphology and microstructures, will be introduced and discussed as follows.

6.4.1 The comparison of the relic size distribution

The relic size distribution diagrams were built using ethanol with 2%wt TiO_2 particles (**Figure 6.7**). The adding of small amount TiO_2 particles is to facilitate the observation and measurement of ethanol relics using optical microscope. It was found that the main relic size dramatically decreases with the decrease of needle orifice angle. The main deposited relic size varies between 2 to 3μm using a needle of 15° tip angle, which is nearly one third of the main relic size range when using 90°needle. The main relic size range shifts from the lowest range to the highest with the increase of the needle orifice angle.

Not only the main relic size range, but also the relic size distribution has been significantly influenced by the angular needle tip. As shown in **Figure 6.7**, the relics produced using the needle of 15° tip angle varied from 0-5 μm. However, while using a needle of 90° angle, the relics widely distributed from 2-11 μm, which nearly doubles the relic distribution range when using 15° angular needle. To quantitatively analyse this evolution, the polydispersivity index, which stands for the standard deviation percentage of the mean value, was calculated on each relic range produced using different needles. As shown in **Figure 6.8**, when the needle tip angle was increased from 15° to 90°, the standard deviation over the mean relic size grows from 18.7 to 28.1 percents. This means that the encountered electric concentration due to the needle tip angle not only decreases the main size of relics, but also narrows the relic size

distribution. The relics produced using a needle of 15° angular needle showed the lowest polydispersivity index, and therefore the most uniform relics in size among all the angular needles, which is needed for prepared uniform coatings with low roughness using EHDA deposition.

6.4.2 Mechanism of the tip angle influence on relic size distribution

This phenomenon is mainly due to the electric field concentration previously demonstrated. As the same flow rate was set for the relics collection, more electric charge presented at the liquid cone form at the sharper needle tip. Subsequently, the liquid cone formed a jet and then break-up into droplets. Accordingly, the droplets, which emitted from the cone-jet mode formed under a needle of smaller orifice angle, were of more electric charge in the droplets' liquid surface. It is much easier for such highly charged droplets to reach the Reyleigh charge limit (Section 2.4.3.4), as showed in the following formula.

$$q_R = 8\pi(\gamma\varepsilon_0 r_d^3)^{1/2} \quad \textbf{(Equation 6.6)}$$

Where q_R is the Rayleigh charge limit (C), γ is the surface tension, ε_0 is the dielectric constant of the vacuum and r_d is the droplet radius (m)

When the charge on a single droplet reaches the limit, droplet is divided into two or more smaller droplets by the over-limited charge. Therefore, when using the needle of 15°, droplet fission occurred and smaller liquid droplets were therefore formed under concentrated electric field as shown in the cartoon (**Figure 6.9**).

6.4.3 The influence of the electric field asymmetry

As previously demonstrated, the concentration of the electric field at the shape needle tip significantly reduces the liquid droplet main relic size and size distribution during EHDA spraying. The electric field distribution at the needle tip is also found to have a big impact on the stable cone-jet domain and the relic size distribution. As shown in **Figure 6.10**a, the cone-jet mode achieved using a needle of 550 μm diameter and 90° exit angle exhibits the same shape and dimension as the cone-jet mode achieved using a needle of 1100 μm diameter and 45°. The diameter of the equivalent needle of the needle of 45°, which is 550μm, is similar to the needle used. According to the previous demonstration, the magnitude of electric field at the tips of both needles should be similar. However, the stable cone-jet domain has been significantly enlarged by using the needle of 45° exit angle as shown in **Figure 6.10**b. The maximal flow rate for stable cone-jet mode using the titled needle was found to be more than 4 times higher than using a needle of the same dimension of its equivalent needle. Furthermore, the relic size distributions, which were achieved using the same process parameters (10μl/min flow rate, 40mm needle-substrate distance) but different needles, were found to dramatically differ as shown in **Figure 6.11**. The main ethanol relic size sprayed using the needle of 1100 μm diameter and 45° exit angle was between 3 μm to 6 μm, which is much lower than using another. A much wider relic size range results when using the needle of 550 μm diameter and 90° exit angle.

Therefore, apart of the electric field concentration, the asymmetry of electric field occurred due to the needle with modified tip angle is also significant for the enhanced stability of the stable cone-jet mode as well as the reduced droplet size during EHDA spraying.

6.5 The influence of needle geometry to TAEA patterning resolution

In **Chapter 5**, it was shown that the smaller relics due to the droplet non-spreading effect can lead to the nHA patterns with high resolution. Here, the TAEA patterning setup with a needle of 1100 diameter and 15° tip angle was used to prepared a line shape nHA pattern under the same patterning conditions with **Section 5.3**, which are 6 %wt nHA suspension, 20 μl/min flow rate, 20 mm substrate-needle distance, ambient processing temperature.

As shown in **Figure 6.12**, the HA line pattern of 7.8 μm in width with the standard deviation of 1.1 μm was successfully achieved. This is nearly one tenth in diameter of the patterns previously reported (**Section 5.3**). The less dense morphology present in the nHA pattern was due to the short spraying time (15s) and small relics formed during the process. However, over all, the resolution of TAEA has been dramatically improved. This study shows the potential of these findings for further optimizing the electrohydrodynamic processing.

6.6 Summary

The study showed that the flow rate up-limit for stable cone-jet mode largely increases while reducing the needle orifice angle from 90° . The EHDA spraying using 45° showed the highest flow rate up-limit. More importantly, the main liquid relic size and size distribution were found to significantly decrease with the decrease of the needle tip angle. This is the first systematic study of the needle geometry influence to

electrohydrodynamic processing. The mechanism of such impact was also uncovered in this study. It further proves that the electrohydrodynamic route is a promising technique for processing advanced materials with complex structures. This is an important fundamental step forward of employing electrohydrodynamic coating and patterning technique to prepare the novel depositions and patterns for the orthopaedic applications.

Figures

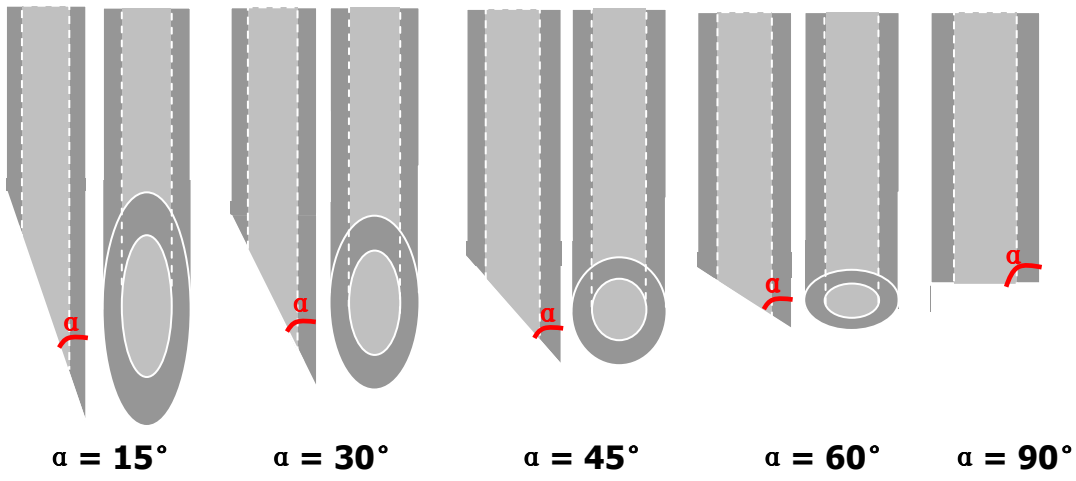

Figure 6.1. Schematic diagram of the needle designs for electrohydrodynamic processing

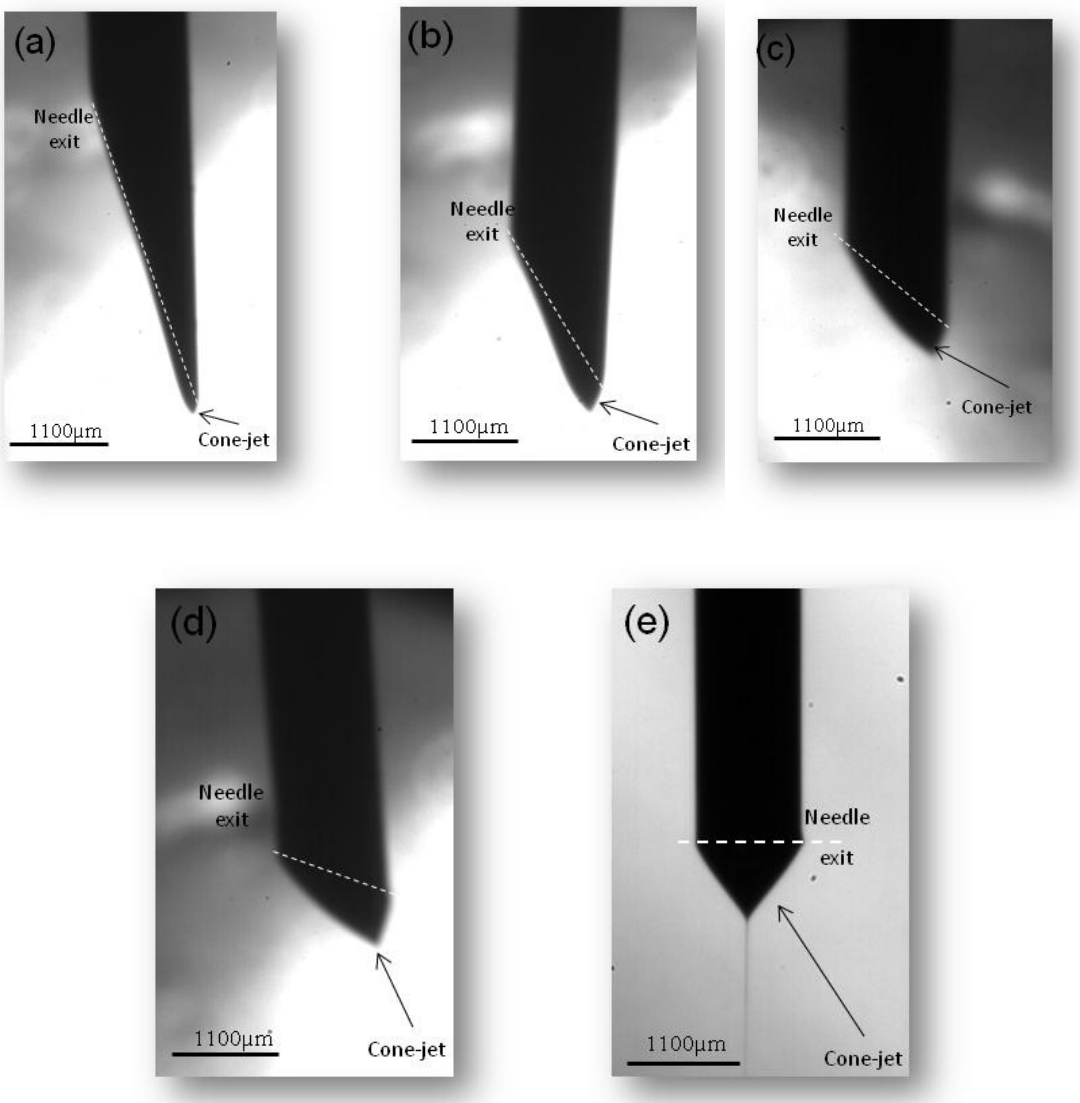

Figure 6.2. . The high-speed camera images of cone-jet mode achieved using the needles of (a)15°, (b)30°, (c)45°, (d)60° and (e)90°.

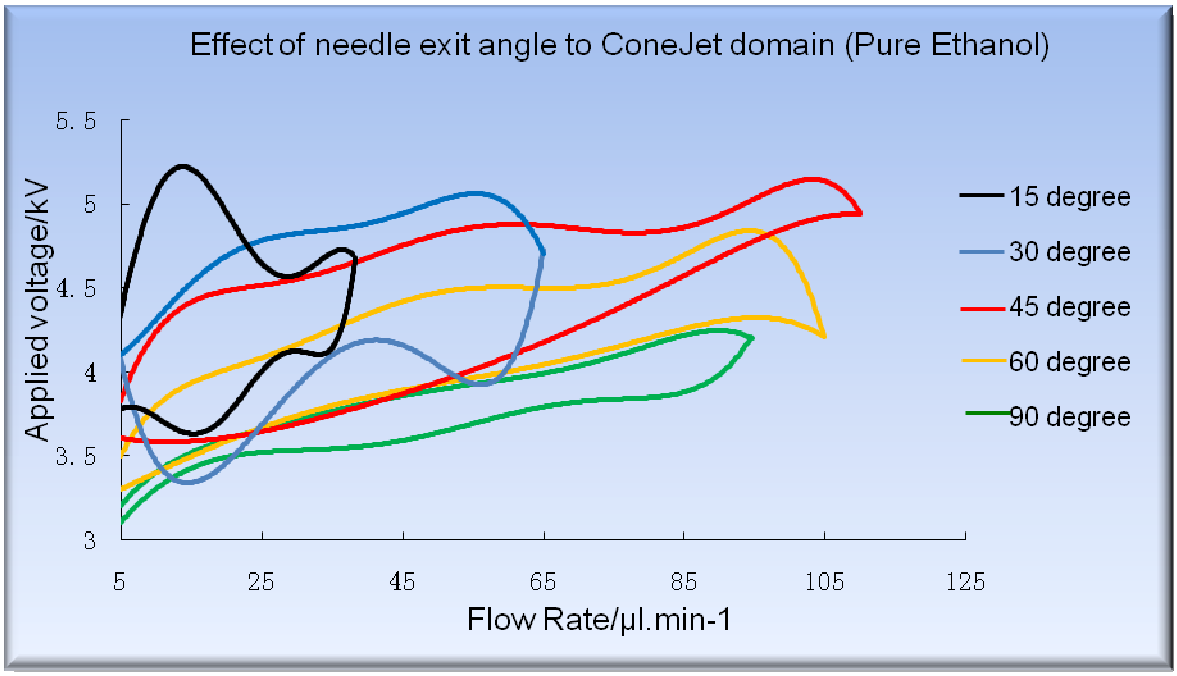

Figure 6.3. Relationship between applied voltage and flow rate for achieving stable cone-jet mode using ethanol

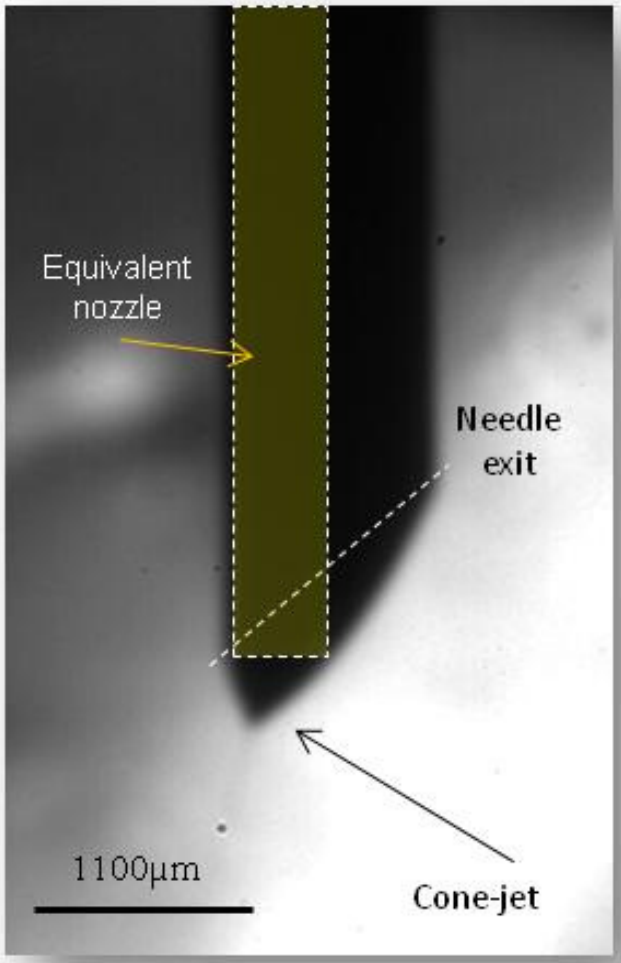

Figure 6.4. The schematic illustration of the equivalent needle when using the titled needle for EHDA spraying

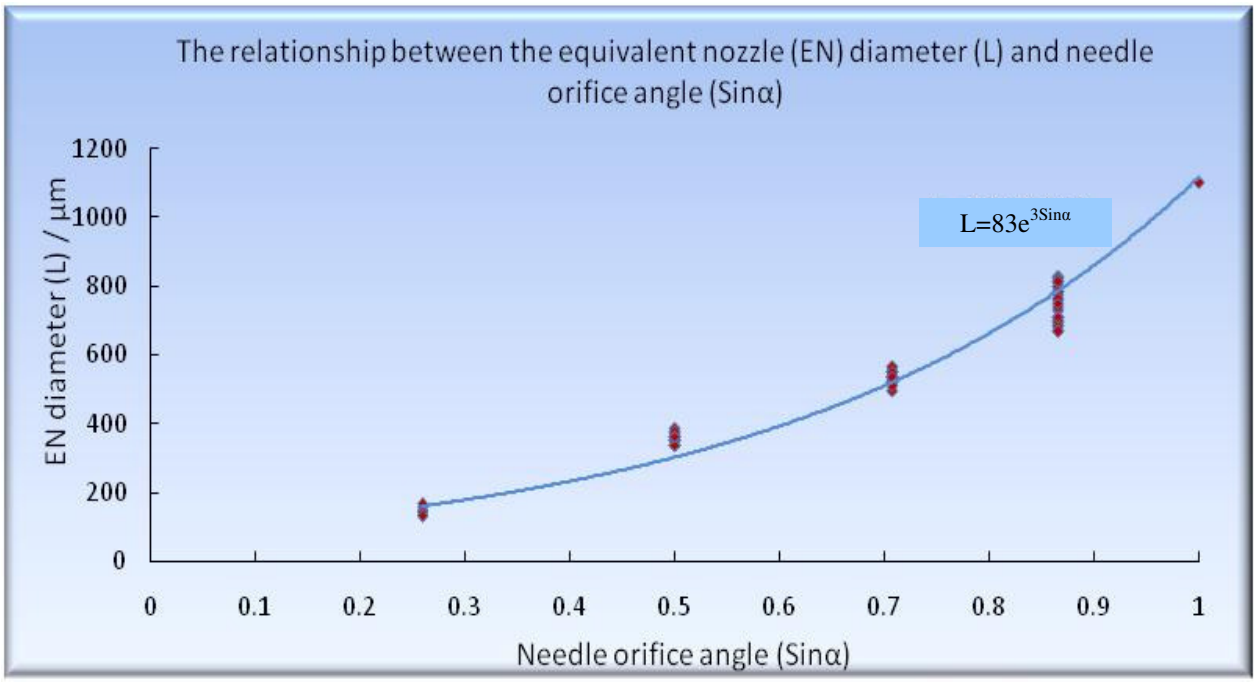

Figure 6.5. The relationship between the equivalent nozzle diameter and needle orifice angle when using ethanol as spraying liquid

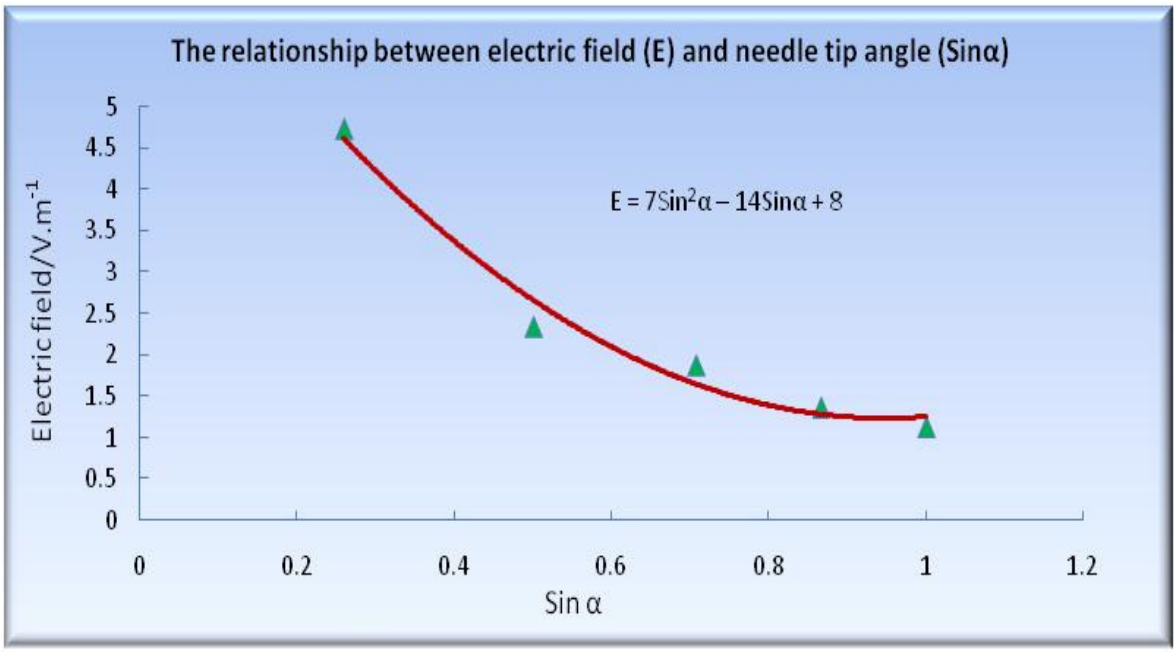

Figure 6.6. The relationship between the magnitude of electric field at the needle tip and needle tip angle

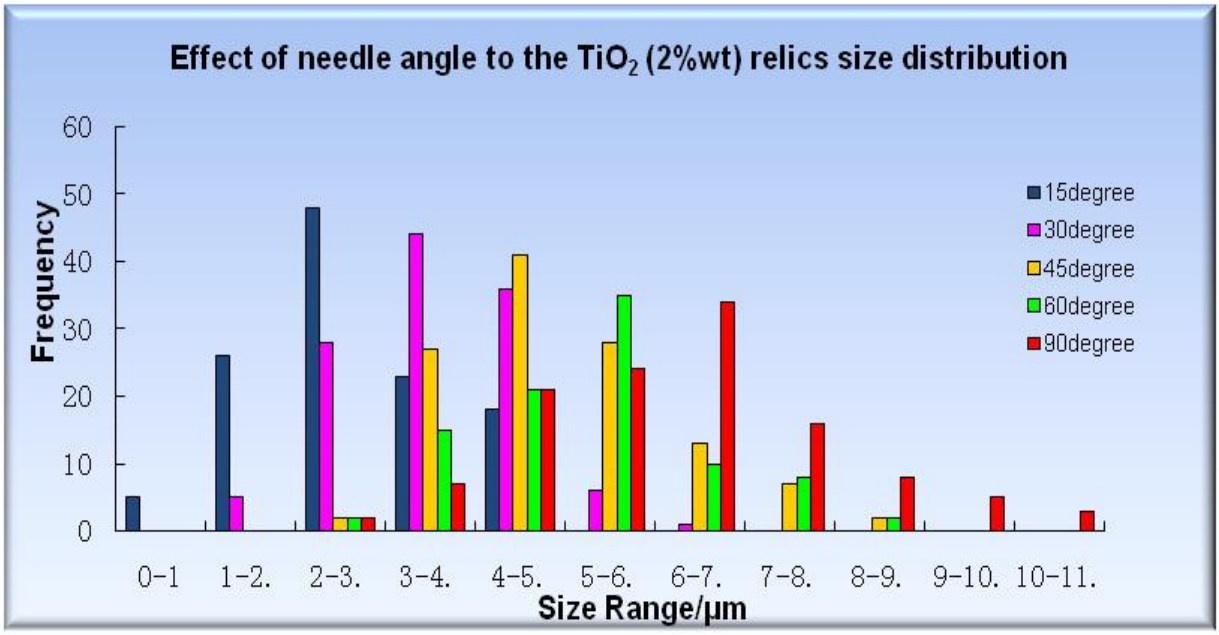

Figure 6.7. Ethanol relics' size distribution using electrohydrodynamic spraying with different nozzle designs.

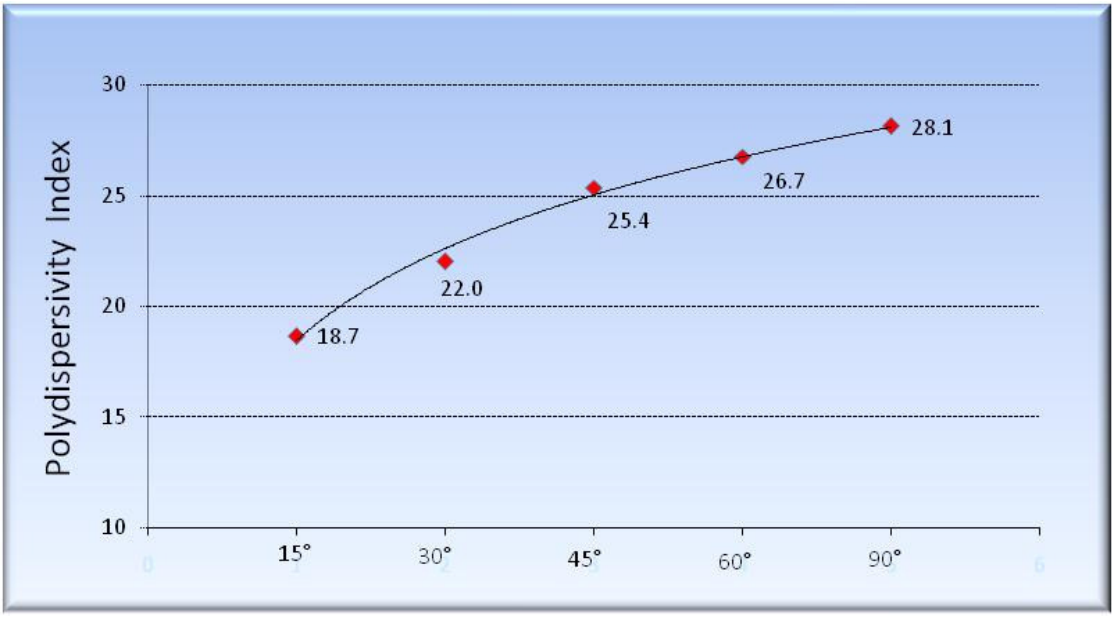

Figure6.8. The relationship between the polydispersivity index of relics' size and needle tip angles.

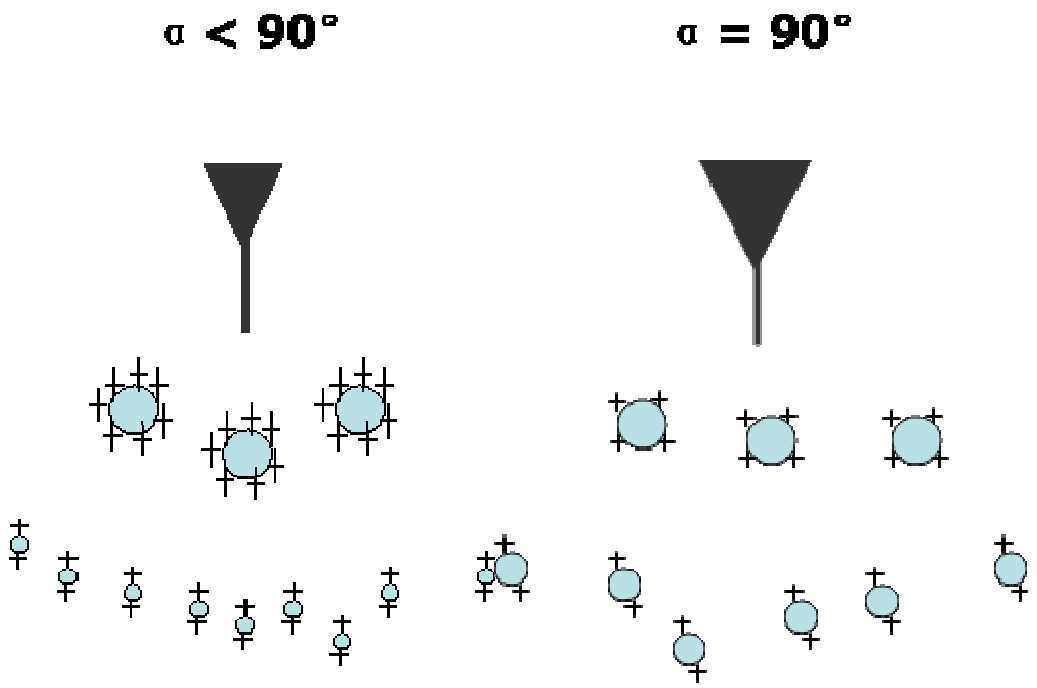

Figure 6.9. Schematic illustration of the highly charged droplets' fission process under (a) titled needle and (b) untitled needle.

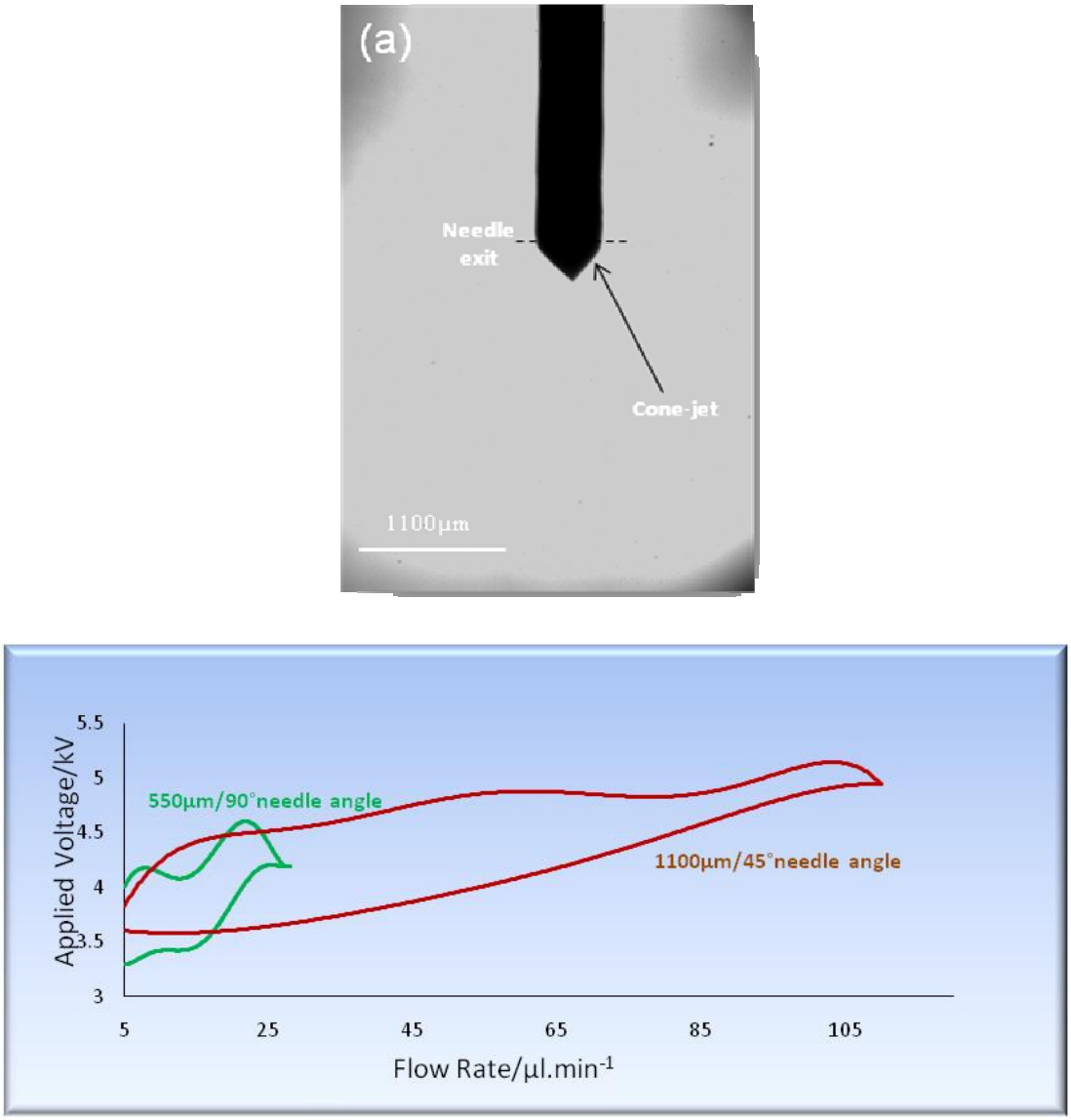

Figure 6.10. The speed camera image of cone-jet mode achieved using a needle of 550µm diameter and 90° needle exit angle, and (b) Relationship between applied voltage and flow rate for achieving stable cone-jet mode using ethanol as spraying liquid

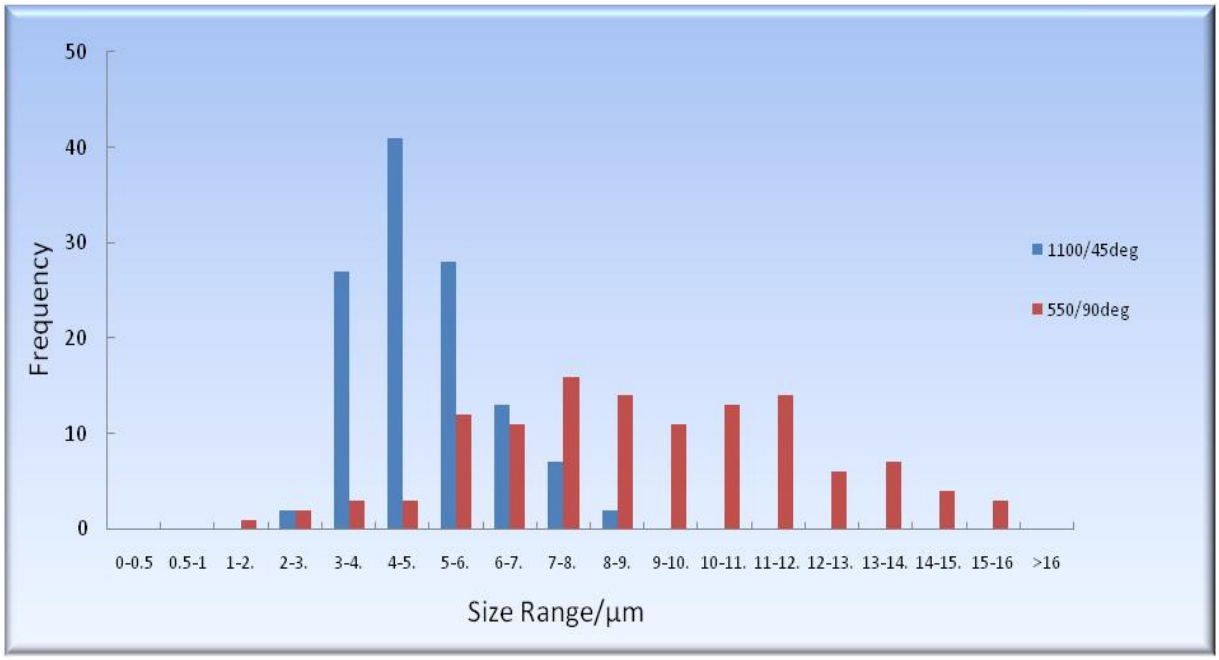

Figure 6.11. Ethanol relics' size distribution sprayed using two needles

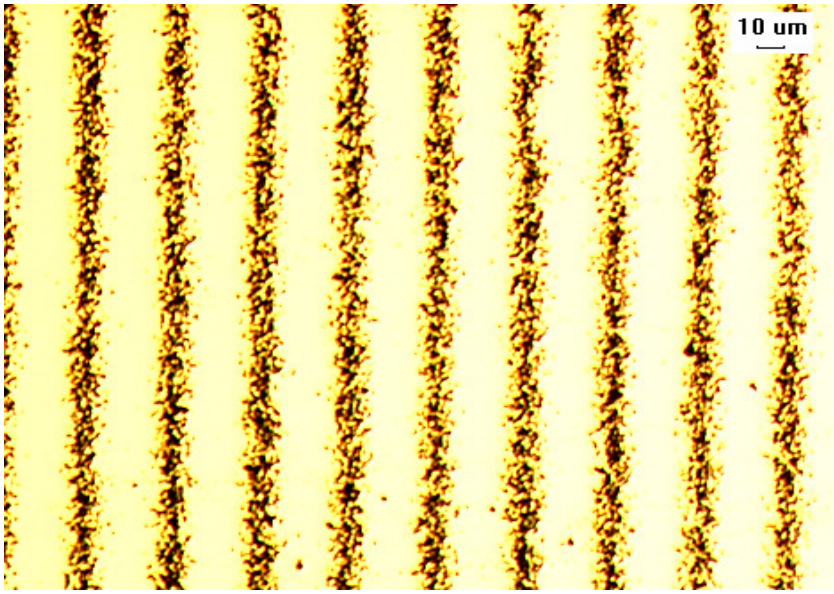

Figure 6.12. Line shape nHA patterns prepared using TAEA spraying with the needle of 15° orifice angle and 1100μm diameter

Chapter 7

Conclusions and Future work

7.1 Conclusions

The conclusions of this research are summarized as follows:

1. The electrohydrodynamic atomisation spraying of 60-70 nm sized hydroxyapatite suspension (6 %wt) in cone-jet mode was studies. It was found that the distance between the needle and substrate, the suspension flow rate, the applied voltage and the spraying time had a very significant influence on the morphology of the nHA coating prepared.

2. Due to the significant impact of the needle-substrate distance during the EHDA deposition process, a study of the effect of such parameter to the nHA coating morphology was carried out. 20 mm was recognized to be the optimal distance for nHA coating preparation using electrohydrodynamic deposition.

3. A study of the influence of the suspension flow rate to the nHA coating morphology was carried out. A 3-D was built up in this study to optimise this parameter. When the needle-substrate distance was set at 20 mm, the uniform and fully covered nHA coating was achieved on Ti substrate at 20 μl/min flow rate. When the flow rate used was set below this value, the nHA coating presented less coverage. However, when the flow rate set was above this value, the coating prepared using EHDA technique was of rough morphology.

4. A map of applied voltage – flow rate for achieving the stable cone-jet electrohydrodynamic mode was constructed to study the applied voltage range for nHA deposition preparation. It was found that the stable cone-jet mode can only be achieved when the flow rate and the applied voltage are in a distinctive envelope. When the flow rate is set 20 μl/min, the applied voltage needs to be between 4.3 – 5.2 kV. Otherwise, the unstable cone-jet mode or the multi-jet mode will be in operation.

5. It was found that the HA coating surface exhibited uniform topography and no cracks were observed when the spraying time was controlled 30s. When the spray time increased to 60s, overall, the uniformity still prevailed and the coating was crack-free, although aggregation of HA nanoparticles was found occasionally. Small cracks were observed in the coating when the spray time was 300s. If the spraying time was much longer (20 minutes), cracking increased appreciably.

6. When the spraying time was 15s, the thickness of the nHA deposit is approximately 1.4μm, along with the increase of the spraying time, the thickness of the deposit was found to increase to 4.9±0.3μm at 120s. Therefore, as expected, the deposit thickness is directly proportional to the spraying time.

7. The heat treatment study was carried out on the nHA coatings prepared under the previous processing parameters. It was found that the heat treatment in argon can prevent the Ti substrate oxidation while improving the coating adhesion. It was found that the coating morphology can be changed due to the microstructure evolution during the heat treatment. However, the marginal change of the surface roughness did not influence the osteoblast proliferation and cell morphology from the observation during the *in-vitro* study.

8. A new method for the creation of micro-scale defined topographies with bioactive material, namely template-assisted electrohydrodynamic atomisation (TAEA) spraying, was developed from EHDA process. A comparative study was carried out during the investigation. It was found that the in-direct ground electrode configuration was more efficient for the patterning process.

9. A range of square shape, hexagonal shape and line shape nHA patterns with uniform micro-scale topographies was successfully prepared on the titanium substrates when different templates were using during TAEA processing. The width/diameter of the patterns can be controlled with 100 μm.

10. A study of the TAEA patterning resolution improvement was carried out. It was found that the suspensions solvent has significant impact on the droplets spreading. Ethanol has been chosen to be suitable solvent for patterning nHA topographies due to its high evaporability. Furthermore, the substrate temperature was found to be an effective way to limit the nHA suspension droplets spreading effect. A line shape nHA pattern with the width controlled within 15 μm has been successfully achieved using TAEA patterning process when the substrate was heated up to 80°C. This is significant improvement compare to the previously achieved nHA patterns.

11. An *in-vitro* study using human osteoblast was carried out to characterise the biological properties of the nHA patterned Ti plates. It was found that the cells were effectively guided on the patterned surfaces rather than random cellular attachment on the uniform coatings. It was also observed that the cellular attachment was significantly influenced by the line shape pattern dimensions. The osteoblast cells were able to attach

and grow on the nHA pattern when the patterns width and height were 32 μm and 6 μm, respectively. In contrast, the cells were guided to bridge the nHA patterns on the nHA patterned surface when the patterns width and height were 15 μm and 16 μm, respectively.

12. Combining the chemical and mechanical bonding enhancement concept, a TiO_2 interlocked nHA coating was successfully achieved on a titanium substrate via the combination of EHDA deposition and TAEA patterning.

13. The needle geometry effect on the electrohydrodynamic processing was investigated. It was found that the flow rate upper-limit for stable cone-jet mode largely increases while reducing the needle orifice angle from 90° . The EHDA spraying using 45° showed the highest flow rate upper-limit.

14. The main liquid relic size and size distribution were found to significantly decrease with the decrease of the needle tip angle. When the needle with the 1100 μm diameter but 15° tip angle was used for electrohydrodynamic process, the main nHA relics were successfully controlled within 3 μm. The reason of this significant size reduction is the electric field concentration occurs due to the needle with sharp tip used. Furthermore, the relationship between the needle angle and electric field magnitude was also established.

15. Based on this finding that the liquid relics can be significantly reduced via changing the needle geometry, a line shape nHA pattern with the width controlled within 10 μm was successfully prepared using TAEA with the 15° tip angular needle. This is a crucial step forward to the research of TAEA patterning technique.

7.2 Future work

Based on the research conducted and the outcome of this research, several aspects of future work are recommended as follows:

During this research, pure ethanol was used as the liquid carrier for the nHA suspension for the nHA coating preparation using electrohydrodynamic processing. More solvents should be tried to prepare the nHA suspension to find out the most optimal raw materials for the coating processing. Furthermore, due to the advantage of sol compared to the suspensions, such as aging stability, nHA sols with different concentrations are strongly suggested to be prepared and studied. The nHA uniform coating on the metal implant materials could be further improved by using the nHA sols for EHDA deposition process.

Nano-size hydroxyapatite suspension has been used to prepared nHA coatings on Ti substrate in this research. The research should move to other novel bioceramics coatings preparation using electrohydrodynamic processing. Silicon substituted hydroxyapatite (SiHA) should be synthesised, characterised and electrosprayed on the implant metals. The optimal processing parameters, including substrate-needle distance, spraying time, flow rate and applied voltage, should be investigated in the future work. Furthermore, the *in-vitro* studies need to be carried out on nHA and SiHA coated Ti plates to compare the biological properties of these two materials, such as cell proliferation, differentiation. Furthermore, other antibacterial elements, e.g. Ag, could be mixed or substituted in the nHA suspension. The novel coating prepared using this kind of raw materials could lead to a new generation multifunctional implant materials.

The bonding strength of the bioactive coating to the substrate is also crucial for its implantation applications. Therefore, it's suggested that a systematic characterisation of the adhesion strength of the nHA and SiHA coatings needs to be carried out after the biological characterisation and comparison. Since the shear strength of the coatings is particularly significant to implant materials, scratching test technique should be used as the characterisation method. The shear strength of both coatings should be compared with the commercial plasma-sprayed HA coated titanium implant.

Based on the previous characterisation study, the enhancement of the adhesion strength of the nHA and SiHA coatings should be studied and investigated. Two approaches are suggested here for this investigation. One is the direct post heat treatment. The appropriate heat treatment conditions need to be investigated. In this study, two factors, which are substrate oxidation and hydroxyaptite decomposition at high temperature, need to be taken in account while enhancing the adhesion strength. Another approach suggested is to add an adhesive buffer layer between the substrate and the coating. TiO_2 is suggested for this buffer layer. However, a systematic investigation should be carried out to find out the optimal buffer layer material, buffer layer thickness, and again the heat treatment conditions. Furthermore, the adhesion enhanced nHA or SiHA coatings should be scratch tested and compared with the commercially used plasma-sprayed HA coated titanium implant materials.

TAEA patterning technique was proven to be a powerful tool for creating defined implant surface topographies for guiding cellular orientation in this research. However, more investigations should be carried out to quantitatively study the relationship between the nHA pattern dimensions and the cell orientation. It could be significant to

fully understand the osteoblast cell behaviour on the defined surface structures. The nHA patterned Ti with different pattern heights, pattern widths and pattern distances should be prepared using TAEA processing and cultured in the cell media for a short period to investigate the initial cell attachment and orientation.

Based on the investigation of the TiO_2 interlocked hydroxyapatite (HA) coatings, more work is suggested to carried out to further develop this novel bonding enhanced HA coated implant material. The studies suggested include the characterization of the shear strength of a range of TiO_2 interlocked hydroxyapatite different coated titanium plates and a comparative study with the current commercial HA coated implant materials. Six tasks should be included in this study, designing and ordering templates from provider, optimised TiO_2 pillar shape determination, optimised pillar width/diameter determination, pillar height investigation and hydroxyapatite top layer thickness determination. During these investigations, the commercially used plasma-sprayed HA coated Ti implant will be used as a control to compare the new coating practise.

The optimized shape of the interlocking pillars for the coating shear strength, a major factor for successful implantation surgery and the healing, needs to be investigated. A range of different copper templates with different grid shapes and dimensions should be designed and ordered. since such parameters of the template are crucial for the quality, shape and dimension of the TiO_2 interlocking pillars. It has been confirmed that such specific designs can be manufactured by Agar Scientific Ltd. Three or more TiO_2 interlocking layers with different shapes but similar width/diameter will be patterned on the Ti substrates at the same height. The patterned surfaces will then coated with HA coatings of the same thickness. The shear strength of the coated specimens will be tested using a micro-scratch testing machine (CSM Ltd., Switzerland). This will

determine the preferable interlocking pillar shape. A preliminary was carried out to test the interfacial shear strength of the EHDA sprayed HA coated Ti substrate. The results proved that such CSM micro-scratch testing machine can be used to precisely characterise the shear strength of the HA coating of a few micrometers.

After determining the interlocking pillar shape, the width/diameter W (Figure 4c) of the pillars will be varied a using different template. The relationship between the interfacial shear strength of the TiO_2/HA coating and its defining parameters, such as the interlocking pillar height, width and HA coating thickness should be systematically investigated. Furthermore, a comparative study with the current commercially used plasma-sprayed HA coated implant materials is also suggested to be carried to further prove the advantages of this novel TiO_2-interlocked-HA coated implant materials. Again, the pillar height and HA coating thickness T remain the same during the process. The shear strength test of these specimens will be also measured as in the previous TiO_2 pillar shape determination. To study the height of the interlocking pillars effect to the shearing resistance of the coated Ti implant materials, a range of different patterning periods will be using to achieve various pillar heights on titanium substrates. Subsequently, the patterned titanium plates will be coating with HA (same thickness). These specimens will then be scratch tested to determine the crucial TiO_2 pattern height of the composite coating. Based on the previous investigations, fixing the previously investigated pattern parameters, the similar procedure will be carried out to investigate the optimized HA coating thickness for the enhanced shear strength. In the mean time, the commercially used HA plasma-coated implant materials will be subjected to the shear strength test using the same instrument for the comparison with new TiO_2-interlocked-HA coated implant materials.

The relationship between the needle geometry and liquid droplet relic size distribution was investigated in this research. The relics were controlled within 3 μm. Certainly it's not the end. More studies should be carried out to further decrease the relic size and the size standard deviation. It's suggested to combine the substrate temperature factor with the needle geometry influence in the future study. This could be significant to improve the EHDA deposition and TAEA patterning techniques to a more advanced level.

More nHA coatings and patterns should be prepared using electrohydrodynamic processing with the modified needles. This study is to systematically investigate the relationship between the reduced nHA relics and nHA coatings or patterns surface morphology. The influence of the nHA relic size to the nHA coating density and surface roughness should be explored in the investigation. Furthermore, the precision of the TAEA patterning should be further improved. This study is to prove the significance of these fundamental findings to the processing, and further improve EHDA deposition technique and TAEA patterning technique to process more advanced implant materials for the biomedical applications.

References

- A -

Ahmad Z., Huang J., Edirisinghe M.J., Jayasinghe S.N., Best S.M., Bonfield W., Brooks R.A. and Rushton N. (2007) Electrohydrodynamic print-patterning of nano-hydroxyapatite. *J. Biomed. Nanotech*. 2, 201-207.

Albrektsson T. and Wennerberg A. (2004) 'Oral implant surfaces: Part 1 – review focusing on topographic and chemical properties of different surfaces and in vivo responses to them', *Int. J. Prosthodont*. 17, 536-543.

Aoki H. (1991), Science and medical application of hydroxyapatite. Japanese Association of Apatite Science: Takayama Press System Centre Co., Tokyo.

de Aza P.N., Guitian F., Merlos A., Tmayo E.L. and de Aza S. (1996), Bioceramics – simulated body fuid interfaces: pH and its influence of hydroxyapatite formation, *J. Mater. Sci.: -Mater Med.* 14, 419-425.

- B -

Behiri J.C. and Bonfield W. (1984), Fracture mechanics of bone – The effects of density, specimen thickness and crack velocity on longitudinal fracture, *J. Biomech.* 17, 25-34.

Berndt C.C., Haddad G.N., Farmer A.J.D. and Gross K.A. (1990), Review article: thermal spraying for bioceramic applications. *Mater Forum* 14, 161-173.

Besra L. and Liu M. (2007), A review on fundamentals and applications of electrophoretic deposition (EPD). *Prog. Mater. Sci*. 52, 1-61.

Bett J.A.S., Christner L.F. and Keith Hall W. (1967), Studies of the hydrogen held by solids XII: Hydroxyapatite catalysts. *J. Am. Chem. Sc*. 89, 5535-5541.

Black J. and Hastings G. (1998), Handbook of biomaterial properties, London, Chapman and Hall.

van Blitterswijk C.A., Grote J.J., Koerten H.K. and Kuijpers W. (1986), Biological performance of beta-whitlockite. A study in the noon-infected and infected rat middle ears, *J. Biomed. Mater. Res.* 20, 1191-1217.

van Blitterswijk C.A., Grote J.J., Kuijpers W., Blokvan Hoek C.J.G. and Daems W.T. (1985), Bioreactions at tissue/hydroxyapatite interfaces, *Biomaterials* 6, 243-251.

van Blitterswijk C.A., Hesseling S.C., Grote J.J., Koerten H.K. and de Groot, K. (1990), The biocompatibility of hydroxyapatite ceramics. A study of retrieved human middle ear implants, *J. Biomed. Mater. Res.* 24, 433-443.

Bonfield W. and Grynpas M.D. (1977), Anisotropy of Young's modulus of bone, *Nature*, 270, 453-454.

- C -

Capello W.N., D'Antonio J.A., Feinberg J.R. and Manley M.T. (1997), Hydroxyapatite-coated total hip femoral components in patients less than fifty year old, *Journal of Bone and Joint Surgery* 79(A), 1023-1029.

Chen C.H., Emond M.H.J., Kelder E.M., Meester B. and Schoonman J. (1999), Electrostatic sol-spray deposition of nanostructured ceramic thin films. *J. Aerosol. Sci.* 30, 959-967.

Choy K.L. (2002) Innovative processing of films and nanocrystalline powders, U.K., Imperial College Press.

Cleries L., Fernandez-Pradas J.M., Sardin G. and Morenza J.L. (1998) Dissolution behaviour of calcium phosphate coatings obtained by laser ablation. *Biomaterials* 19, 1483-1487.

Cloupeau M. and Prunet-Foch B. (1989), Eletrostatic spraying of liquids in cone-jet mode, *J. Electrostatics* 22,135-139.

Cloupeau M. and Prunet-Foch B. (1990), Eletrostatic spraying of liquids: Main functioning modes, *J. Electrostatics* 25,165-184.

Coathup M.J., Blunn G.W., Flynn N., Williams C. and Thomas N.P. (2000), A comparison of bone remodelling around hydroxyapatite-coated, porous-coated and grit-blasted hip replacements retrieved at post-mortem, *Journal of Bone and Joint Surgery* (82B), 118-123.

Cotell C.M., Chrisey D.B., Grabowski K.S., Sprague J.A. and Gossett C.R. (1992), Pulsed laser deposition of hydroxyapatite thin-films on Ti-6Al-4V. *J. Appl. Biomater*. 3, 87-93.

Currey J.D. (1981), What is bone for? Property-function relationships in bone, in Mechanical properties of Bone, edited by Cowin S.C., New York, 13-26

Currey J.D. (1983), Biological Composites, in: Handbook of Composite: Kelly A., Mileiko S.T. (Eds.). Amsterdam, New York: Elsevier Science Publisher B.V., Vol.4, pp.501-563.

Curtis A. and Wilkinson C. (1997) Topographical control of cells. *Biomaterials* 18, 1573-1583.

- D-

Denissen H.W., de Groot K., Makkes P.C., van der Hooff A. and Klopper P.J. (1980), Tissue response to sense apatite implants in rats. *J. Biomed. Mater. Res.* 14, 713-721.

Deram V., Minichiell C., Vannier R.N., Le Maguer A., Pawlowski L. and Murano D. (2003), Microstructural characterisation of plasma sprayed hydroxyapatite coatings, *Surf. Coat. Technol*. 166, 153-159.

Dickson R.J. and Lepoutre P. (1997) Mechnical interlocking in coating adhesion to paper. *Tappi. J*. 80, 149-157.

van Dijk K., Schaeken H.G., Wolke J.C.G., Maree C.H.M., Habraken F.H.P.M., Verhoeven J. and Jansen J.A. (1995a), Influence of discharge power level on the properties of hydroxyapatite film deposited on Ti6Al4V with RF magnetron sputtering, *J.Biomed. Mater. Res.* 29, 269-276.

van Dijk K., Schaeken H.G., Wolke J.C.G., Maree C.H.M., Habraken F.H.P.M., Verhoeven J. and Jansen J.A. (1995b), Influence of Ar pressure on RF magnetron-sputtered Ca5(PO4)3OH layers. *Surface and coating Technology* 76-77, 206-210.

van Dijk K., Schaeken H.G., Wolke J.C.G. and Jansen J.A. (1996), Influence of annealing temperature on RF magnetron sputtered calcium phosphate coatings, *Biomaterials* 17, 405-410.

Ding S.J., Ju C.P. and Chen Lin J.H. (1999), Immersion behaviour of RF magnetron-assisted sputtered hydroxyapatite/titanium coatings in simulated body fluids, *J. Biomed. Mater. Res.* 47, 551-563.

- F -

Fenn J.B., Mann M., Meng C.K. and Wong S.F. (1989), Electrospray ionization for mass spectroscopy of large biomolecules. *Science* 246, 64-71.

Fujiu T. and Ogino M. (1984), Difference of bone bonding behaviour among surface active glasses and sintered apatite, *J.Biomed. Mater. Res.,* 18, 845-859.

Funada T. and Joseph D.D. (2002), Viscous potential flow analysis of capillary instability. *Int. J. Multiphase. Flow* 28, 1459-1478.

- G -

Ganan-Calvo A.M., Lasheras J.C., Davila J. and Barrero A. (1994), The electrostatic spray emitted from an electrified conical meniscus. *J. Aerosol. Sci*. 25, 1121-1142.

Ganan-Calvo A.M., Ripoll A.B. and Rubino C.P. (1996), The equilibrium shapes of liquid menisci emitting liquid and charges in steady cone-jet mode. *J. Aerosol. Sci.* 27, S187-S188.

Ganan-Calvo A.M., Davila J. and Barrero A. (1997), Current and droplet size in the electrospraying of liquids. Scaling laws. *J. Aerosol. Sci*. 28, 249-275.

Ganan-Calvo A.M. (1999), The surface charge in electrospraying: Its nature and its universal scaling laws. J. Aerosol. Sci. 30, 863-872.

Gao X., Jensen R.E., Li W., Deitzel J., McKnight S.H.. Gillespie J.W. (2008) Effect of fiber surface texture created from silane blends on the strength and energy absorption of the glass fiber/epoxy interphase. *J. Compos. Mater*., 42, 513-534.

Garciasanz F.J., Mayor M.B., Arias J.L., Pou J., Leon B. and PerezAmor M. (1997) Hydroxyapatite coatings: a comparative study between plasma-spray and pulsed laser deposition techniques. *J. Mater. Sci. –Mater. Med.* 8, 861-865.

Gledhill H.C., Tuner I.G. and Doyle C. (1999), Direct morphological comparison of vacuum plasma sprayed and detonation gun sprayed hydroxyapatite coatings for orthopaedic applications. *Biomaterials* 20, 315-322.

Gomez A. and Tang K. (1994), Charge and fission of droplets in electrostatic sprays. *Phys. Fluids.* 6, 404-414.

Grace J.M. and Marijnissen J.C.M. (1994), A review of liquid atomization by electrical means. *J. Aerosol. Sci.* 25, 1005-1019.

de Groot K., Geesink R., Klein C.P., Serekian P. (1987), Plasma sprayed coatings of hydroxyapatite**.** *J. Biomed. Mater. Res*. 21, 1375-1381.

de Groot K. and LeGeros R.Z. (1998), Significance of porosity and physical chemistry of calcium phosphate ceramic, *Bioceramics* 9, 523-529.

de Groot K., Wolke J.G.C., Jansen J.A. (1998), Calcium phosphate coatings for medical implants. *Proc. Inst. Mech. Eng. Part H-J. Eng. Med.* 212, 137-147.

Gross K.A. and Berndt C.C. (1997), The amorphous phase is plasma sprayed hydroxyapatite coatings, *Bioceramcis* 8, 361-366.

Gross K.A., Chai C.S., Kannangara G.S.K., Ben-Nissan B. and Hanley L. (1998), Thin hydroxyapatite coatings via sol-gel synthesis, *J. Mater. Sci.: Mater. Med*. 9, 839-843.

- H -

Haman J.D., Lucas L.C. and Crawmer D. (1995), Characterisation of high-velocity oxy-fuel combustion sprayed hydroxyapatite. *Biomaterials* 16, 229-237.

Hartman R.P.A., Borra J.P., Brunner D.J., Marijnissen J.C.M. and Scarlett B. (1999a), The evolution of electrohydrodynamic sprays produced in the cone-jet mode, a physical model. *J. Electrostatics*. 47, 143-170.

Hartman R.P.A., Brunner D.J., Camelot D.M.A., Marijnissen J.C.M. and Scarlett B. (1999b), Electrohydrodynamic atomization in the cone-jet mode physical modelling of the liquid cone and jet. *J. Aerosol. Sci*. 30, 823-849.

Hartman R.P.A., Brunner D.J., Camelot D.M.A., Marijnissen J.C.M. and Scarlett B. (2000), Jet break-up in electrohydrodynamic atomization in the cone-jet mode, *J. Aerosol. Sci.* 30, 823-849.

Hench L.L. (1991), Bioceramics-from concept to clinic. . *J. Am. Ceram. Soc.* 74, 1487-1510.

Hench L.L. (1998), Bioceramics. *J. Am. Ceram. Soc.* 81, 1705-1728.

Huang J., Best S.M., Bonfield W., Brooks R.A., Rushton N., Jayasinghe S.N. and Edirisinghe M.J. (2004a) In vitro assessment of the biological response to nano-sized hydroxyapatite. *J. Mater. Sci: Mater. Med.* 15, 441-445.

Huang J., Jayasinghe S.N., Best S.M., Edirisinghe M.J., Brooks R.A. and Bonfield W. (2004b) Electrospraying of a nano-hydroxyapatite suspension. *J. Mater. Sci.* 39, 1029-1032.

Hulshoff J.E.G., van Dijk K., van der Waerden J.P.C.M., Wolke J.G.C., Ginsel L.A. and Jansen J.A. (1995), Biological evaluation of the effect of magentron sputtered Ca/P coatings on osteoblast-like cells *in-vitro. J. Biomed. Mater. Res*. 29, 967-975.

- I -

Ito A., Maekawa K., Tsutsumi S., Ikazaki F. and Tateishi T. (1997), Solubility product of OH-carbonated hydroxyapatite, *J. Biomed. Mater. Res*. 36, 522-528.

- J -

Jansen J.A., van der Waerden J.P.C.M., van der Lubbe H.B.M. and de Groot K. (1990), Tissue response to percutaneous implants in rabbits, *J. Biomed. Mater. Res*. 24, 295-307.

Jaworek A. and Krupa A (1996), Generation and characteristics of the precession mode EHD spraying. *J. Aerosol Sci*. 27, 75-77.

Jaworek A. and Krupa A. (1999a), Classification of the modes of EHD spraying. *J. Aerosol. Sci.* 30, 873-893.

Jaworek A. and Krupa A. (1999b), Jet and drops formation in electrohydrodynamic spraying of liquids. A systematic approach. *Experiment in Fluids.* 27, 43-52.

Jayadevan K.P. and Tseng T.Y. (2002), Composite and multilayer ferroelectric thin films: processing, properties and applications. *J. Mater. Sci.: Mater. Electro*. 13, 439-459.

Jayasinghe S.N. and Edirisinghe M.J. (2002), Effect of viscosity on the size of relics produced by electrostatic atomization. *J. Aerosol. Sci.* 33, 1379-1388.

Jayasinghe S.N. and Edirisinghe M.J. (2004), Electrically forced jets and microthreads of high viscosity dielectric liquids. *J. Aerosol. Sci.* 35, 233-243.

Jones A.R. and Thong K.C. (1971), The production of charged monodisperse fuel droplets by electrical dispersion. *J. Phys. D: Appl. Phys.* 4, 1159-1166.

- K -

Kim H.W., Koh Y.H., Li L.H, Lee S. and Kim H.E. (2004), Hydroxyapatite coating on titanium substrate with titania buffer layer processed by sol-gel method. *Biomaterials* 25, 2533-2538.

Klein C.P.A.T., Wolker J.C.G., de Blieck-Hogervorst J.M.A. and de Groot K. (1994), Features of calcium phosphate plasma-sprayed coatings: An *in-vitro* study. *J. Biomed. Mater. Res*. 28, 961-967.

Kukla R. (1997), Magnetron sputtering on large scale substrates: An overview on the state of the art, *Surface Coating Technologies* 93, 1-6.

- L -

Leeuwenburgh S., Wolke J., Schoonman J., Jansen J. (2003), Electrostatic spray deposition (ESD) of calcium phosphate coatings. *J. Biomed. Mater. Res. A* 66, 330-334.

Leeuwenburgh S., Wolke J., Schoonman J. and Jansen J. (2005), Influence of deposition parameters on chemical properties of calcium phosphate coatings prepared by using electrostatic spray deposition. *J. Biomed. Mater. Res. A* 74, 275-284.

LeGeros R.Z. (1993), Biodegradation and bioresorption of calcium phosphate ceramics, *Clinical Materials* 14, 65-68.

LeGeros R.Z. and LeGeros J.P. (1993), Dense hydroxyapatite, in *An Introduction to Bioceramics*, edited by L.L. Hench and J. Wilson, World Scientific, Singapore, 139-180.

Lewandrowski K., Bondre S.P., Wise D.L. and Trantolo D.J. (2003), Enhanced bioactivity of a poly (propylene fumarate) bone graft substitute by augmentation with nano-hydroxyapatite. *Bio-Med. Mater. Eng.* 13, 115-124.

Lewis G. (2000), Hydroxyapatite-coated bialloy surface: Current status and future challenges. *BioMed. Mater. Eng.* 10, 157-188.

Li F., Feng Q.L., Cui F.Z., Li H.D. and Schubert H. (2002), A simple biomimetic method for calcium phosphate coating. *Surf. Coat. Tech.* 154, 88-93

Li H., Khor K.A. and Cheang P. (2007), Adhesive and bending failure of thermal sprayed hydroxyapatite coatings: Effect of nanostructures at interface and crack propagation phenomenon during bending. *Eng. Fract. Mech*. 74. 1894-1903.

Li X., Huang J. and Edirisinghe M.J. (2007), Electrohydrodynamic coating of metal with nano-sized hydroxyapatite. *J. Biomed. Mater. Eng.* 17, 335-346.

Lide D.R. (1990), Handbook of Chemistry and Physics, 71st Ed., Boca Raton, Florida: CRC Press, pp.8-39.

Lin C.M. and Yen S.K. (2005), Characterisation and bond strength of electrolytic HA/TiO_2 double layers for orthopaedic applications. *J. Mater. Sci. -Mater. Med.* 16, 889-897.

Lopez-Herrera J.M. Canan-Calvo A.M. and Perez-Saborid M. (1999), One dimensional simulation of the breakup of capillary jets of conducting liquids. Application to E.H.D. spraying. *J. Aerosol Sci*. 30, 895-912.

- M -

Mavis B., Tas A.C. (2000), Dip coating of calcium hydroxyapatite on Ti-6Al-4V substrates. *J. Am. Cer. Soc* 83, 989-991.

McPherson R., Gane N., Bastow T.J. (1995), Structural characterization of plasma-sprayed hydroxylapatite coatings, *J. Mater. Sci. –Mater. Med* 6, 327-334.

Mimura K., Watanabe K., Okawa S., Kobayashi M. and Miyakawa O. (2004), Morphological and chemical characterization of the interface of a hydroxyapatite-coated implant. *Dental. Mater. J.* 23, 353-360.

Mutoh M., Kaieda S. and Kamimura K. (1979), Comvergence and disintegration of liquid jets induced by an electrostatic field. *J. Appl. Phy.* 50, 3174-3179.

Myer K, (2003), Standard handbook of biomedical engineering and design, McGraw-Hill.

- N -

Nagorynti V.S. and Bezrukov V.I. (1980), Droplet emission in an electrostatic field. *Magn Gidrodin USSR* 16, 111.

- O -

Oktar F.N., Meydanoglu O., Goller G., Agathopoulos S., Rocha G., Ozyegin S., Peker I., Eruslu N. and Kayali S. (2006), Sintering effects on mechanical properties of hydroxyapatite-titanium dioxide (HA-TiO_2) composites, *Key. Eng. Mater.* 309-311, 355-358.

Oliveira A.L., Alves C.M. and Reis R.L. (2002), Cell adhesion and proliferation on biomimetic calcium-phosphate coatings produced by a sodium silicate gel methodology. *J. Mater. Sci.: Mater. Med.* 13, 1181-1188.

Ong J.L., Bessho K., Cavin R. and Carnes D.L. (2002), Bone response to radio frequency sputtered calcium phosphate implants and titanium implants *in-vivo. J. Biomed. Mater. Res*. 59, 184-190.

Ong J.L., Lucas L.C., Lacefield W.R. and Rigney E.D. (1992), Bone response to radio frequency sputtered calcium phosphate implants and titanium implants *in-vivo. J. Biomed. Mater. Res.* 59, 184-190.

Ozeki K., Yuhta T., Aoki H., Nishimura I. and Fukui Y. (2001), Push-out strength of hydroxyapatite coated by sputtering technique in bone. *Bio-Med. Mater. Eng*. 11, 63-68.

Ozeki K., Yuhta T., Fukui Y., Aoki H. and Nishimura I. (*2*002), A functionally graded titanium/hydroxyapatite film obtained by sputtering. *J. Mater. Sci. -Mater. Med.* 13, 253-258.

- P -

Park J.B. (1987), Biomaterials Science and Engineering, New York, London: Pleum Press.

Park J.U., Hardy M., Kang S.J., Barton K., Adair K., Mukhopadhyay D.K., Lee C.Y., Strano M.S., Alleyne A.G., Georgiadis J.G., Ferreira P.M. and Rogers J.A. (2007), High-resolution electrohydrodynamic jet printing. *Nature Materials* 6, 782-789.

Posner A.S., Perloff A. and Diorio A.F (1958), Refinement of the hydroxyapatite structure. *Acta Crystallography* 11, 308-309.

- R -

Radin S.R. and Ducheyne P. (1992), Plasma spraying induced changes of calcium phosphate ceramic characteristics and the effect on *in vitro* stability, *J. Mater. Sci. – Mater. Med* 3, 33-42.

Rayleigh F.R.S. (1978), On the instability of jets. *Proc. London. Math. Soc*. 10, 4-13.

Reilly D.T. and Burstein A.H. (1975), The elastic and ultimated properties of compact bone tissue, *Journal of Biomechanics* 8, 393-405.

Reuter H. (1991), Sol-gel processes. *Adv. Mater*. 3, 258-259.

da Rocha S. S., Adabo G. L., Vaz L. G. and Henriques G. E. P. (2005), Effect of thermal treatments on tensile strength of commercially cast pure titanium and Ti-6Al-4V alloys, *J. Mater. Sci. –Mater. Med*. 16, 759-766.

Roop Kumar R. and Wang M. (2002), Functionally graded bioactive coatings of hydroxyapatite/titanium oxide composite system. *Mater.lett.* 55, 133-137.

Rosa A.L., Beloti M.M. and van Noort R. (2003), Osteoblastic differentiation of cultured rat bone marrow cells on hydroxyapatite with different surface topography. *Dent. Mater.* 19, 768-772.

Ruddell D.E., Thompson J.Y. and Stoner B.R. (2000), Mechanical properties of a dental ceramic coated by RF magnetron sputtering, *J. Biomed. Mater. Res*. 51, 316-320.

Rulison A.J. and Flagan R.C. (1994), Electrospray atomization of electrolytic solution, *J. Colloid. Interface. Sci.* 167, 135-145.

- S -

Smith D.P.H. (1986), The electrohydrodynamic atomization of liquids. *IEEE Trans. Industry. Appl*. IA-22, 527-535.

Sun L.M., Berndt C.C., Gross K.A. and Kucuk A. (2001), Material fundamentals and clinical performance of plasma-sprayed hydroxyapatite coatings: A review. *J. Biomed. Mater. Res.* 58, 570-592.

- T -

Tan J. and Saltzman W.M. (2004), Biomaterials with hierarchically defined micro- and nanoscale structure. *Biomaterials* 25, 3593-3601.

Tanashi M., Yao T., Kokubo T., Minoda M., Miyamoto T., Nakamura T. and Tamamuro T. (1994), Apatite coating on organic polymers by a biomimetic process, *J. Am. Ceram. Soc. 77*, 2805-2808.

Tang K. and Gomez A. (1995), Generation of monodisperse water droplets from electrosprays in a corona assisted cone-jet mode. *J. Colloid. Interface. Sci*. 175, 326-332.

TaoW., Hideke A., Junta H. and Jun Hee L. (2007), RF-magnetron sputtering technique for producing hydroxyapatite coating film on various substrates. *Bio. Med. Mater. Eng*. 17, 291-297.

Taylor G. (1964), Disintegration of water drops in an electric field. *Proc. R. Soc. A-Math. Phys. Eng. Sci* 280, 383-397.

Teoh S.H. 2004, Engineering materials for biomedical applications, Singapore, World scientific

Toth J.M., Lynch K.L. and Devine J.R. (1995), Mechanical and biological characterisation of calcium phosphates for use as a biomaterials, in: Encyclopedic Handbook of Biomaterials and Engineering, 2, pp.1466-1501.

Tsui Y.C., Doyle C. and Clyne T.W. (1998), Plasma sprayed hydroxyapatite coatings on titanium substrates. Part I: Mechanical properties and residual stress levels, *Biomaterials* 19, 2015-2029.

- W -

Wang C.K., Chen Lin J.H., Ju C.P., Ong H.C. and Chang R.P.H. (1997), Structureal characterization of pulsed laser-deposited hydroxyapatite film on titanium substrate, *Biomaterials* 18, 1331-1338.

Wang D.Z., Jayasinghe S.N., Edirisinghe M.J. (2005), Instrument for electrohydrodynamic print-patterning three-dimensional complex structures. *Rev. Sci. Instrum.* 76, art. no. 075105.

Wang H., Chen C.Z. and Wang D.G. (2006), Development of hydroxyapatite coating prepared by sol-gel technique. *Surf. Rev. Lett.* 13, 737-745.

Wang Y.F., Yan Y.H., Ren W., Cao X.Y. and Li S.P. (2004), Preparation and characterization of nano hydroxyapatite sol. *Trans. Nonferrous Met. Soc. China.* 14, 29-32.

Weber C. (1931), On the breakdown of a fluid jet. *Journal of Mechanics and Applied Mathematics* 11, 136-159.

Wei M., Ruys A.J., Swain M.V., Kim S.H., Milthorpe B.K. and Sorrel C.C. (1999a), Solution ripening of hydroxyapatite nanoparticles: effects on electrophoretic deposition. *J. Biomed. Mater. Res.* 45, 11-19.

Wei M., Ruys A.J., Swain M.V., Kim S.H., Milthorpe B.K. and Sorrel C.C. (1999b), Interfacial bond strength of electrophoretically deposited hydroxyapatite coatings on metals. *J. Mater. Sci.: -Mater. Med.* 10, 401-409.

Weng W. and Baptista J.L. (1999), Preparation and characterisation of hydroxyapatite coatings on Ti-6Al-4V alloy by a sol-gel method. *J. Am. Ceram. Soc.* 82, 27-32.

Wennerberg, A. (2003), Implant design and surface factors, *Int. J. Prosthodont.* 16, 7-51.

Wennerberg A., Albrektsson T., Johansson C. and Andersson B. (1996a), 'Experimental study of turned and grit-blasted scrow-shaped implants with special emphasis on effects of blasting material and surface topography', *Biomaterial*s 17, 15-22.

Wennerberg A., Ohlsson R., Rosen B.G. and Andersson B. (1996b), Characterizing three-dimentional topography of engineering and biomaterial surfaces by confocal laser scanning and stylus techniques, *Med. Eng. Phys.* 18, 548-556.

Wilhelm O., Madler L. and Pratsinis S.E. (2003), Electrospray evaporation and deposition. *J. Aerosol Sci.* 34, 815-836.

Wong M., Eulenberger J., Schenk R. and Hunziker E. (1995), Bioglass middle ear devices: ten year clinical results, *J. Biomed. Mater. Res.* 29, 1567-1575.

Wolke J.G.C., van Dijk K., Schaeken H.G., de Groot K. and Jansen J.A. (1994), Study of the surface characteristics of magnetron-sputtered calcium phosphate coatings, *J. Biomed. Mater. Res.* 28, 1477-1484.

- Y -

Yan Y.G., Wolke J.G.C., Li Y.B. and Jansen J.A. (2006), Preparation and characterization of RF magnetron sputtered calcium pyrophosphate coatings. *J. Biomed. Mater. Res. A.* 76A, 744-752.

Young R.A. (1967), Dependence of apatite properties on crystal details, in: Transaction of New York Academy Science, Series II, Vol. 29, pp.949-959.

- Z -

Zeleny J. (1914), The electrical discharge from liquids points and a hydrostatic method of measuring the electric intensities at their surfaces. *Phys. Rev. E* 3, 69-91.

Zeng H. and Lacefield W.R. (2000a), The study of surface transformation of pulsed laser deposited hydroxyapatite coatings. *J. Biomed. Mater. Res.* 50, 239-247.

Zeng H. and Lacefield W.R. (2000b), XPS, EDX and FTIR analysis of pulsed laser deposited calcium phosphate bioceramic coatings: The effects of various process parameters, *Biomaterials* 21, 23-30.

Zeng H. and Lacefield W.R. (2000c), Structural and morphological study of pulsed laser deposited calcium phosphate bioceramic coatings: Influence of deposition conditions, laser parameters, and target properties, *J. Biomed. Mater. Res.* 50, 248-258.

Zhang C., Leng Y. and Chen J.Y. (2001), In vitro mechanical integrity of hydroxyapatite coatings on Ti-6AL-4V implants under shear loading. *J. Biomed. Mater. Res.* 56, 342-350.